

Investigating the Timescales and Pathways of Southern Ocean Water Masses Using Transient Tracers and ECCOv4

Submitted by Genevieve Josephine Grace Hinde
to the University of Exeter as a thesis for the degree of
Doctor of Philosophy in Physical Geography
December 2021

This thesis is available for Library use on the understanding that it is copyright material and that no quotation from the thesis may be published without proper acknowledgement.

I certify that all material in this thesis which is not my own work has been identified and that any material that has previously been submitted and approved for the award of a degree by this or any other University has been acknowledged.

Signature.....

Abstract

It is widely accepted that we live in a changing climate, with rising global temperatures and an increasing concentration of atmospheric CO₂. The Southern Ocean, despite only accounting for 30% of global ocean surface area, is estimated to have been responsible for 43% of anthropogenic CO₂ and 75% of heat uptake over the period 1861-2005 (Frölicher et al., 2015). This excess heat and carbon is transported from the surface ocean to the interior ocean predominately by two water masses, Antarctic Intermediate Water (AAIW) and Antarctic Bottom Water (AABW). However, little is known about the timescales of this transport and how these timescales may be changing in response to climate change. This research uses transient tracers (CFCs and SF₆) to identify these timescales. A Maximum Entropy Method (MEM) is applied to tracer measurements taken at 24°S in the South Atlantic in 2009 and 2018, in order to diagnose the location and point in recent history that these waters were last in contact with the atmosphere. Additionally, passive tracer experiments in ECCOv4 are used to validate the results obtained by the MEM. Multiple temporal origins are identified in AAIW at 24°S. They suggest a contribution from young waters of 5 - 25 years from north of the Subantarctic Front, and older waters of 35 - 55 years, from south of the Polar Front. When these ages are compared between the 2009 and 2018 data, the younger less dense waters appear to age by 3 years and the more dense older waters appear to age by 9 years. Multiple theories surrounding the ageing of this water are explored, including the possibility of an influence from water formed by the Weddell Polynya in the early 1970s. Analysis of the AABW at 24°S confirms a strong influence of water from the Weddell Sea, and suggests a timescale of 30 years for this surface water to reach 24°S. These results provide the information needed to estimate the uptake of anthropogenic carbon and added heat by Southern Ocean water masses. They also act as a baseline for assessing future changes in circulation, a task particularly pertinent in our warming world.

Contents

Chapter 1: Introduction and Background	13
1.1 Introduction	13
1.2 Southern Ocean Circulation	16
1.2.1 Winds	16
1.2.2 Meridional Overturning	17
1.2.3 AAIW Formation	19
1.2.4 AAIW Circulation	21
1.2.5 Agulhas Leakage and Agulhas Rings	25
1.2.6 AABW Formation	26
1.2.7 AABW Circulation	27
1.3 Changes in the Southern Ocean	28
1.3.1 The Upper Limb	28
1.3.2 The Lower Limb	31
1.4 Transient Tracers & Radiocarbon	35
1.4.1 Transient Tracers	35
1.4.2 Radiocarbon	36
1.4.3 Studying Circulation Using Transient Tracers	38
1.5 Aims and Objectives	40
Chapter 2: Data	41
2.1 Cruise Overview	41
2.2 Water Mass Definitions	47
2.2.1 Antarctic Intermediate Water	47
2.2.2 Antarctic Bottom Water	50
2.3 Transient Tracer Sampling at 24°S	51
2.4 SF ₆ Tracer Release Contamination	53
2.5 Interior C-14 data	54
Chapter 3: Methods	55
3.1 Maximum Entropy Method: Applying the Method	55
3.1.1 Introduction	55
3.1.2 The Principles	56
3.1.3 Constraining Data	57
3.1.4 Data Standardisation & Tracer Weighting	61
3.1.5 Prior	62
3.1.5.1 <i>Generating the Inverse Gaussian Temporal Prior</i>	64
3.1.5.2 <i>Generating the ECCO Spatial Prior</i>	65
3.2 Maximum Entropy Method: Data Interpretation Methods & Metrics	65
3.2.1 Calculating Errors	65
3.2.2 Choosing the Regions	66
3.2.3 Visualising 3D Data	68
3.2.4 Water Age	69
3.3 Ocean Modelling Methods	70

3.3.1	ECCOv4r2 Configuration of MITgcm	70
3.3.2	Global Ocean Passive Tracer Experiment	72
3.3.3	Southern Ocean Fronts in ECCO	73
3.3.4	Comparing ECCO to Observations	76
3.3.5	Model Stability	79
3.3.6	Weddell Polynya Experiment	82
3.3.7	Calculating ECCO Arrival Times	82
Chapter 4: Temporal and Spatial Origins of AAIW at 24°S, from a Combined Maximum Entropy Method and ECCOv4 Approach		85
4.1	Introduction	86
4.1.1	Background of AAIW at 24°S	87
4.1.2	Methods Specific to the AAIW Analysis	88
4.2	Spatial Origin of Water	89
4.2.1	At the Salinity Minimum	89
4.2.2	Variations with Depth	90
4.3	Temporal Origin of Water	94
4.3.1	Origin of Each AAIW Class	94
4.3.2	Variations across the Section	99
4.3.2.1	<i>S of PF</i>	99
4.3.2.2	<i>PF to SAF</i>	102
4.3.2.3	<i>N of SAF</i>	102
4.4	Seasonality	103
4.5	ECCO Passive Tracer Results	104
4.5.1	ECCO Average Tracer Profiles at 24°S	105
4.5.2	Water from N of SAF in the Indian Ocean: Pathways and Timescales in ECCO	107
4.5.3	Waters from S of PF in the Pacific and Atlantic Oceans: Pathways and Timescales in ECCO	111
4.5.4	Waters from PF to SAF in the Pacific Ocean: Pathways and Timescales in ECCO	116
4.6	Comparing MEM and ECCO Results to the Literature	118
4.6.1	AASW Source	119
4.6.2	Southeast Pacific Source	121
4.6.3	Indian Ocean Source	124
4.7	Comparing Temporal Patterns in Decadal Repeat Observations	127
4.8	Influence of the Prior	134
4.9	Summary & Conclusion	138
Chapter 5: Evaluating the Reach of Waters Formed in the Weddell Polynya Using Passive Tracers in ECCO		140
5.1	Motivation & Background	140
5.2	Polynya Specific Methods	144
5.3	Polynya Development and Spread within the Weddell Sea	148
5.3.1	Polynya Development in Year 1	149
5.3.2	Signatures of Polynyas in Sea Ice (Years 1-5)	151
5.3.3	Pathways of Polynya Water	154
5.3.4	Volume of Polynya Water	157

5.3.5	Additional Polynya	158
5.5	Long-term Impact of the Polynya	160
5.5.1	Changes to Southern Ocean Circulation	161
5.5.2	Where does Polynya Water End Up?	164
5.5.3	Zonal Basin Averages at Year 80	168
5.5.4	Signals at 24°S	170
5.6	Further Discussion & Conclusion	170
Chapter 6: Temporal and Spatial Origins of AABW at 24°S, from a Combined Maximum Entropy Method and ECCOv4 Approach		174
6.1	Introduction	175
6.1.1	Background of AABW at 24°S	175
6.1.2	Methods Specific to the AABW Analysis	176
6.2	Spatial Origin of Water	177
6.3	Temporal Origin of Water	179
6.4	Comparing Patterns in Decadal Repeat Observations	183
6.5	Seasonality	185
6.6	Influence of the Prior	187
6.7	Excluding ^{14}C as a Constraining Tracer	190
6.8	Comparison of MEM Results to ECCO	193
6.9	Comparison of Main Findings to the Literature	197
6.10	Conclusion	198
Chapter 7: Overall Conclusion		202
References		207

List of Figures

1.1	Schematic of Southern Hemisphere Westerly Winds	13
1.2	Schematic of the Southern Ocean meridional overturning circulation	14
1.3	Schematic of the 3D Southern Ocean circulation	15
1.4	Map of relevant currents and locations in the Southern Ocean	20
1.5	Schematic of intermediate water circulation between the Indian and Atlantic Oceans	23
1.6	Schematic of the circulation of AAIW in the Indian Ocean	24
1.7	Atmospheric history of transient tracers	35
2.1	Map of station locations	42
2.2	Sections of conservative temperature, absolute salinity, oxygen and P* at 24°S in 2009	43
2.3	Sections of CFC-11, CFC-12, and SF ₆ at 24°S in 2009 and section of GLODAP ¹⁴ C gridded values at 24°S	44
2.4	Sections of conservative temperature, absolute salinity, oxygen and P* at 24°S in 2018	45
2.5	Sections of CFC-11, CFC-12, and SF ₆ at 24°S in 2018	46
2.6	Temperature – Salinity diagrams for the 2009 and 2018 data	47
3.1	Schematic of the Maximum Entropy Method	63
3.2	Maps of regions used for analysis	67
3.3	Comparison of climatological Polar Front and Subantarctic Front positions with those in ECCO	75
3.4	Section comparisons of potential temperature and salinity observations with ECCO at 24°S	77
3.5	Comparison of depth profiles of potential temperature, salinity and neutral density, between observations and ECCO	78
3.6	Atlantic/Southern Ocean residual overturning circulation at 280-300 years in ECCO, and anomaly from initial 20 years	79
3.7	Map of barotropic streamfunction at 280-300 yrs in ECCO	80

3.8	Time series of domain average temperature and Drake Passage transport in ECCO	81
4.1	Enlarged map of regions used in analysis	86
4.2	Profiles of regional contributions predicted by the MEM using the 2009 data	91
4.3	Profiles of regional contributions predicted by the MEM using the 2018 data	92
4.4	MEM predicted temporal origin for AAIW 1, AAIW 2 and AAIW 3, for the 2009 and 2018 data	95
4.5	MEM predicted temporal origin for AAIW 1, AAIW 2, and AAIW 3, subdivided by Southern Ocean region, for the 2009 data	97
4.6	MEM predicted temporal origin for AAIW 1, AAIW 2, and AAIW 3, subdivided by Southern Ocean region, for the 2018 data	98
4.7	Sections of temporal probability predicted by the MEM, subdivided by Southern Ocean region, for the 2009 data	100
4.8	Sections of temporal probability predicted by the MEM, subdivided by Southern Ocean region, for the 2018 data	101
4.9	Seasonality of MEM predicted temporal origin of AAIW, for both the 2009 and 2018 data	103
4.10	Profiles of passive tracer concentration and salinity at 24°S in ECCO at 300 years	105
4.11	Maps of Indian N of SAF ECCO passive tracer on density surface $\sigma_n = 26.7 \text{ kg m}^{-3}$, and depth of density surface at 15 years	108
4.12	Sections of Indian N of SAF ECCO passive tracer at 50 yrs at 24°S, 10 yrs at 20°E, 10 years at 50°E, and 10 yrs at 80°E	109
4.13	Time series of ECCO passive tracer concentration and rate of arrival at AAIW depths at 24°S	110
4.14	Maps of Pacific S of PF ECCO passive tracer on density surface $\sigma_n = 27.4 \text{ kg m}^{-3}$, and depth of density surface at 15 years	112
4.15	Sections of Pacific S of PF ECCO passive tracer at 50 yrs at 24°S, 15 yrs at 47°S, 15 yrs at 185°W, 15 yrs at 110°W and 15 yrs at 55°W	113
4.16	Map of Atlantic S of PF ECCO passive tracer on density surface $\sigma_n = 27.4 \text{ kg m}^{-3}$ at 15 yrs	115
4.17	Sections of Atlantic S of PF ECCO passive tracer at 50 yrs at 24°S and 15 yrs at 30°W	116
4.18	Map of Pacific PF to SAF ECCO passive tracer on density surface $\sigma_n = 27.4 \text{ kg m}^{-3}$ at 15 yrs	117
4.19	Sections of Pacific PF to SAF ECCO passive tracer at 50 yrs at 24°S, 15 yrs at 90°W and 15 yrs at 30°W	118
4.20	MEM predicted temporal origin for AAIW 1 for the 2009 and 2018 data, comparing on an axis of age and date	128

4.21	Profiles of Southern Ocean regional contributions predicted by the MEM for the 2009 and 2018 data, under different prior scenarios	135
4.22	Probability distribution of MEM predicted temporal origin for AAIW 1, AAIW 2 and AAIW 3, under different prior scenarios	137
5.1	Map of Atlantic sector of the Southern Ocean, showing area of polynya forcing	145
5.2	Atlantic/Southern Ocean residual overturning circulation at 70-80 years, and residual overturning anomaly at 70-80 years in the ECCO Forced Polynya experiment	147
5.3	Sections of temperature and PolSurTr at the location of the polynya forcing during Year 1	150
5.4	Maps of monthly sea-ice concentration for Year 1 of Forced Polynya experiment	151
5.5	Maps of monthly sea-ice concentration for Year 2, 3 and 4 of Forced Polynya experiment	152
5.6	Map and sections showing the spread of Polynya Water within the Weddell Sea at 1.4 years	155
5.7	Map and sections showing the spread of Polynya Water within the Weddell Sea at 5.5 years	156
5.8	Sections plots of temperature and WedSurTr at the location of the additional polynya in Year 3	159
5.9	Time series of Drake Passage transport in CTRL and Forced Polynya experiment	161
5.10	Anomaly of zonal mean bolus meridional overturning for Years 5 & 6 and zonal mean of density anomaly for the western Weddell Sea	162
5.11	Histograms of volume of Polynya Water in different density classes at 2, 5, 10, 20, 25 and 80 Years	164
5.12	Maps of WedSurTr on the $\sigma_0 = 27.85 \text{ kg m}^{-3}$ at 10, 45 and 80 yrs	166
5.13	Maps of WedSurTr on the $\sigma_0 = 27.92 \text{ kg m}^{-3}$ at 40 and 80 yrs	167
5.14	Sections of zonal basin average WedSurTr anomaly at 80 yrs	169
5.15	Zonal section of WedSurTr anomaly at 24°S at 80 yrs	170
5.16	Mean ρ_0 for the surface 2000 m of CTRL in September Year 1	172
6.1	Map of MEM predicted spatial origin of cAABW and pAABW using the 2009 and 2018 data	177
6.2	Sections of MEM predicted contribution of Weddell and Lab & GIN Seas to AABW, 2009 and 2018 data	178
6.3	MEM predicted temporal origin of AABW, for 2009 and 2018 data	179

6.4	Sections of MEM predicted contribution from different time periods (pre 1975, 1975-2000, and post 2000) at 24°S, for 2009 and 2018 data	181
6.5	MEM predicted temporal origin of AABW, for 2009 and 2018 data, compared to history of surface ocean CFC-11/CFC-12 ratio	183
6.6	Seasonality of MEM predicted temporal origin of cAABW, for both the 2009 and 2018 data	186
6.7	Maps of MEM predicted spatial origin of cAABW, using the 2009 data, under four different prior scenarios	188
6.8	MEM predicted temporal origin of cAABW, under four different prior scenarios	189
6.9	MEM predicted temporal origin of AABW with and without ^{14}C as a constraining tracer	191
6.10	Map of gridded ^{14}C values and bottle sample values in the surface Weddell Sea	192
6.11	Sections of Weddell and Lab & GIN seas tracer at 24°S and maps of ECCO predicted region of origin for pAABW and cAABW	194
6.12	Time series of ECCO passive tracer concentration and rate of arrival at AABW point core at 24°S	196

List of Tables

1.1	Summary of studies of the cold and warm pathway of AAIW	22
1.2	^{14}C derived water ages per basin	38
2.1	Summary of cruise information	42
2.2	Summary of AAIW definitions from the literature	48
2.3	Average tracer values on JC032 for each defined water mass	49
2.4	Average tracer values on JC159 for each defined water mass	49
2.5	Precision of CFC and SF ₆ measurements	52
4.1	Regional contribution to the AAIW salinity minimum as predicted by the MEM	89
6.1	Measured ^{14}C values for cAABW and pAABW samples	192
6.2	MEM and ECCO predicted percentage contributions of Weddell Sea and Lab & GIN Seas water to pAABW and cAABW at 24°S	194

Acronyms & Initialisms

AABW	Antarctic Bottom Water
AAIW	Antarctic Intermediate Water
AAWW	Antarctic Winter Water
ACC	Antarctic Circumpolar Current
ADCP	Acoustic Doppler Current Profiler
AMOC	Atlantic Meridional Overturning Circulation
ANDREX	Antarctic Deep Water Rates of Export (Project)
AOU	Apparent Oxygen Utilisation
C _{ant}	Anthropogenic Carbon
CDW	Circumpolar Deep Water
CTD	Conductivity-Temperature-Depth
CTRL	Control Experiment
ECCO	Estimating the Circulation and Climate of the Ocean (project/model)
FP	Forced Polynya Experiment
HSSW	High Salinity Shelf Water
IG	Inverse Gaussian
LCDW	Lower Circumpolar Deep Water
mCDW	Modified Circumpolar Deep Water
MEM	Maximum Entropy Method
NADW	North Atlantic Deep Water
NOAA	National Oceanic and Atmospheric Administration
PF	Polar Front
PW	Polynya Water
RSW	Red Sea Water
SAF	Subantarctic Front
SAMW	Subantarctic Mode Water
SO	Southern Ocean
SROCC	Special Report on the Oceans and Cryosphere in a Changing Climate
TICTOC	Transient tracer-based Investigation of Circulation and Thermal Ocean Change (Project)
TTD	Time Transit Distribution
UCDW	Upper Circumpolar Deep Water
WDW	Warm Deep Water
WSBW	Weddell Sea Bottom Water
WSDW	Weddell Sea Deep Water

Acknowledgements

Many thanks go to all my supervisors who have provided their knowledge and experience throughout my PhD and to the Natural Environment Research Council for funding my studentship.

I would like to particularly thank Dr Marie-Jose Messias for all the hard work she has put into the research cruises on which my data was collected and for sharing her expertise on transient tracers with me. I would also like to thank Dr Dave Munday for many a skype meeting (before the world started to zoom!), for continual encouragement and support throughout my PhD, and for teaching me all I know about the world of ocean modelling. Finally, I would like to thank Professor Mike Meredith for always having a paper to recommend and for his Southern Ocean expertise, and Dr Paul Halloran for helping to steer the project it its early days.

My thanks also go to all those who facilitated and accompanied me on my fieldwork, to the South Atlantic and Southern Ocean. To all the crew on board the RRS James Cook and the RRS James Clark Ross, who looked after us and persevered through bad weather and set-backs to deploy hundreds of CTDs. My special thanks go to Jack Hughes and the late Dr Gary Murphy who were the best company, and kept me sane through many dark night shifts in the container. Gary, you are greatly missed by all.

I would like to thank all of my officemates in Exeter for great company on long days sat behind a computer. I would particularly like to thank Dr Neill Mackay for his informal mentoring and encouragement with my PhD. I would also particularly like to thank my desk neighbour, Aimee Coggins, with whom I shared a ‘plant menagerie’ for the years we were in the office, and whose weekly ‘Thesis Friday’ Teams calls have helped to keep up my spirits throughout all the time working from home.

Finally I would like to thank my friends and family for their support and also for providing some distraction from my PhD. To Katie, Nicola, Lewis, Lauren, Charlotte, and many more, who were always behind me when I needed them, and of course Alex, for his patience and unwavering support, and for countless homemade dinners over the past months.

Chapter 1:

Introduction and Background

1.1 Introduction

It is widely accepted that we live in a changing climate, with rising global temperatures and an increasing concentration of atmospheric CO₂. Within the earth system the oceans provide a sink for some of this additional heat and CO₂. The Southern Ocean, despite only accounting for 30% of global ocean surface area, is estimated to be responsible for 43% of anthropogenic CO₂ and 75% of heat uptake over the 1861-2005 period (Frölicher *et al.*, 2015). This uptake is significant not only for its impact on rising global temperatures, but also for the additional consequences to the oceans, such as ocean acidification and sea level rise.

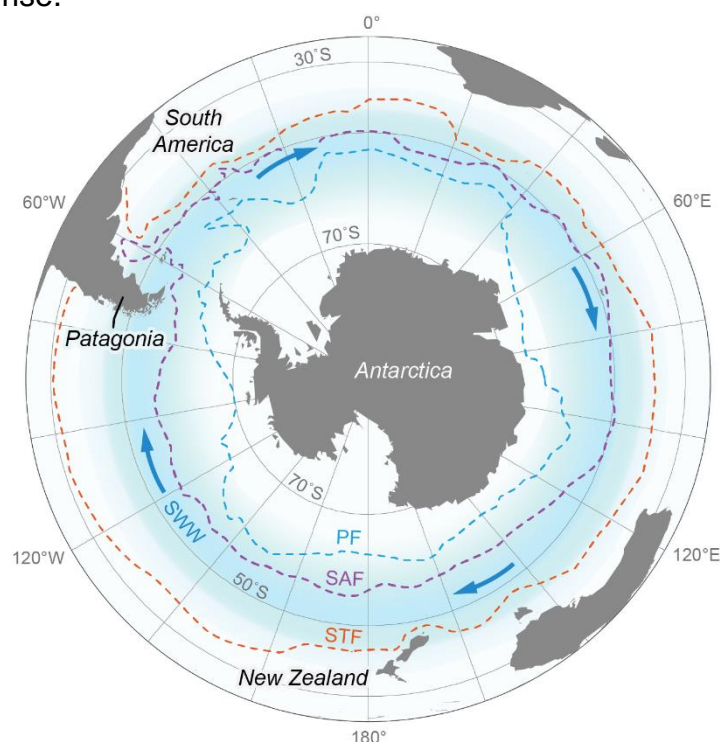


Figure 1.1 – Schematic of the circumpolar Southern Hemisphere Westerly Winds (labelled SWW), blue shading indicates the position of the wind belt. Dashed lines indicate the positions of Southern Ocean fronts; PF = Polar Front, SAF = Subantarctic Front, and STF = Subtropical Front. Reproduced from Davies (2020).

A study in 2007 (Le Quéré *et al.*, 2007), which used atmospheric CO₂ concentrations in an inverse model, found the strength of the Southern Ocean carbon sink to be weakening between 1981 and 2004 and speculated this change was due to human induced strengthening of the Southern Ocean winds (see Section 1.2.1; Figure 1.1). However, more recent studies have suggested that although the sink weakened in the 1990s, it strengthened during the period 2002-2012 (Landschützer *et al.*, 2015; Mikaloff-Fletcher, 2015). This variability highlights the complexity of the Southern Ocean and its response to different forcings. Modelling allows us an opportunity to predict some of the future responses to changes in forcings such as wind, however currently the largest uncertainties in model predictions come from the Southern Ocean region (Frölicher *et al.*, 2015).

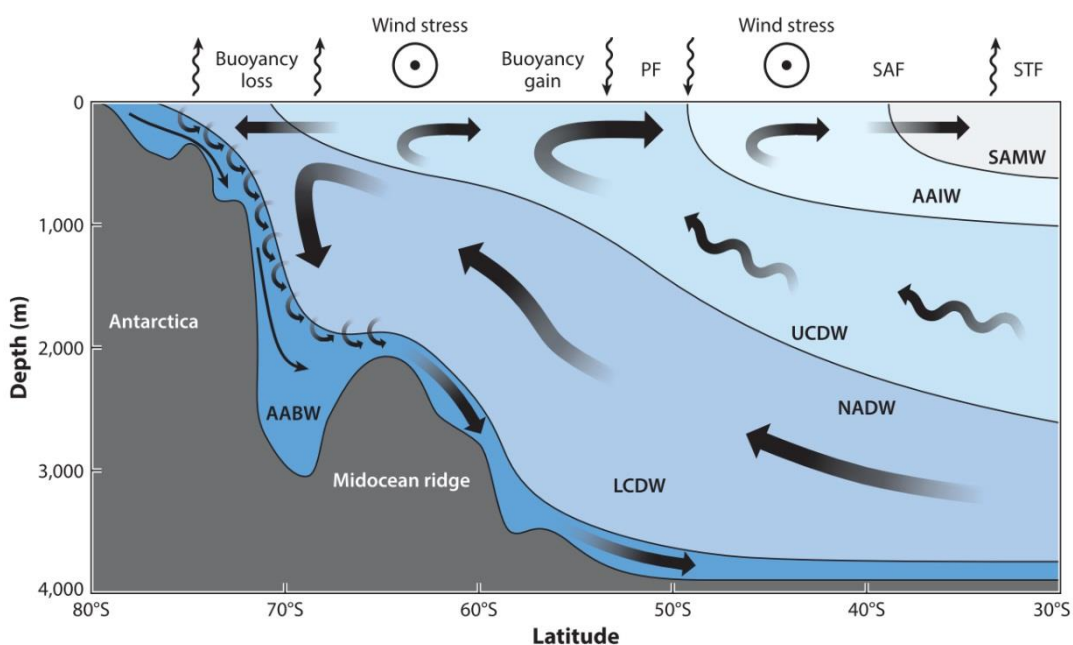


Figure 1.2 – Schematic of the Southern Ocean Meridional Overturning Circulation. PF = Polar Front, SAF = Subantarctic Front, STF = Subtropical Front, AABW = Antarctic Bottom Water, LCDW = Lower Circumpolar Deep Water, NADW = North Atlantic Deep Water, UCDW = Upper Circumpolar Deep Water, AAIW = Antarctic Intermediate Water, SAMW = Subantarctic Mode Water. Reproduced from Gent (2016). For further explanation see Section 1.2.2.

There is a general view that a warming planet will see more stratified oceans, isolating the deep ocean and reducing carbon and heat uptake. However, it is thought that due to the complex dynamics and circulation of the Southern Ocean (see Section 1.2; Figures 1.2 & 1.3) this reduction may not be seen there in the same way (Russell *et al.*, 2006). Globally, warming has been observed in the ocean at depths of 700-2000 m for the period 1957-2009, and in waters below 3000 m between 1992 and 2005. The largest contribution to this warming signal has come from the Southern Ocean (Rhein *et al.*, 2013). Under all future IPCC RCP scenarios, the deep ocean is predicted to continue to warm, with the most pronounced predicted warming in the Southern Ocean (Collins *et al.*, 2013). To improve the representation of Southern Ocean heat and carbon uptake in models, estimates of current uptake, and understanding of the drivers of this uptake, must be improved.

This initial chapter therefore reviews the existing knowledge of Southern Ocean circulation and how the system is changing, as well as introducing the use of transient tracers to study timescales of circulation.

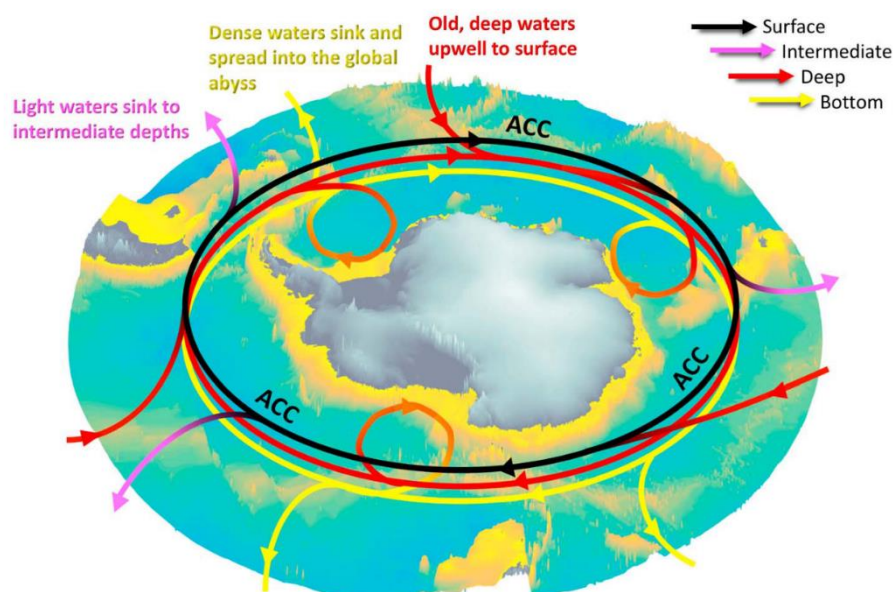


Figure 1.3 – Schematic of the three-dimensional circulation within the Southern Ocean.
Reproduced from Meredith, (2016). For further explanation see Section 1.2.2.

1.2 Southern Ocean Circulation

1.2.1 Winds

In order to understand the Southern Ocean circulation, the winds must first be considered, as wind stress on the ocean surface is a major input of energy to the oceans. The Southern Ocean is exposed to the strongest time-mean oceanic winds in the world, the Southern Hemisphere Westerlies (Russell *et al.*, 2006). These winds, like the oceanic Antarctic Circumpolar Current (ACC) which they drive, travel around the world uninterrupted by land (Figure 1.1).

The Southern Annular Mode (SAM) index is defined by the difference in zonal mean sea-level pressure between 40°S and 60°S, and describes the variable latitudinal position and strength of this wind belt. In recent years the SAM index has been dominated by the positive phase (Marshall *et al.*, 2018), meaning an intensification and poleward shift of the Southern Hemisphere Westerlies. This trend is thought to be partly caused by the reduction of ozone in the stratosphere, combined with increasing levels of greenhouse gases (GHGs) (Thompson and Solomon, 2002).

Future predictions of the strength and position of the winds vary between studies. One study using a CCMVal (Chemistry-Climate Model Validation) model, which has interactive stratospheric chemistry, predicted the poleward side of the Southern Hemisphere Westerlies to weaken as the stratospheric ozone levels recovered (Son *et al.*, 2008). Conversely, the IPCC AR5 report predicts that increasing greenhouse gas emissions will compensate for the weakening effect of the recovering ozone levels, and suggests it is likely that the Southern Hemisphere Westerlies will continue to shift poleward, but at a less rapid rate (Kirtman *et al.*, 2013).

1.2.2 Meridional Overturning

Energy is required to bring deep, dense waters to the surface of the ocean. In the Southern Ocean this energy comes from the Southern Hemisphere Westerly Winds. Eastward wind stress on the ocean surface combines with the Coriolis force to create a northward Ekman flow. This in turn leads to surface divergence, which causes water deeper in the water column to upwell along sloping isopycnals (Morrison *et al.*, 2015). This sets up a meridional circulation, known as the Southern Ocean Meridional Overturning Circulation which is comprised of an upper cell and a lower cell (Figure 1.2). The waters flowing northward as part of the upper cell interact with the atmosphere and gain buoyancy to later form Antarctic Intermediate Water (AAIW) and Subantarctic Mode Water (SAMW), whilst the water that upwelled close to the Antarctic continent as part of the lower cell loses buoyancy (increases in density), mixes with High Salinity Shelf Waters (HSSW) and sinks to form Antarctic Bottom Water (AABW) (Jacobs *et al.*, 1985; Speer *et al.*, 2000).

This meridional circulation sets the density structure of the Southern Ocean, and the meridional pressure gradient set by this circulation ultimately controls the velocity of the ACC which transports water between the Atlantic, Pacific and Indian Ocean basins (Olbers *et al.*, 2004). The ACC is not a single current travelling around Antarctica, but is in fact split into multiple jets associated with the different fronts. The distinctness of these jets vary around Antarctica. However, at Drake Passage three ocean jets are identified as being responsible for the majority of the ACC zonal transport. These are the jets found at the Polar Front (PF), the Subantarctic Front (SAF) and the Southern ACC Front, which lies poleward of the PF (Orsi *et al.*, 1995).

This system seems simple at its basic level of explanation, however when one looks into the response of this system to, for example, a strengthening of the winds, one starts to see the complexities within it. It has been suggested (e.g. Hall and Visbeck, 2002) that a strengthening of the winds would lead to increased Ekman transport to the north, causing greater surface divergence and more upwelling, which would lead to more steeply sloped isopycnals. However, observations suggest that isopycnals have not steepened with an increase in the strength of the winds (Böning *et al.*, 2008). An explanation for why no change in the slope of the isopycnals is seen, is the concept of ‘eddy compensation’ where southward eddy fluxes compensate for increases in the northward Ekman transport caused by stronger westerly winds (Marshall and Speer, 2012). Although this concept is generally accepted, many of the present global models do not have resolutions high enough to resolve these mesoscale eddies.

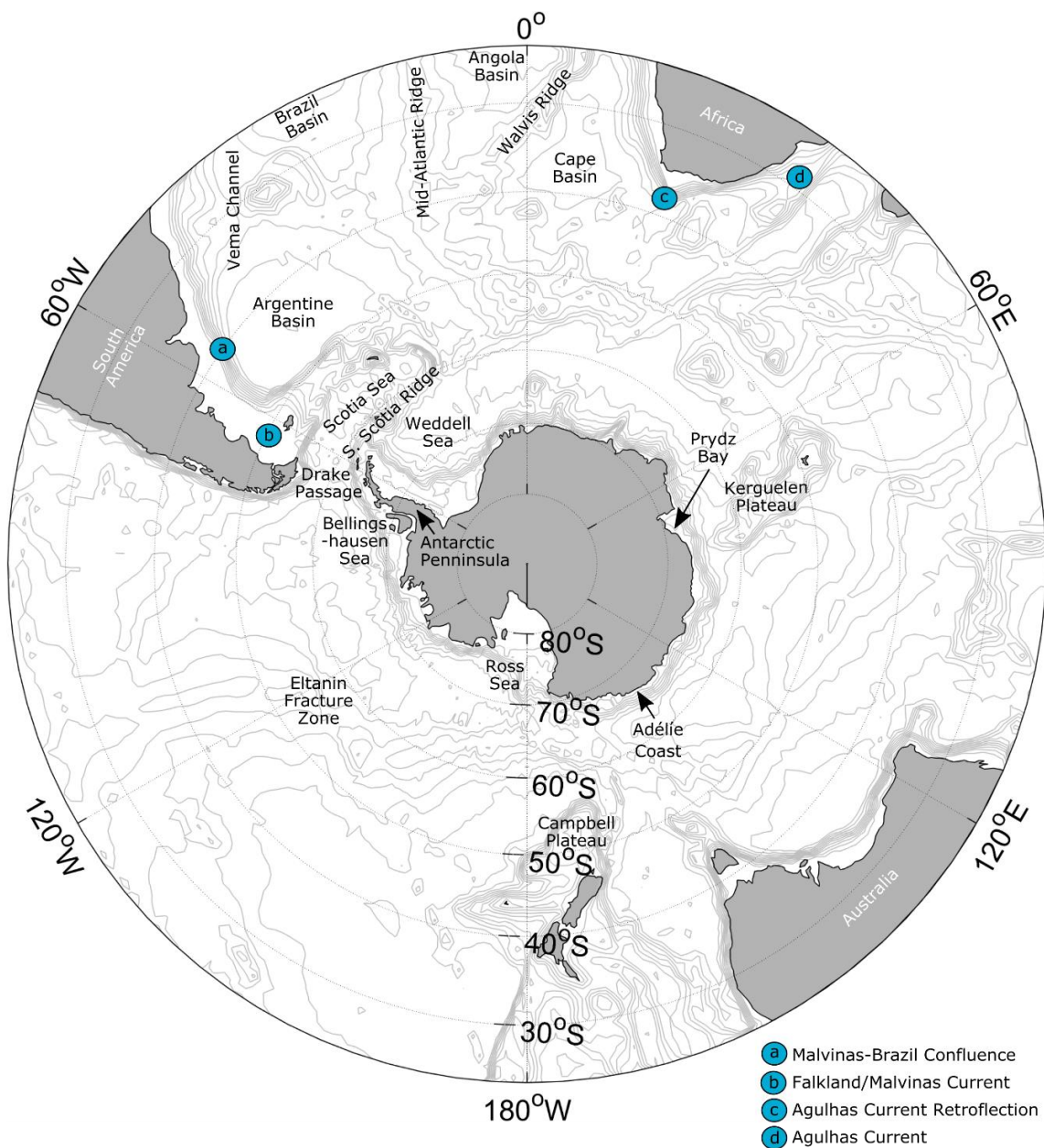
The system is further complicated by the three-dimensional nature (Figure 1.3) of the Southern Ocean circulation, with the ACC carrying water eastward perpendicular to the meridional overturning. Although the circulation is often viewed as a zonal average (e.g. Figure 1.2), in reality there are also ways in which water is transformed from the lower limb of the circulation to the upper limb (Lumpkin and Speer, 2007), though these processes are not well understood (Marsh *et al.*, 2000).

A strong motivation for studying the Southern Ocean meridional overturning is the need to gain a better understanding of the Southern Ocean’s role in the uptake of anthropogenic carbon (C_{ant}) and heat. In the Southern Ocean, Circumpolar Deep Water (CDW) is thought to be responsible for the largest amount of C_{ant} storage ($34 \pm 4\%$) with AAIW responsible for $20 \pm 5\%$,

and AABW responsible for $9 \pm 1\%$ Pardo *et al.* (2014). Though AABW and AAIW are not responsible for the largest C_{ant} content, this thesis focusses on them, as they are the water masses that take surface waters to deep and intermediate depths. The following paragraphs explore the formation and circulation of these two key water masses.

1.2.3 AAIW Formation

The exact mechanisms of AAIW formation and the locations at which these processes take place has been a point of discussion for many years. The earliest theory of AAIW formation, and the simple picture often painted by schematics of Southern Ocean meridional overturning, is that deep water is upwelled south of the PF, cools and freshens via air-sea exchange on its journey northward, and then sinks beneath Subantarctic Surface Water (Sverdrup, Johnson & Fleming, 1942). An alternate mechanism was later proposed by McCartney (1977) whereby AAIW forms as the most dense variety of SAMW. He argued that the salinities and temperatures of the deep mixed layers in the southeast Pacific at the end of winter match those of the AAIW in the subtropical gyres. He suggested that this cold form of SAMW formed in the southeast Pacific and Scotia Sea, passed through Drake Passage and then circulated northward in the Falkland Current, entering the South Atlantic at the Malvinas-Brazil Confluence, and contributing to the lower temperature, lower salinity variety of AAIW observed in the Atlantic (see Figure 1.4 for locations).



Since these two theories were established, numerous studies have explored different elements of them. Jacobs and Georgi (1977) raised suspicions over the Antarctic Surface Water (surface water from south of the PF; AASW) origin of AAIW, as they note that nutrient levels in AAIW are higher than would be expected for an origin south of the Polar Front. However, in a more recent study at Drake Passage, Naveira Garabato *et al.* (2009) found the characteristics of AAIW in Drake Passage to be closely linked to the properties

of surface water in the Bellingshausen Sea the previous winter, supporting the idea of AASW as a precursor to AAIW.

Salée *et al.* (2010) looked at areas of subduction for both SAMW and AAIW in the Southern Ocean based on mixed layer properties. They identified areas in the Indian and Pacific oceans (near Kerguelen, Campbell Plateau and the Eltanin Fracture Zone) as regions of SAMW subduction, and identified Drake Passage as the only area where water directly subducts into AAIW density classes from the mixed layer. However, they do not mention where this area was in relation to the fronts. Sloyan *et al.* (2010) focussed further on this southeast Pacific region and suggested that reduced stratification north of the SAF helps to precondition the waters here for formation of AAIW, providing evidence to support the theory of McCartney (1977). In a coupled climate model, Santoso & England (2004) found AAIW to form in a circumpolar fashion, mostly from AASW. With evidence for both theories of formation in both models and observations, there is no clear consensus on which mechanism (if not both) is correct, or, if both mechanisms contribute to AAIW, what the relative importance of the two is.

1.2.4 AAIW Circulation

Theories of circulation of AAIW within the South Atlantic develop alongside new ideas of AAIW formation regions. It was originally thought that after being formed in the Southern Ocean, AAIW travelled northward in the Falklands (Malvinas) Current and then proceeded to travel northward along the western boundary towards the equator (Wust, 1935). Later studies (Buscaglia, 1971; Reid *et al.*, 1977; Reid, 1989) reviewed this circulation and suggested that between 40°S and 25°S in the Atlantic the intermediate water travelled in

Study	Cold contribution	Warm contribution	Method outline
You, 2002	$64 \pm 2\%$	$36 \pm 2\%$	Water mass mixing model, three end members: Drake AAIW, Indian AAIW and a combined end member (Atlantic AAIW).
Gordon <i>et al.</i> , 1992	50%	50%	Salinity, temperature and chluorofluoromethane observational study.

Table 1.1 – Summary of studies quantifying the ‘warm’ and ‘cold’ contributions to AAIW in the Atlantic.

the anticyclonic gyre system, first heading east, branching at the eastern boundary, with some water continuing north and then west to return to the western boundary before continuing to travel north. This pathway had not previously been considered, as Wust (1935) had thought that the wind-driven gyre circulation did not extend deep enough in the water column to influence the circulation of AAIW, and that the equatorward transport of AAIW was principally thermohaline transport. It is the more recently proposed pathway that is now accepted as the pathway of AAIW.

The work of Gordon *et al.* (1992) built further on this proposed circulation, suggesting that the AAIW found in the Atlantic was not solely water from Drake Passage/the southeast Pacific, but that there was a strong Indian Ocean influence. Numerous studies have debated this, and have investigated the mechanism and magnitude of this connection (e.g. Rintoul, 1991; Gordon *et al.*, 1992; You, 2002). Table 1.1 summarises two studies which quantify the contributions of the cold pathway (through Drake Passage) and the warm pathway (Indian Ocean contribution). The contribution from Drake Passage is thought to be relatively young, with low apparent oxygen utilization (AOU) and to also be fresher, in comparison to older, saltier, higher AOU water from the Indian Ocean (McCarthy *et al.*, 2011).

The warm pathway involves waters of Indian Ocean origin entering the South Atlantic via the Agulhas Current Retroflection; a current to the south of South Africa which originates in the Indian Ocean, travels into the southeast Atlantic and then returns eastward back into the Indian Ocean at a lower latitude (see Figure 1.5). Fine *et al.* (1988) studied this region using chlorofluoromethane in order to compare waters in the inflow of the retroflection current, with those returning back into the Indian Ocean, in order to understand the mixing and exchange of Indian Ocean waters with Atlantic Ocean waters in the retroflection. They found evidence to support strong mixing between Indian and Atlantic waters and to support the magnitude of Agulhas Leakage (see Section 1.2.5) proposed by Gordon (1985) and Gordon *et al.* (1987). They also explored the origins of the Indian Ocean water at intermediate depths and suggested that 50-75% of AAIW in the Agulhas Retroflection region had been diluted from its original core. It had previously been suggested that saline Red Sea Water (RSW) travelled south in the Agulhas Current and mixed with AAIW within the retroflection, eroding the salinity minimum (Jacobs and Georgi, 1977).

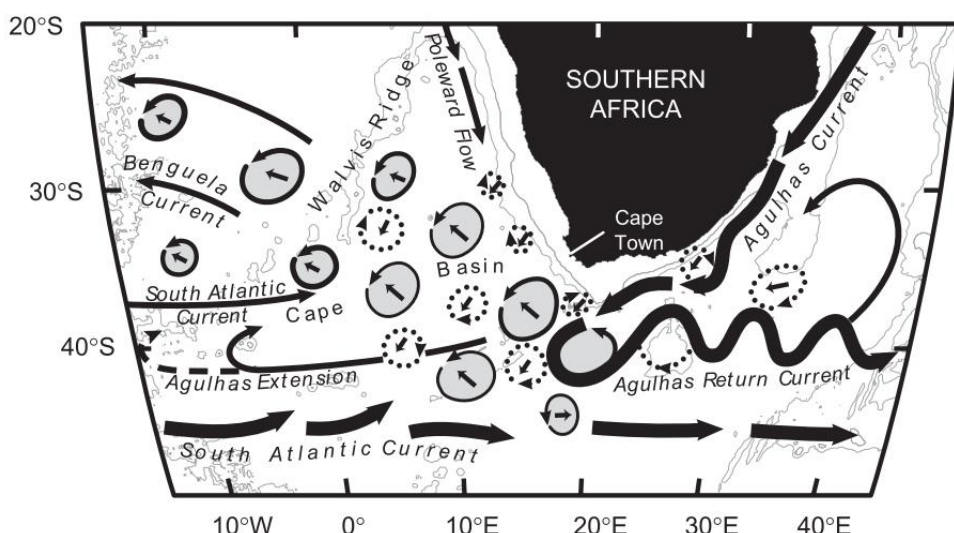


Figure 1.5 - Schematic map of the circulation of intermediate water between the southwest Indian Ocean and the southeast Atlantic Ocean. Cyclonic eddies are shown with dotted rings, Agulhas Rings (anti-cyclonic) are shown by solid rings. Arrows in the centre of each ring indicate their direction of propagation. Reproduced from Richardson (2007).

Fine *et al.* (1988) supported this and said that some of the observed dilution was likely due to mixing with RSW.

The origin of the AAIW core in the retroflection is thought to be a combination of Atlantic AAIW which has entered into the Indian Ocean and circulated around the gyre (Fine, 1993) and a new form of Indian AAIW formed within the PF within the Indian Sector (which in this location is combined with the SAF) (Molinelli, 1981). This newly formed Indian Sector AAIW is thought to spread northward across the Subantarctic Zone at a depth of 600 m, before descending to a depth of 1300 m as it reaches the Subtropical Front/Agulhas Front (Read and Pollard, 1993), before entering the retroflection region. Using a water mass mixing model, You (1998) also suggested that the Indian Sector of the Southern Ocean was a site of AAIW formation (see Figure 1.6). He identified two locations of formation, the first to the west of 70°E (similar to that

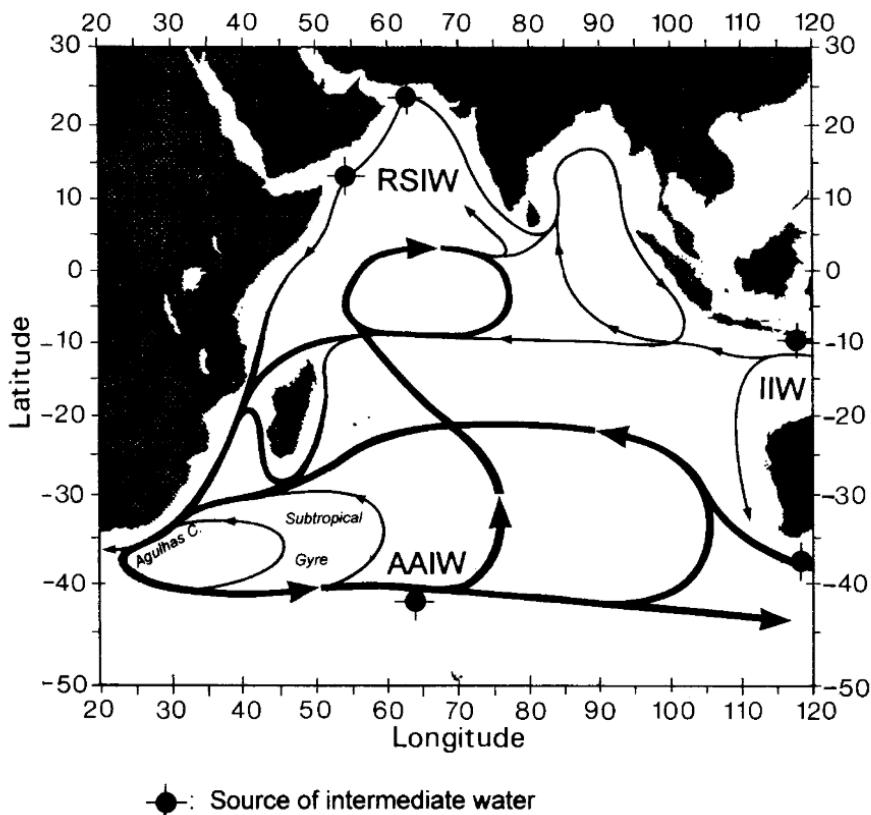


Figure 1.6 – Schematic summarising the circulation of intermediate waters in the Indian Ocean and highlighting areas identified as possible AAIW formation regions. Reproduced from You (1998).

suggested by Read and Pollard) and the second south of Australia.

1.2.5 Agulhas Leakage and Agulhas Rings

The Agulhas Current initially travels west to the south of South Africa before sharply turning back on itself in the Agulhas Retroflection and travelling eastward to the south of the westward branch (Figure 1.5). Eddies (known as Agulhas Rings) form in the Agulhas Retroflection, transporting Indian Ocean waters into the Atlantic. Water that escapes the Retroflection in these Agulhas Rings or by other means is termed Agulhas Leakage. In previous calculations it has often been assumed that the Agulhas Rings transport water at thermocline depths, but have less influence on the transport of intermediate waters.

McDonagh *et al.* (1999) showed that Agulhas Rings do transport intermediate water from the Indian Ocean to the Atlantic, but that the intermediate waters brought into the Atlantic are released by the eddy as it transits northward, so that the Agulhas Rings sampled further north no longer have the associated intermediate waters, but likely did in the past.

The pathways and prevalence of these eddies is also important to understand, as it can give an idea of where these intermediate waters may be released. Though the speed and direction of travel of the rings depends on local topography and the dynamics of the ring, it is the advection of the eddy within the mean flow that dominates the pathway of the eddy (McDonagh *et al.*, 1999). As shown by float data (Nunez-Riboni *et al.*, 2005), the circulation that transports these eddies northwest from South Africa, is the eastern boundary of the anticyclonic Subtropical Gyre.

Initial estimates of the number of Agulhas Rings generated annually was six (de Ruijter *et al.*, 1999), but Schouten *et al.* (2000) used altimetry data to

suggest an annual formation rate of 8.25 rings/year. Richardson (2007) used subsurface floats and surface drifters to estimate an Agulhas Leakage of 10-13 Sv based on this annual formation rate of 8.25 rings/year. He also suggested that some Indian Ocean water also enters the Atlantic via the westward flowing Agulhas extension, and that this water blends with the Atlantic water, eventually finding itself in the Bengula Current, adding a further 2.6 Sv to the leakage in the top 1000 m. Similar transports are estimated by Schmidt *et al.* (2021), who predict a mean Agulhas Leakage transport of 9.7-9.9 Sv for the period 1958-2014 based on a set of lagrangian model experiments. In the past two decades this Agulhas Leakage has increased (Biastoch *et al.*, 2009, 2015). It is thought that this change is driven by a changes in the westerly winds (Durgadoo *et al.*, 2013; Loveday *et al.*, 2015) and so may continue to increase with the predicted strengthening and poleward shift of these winds in the future (Toggweiler, 2009; Bracegirdle *et al.*, 2020).

1.2.6 AABW Formation

AABW is known to form at four locations along the Antarctic continental shelf. These are the Weddell Sea, the Ross Sea, Prydz Bay and the Adélie Coast (Orsi *et al.*, 1999; Yabuki *et al.*, 2006). In these areas a dense pool of shelf water forms, referred to as HSSW. This dense water forms due to cold polar air spreading seaward, creating coastal polynyas in addition to directly removing heat from the surface waters. The coastal polynyas cause salinification of the underlying waters due to brine rejection resulting from high rates of sea-ice production within the polynyas (Jacobs *et al.*, 1985). This dense shelf water is then exported over the continental slope in thin plumes (Heywood *et al.*, 2014, Gordon, 2009).

As this shelf water travels down the continental slope it mixes with entrained Warm Deep Water (WDW; also known as modified Circumpolar Deep Water, mCDW). Within the Weddell Sea the HSSW mixes more specifically with Weddell Sea Deep Water (WSDW). The resultant mixture is the AABW found in the deep ocean basins (Gordon, 2009). The characteristics of this shelf water varies between each of these formation regions, which leads to different varieties of AABW being produced. The Ross Sea produces the saltiest AABW with a characteristic temperature of -0.8°C and salinity of 34.70 (Gordon *et al.*, 2015; Jacobs and Comiso, 1989; Purkey *et al.*, 2018). The Weddell Sea produces a colder but fresher variety with characteristic temperature -1°C and salinity 34.64 (Gordon *et al.*, 2010).

1.2.7 AABW Circulation

Transient tracers have allowed the deep circulation pathways of these different types of AABW to be explored. The Weddell AABW flows into the Atlantic Basin, and is observed to be concentrated within the deep western boundary current at 32°S. Weddell AABW also enters the West Indian Ocean, with the highest concentrations again seen in the deep western boundary current (Purkey *et al.*, 2018). AABW originating from the Ross Sea and Adélie Coast are carried westward, away from the Atlantic, in the coastal current close to the continental slope (Williams *et al.*, 2010). These waters from the Indo-Pacific eventually ventilate the deep eastern Indian Ocean (Mantyla and Reid, 1995) and the Pacific (Nakano and Sugino, 2002). Some Ross Sea AABW enters the Ross Gyre in the Pacific via a more direct path, but the Ross Sea AABW is very slow to enter the Bellingshausen Basin (Purkey *et al.*, 2018). This would suggest that the AABW in the Atlantic is predominantly the Weddell variety.

Overall, AABW is thought to be produced globally at a rate of 8.1-9.4 Sv, with the Atlantic, Pacific and Indian Southern Ocean sectors being responsible for 61%, 22% and 17% of this input respectively (Orsi *et al.*, 1999, 2002). Meredith *et al.* (2001) estimated the Weddell region to produce 3.7 Sv of AABW, 0.9 Sv of which is thought to enter the South Atlantic via the Vema Channel. No timescale has yet been associated with this northward transport in the Atlantic but water in the northern deep core leaving the Weddell Gyre (58°S - 61°S) at 4000-4500 m on the Greenwich Meridian was predicted to have a transit time of 13.5 ± 2.5 years (Klatt *et al.*, 2002). This suggests that AABW leaving the Weddell Basin would be approximately this age.

1.3 Changes in the Southern Ocean

Although no change has been observed in the slope of the isopycnals in the Southern Ocean (Böning *et al.*, 2008; Section 1.2.2), much change has nevertheless been seen in the Southern Ocean water masses which are formed within the Southern Ocean meridional overturning circulation. Here changes to the water masses of the upper and lower limb are explored in more detail.

1.3.1 The Upper Limb

The upper limb of the overturning is comprised of upwelling CDW and subducting AAIW. Changes in AAIW can provide insight as to the state of the upper limb of the Southern Ocean overturning and how it is responding to climate change.

In the Atlantic AAIW was observed to freshen between the 1950s to the 1990s (Curry *et al.*, 2003) and more recently between 2005 and 2014 (Yao *et al.*, 2017). In the Indian and Pacific Oceans, AAIW was also observed to freshen (and cool) on density surfaces when hydrographic sections from the

period 1985 to 1994 were compared to historic data from 1930 to 1980 (Wong, 1999). Closer to the formation regions of AAIW, Naveira Garabato *et al.* (2009) studied repeat sections at Drake Passage between 1969 and 2005. They observed a net freshening of AAIW of ~0.02 from the 1970s to the twenty-first century, with no significant decadal variability in temperature. Böning *et al.* (2008) also focussed on changes within the Southern Ocean (1960s to 2000s), but within the Indian and West Pacific sectors and found a dipole pattern of change above and below the salinity minimum. They observed cooling and freshening on isopycnals above the salinity minimum (more thermocline dominated waters) and warming and salinification on isopycnals below the salinity minimum (waters closer to Upper Circumpolar Deep Water, UCDW). This was also largely in agreement with the findings of Hutchinson *et al.* (2016) who, using an enhanced Altimetry Gravest Empirical Mode method, found cooling and freshening of AAIW in the Subantarctic Zone and warming and salinification of AAIW waters south of the Subantarctic Zone.

The SROCC (Special Report on the Oceans and Cryosphere in a Changing Climate; Meredith *et al.*, 2019) reported that on a global scale, AAIW has undergone freshening between 1950 and 2018. However it is clear that as with most global long-term patterns of change there is a great deal of spatial and temporal variability of change within these trends. For example, at 24°S in the South Atlantic the mean salinity at the AAIW core increased between 1958 and 1983, but showed no change between 1983 and 2009 (McCarthy *et al.*, 2011). However, the shift to a higher salinity that occurred between 1958 and 1983 was thought to be due to a change in the contribution of end members (the water masses which are mixed together to form a resulting water mass).

Other studies have explored the changes in the volume of AAIW. Santos *et al.* (2016) found the thickness of the AAIW to have increased in the Eastern Tropical North Atlantic and the Eastern Tropical South Atlantic by 1.67 ± 0.71 m yr⁻¹ over the period 1960 to 2015. However, using the Argo dataset and the ECCOv4 reanalysis, Portela *et al.* (2020) found the volume of AAIW to be reducing globally, with the strongest volume loss seen in the South Indian and South Atlantic basins.

No consensus has been reached on the cause of the observed freshening of AAIW. However, links have been drawn between the observed changes and climate change (Banks *et al.*, 2000). Bindoff *et al.* (2007) note the consistency between the freshening pattern and patterns of the acceleration of the atmospheric hydrological cycle, which leads to increased precipitation at high latitudes. Whilst Naveira Garabato *et al.* (2009) more specifically linked the freshening in Drake Passage to a freshening of the Winter Water to the west of the Antarctic Peninsula, where extreme climate change has occurred in the form of increased precipitation and a retreat of the winter sea-ice edge, links have also been drawn between sea-ice transport and freshening of Southern Ocean surface waters, with increased transport of sea-ice to the north bringing more freshwater into the area where AAIW is formed (Haumann *et al.*, 2016).

Over the next century the freshening trend observed in AAIW is predicted to continue (Silvy *et al.*, 2020) and the subduction of intermediate waters is predicted to increase (Salée *et al.*, 2013; Waugh *et al.*, 2019), strengthening the upper cell of the AMOC. The current assessment of this change is predominantly based on transient tracer studies. Using transient tracers and the time-transit distribution (TTD) method (see Section 1.4.3), Waugh *et al.* (2013) found SAMW to consistently decrease in age (get younger) and CDW to

consistently increase in age over all Southern Ocean sectors between the early 1990s and the mid-late 2000s, suggesting a strengthening of the upper cell. Ting and Holzer (2017) also used transient tracers to study changes in the Southern Ocean, but applied a Maximum Entropy Method (MEM). They found a very similar pattern to that of Waugh *et al.* with the SAMW decreasing in age north of 40°S and the CDW increasing in age south of 40°S between the early 1990s and mid-late 2000s. Using the Community Climate System Model, Waugh (2014) related these age changes to an increase in wind-stress curl and strengthening of the subtropical gyres.

The freshening of AAIW appears to be a coherent signal and has been shown to be greater than internal variability (Silvy *et al.*, 2020). Assessing the effect this freshening has on formation rates is however more complicated and still an area of on-going research, with the AR5 IPCC report (Rhein *et al.*, 2013) noting that there was not currently enough data to draw a conclusion on the effect on formation rates.

1.3.2 The Lower Limb

Global-scale warming of AABW has been observed in recent decades (1990s and 2000s) (Purkey and Johnson, 2010) associated with a reduction in the volume of AABW in the Southern Ocean and southern bottom branches of the meridional overturning circulation (Purkey and Johnson, 2012). Azaneu *et al.* (2013) suggests a thinning of the AABW layer by 8.1 m yr^{-1} since the 1950s. Such a thinning is thought to be responsible for the observed deepening of density surfaces and warming on depth surfaces below 2000 m due to isopycnal heave (Purkey and Johnson, 2013; Desbruyères *et al.*, 2017).

As mentioned previously (Section 1.2.6), Weddell Sea Deep Water is the predominant precursor to the AABW found in the Atlantic. At the Greenwich Meridian, both Weddell Sea Bottom Water and Weddell Sea Deep Water were observed to warm between 1984-2008 (Fahrbach *et al.*, 2011) and warming was observed in the wider Weddell Sea region in the 1990s (Fahrbach *et al.*, 2004). However in the early 2000s this warming trend slowed (Fahrbach *et al.*, 2004). As in the global ocean, Purkey and Johnson (2012) attributed this apparent Weddell Sea warming to isopycnal heave caused by a volume retraction of Weddell Sea Bottom Water. There is however an alternate theory that suggests the measured warming could actually be the system returning to a warmer state after a cooling caused by the Weddell Polynya in the 1970s (Zanowski *et al.*, 2015).

Signals from the Weddell Sea can be traced northward into the deep Atlantic Basins. As early as the 1980s Coles *et al.* (1996) observed a reduction in volume of AABW in the Argentine Basin. Johnson and Doney (2006) observed a warming of waters in both the Argentine Basin, Brazil Basin and Scotia Seas between the 1980s/1990s to the early 2000s. However the warming pattern did not continue in all basins into the 2010s, as in 2014 Johnson *et al.* (2014) observed cooling in the deep Scotia Seas and Argentine Basin. A time series of measurements in the Vema Channel (the deep connection between the Argentine and Brazil basin) demonstrates the variability of this warming signal with an overall warming trend seen in AABW, but with some years showing a decrease in temperature relative to the previous measurement (Zenk and Morozov, 2007; Zenk and Visbeck, 2013).

Although it would be obvious to draw a direct connection between the reduction in AABW volume observed in the South Atlantic and the reduction of

Weddell Sea Deep Water observed in the Weddell Sea. It is thought that the relationship may be more complex than it initially appears, and that winds may play an important role in determining the connectivity of different basins and ultimately the properties of AABW in the Atlantic (Gordon *et al.*, 2010, Meredith *et al.*, 2014). One such mechanism proposed by Meredith *et al.* (2008) related the doming of isopycnals within the Weddell Sea to the strength of the Weddell Gyre, which is itself controlled by the winds. They proposed that stronger cyclonic forcing over the Weddell Gyre, leads to a doming of isopycnals allowing a less dense (warmer) outflow of Weddell Sea Deep Water across the South Scotia Ridge.

It is the warming signal that generally dominates discussion on the changes in Atlantic AABW; however there is also some evidence of freshening in certain regions. Some water exiting the Weddell Sea as Weddell Sea Deep Water travels west to Drake Passage, where a freshening in the bottom waters has been observed. This freshening can be linked to freshening of the shelf waters of the north-western Weddell Sea (Meredith *et al.*, 2014) thought to be a consequence of the collapse of nearby ice shelves (Jullion *et al.*, 2013).

Freshening is much more commonly seen in the Indo-Pacific AABW than in the Atlantic. This Indo-Pacific freshening, observed since the 1950s, has been linked to a freshening of 0.03 decade^{-1} of the HSSW and ice shelf water (ISW) of the Ross Sea, a precursor to Ross Sea Bottom Water and Indo-Pacific AABW (Jacobs and Giulivi, 2010). It is thought that these changes in the Ross Sea may be due to increased precipitation, reduced sea-ice formation and increased glacial melting in West Antarctica (Jacobs *et al.*, 2002). A second theory is that the freshening in the Indo-Pacific AABW is a result of a change in the contribution of different end members, with a reduced contribution from

Ross Sea Bottom Water and an increased contribution from the fresher Adélie Land Bottom Water (Ozaki *et al.*, 2009; Katsumata *et al.*, 2015). The Indo-Pacific waters that experience freshening do also experience warming (Desbruyères *et al.*, 2016) which as in the Atlantic, is attributed to isotherm heave caused by a decline in northward flowing AABW (Purkey and Johnson, 2013).

The interest in the changes observed globally in AABW is primarily due to the desire to quantify the role of AABW in transporting heat and carbon northward in the deep ocean, and because of the relationship between these waters and the strength of the AMOC. In the future, a warming and freshening of AABW source waters is predicted to lead to continual reduction in the formation and export of AABW (Heuze *et al.*, 2015). In most of the CMIP5 models this reduction in AABW corresponds to a weakening of the AMOC (Heuze *et al.*, 2015). However this is not the case in all modelling experiments as Patara and Böning (2014) found the upper cell of the AMOC to strengthen whilst the AABW warms and the lower AMOC weakens. This said, there is still a great deal of uncertainty surrounding future predictions of AABW formation and transport, particularly in CMIP5 models, as AABW production relies on many processes not represented or resolved in climate models, such as meltwater input from the Antarctic Ice shelves (Bronselaer *et al.*, 2018). However, even without considering the validity of future projections, it is clear that major changes in AABW have already been observed. Evidence of such change comes from CFC measurements in the Weddell Sea over the period 1984-2011, which suggest a 15-21% decline in the ventilation of Weddell Sea Bottom Water (Huhn *et al.*, 2013). These changes also have clear consequences for the uptake and storage of C_{ant} with the changes observed by Huhn *et al.* thought to

be equivalent to a slowdown in the uptake of C_{ant} by 14-21%.

1.4 Transient Tracers & Radiocarbon

1.4.1 Transient Tracers

A transient tracer is a chemical found in the ocean which has a time-varying atmospheric history, and so can be used to identify when a particular water mass was last in contact with the atmosphere. Here, a focus is given to the following transient tracers: chlorofluorocarbons CFC-11 and CFC-12, and sulfur hexafluoride (SF₆). They are all manmade chemicals and so act as an anthropogenic signal; CFCs were widely used as refrigerants and propellants before they were banned under the Montreal Protocol in 1989 after they were found to be contributing to a hole in the ozone layer (Farman *et al.*, 1985).

Sulfur hexafluoride continues to be used today, and its main use is as an electrical insulator. As can be seen in Figure 1.7, the concentration of CFCs in

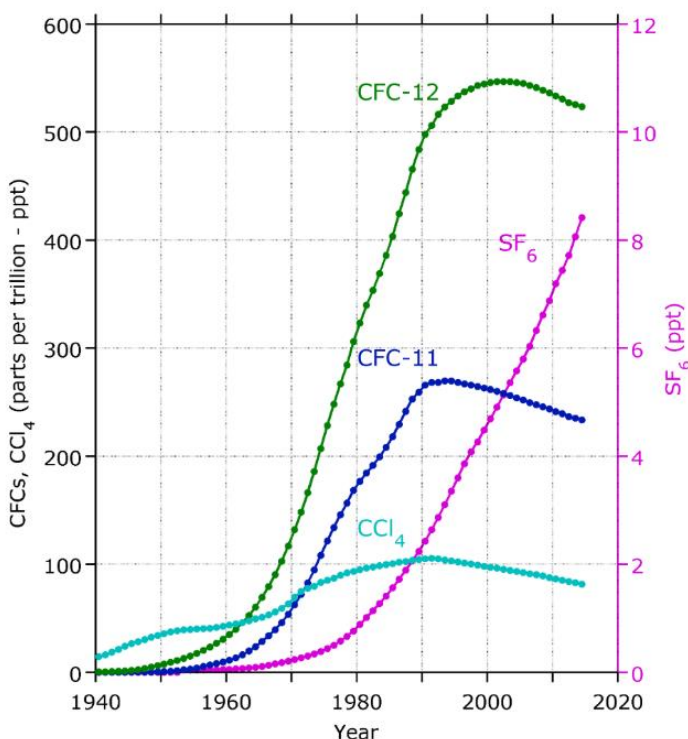
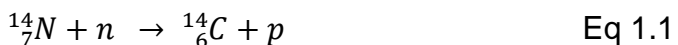


Figure 1.7 – Atmospheric history of Northern Hemisphere concentrations of CFC-11, CFC-12, CCl₄ and SF₆. Reproduced from PMEL (n.d.)

the atmosphere is now decreasing, meaning that there is now potential for an atmospheric concentration to relate to two different points in time. This is why it is important to consider multiple tracers together, and why SF₆ measurements are particularly useful to study recent history, as its atmospheric concentration continues to increase. Interestingly there have been recent observations of a slow-down in the rate of decrease of CFC-11 in the atmosphere due to unreported new production (Montzka *et al.*, 2018).

1.4.2 Radiocarbon

Radiocarbon (¹⁴C) is a heavy isotope of ¹²C, it does not have a time varying atmospheric history in the same way as the transient tracers, but it can still be used as a temporal tracer. It is formed by a variety of mechanisms, but the dominant source of ¹⁴C is found in the upper atmospheric layers at approximately 15 km above sea level (Lingenfelter, 1963). At this height, ¹⁴C is created when cosmic radiation interacts with atmospheric nitrogen in the following reaction:



where *n* is a neutron and *p* is a proton. In the atmosphere this ¹⁴C is then oxidised, becoming ¹⁴CO₂ (Alvers *et al.*, 2018). ¹⁴C is not a stable isotope of carbon and so will undergo radioactive decay. This decay is slow as ¹⁴C has a long half-life (5568 years according to Alvers *et al.*, 2018; 5730 years according to Key, 2001). This heavy molecule of CO₂ has very similar characteristics to the stable ¹²CO₂ (and stable ¹³CO₂) and so enters the surface ocean via the same physical air-sea exchange mechanisms (in addition to being used by biota in photosynthesis). A difference is that these different isotopes will undergo these processes at different rates, causing the ratio of ¹⁴C/¹²C to differ between

the atmosphere and ocean (and the atmosphere and biota). In oceanography, radiocarbon is reported as $\Delta^{14}\text{C}$, which is a description of the activity of ^{14}C relative to a standard, and uses the units of ppt (see Key, 2001). Negative values indicate the ocean is depleted in ^{14}C relative to the standard.

In the atmosphere $\Delta^{14}\text{C}$ remains relatively stable as new ^{14}C is continually formed, whilst existing ^{14}C undergoes radioactive decay. Tree ring records attest to this, indicating only small variations in atmospheric $\Delta^{14}\text{C}$ on centennial timescales (see Key, 2001). Two phenomena have caused atmospheric $\Delta^{14}\text{C}$ values to recently deviate from this relatively stable situation. The first is due to atomic bomb testing in the 1940s-1960s, which enriched the atmosphere in ^{14}C . The second is termed the ‘Suess effect’, and is an apparent depletion in atmospheric ^{14}C after 1880, due to the addition of stable CO_2 to the atmosphere by the combustion of fossil fuels (Grey, 1969).

In the ocean $\Delta^{14}\text{C}$ will grow more negative as the water ages. This is because the ^{14}C is undergoing radioactive decay, but unlike in the atmosphere, there is no replenishment of ^{14}C from production, as the parcel of water is removed from exchange with the atmosphere. This natural isolation of the ^{14}C from its source also allows for ^{14}C to be used as a form of clock to estimate the time since a parcel of water was last in contact with the atmosphere (its age). Table 1.2 summarises ^{14}C derived ages for the deep waters within each ocean, and compares a conventional approach to the calculation and an approach which accounts for ocean surface waters having a non-zero age prior to their subduction (see Matsumoto, 2007).

	Conventional ^{14}C Age [Years]	Circulation ^{14}C Age [Years]
Atlantic	984	288
Pacific	1891	889
Indian	1627	716
Southern Ocean	1320	295

Table 1.2 – ^{14}C derived water ages per basin. The Southern Ocean is defined as south of 50°S. Conventional Age refers to the conventional method of using ^{14}C to determine water age, the Circulation Age refers to a calculation which accounts for surface waters having a non-zero age prior to their subduction, and deep water being formed in both the North Atlantic and around Antarctica. Reproduced from Matsumoto (2007).

1.4.3 Studying Circulation Using Transient Tracers

A number of different methods have been used over the last few decades to convert transient tracer concentrations into some meaningful measure of time, in order to investigate ocean circulation. The basic method initially used involves simply converting the tracer concentrations into partial pressures, using the solubility calculated from temperature and salinity measurements (Bullister *et al.*, 2002; Warner and Weiss, 1985), and then matching this partial pressure to a particular year in the atmospheric history. The biggest weakness of this basic method is that it assumes that water does not mix, and so only accounts for advective transport. In order to improve this, the TTD method was developed. This method accounts for mixing by assuming the water parcel is made up of many different contributing water parcels, each with a different age. The TTD itself is a probability density function created using a Green's function. The function is constrained using the tracer data; however, even when using a number of different tracers the function is highly underdetermined. Generally the older the water the wider the shape of the probability density function, as the water has undergone more mixing (Holzer and Hall, 2000; Purkey *et al.*, 2018; Waugh, 2003).

There has been a move in recent years to an advancement of the TTD method, which is commonly termed the MEM. This method, instead of treating

the ocean surface as one boundary, treats different regions of the ocean as different sources. This means that the concentration of the tracer at a point location can be described as a function of the transit time, source of water, and fraction of the source water. A probability is associated with each parcel of water, and represents the probability of that parcel of water being in contact with the atmosphere in a certain source region a certain amount of time ago. In order to find the best choice of these probabilities a Maximum Entropy approach is applied, constrained by the measured tracer concentration of the sample. For each calculation a prior must be provided which is a previous estimate of the TTD (Holzer *et al.*, 2010).

Although this method is still relatively new it is seen as superior to the TTD method which assumes an Inverse Gaussian distribution for the boundary propagator (Stöven *et al.*, 2015). The TTD method is built upon the assumption of a steady and 1D advective velocity and diffusion gradient (Stöven *et al.*, 2014). The Southern Ocean is an area with considerable diapycnal mixing (Naveira Garabato *et al.*, 2007); something that the TTD method cannot account for. This means that in the Southern Ocean the application of the TTD method is limited to areas north of the Subantarctic Front and to waters above the extent of AAIW (Stöven *et al.*, 2015). The MEM has more validity in the Southern Ocean than the TTD method, as it does not assume an Inverse Gaussian form and considers multiple end members, and so can consider mixing between more than one source (Holzer and Primeau, 2010).

1.5 Aims and Objectives

This thesis aims to further develop knowledge of the transport of AAIW and AABW in the South Atlantic Basin by assigning timescales to this northward transport, and assessing whether these timescales have changed between 2009 and 2018.

This will be achieved by applying the MEM to ship-based transient tracer measurements taken on-board the RRS James Cook in 2009 and 2018. Ocean model output will be used to evaluate the results obtained from the MEM and to further explore scientific questions raised by the initial results.

The observational data used is described in Chapter 2 and the methods applied to this observational data and the methods by which the ocean model data are generated are described in Chapter 3. Chapter 4 explores the temporal and spatial origin of AAIW at 24°S and assesses differences between the 2009 and 2018 results. Chapter 5 develops on the results of Chapter 4 by exploring the pathways of water produced in a Weddell Polynya using an ocean model. Chapter 6 focusses on the temporal and spatial origins of AABW at 24°S, again assessing the differences between the 2009 and 2018 results. Finally, the findings of the thesis are summarised in Chapter 7.

Chapter 2:

Data

This study uses both observational and model data. The observational data are comprised of shipboard measurements from two cruises at 24°S in the South Atlantic. The model data are generated using the ECCO configuration of MITgcm. This chapter covers data collection methods for the observational data, data locations, and water mass definitions. Details of the generation of the model data and the methods applied to the observational data are covered in Chapter 3.

2.1 Cruise Overview

This study uses data from two occupations of the 24°S (WOCE A09.5) South Atlantic section, which stretches from Rio de Janeiro, Brazil, to Namibia. The section is split into three basins; the Brazil Basin to the west of the Mid Atlantic Ridge (MAR), the Angola Basin to the east of the MAR and the west of Walvis Ridge, and the Cape Basin to the east of the Walvis Ridge and the west of the African continent. The section has been occupied several times in the past century (see McCarthy *et al.*, 2011). This study uses data from the 2009 (Cruise JC032) and 2018 (Cruise JC159) occupation, as transient tracer measurements were collected on both of these cruises. The locations of the CTD (Conductivity Temperature Depth) stations are shown in Figure 2.1 and the number of stations occupied is shown in Table 2.1.

Cruise	Date	Transect Name	No. of Stations	Principal Scientist
JC032	07/03/2009 – 21/04/2009	24°S / A9.5	95	B. A. King
JC159	28/02/2018 – 10/04/2018	24°S / A9.5	125	B. A. King

Table 2.1 – Summary of cruise information.

Measurements of relevance to this study include in-situ temperature, absolute salinity, pressure, phosphate, oxygen, chlorofluorocarbon - 11 (CFC-11), chlorofluorocarbon - 12 (CFC-12), sulphur hexafluoride (SF_6) and carbon – 14 (^{14}C). Measurements of all of the above parameters were collected on both cruises, with the exception of ^{14}C which was only collected in 2018. Figures 2.2–2.5 show the spatial distribution of these parameters at 24°S for both cruises.

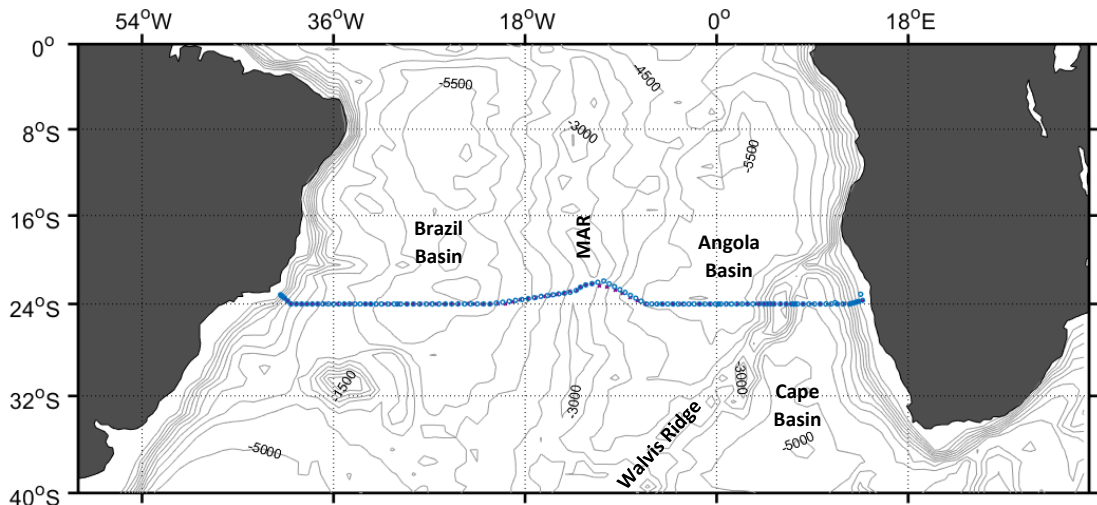


Figure 2.1 – CTD station locations for cruises JC032 - 2009 (purple) and JC159 - 2018 (blue). Bathymetry shown in 500 m contours.

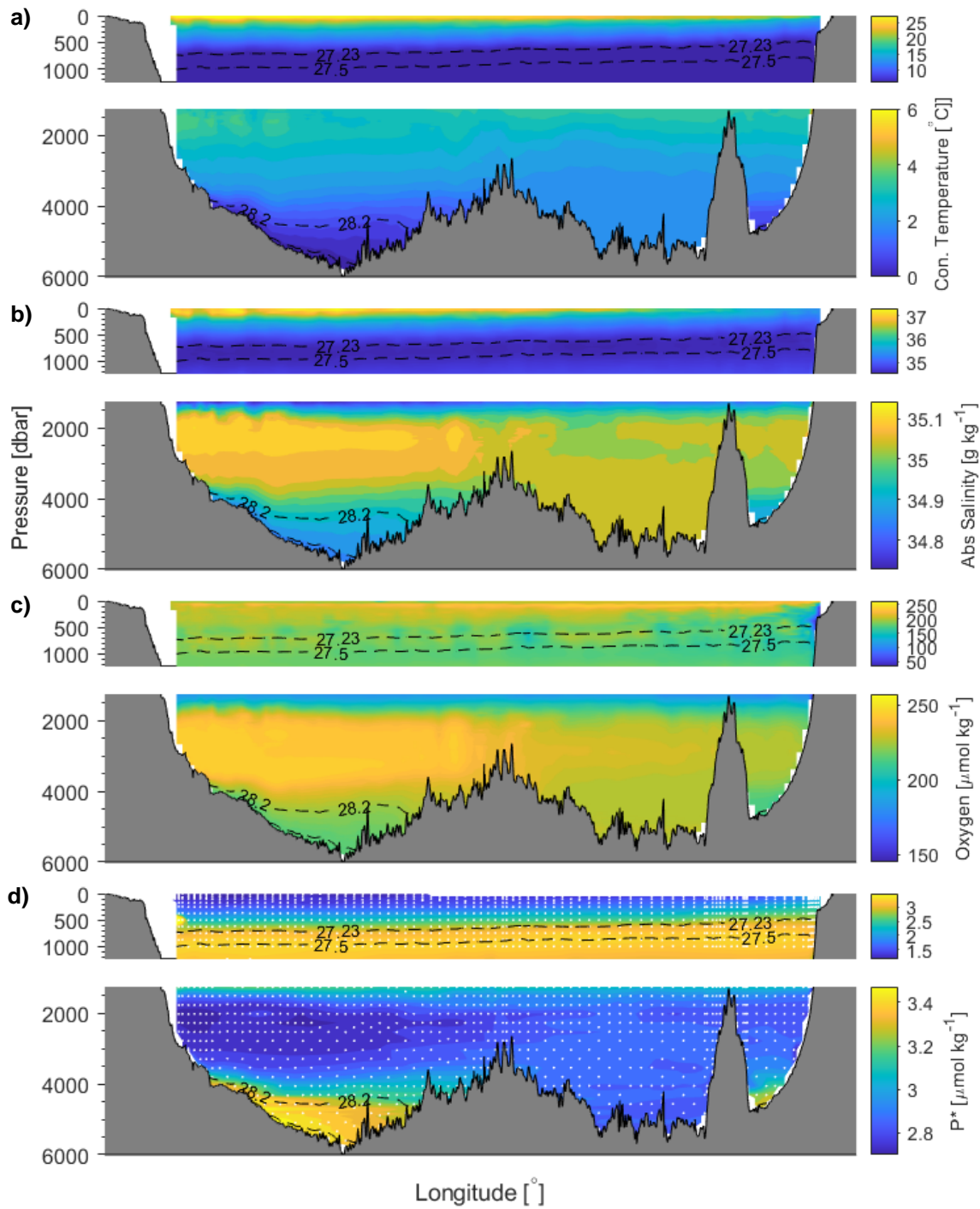


Figure 2.2 – Sections of conservative temperature, absolute salinity, oxygen and P^* (assimilated phosphate, see Section 3.1.3 for definition) at 24°S in 2009 (Cruise JC032). In some instances the colour axis is restricted. Neutral density contours for 27.23, 27.50, 28.2 and 28.27 kg m⁻³ indicate the boundary of the AAIW and AABW definitions (see Section 2.2). Where bottle data is used, instead of CTD sensor data, bottle locations are indicated by white dots. Vertical axis is split into 0 – 1250 m and 1250 – 6000 m.

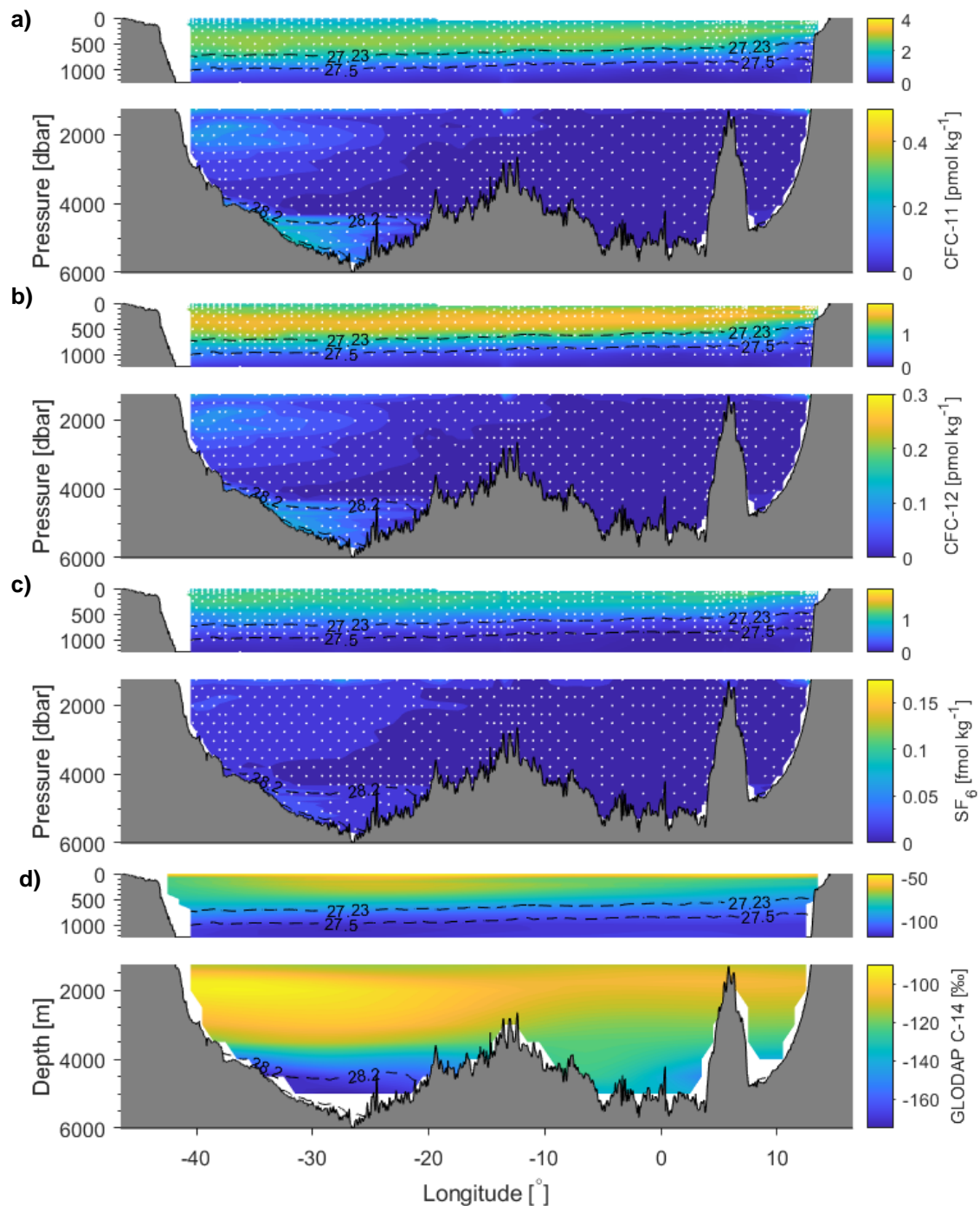


Figure 2.3 – Sections of CFC-11, CFC-12, and SF_6 at 24°S in 2009 (Cruise JC032) and section of and GLODAP ^{14}C gridded values at 24°S. In some instances the colour axis is restricted. Neutral density contours for 27.23, 27.50, 28.2 and 28.27 kg m^{-3} indicate the boundary of the AAIW and AABW definitions (see Section 2.2). Where bottle data is used, instead of gridded data, bottle locations are indicated by white dots. Vertical axis is split into 0 – 1250 m and 1250 – 6000 m.

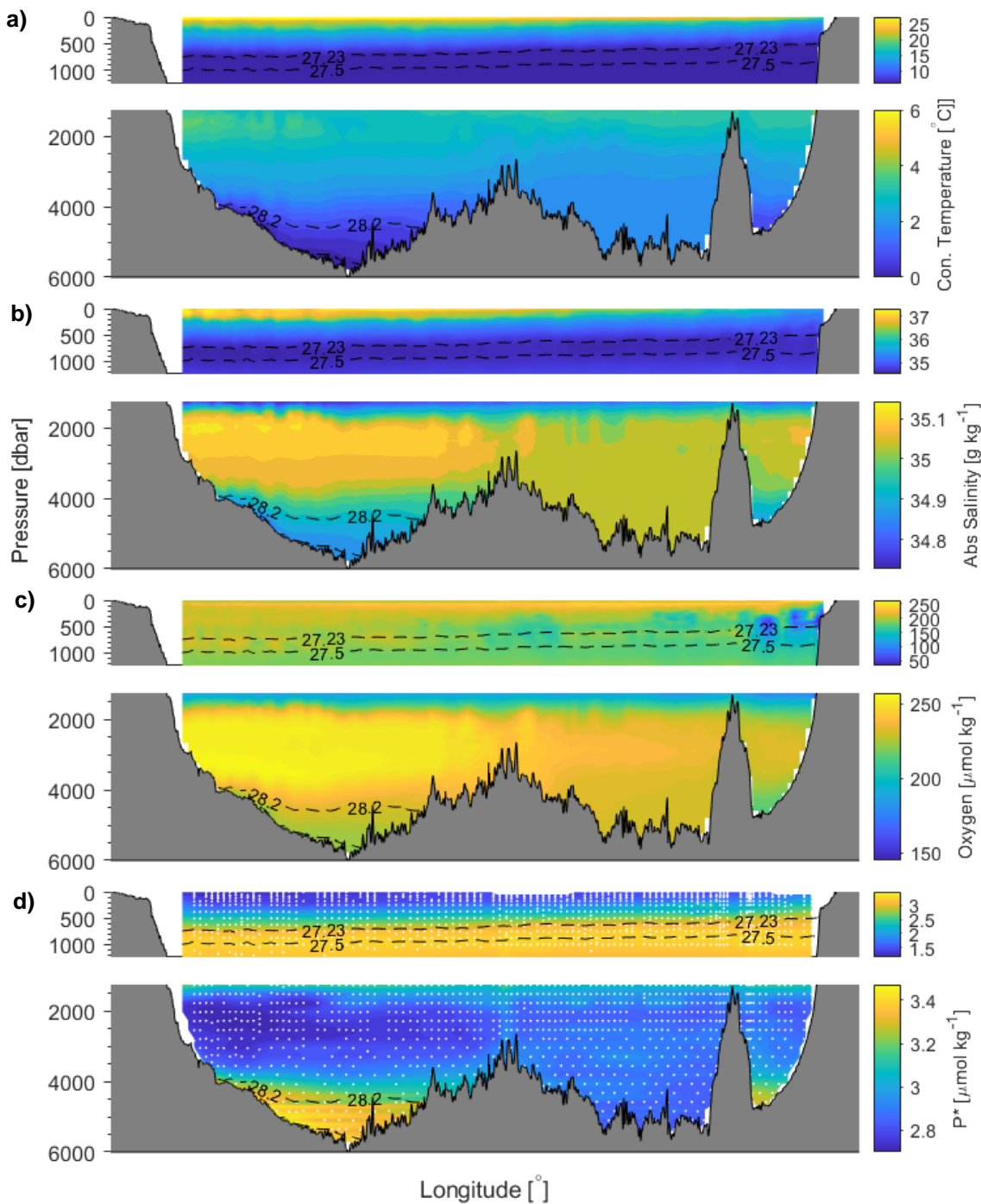


Figure 2.4 – Sections of conservative temperature, absolute salinity, oxygen and P^* (assimilated phosphate, see Section 3.1.3 for definition) at 24°S in 2018 (Cruise JC159). In some instances the colour axis is restricted. Neutral density contours for 27.23, 27.50, 28.2 and 28.27 kg m^{-3} indicate the boundary of the AAIW and AABW definitions (see Section 2.2). Where bottle data is used, instead of CTD sensor data, bottle locations are indicated by white dots. Vertical axis is split into 0 – 1250 m and 1250 – 6000 m.

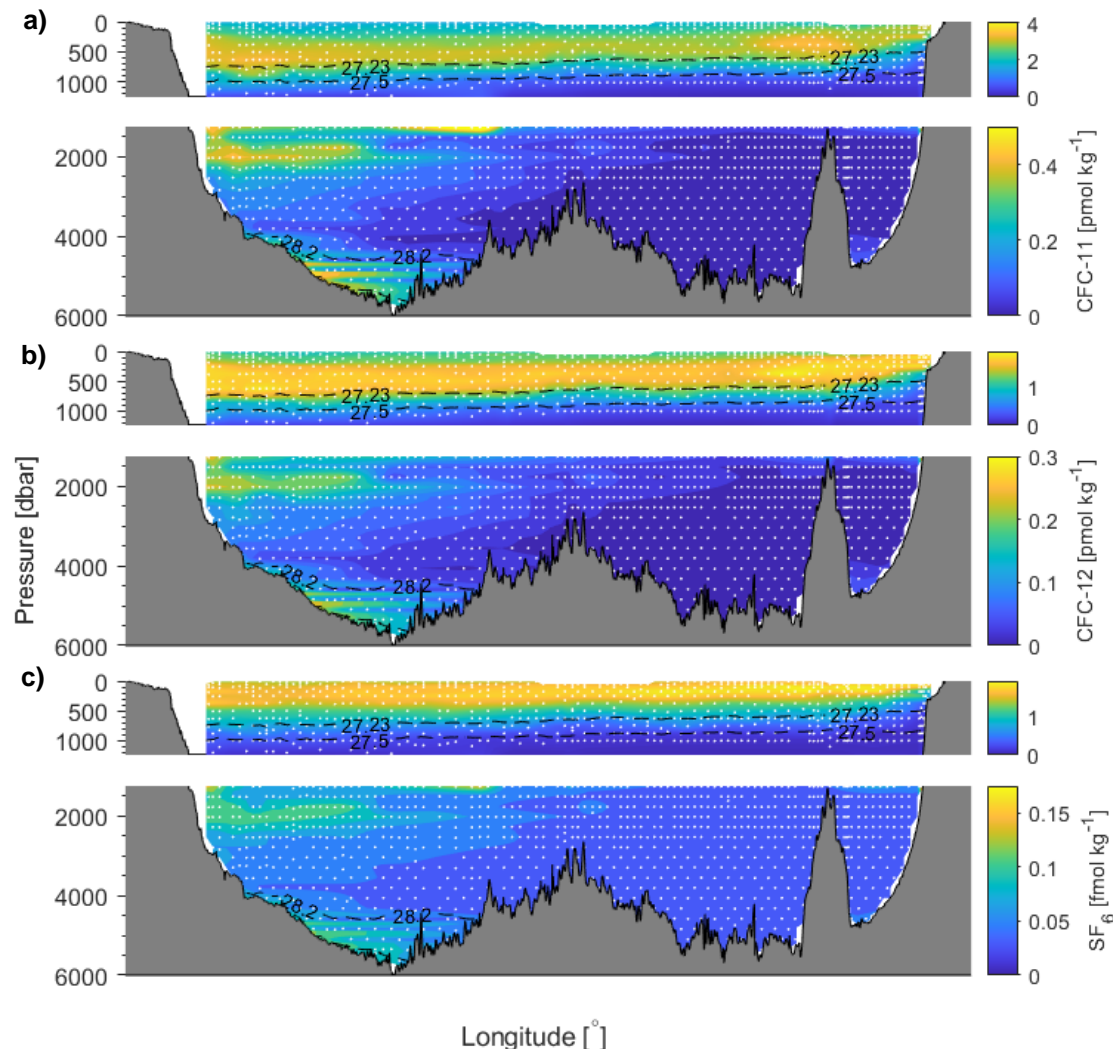


Figure 2.5 – Sections of CFC-11, CFC-12, and SF₆ at 24°S in 2018 (Cruise JC159). In some instances the colour axis is restricted. Neutral density contours for 27.23, 27.50, 28.2 and 28.27 kg m⁻³ indicate the boundary of the AAIW and AABW definitions (see Section 2.2). Where bottle data is used, instead of gridded data, bottle locations are indicated by white dots. Vertical axis is split into 0 – 1250 m and 1250 – 6000 m.

2.2 Water Mass Definitions

As the section spans the entire width of the South Atlantic, numerous different water masses can be identified. Figure 2.6 shows the distribution of all bottle samples in temperature-salinity space. The samples can be grouped into four dominant water masses; surface waters, AAIW, North Atlantic Deep Water (NADW) and AABW.

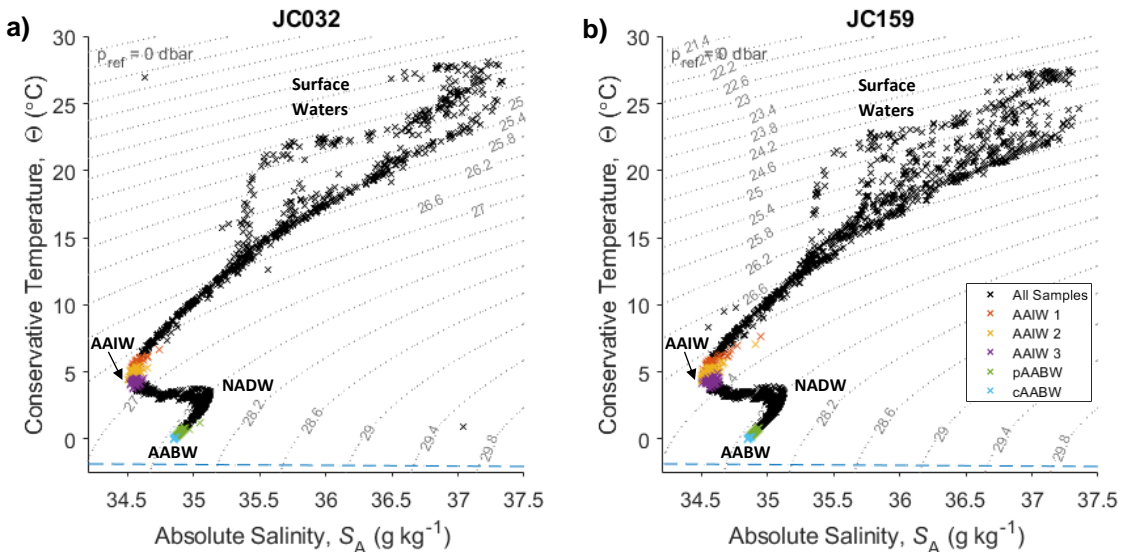


Figure 2.6 – Temperature-Salinity plot for all bottle samples on JC032 (a) and JC159 (b). AAIW and AABW subdivisions are defined as: AAIW 1 ($\sigma_n = 27.23\text{--}27.3 \text{ kg m}^{-3}$), AAIW 2 ($\sigma_n = 27.3\text{--}27.4 \text{ kg m}^{-3}$), AAIW 3 ($\sigma_n = 27.4\text{--}27.5 \text{ kg m}^{-3}$), pAABW ($\sigma_n = 28.20\text{--}28.27 \text{ kg m}^{-3}$), cAABW ($\sigma_n > 28.27 \text{ kg m}^{-3}$); see Sections 2.2.1 and 2.2.2 for explanation of definitions. Inflections in the curve are labelled with the corresponding water mass. Blue dashed line indicates the conservative temperature freezing point. Grey dotted lines show contours of potential density (calculated according to the 75-term equation of Roquet *et al.* (2015)).

This study focusses on two of these water masses, AAIW and AABW due to their importance in transporting heat and carbon northwards from the Southern Ocean. Although oceanographers often conceptualise the ocean to be comprised of distinct layers of water of different origin, in reality there is often no clear boundary where one water mass ‘stops’ and the other ‘starts’.

2.2.1 Antarctic Intermediate Water

Multiple parameters are often used to define AAIW (see Table 2.2). These range from brackets of potential or neutral density to intervals of

pressure and salinity. The overwhelming consensus, however, is that the core of AAIW is defined as the vertical salinity minimum. This study uses the vertical salinity minimum to define the core of AAIW and the definition of Evans *et al.* (2017) which divides AAIW into three layers; AAIW 1 ($\sigma_n = 27.23\text{-}27.3 \text{ kg m}^{-3}$), AAIW 2 ($\sigma_n = 27.3\text{-}27.4 \text{ kg m}^{-3}$), AAIW 3 ($\sigma_n = 27.4\text{-}27.5 \text{ kg m}^{-3}$). At 24°S the salinity minimum falls close to the boundary of AAIW 2 and AAIW 3. Tables 2.3 & 2.4 indicate the number of samples used in the analysis that fall within these three classes, as well as indicating the mean value and standard deviation within each class for each tracer used in the analysis. In this study, neutral density is calculated using EOS-80.

Paper	Study type/area	AAIW definition
McCarthy <i>et al.</i> (2011) (based on Wust, 1935 and Talley, 1996)	Observations at 24°S, South Atlantic	Salinity minimum Salinity < 34.4 Pressure $\sim 800 \text{ dbar}$
Santoso and England (2004)	Global model study	$\sigma_\theta = 27.2 \text{ kg m}^{-3}$, chosen as it coincides with model and observed intermediate water salinity minimum 700-1000 m to the north of 40°S.
Kamenkovich <i>et al.</i> (2017)	Model study, 30°S - 35°S	$S = 32.2 - 32.4 \text{ or}$ $\sigma_\theta = 27.05 - 27.40 \text{ kg m}^{-3}$
Naviera Garabato <i>et al.</i> (2009)	Observations at Drake Passage	$27.23 < \gamma^n < 27.50 \text{ kg m}^{-3}$ $0.54 < \phi < 0.70$
Sallée <i>et al.</i> (2010)	ARGO observations, Southern Ocean	$\sigma_\theta = 27.0 - 27.3$
Downes <i>et al.</i> (2011)	Model study, Southern Ocean	$\sigma_\theta = 26.5 - 27.0$
Downes <i>et al.</i> (2010)	Model study, Southern Ocean	Salinity minimum
You (2002)	Observations in the South Atlantic	5 levels between 700 - 1200 dbar $\gamma^n = 27.25, 27.32, 27.40, 27.45, 27.55 \text{ kg m}^{-3}$
Schmidtko and Johnson (2012)	ARGO observations, 20°N - 60°S	Local vertical salinity minimum found between $26.98 < \sigma_\theta < 27.8 \text{ kg m}^{-3}$
Evans <i>et al.</i> (2017)	Observations at 24°S, Drake Passage and 30°E (Southern Ocean)	$27.23 < \gamma^n < 27.50 \text{ kg m}^{-3}$ AAIW 1 = $27.23 - 27.30 \text{ kg m}^{-3}$ AAIW 2 = $27.30 - 27.40 \text{ kg m}^{-3}$ AAIW 3 = $27.40 - 27.50 \text{ kg m}^{-3}$

Table 2.2 – A selection of AAIW definitions from the literature.

Tracer	AAIW 1		AAIW 2		AAIW 3		cAABW		pAABW	
	Mean	Std. dev.	Mean	Std. dev.	Mean	Std. dev.	Mean	Std. dev.	Mean	Std. dev.
CFC-11 [pmol kg ⁻¹]	2.16	0.47	1.72	0.51	1.10	0.33	0.22	0.06	0.08	0.07
CFC-12 [pmol kg ⁻¹]	1.13	0.25	0.89	0.26	0.56	0.16	0.11	0.03	0.04	0.03
SF ₆ [fmol kg ⁻¹]	0.42	0.19	0.30	0.14	0.18	0.06	0.03	0.01	0.02	0.01
Con. Temp. [°C]	5.55	0.35	4.89	0.36	4.23	0.17	0.06	0.07	0.59	0.37
Abs. Sal.	34.56	0.06	34.54	0.05	34.56	0.02	34.86	0.01	34.92	0.08
P* [μmol kg ⁻¹]	3.07	0.07	3.16	0.05	3.24	0.03	3.45	0.03	3.30	0.11
¹⁴ C [%]	-97.04	2.37	-101.20	3.79	-106.81	2.48				
No. of samples in class	37		36		38		29		65	

Table 2.3 – Mean and standard deviation of all 7 tracers used as constraints in the MEM analysis, for the defined density brackets corresponding to AAIW 1, AAIW 2, AAIW 3, cAABW and pAABW. Number of samples within each definition is also stated. With the exception of ¹⁴C which is taken from the GLODAP gridded dataset (see Section 2.4), all values relate to the 2009 cruise (JC032).

Tracer	AAIW 1		AAIW 2		AAIW 3		cAABW		pAABW	
	Mean	Std. dev.	Mean	Std. dev.	Mean	Std. dev.	Mean	Std. dev.	Mean	Std. dev.
CFC-11 [pmol kg ⁻¹]	2.41	0.52	2.01	0.55	1.24	0.51	0.36	0.08	0.14	0.09
CFC-12 [pmol kg ⁻¹]	1.25	0.26	1.01	0.28	0.62	0.25	0.19	0.04	0.08	0.04
SF ₆ [fmol kg ⁻¹]	0.62	0.15	0.49	0.17	0.26	0.12	0.10	0.02	0.06	0.02
Con. Temp. [°C]	5.78	0.28	4.93	0.33	4.25	0.22	0.08	0.08	0.56	0.19
Abs. Sal.	34.59	0.04	34.56	0.03	34.58	0.03	34.86	0.01	34.91	0.02
P* [μmol kg ⁻¹]	3.06	0.05	3.17	0.05	3.24	0.05	3.43	0.04	3.30	0.05
¹⁴ C [%]	-97.42	1.81	-103.16	2.70	-108.64	2.54				
No. of samples in class	38		41		31		16		56	

Table 2.4 – Mean and standard deviation of all 7 tracers used as constraints in the MEM analysis, for the defined density brackets corresponding to AAIW 1, AAIW 2, AAIW 3, cAABW and pAABW. Number of samples within each definition is also stated. With the exception of ¹⁴C which is taken from the GLODAP gridded dataset (see Section 2.4), all values relate to the 2018 cruise (JC159).

2.2.2 Antarctic Bottom Water

AABW is often characterised as the most dense water mass in the Atlantic. It can also be recognised by its high nutrient levels. At 24°S it is observed in the far western Brazil Basin and the far eastern Cape Basin but not in the Angola Basin. This is because the Walvis Ridge forms a barrier north-eastward from the MAR, funnelling the northward transiting AABW to the east within the Cape Basin, and preventing it from entering the Angola Basin (see Figure 2.1). Evans *et al.* (2017) define two layers of AABW; $\sigma_n = 28.27\text{-}28.35 \text{ kg m}^{-3}$ and $\sigma_n > 28.35 \text{ kg m}^{-3}$. Waters in the denser of the two classes are not present at 24°S. Waters of the lighter of the two classes are present, but as can be seen in Figures 2.2 and 2.4, this definition only encompasses a very small amount of the relatively low salinity, low oxygen, low temperature and high P* water observed in the bottom waters of the Brazil and Cape Basins.

As AABW travels northward it is known to warm and mix with overlying water masses. This results in a reduction in density of AABW and a dilution of its characteristics. In order to encompass the water which has a clear AABW origin but does not fall within the definition of Evans *et al.*, here a new definition is introduced. This definition is referred to as periphery AABW (pAABW), whilst waters following the definition of Evans *et al.* are termed core AABW (cAABW). pAABW is defined as waters within the density class of $\sigma_n = 28.20\text{-}28.27 \text{ kg m}^{-3}$ and cAABW is defined as waters within the density class $\sigma_n > 28.27 \text{ kg m}^{-3}$. Tables 2.3 & 2.4 indicate the number of samples used in the analysis that fall within the pAABW and cAABW classes, as well as indicating the mean value and standard deviation within each class for each tracer used in the analysis.

2.3 Transient Tracer Sampling at 24°S

Transient tracer samples were collected and analysed on the 2018 cruise as part of this study and of the wider ‘Transient tracer-based Investigation of Circulation and Thermal Ocean Change’ (TICTOC) project. Below is a brief outline of the sampling and analysis procedure.

Samples were collected from the full water-column using Niskin bottles mounted on a CTD-rosette. Due to time limitations not all bottle depths were analysed at each CTD station but the depths analysed were alternated between stations. Water samples were collected in 500 ml glass bottles using Tygon tubing which was stored in seawater to limit contamination from the high levels of trace gases in the atmosphere. Each sample bottle was rinsed with water from the Niskin bottle and each sample was allowed to overflow the sample bottle three times, to ensure none of the final sample had been in contact with the atmosphere. An ungreased rinsed glass stopper was used to seal the sample, displacing the water in the neck of the bottle, and ensuring no bubbles of air were sealed with the sample.

Elastic bands were used to hold the stopper in place and all samples were stored in a seawater bath at a similar temperature to the sampled water. This was to prevent degassing and to avoid expansion or contraction of the sample within the bottle, which may have led to contamination from the air.

Samples were analysed on-board the ship using a purge and trap system and electron capture gas chromatography (Smethie *et al.*, 2000; Law *et al.*, 1994). This process is briefly outlined below:

1. The water sample is transferred to two calibrated volume flasks using the pressure of oxygen-free nitrogen gas.
2. The measured volumes are then transferred into two separate purge and trap systems, where the samples are purged of CFCs and SF₆ by oxygen-free nitrogen gas.
3. The CFC and SF₆ gases are then trapped by a cooling and heating process, prior to being injected into a gas chromatograph.
4. Each gas chromatograph produces a graph, for which the peaks relating to the different compounds can be integrated, and used together with results from standards, to calculate the concentrations.

National Oceanic and Atmospheric Administration (NOAA) atmospheric standards were analysed alongside the samples in order to calibrate the data. To assess precision, 100 duplicate samples were taken during the cruise (two samples from the same Niskin). The standard deviations from these samples are shown in Table 2.5, and indicate a high standard of precision.

Tracer	Sample Type	Precision
CFC-11	for surface values	± 0.85%
	for values < 0.50 pmol kg ⁻¹	± 0.0046 pmol kg ⁻¹
CFC-12	for surface values	± 0.86 %
	for values < 0.25 pmol kg ⁻¹	± 0.0029 pmol kg ⁻¹
SF ₆	for surface values	± 1.24%
	for values < 0.25 fmol kg ⁻¹	± 0.015 fmol kg ⁻¹

Table 2.5 – The standard deviation of water samples on JC159. Based on 100 duplicate samples (200 total samples).

2.4 SF₆ Tracer Release Contamination

Although the primary source of SF₆ in the ocean is from exchange with the polluted atmosphere, there is a small artificial source of SF₆ directly into the ocean. This small artificial source is from tracer release experiments conducted by oceanographers. In these experiments a tracer is released at a point location and the spread of the tracer away from that point is used to study circulation and mixing. SF₆ was used for these tracer release experiments when background levels of SF₆ in the ocean from atmospheric input were low. Now that these background levels are higher, and there is a benefit to not contaminating these background levels, other chemicals are used in such tracer release experiments. At 24°S contamination from the Brazil Basin Tracer Release Experiment, which released tracer in February/March 1996 (Toole *et al.*, 1997), was detected in the deeper waters in the western part of the transect.

In order to separate the signal of the released tracer from that of the background SF₆ signal (SF₆ which entered the ocean through air-sea exchange) the following calculation (based upon a method used by Rye *et al.*, 2012) was undertaken by M.J. Messias (personal communication, November 2019 & April 2020).

A quadratic relationship was found between SF₆ and CFC-12 for samples with low SF₆ concentrations (< 0.3 fmol kg⁻¹) in the east of the 24°S transect above 1500 m (JC032: east of 6.7°W, JC159: east of 0°E), as this was deemed to be away from the influence of the SF₆ contamination. In order to remove the artificial signal of SF₆, CFC-12 values in waters below 1500 m in the west of the transect were then used to predict the background SF₆ values based upon the calculated quadratic relationship for each cruise respectively. This necessary removal of artificial SF₆ will not impact the results for the AAIW analysis as

these waters are above 1500 m. However, the contamination is observed within the AABW density class, and so this contamination is likely to have a detrimental impact on the quality of the AABW results.

2.5 Interior ^{14}C data

Due to an absence of ^{14}C measurements on the 2009 cruise, and the long timescales taken to analyse the ^{14}C samples from the 2018 cruise, ^{14}C data are not available for 24°S for the AAIW analysis. In the absence of these data, interpolated fields are created from the GLODAP V1 interior gridded ^{14}C dataset (Key *et al.*, 2004). The gridded data are interpolated onto the locations of the bottle samples based on the latitude, longitude and depth of the sample, using 3D linear interpolation.

Chapter 3:

Methods

In this chapter we explore how a Maximum Entropy Method is applied to observational cruise data (Section 3.1) and then proceed to explain the methods and metrics used to probe the output of this method (Section 3.2). Section 3.3 then introduces the modelling aspect of the project, including experiment set-up and metrics used for analysis.

3.1 Maximum Entropy Method: Applying the Method

The MEM (Maximum Entropy Method) is a deconvolution method used for highly undetermined systems. It allows us to attempt to predict the numerous different sources of water and the fractions in which they are mixed together, to form the parcel of water which is sampled. Here, we will address the inputs that this method requires and how these inputs are drawn on through the application of an iterative solver.

3.1.1 Introduction

For the MEM analysis seven tracers are used, each holding their own information. These tracers are conservative temperature, absolute salinity, assimilated phosphate (P^*), chlorofluorocarbon – 11 (CFC-11), chlorofluorocarbon – 12 (CFC-12), sulfur hexafluoride (SF_6) and natural radiocarbon (^{14}C). All tracers are treated as conservative, however P^* and ^{14}C are not truly conservative.

Salinity, temperature and P^* are used to provide a spatial constraint as they have large spatial heterogeneity globally in the ocean mixed layer (see Figure 3.1). For example, a sample high in P^* but low in temperature is likely to originate from the Antarctic polar regions as opposed to the phosphate poor Arctic polar regions.

CFC-11, CFC-12 and SF₆ are known as transient tracers and have a time varying atmospheric history, so act as a temporal constraint. These transient tracers have a purely anthropogenic source and do not break down in the water column. This means that younger water masses (i.e. those more recently ventilated) have higher concentrations of transient tracers. Waters that have not had contact with the atmosphere since before the first of these tracers were introduced into the atmosphere (~1930), will contain no transient tracers.

3.1.2 The Principles

The concentration of each of these tracers in a measured sample can be described as a mixture of values of the tracer at different surface locations and points in time (Eq 3.1):

$$C_j^I(r_I, t) = \int_{space} \int_{-\infty}^t G(r_s, t') C_j^s(r_s, t') dt' ds \quad \text{Eq 3.1}$$

where C_j^I represents the concentration (C) of tracer species j at an interior point (I), r_I the geographical location of the sample, t the date when the sample was taken (cruise date), G the boundary propagator Green's function, r_s the geographical location of the source region, and t' times earlier than t .

The MEM aims to find a discretised version of the boundary propagator G . The discretised form will hence be referred to as P . Equation 3.2 is the discretised version of Equation 3.1:

$$C_j^I(r_I, t) = \sum_s \sum_{n=0}^{n=2000} P(r_s, t') C_j^s(r_s, t') \quad \text{Eq 3.2}$$

The assumption is made that water must originate from some location at some point in the past and so:

$$\sum_s \sum_{n=0}^{n=2000} P(r_s, t') = 1 \quad \text{Eq 3.3}$$

In this analysis the timeframe spans from present day to 2000 years ago as all water masses studied are considered to be substantially younger than 2000 years.

The method finds a solution for P based on the principles of information entropy, as described in detail by Holzer *et al.* (2010). The analysis uses the `fsolve` function in MATLAB and was based upon a script written by A. Shao (personal communication, 2017 & 2018). The MEM requires sample concentration, tracer mixed layer history, and a prior as inputs, all of which are discussed further below.

3.1.3 Constraining Data

Tracer properties of a parcel of water are defined in the area from which that water originated. The MEM requires data describing the concentrations of all seven tracers within the mixed layer over the whole global ocean. This is so that the method has the opportunity to pick from any area as a source region. Some of these values also have strong seasonality or variability over longer timescales, and so more than just a single time point is required. The sources of the data used and how each was formatted for use in the MEM are outlined below.

Mixed layer temperature, salinity and P^* all have strong seasonality; although they vary in time, here (as in Holzer *et al.*, 2018) cyclostationarity is assumed. Monthly climatological values of mixed layer temperature and salinity are taken from the Monthly Isopycnal & Mixed-layer Ocean Climatology (MIMOC) (Schmidtko *et al.*, 2013). This climatology is built from ARGO data and shipboard and Ice-tethered CTD data, and is pressure gridded at a resolution of $0.5^\circ \times 0.5^\circ$.

Monthly climatological fields of assimilated phosphate are generated using both oxygen and phosphate fields from the 2013 World Ocean Atlas (WOA13), according to the definition $[P^*] = [P] + [O]/175$ (Broecker *et al.*, 1998). In order to be away from the surface microstructure, but above the mixed layer depth globally, an arbitrary depth of 25 m is chosen to be representative of the mixed layer.

Transient tracer (CFC-11, CFC-12 and SF₆) data is obtained from an offline tracer model with physical fields derived from the Hallberg Isopycnal Model (HIM) (Shao *et al.*, 2013). As such transient tracers have a time varying history, climatological values are not used, and instead monthly values over the entire span of the data product (1936 – 2010) are used. Concentrations of all three transient tracers before this period are assumed to be zero. In order to obtain values post 2010, mixed layer values were scaled forward in proportion to atmospheric transient tracer concentrations (Bullister, 2017; NOAA/ESRL, 2021).

As mentioned in Section 1.4.2, ¹⁴C in the atmosphere contains a component of ‘bomb carbon’ in addition to ¹⁴C naturally produced by the interaction of cosmic radiation with nitrogen. Here only natural ¹⁴C is used as

this provides a temporal constraint which extends beyond the timescales of the CFCs and SF₆. However, the natural signal is contaminated with the bomb ¹⁴C signal and so has to be separated. GLODAP have created a gridded dataset of natural ¹⁴C in the ocean, based on observational cruise bottle data (Key *et al.*, 2004). The GLODAP dataset is updated regularly but has two main versions, V1 and V2. V1 contains a background ¹⁴C variable whereas V2 does not. V1 background ¹⁴C values from 20 m were taken to be representative of the mixed-layer. In the Arctic region where values were not available from V1, values were estimated using the alkalinity data from V2 and the method described by Rubin and Key (2002). These estimated values for the Arctic were provided courtesy of M-J. Messias and H. Mercier (personal communication, August 2019).

¹⁴C provides a time constraint to the method due to the radioactive decay of ¹⁴C. The longer the water has been separated from the atmospheric source of ¹⁴C, the more decay the ¹⁴C in the water sample will have undergone, and so the more negative the $\Delta^{14}\text{C}$ value. The $\Delta^{14}\text{C}$ of the atmosphere, and therefore the $\Delta^{14}\text{C}$ of the surface ocean, is not constant in time with variations due to solar activity (Stuiver and Quay, 1980), and more noticeably recently the ‘Suess effect’ (Grey, 1969). Due to the expense and time needed to analyse water samples for ¹⁴C, data are sparse, not only spatially but also temporally. For this reason the GLODAP V1 background ¹⁴C values are not normalised to a single year and data used to form the V1 product was from between 1972-1999. Because ¹⁴C is primarily used in the MEM as a constraint for water over 70 years (as this is the period not covered by the transient tracers), no attempt is made to impose the variation of background history (including the Suess effect) on the surface data.

^{14}C differs from the CFC/SF₆ tracers in the principles of how it provides temporal information. Water age can be found using transient tracers as the atmosphere has a time varying concentration of tracer, but tracer concentration in a parcel of water does not change once it is removed from the surface ocean. Water age can be found using ^{14}C as the atmospheric concentration is near constant (note discussion above), but once a parcel of water is removed from the surface that concentration will start to reduce in proportion to the time since that water was at the surface (i.e. its age), due to radioactive decay. In order to use ^{14}C in the MEM, the ^{14}C data has to be represented in the same format as the transient tracer data. To do this an artificial ‘surface history’ is created after which ^{14}C is treated like a transient tracer and assumed to be conserved in the water. To create the artificial surface history the cruise year (i.e. year 0) is given the surface concentrations from the GLODAP dataset and each preceding year is assigned a reduced concentration according to a linear decay rate of 8.1 ppt yr⁻¹ (Key, 2001).

All data are re-gridded and averaged onto a 5° x 5° grid, with monthly resolution in time. For each cruise, the time dimension varies as a function of cruise date. As the larger the number of years used as constraints the higher the computing demand, a non-linear resolution in time is used, with higher resolution in the most recent years. The years used are 0,1,2,...,75,80,90,120,160,200,250,300,400,...,1000,1200,1500,2000 years since the cruise date, with a value for each month within those years (i.e. a total of 1104 time points).

3.1.4 Data Standardisation & Tracer Weighting

In order to maintain numerical stability and allow the iterative solver to converge, the values for each of the seven tracers are standardised. In the work of Ting (2015) each value was standardised using the mean and standard deviations of the source data, according to Equation 3.4, where \hat{C}_j^I is the standardised interior concentration of tracer j , C_j^I the non-standardised value, \bar{C}_j the mean of all values in the source dataset for tracer j , and σ_j the standard deviation of tracer j values in the source data.

$$\hat{C}_j^I = (C_j^I - \bar{C}_j) / \sigma_j \quad \text{Eq 3.4}$$

However here, the mean and standard deviations (\bar{C}_j and σ_j) used in the standardisation (still according to Equation 3.4) are that of the cruise transect data and not the source region data. The mean and standard deviation are calculated across both cruises, as opposed to individually for each cruise. This modification to the method is primarily made for the following reason. If standardising based on the mean and standard deviation of source data, these values would be sensitive to the time resolution of the source data (e.g. for CFCs mean values calculated for the source region data over the 2000 year period would be very low as the mean would be strongly biased by a concentration of zero in the majority of years, which would be inappropriate to use to standardise the cruise data). Both the source data and interior (cruise) data were standardised using the same values.

In this analysis all tracers were equally weighted, however tests carried out to explore the impact of tracers being weighted differently found output to be largely insensitive to the input tracer weightings.

3.1.5 Prior

The prior is a ‘first guess’ that is given to the solver as a starting point, in order to guide the iterative solver to a solution that is reasonable. Choosing the right prior is important and that is why here the impact of using different priors is evaluated. A prior that is too weak will let the solver go in any direction that it wants, and can lead to wildly unphysical results. A prior that is too strong can mean that the results are dominated by the information provided by the prior as opposed to being constrained by the real data.

Here the prior is in the form of a probability associated with each $5^\circ \times 5^\circ$ grid cell at each point in time. The probabilities from all points in space and time sum to one, under the assumption that water has to have originated from the mixed layer somewhere, at some point. Temporal and spatial information can be included in the prior by increasing the probability of water originating from some areas or points in time, and decreasing the probability in other areas and points in time.

Here four different types of prior and combinations thereof are discussed.
1) A uniform spatial prior, where the probability of water originating from one $5^\circ \times 5^\circ$ grid box solely depends on the size of the surface within that box. 2) A uniform temporal prior where all points in time are equally likely. 3) An Inverse Gaussian (IG) prior where some times are more likely than others, and 4) an ECCO spatial prior where spatial information has been extracted from the MITgcm ECCO model.

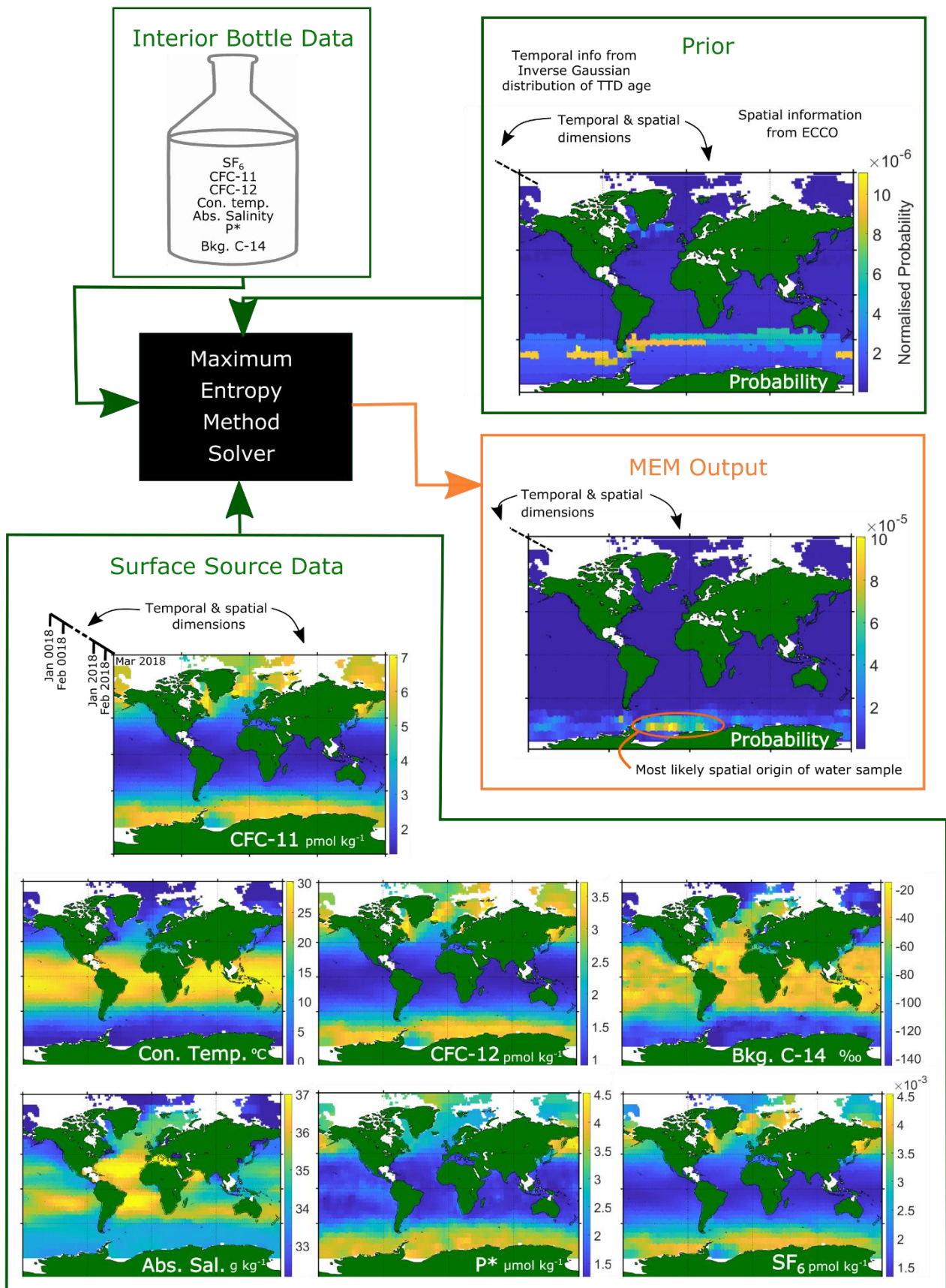


Figure 3.1 – Schematic of the MEM illustrating the spatial and temporal dimensions of the inputs (green outline) and output (orange outline).

The optimal prior, and the prior on which the results of this study are based, is considered to be a prior that combines the spatial information from the ECCO prior with the temporal information of the IG prior. Combining these two as opposed to taking spatial and temporal information from the model runs ensures that the results are not simply being forced to look like the model.

3.1.5.1 Generating the Inverse Gaussian Temporal Prior

It has been shown that the age of a parcel of water can be described by an Inverse Gaussian distribution of water of different ages. The shape of this distribution is controlled by the delta/gamma ratio (Δ/Γ), otherwise known as the ratio of mean age to width. Observations show this ratio to range between 0 and 1.5 (Waugh *et al.*, 2004), with tracer distributions well described by a transit time distribution (TTD) of ratio 1. Here a value of 1 is chosen for the optimal prior. In its most basic form, what this relationship tells us is that older water masses have had a greater opportunity for mixing with other parcels of water. A delta gamma ratio of 0 would correspond to purely advective flow, and an increasing ratio reflects increasing mixing (Waugh *et al.*, 2006). Here values of mean age provided by M-J. Messias (personal communication, 2018 & 2020) are used. These ages have been generated using the TTD method, the method previously widely used in the field of transient tracer research. The prior is then weighted using this distribution (see Figure 3.1 for visual of prior). This prior is individual to each sample as the TTD method uses the concentration of transient tracers in each sample to generate the mean age specific to that sample.

3.1.5.2 Generating the ECCO Spatial Prior

The ECCO spatial prior is generated using the output of the Global Ocean Passive Tracer Experiment (Section 3.3.2). The passive tracer concentration of all 18 surface passive tracers is obtained at all depths at the 24°S section, at model year 300. As not all depths reached an equilibrium tracer concentration at 300 years, a ‘remainder’ is calculated by summing the concentration of all 18 tracers at each grid point and subtracting this from 1. This remainder describes the fraction of a parcel of water which has not been in contact with the atmosphere in the 300 years of the model run, and so could originate from any region. For every grid point this remainder is distributed between the 18 tracers according to the size of the surface patch corresponding to that tracer (i.e. a larger patch would get a larger proportion of the remainder). These tracer concentrations (with the addition of the remainder) are then interpreted as the likelihood of water at that grid point having originated from each of the 18 surface patches. This information is then interpolated onto the locations of the bottle samples in depth and longitude for the zonal section. The probabilities of water at the bottle sample locations originating from each of those 18 regions are then translated into probabilities for each 5° x 5° grid square, accounting for the varying area of each 5° x 5° grid square.

3.2 Maximum Entropy Method: Data Interpretation Methods & Metrics

3.2.1 Calculating Errors

Each stage of this analysis has some form of error associated with it. The cruise data have analytical uncertainty, the source data have error associated

with sample analysis, data sparsity and interpolation, and the MEM itself has uncertainty associated with the convergence of an iterative solver and choice of prior. Where an ECCO derived spatial prior is used, this prior will also include error derived from model error e.g. incorrect representation of water mass formation. Here the ‘optimal’ choice of prior, source data and time resolution are presented, however it is these decisions which generate the largest uncertainty in the results. It has been shown using synthetic data (Holzer and Waugh, 2015) that the spread of results when the MEM is applied using an ensemble of different priors is a conservative (albeit ad-hoc) indicator of the robustness of the MEM results. Following Holzer *et al.* (2018) and Ting and Holzer (2017), an ensemble of 15 priors is generated and the results are used to calculate an uncertainty for the MEM results based on the standard deviation of the ensemble of inversions for any given quantity.

The ensemble of 15 priors are generated using $\Delta/\Gamma = 0.5, 1$ and 1.5 (see Section 3.1.5.1) crossed with five randomly weighted spatial priors. The spatial priors are created by generating five different sets of random numbers, with each set containing 18 random numbers corresponding to each of the 18 regions used to generate the prior. The random numbers are drawn independently from a uniform distribution of the interval 0.1 to 1.9. These random numbers are used to perturb the spatial weightings of the optimal prior and the prior is then re-normalised to one over time and space.

3.2.2 Choosing the Regions

The regions used in the study are based upon those used by Khatiwala *et al.* (2009) (Figure 3.2a) with modifications in the Arctic and Southern Ocean region (Figure 3.2b). The original regions only extended to 60°N and so the

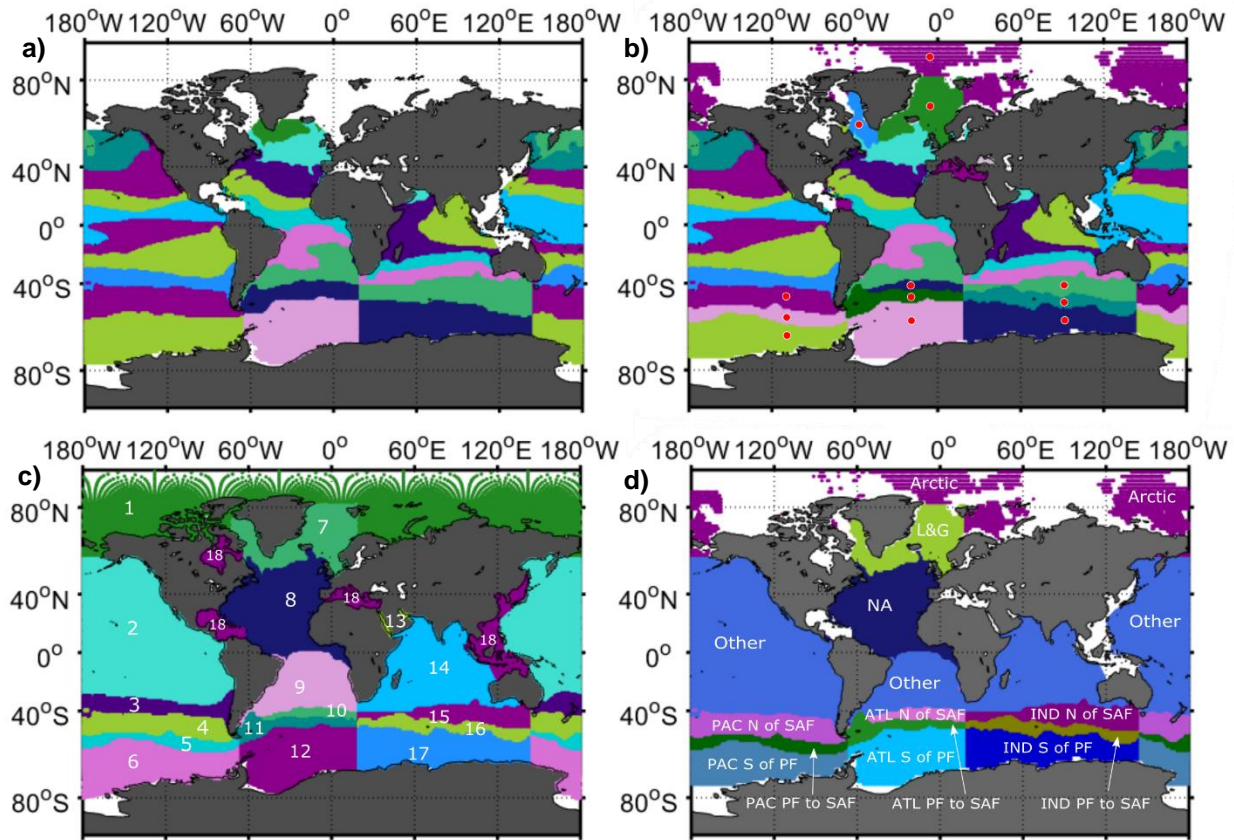


Figure 3.2 – Maps showing global surface regions. (a) Regions of Khatiwala *et al.* (2009). (b) Extended version of Khatiwala *et al.* (2009), red dots indicate regions which have been altered (see Section 3.2.2 for details). (c) Regions used in ECCO Global Ocean Passive Tracer Experiment. (d) Regions referred to in Chapter 4 & 6, these regions are the same as (b) but regions of less interest have been grouped together. An enlarged version of (d) can be seen in Figure 4.1. L&G = Labrador & GIN, NA = North Atlantic, PAC = Pacific, ATL = Atlantic, IND = Indian, N of SAF = North of Subantarctic Front, PF to SAF = Polar Front to Subantarctic Front, and S of PF = South of Polar Front.

existing Labrador Sea patch was extended further north to encompass all of the Labrador Sea and two new patches were added; the first stretching northeast from Iceland to Svalbard and the second encompassing the remainder of the Arctic Ocean. Though the original patches covered the full Southern Ocean, they followed arbitrary density contours and it was felt that it would be more useful to modify the Southern Ocean from two zonal bands to three zonal bands, with the Polar Front and Subantarctic Front acting as the boundaries. The climatological front positions used as boundaries were calculated based on the front positions from (Sallée *et al.*, 2008) which covered the period 1993–2013. These front positions were computed using AVISO satellite altimetry data.

Data was accessed through the Center for Topographic studies of the Ocean and Hydrosphere (CTOH) data catalogue.

In order to limit unnecessary computational work, in the Global Ocean Passive Tracer Experiment some regions of less interest to the study were grouped together in order to reduce the number of passive tracers required. Figure 3.2c shows the 18 regions used. Regions more relevant to the Southern Ocean water masses (e.g. those in the Southern Ocean) were retained in the original size but those in the major ocean basins were grouped. Tracer 18 is used to cover multiple marginal seas as for the purposes of the Global Ocean Passive Tracer Experiment the whole surface ocean needed to be covered by one of the passive tracers. Region 13, the Red Sea and Persian Gulf, was left as a small patch as literature (e.g. Fine et al., 1988) suggested that this region was important as a formation region of a precursor of AAIW. For the presentation of results in Chapters 4 & 6, regions were further grouped together (Figure 3.2d).

3.2.3 Visualising 3D Data

The output of the MEM is three-dimensional. For every interior bottle seawater sample, a probability is associated with every $5^\circ \times 5^\circ$ lat-lon grid cell at every monthly point in time history (0 - 2000 years ago). In order to give these probabilities meaning, the data has to be viewed from multiple perspectives in order to maximise insight. An outline of how these perspectives are generated and some of the metrics used in the forthcoming chapters are outlined briefly below.

The simplest way to visualise the data is to remove one of the dimensions. Where probability is plotted against time a spatial integration has

been performed, where probability is shown divided by region of origin, an integration over time has been applied. The temporal resolution used in the MEM is non-linear, however when the integration is made over time, each point in time is weighted equally. Although this is technically incorrect, here it is deemed an acceptable simplification as the ages of the studied water masses fall within the high resolution of the past 75 years; this would be inappropriate if working with older water masses. Where spatial integrals are made and a probability distribution is shown, the area under the curve is normalised to one and the probability at each point in time is weighted according to the interval of time represented by the value (intervals differ due to non-linear temporal resolution).

As mentioned in Section 3.1.3, for every year of the source data there are monthly values and so the MEM output also has this monthly resolution. In order to look at ages of water over a timescale of years in many of the results the seasonality is removed. This is done by calculating the mean value for each Jan-Dec 12 month period.

3.2.4 Water Age

The term ‘age’ refers to the number of years since a parcel of water was last in contact with the atmosphere (i.e. how long water has taken to travel from the surface waters to the point at which it was sampled from). Age can be calculated in several different ways and the values and meaning of these ages can vary widely. The main two types are mean age and modal age. As a parcel of water is not purely advected through the ocean, but also mixes with surrounding parcels of water, the mean age is the average age of all the parcels

of water that mixed to form the parcel of water which was sampled. Here the modal age is used, as this reflects the age of the core water mass.

3.3 Ocean Modelling Methods

The modelling aspect of this thesis falls under two main themes 1) the Global Ocean Passive Tracer Experiment, and 2) the Weddell Polynya Experiment. The Global Ocean Passive Tracer Experiment was conducted primarily with the aim of producing output that could be used as to generate a prior for the Maximum Entropy Method and to provide a way of studying tracer pathways. The aim of the Weddell Polynya Experiment was to explore the fate of water produced within a Weddell Polynya. Both experiments use the ECCOv4r2 configuration of MITgcm, further details of which can be found below.

3.3.1 ECCOv4r2 Configuration of MITgcm

MITgcm is a general circulation model developed by the Massachusetts Institute of Technology (Marshall *et al.*, 1997; MITgcm Group, 2002; Adcroft *et al.*, 2004). As part of the Estimating the Circulation and Climate of the Ocean (ECCO) project a global state estimate known as ECCO was developed using MITgcm. The aim of a state estimate is to constrain a model using observations in order to provide a more realistic real world version of a model, and ECCO achieves this for the global ocean. To create this state estimate, the adjoint of the model was used to optimally fit the model to observations, through small adjustments to the surface forcing, initial conditions and by varying certain parameters (e.g. viscosity and diffusivity parameters). Unlike a data assimilated model, values (e.g. temperature and salinity) are not artificially adjusted to

agree with observations during the forward run of the model. This means that if no modifications are made to the optimised initial conditions, surface forcing and parameters, the forward run of the model will produce the state estimate which will closely match the observations used to create the state estimate. However, if the initial conditions, surface forcing, or optimised parameters are modified at any point during the 20 year model run, the model will deviate away from the state estimate.

This study uses ECCO version 4 release 2 (ECCOv4r2) (Forget *et al.*, 2015), a state estimate for the period 1992 - 2011. ECCOv4r2 is a forward running model, which uses an hourly time-step. A Lat-Lon-Cap 90 grid is used in order to facilitate the inclusion of the Arctic whilst also allowing the grid vertices (also known as grid poles) to fall over land. This grid consists of five faces, four rectangular faces which sit side by side, stretching from 70°S (Antarctica) to 57°N, and a fifth smaller square face which connects the top of the other four faces and covers the Arctic Ocean; this grid has an approximate resolution of 1°. The model uses z^* (Adcroft *et al.*, 2004) vertical coordinates, meaning that the vertical levels are depth levels (as opposed to e.g. isopycnal levels) but with a non-linear free surface, allowing for variations in sea surface height. There are 50 vertical levels, with initial layer thicknesses ranging from 10 - 100 m within the surface 1250 m, and from 100 - 457 m in the deeper layers. The thickness of these levels is allowed to vary, which is particularly good for tracer conservation.

The GGL (Gaspar *et al.*, 1990) vertical mixing scheme is used with simple convective adjustment. The model includes a fully interactive sea-ice model, it uses a ‘real freshwater flux’ (see Forget *et al.*, 2015) boundary condition, uses 6 hourly ERA-Interim re-analysis fields (Dee *et al.*, 2011) for the

near surface atmospheric state (temperature, humidity, downward radiation and precipitation) and for wind-stress, and a seasonal climatology is used for run-off. Density in the model is evaluated using the Jacket and McDougall (1995) equation of state. The set-up does not include tides.

3.3.2 Global Ocean Passive Tracer Experiment

The Global Ocean Passive Tracer Experiment is an experiment in which passive tracers are continuously added to the surface ocean as a way to trace the surface locations from which different water masses originate. In this study this information is used as a spatial prior for the MEM (see Section 3.1.5.2) and the tracer fields generated by the experiment are also used to trace interior pathways and calculate tracer arrival times (see Section 3.3.7).

Eighteen surface regions are used, covering the entire global ocean surface. A higher resolution of regions is used in the Southern Ocean, as this region is of particular relevance to this study. The Southern Ocean regions are divided by ocean basin and by the PF and SAF (see Section 3.3.3 for a discussion of these front positions). The ptracers package is used to add a different passive tracer in each of the surface regions. In each region the tracer concentration is initially set to 1. Below the surface the initial tracer concentration decays according to a trigonometric function over the top six model levels (5, 15, 25, 35, 45, 55 m) e.g. conc. at 15 m = conc. at $5 \text{ m} \cdot \cos(\pi/10)$, conc. at 25 m = conc. at $5 \text{ m} \cdot \cos(2\pi/10)$ etc. The tracer is restored towards 1 in the surface level of that region and restored to towards 0 at the surface everywhere else, with a timescale of six hours (six time steps).

The experiment is run for a total of 300 years with the 18 tracers continuously added over this period. The experiment uses repeat forcing from

the ECCO 20 year period (1992 - 2011) for the full 300 years of the model run. The assumption is made that if the model was run to a full equilibrium state the sum of all 18 tracers in a single grid cell would total 1. This means that the value of a passive tracer from a region can be interpreted as the fraction of water originating from said region within the timespan of the model run (e.g. Tracer X concentration of 0.3 = 30 % of water originating from Region X). In the initial testing of the experiment, problems arose where negative tracer concentrations were present. This error was minimised in the experiment development process however does persist to a small degree. In the context of the way passive tracer concentrations are used in this study, this small error is not considered large enough to have a noticeable impact on the results.

3.3.3 Southern Ocean Fronts in ECCO

Ocean frontal positions are not fixed in time and space; in both observations and models frontal positions are known to shift seasonally and inter-annually. The tracer regions where the passive tracers are added are fixed and are based on a climatology of Southern Ocean front positions derived from satellite data (see Section 3.2.2). These same observational front positions are used to define the regions in the model, instead of model derived front positions, in order to retain comparability between the results of the MEM and the results of the ECCO tracer experiment. This decision was validated by the minimal differences between the positions of the observation derived fronts and the model derived fronts. A brief comparison of the frontal positions is outlined below.

Both the PF and SAF are associated with strong meridional property gradients. Traditionally the PF is defined as the northern limit of Antarctic Winter

Water (AAWW), which is itself defined as the extent of 2°C water at 200 m (Orsi *et al.*, 1995; Belkin and Gordon, 1996). The SAF is more often defined by a maximum in the meridional gradient of temperature, density or potential vorticity (PV) (Orsi *et al.*, 1995; Belkin and Gordon, 1996; Sokolov and Rintoul, 2002). These Southern Ocean fronts are not continuous but weaken/strengthen and merge/split (Hughes and Ash, 2001; Sokolov and Rintoul, 2007) complicating their definition. In order to define a continuous frontal position it is common to define these fronts (particularly the SAF) by a Sea Surface Height (SSH) contour associated with the characteristics of the front. The observational frontal positions used in this study are those of Sallée *et al.* (2008) who defines the PF as a SSH contour of 0.95 m, associated with the extent of 2°C water at 200 m, and the SAF as an SSH contour of 1.2 m associated with a strong temperature gradient at 300 m and a strong PV gradient at $\sigma_\theta = 27 \text{ kg m}^{-3}$.

To assess the suitability of using these observational frontal positions in the ECCO experiment the position of the PF of Sallée *et al.* (2008) is compared to the boundary of 2°C at 200 m (Figure 3.3). The positions closely match, with the most noticeable discrepancy at the Kerguelan plateau (70°E) where the observations deviate to the south of the front identified in ECCO by up to 5° latitude. For the SAF the SSH contour (0.55 m) which best corresponds to the maximum gradients in SSH, SST, temperature at 300 m and density at 300 m in ECCO is used to define the front position (Figure 3.3). Overall the definition matches closely with the exception of the area around the Falkland Islands where the ECCO definition passes to the south of the islands and the observational definition of Sallée *et al.* passes to the north. However, it should be noted that other observational studies (e.g. Naveira Garabato *et al.*, 2002) do describe the SAF as passing to the south of the Falkland Islands. An

additional consideration when evaluating any differences between the ECCO fronts and the observation based fronts is that of the model grid. As each model grid box is $\sim 1^\circ$, discrepancies of $< 1^\circ$ between the two definitions are insignificant.

Though this comparison shows the SAF position (sometimes referred to as the Southern SAF), it should be noted that for the tracer regions the position of the northern SAF is used to maximise the extent of the PF to SAF region. It is assumed that as the position of the PF and the SAF in ECCO closely match the observational definition, the position of the northern SAF (whose identifying features are not explicitly defined in Sallée *et al.* (2008)), is likely to also closely match.

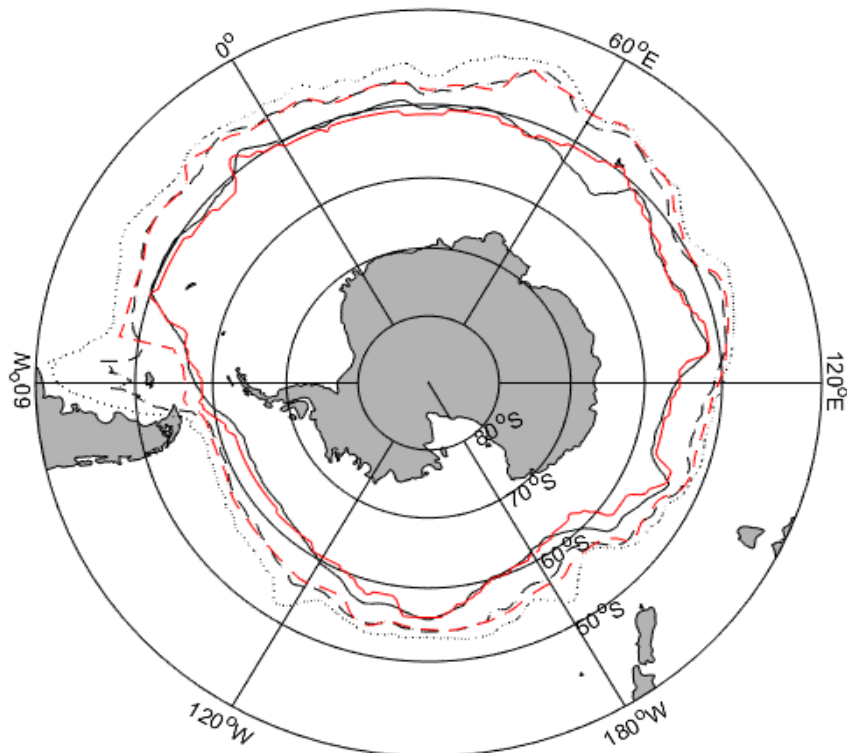


Figure 3.3 – Comparison of PF and SAF positions between ECCO and climatological front positions derived from observations (Sallée *et al.*, 2008). Solid line indicates PF for ECCO (red) and observations (black). Broken lines indicate SAF from observations (black dashed), SAF-North from observations (black dotted) and SAF from ECCO (red dashed). ECCO front positions are based on the mean fields of the first 20 years of the model run.

3.3.4 Comparing ECCO to Observations

ECCO was chosen for use in this thesis as it is a well-constrained model with a realistic ocean that can be compared with observational results. Figure 3.4 compares the potential temperature and salinity fields of ECCO with those observed at 24°S in 2018. The salinity minimum of AAIW is highlighted by the 34.4 salinity contour. This is very similar to observations, although observations show slightly lower salinities in the west and slightly higher salinities in the east (anomaly is < 0.05 either way). In ECCO the presence of the fresher and cooler AABW can be seen in the Brazil Basin (west of the MAR) and Cape Basin (east of Walvis Ridge), and the temperature and salinities in ECCO appear to align very closely with observations. One noticeable difference between the model and observations, is that in the observations the AABW is seen to penetrate higher in the water column close to the bathymetry in the west. This is evident by the positive anomaly in temperature and salinity at 36.5°W at 3900 m (Figure 3.4 b & d).

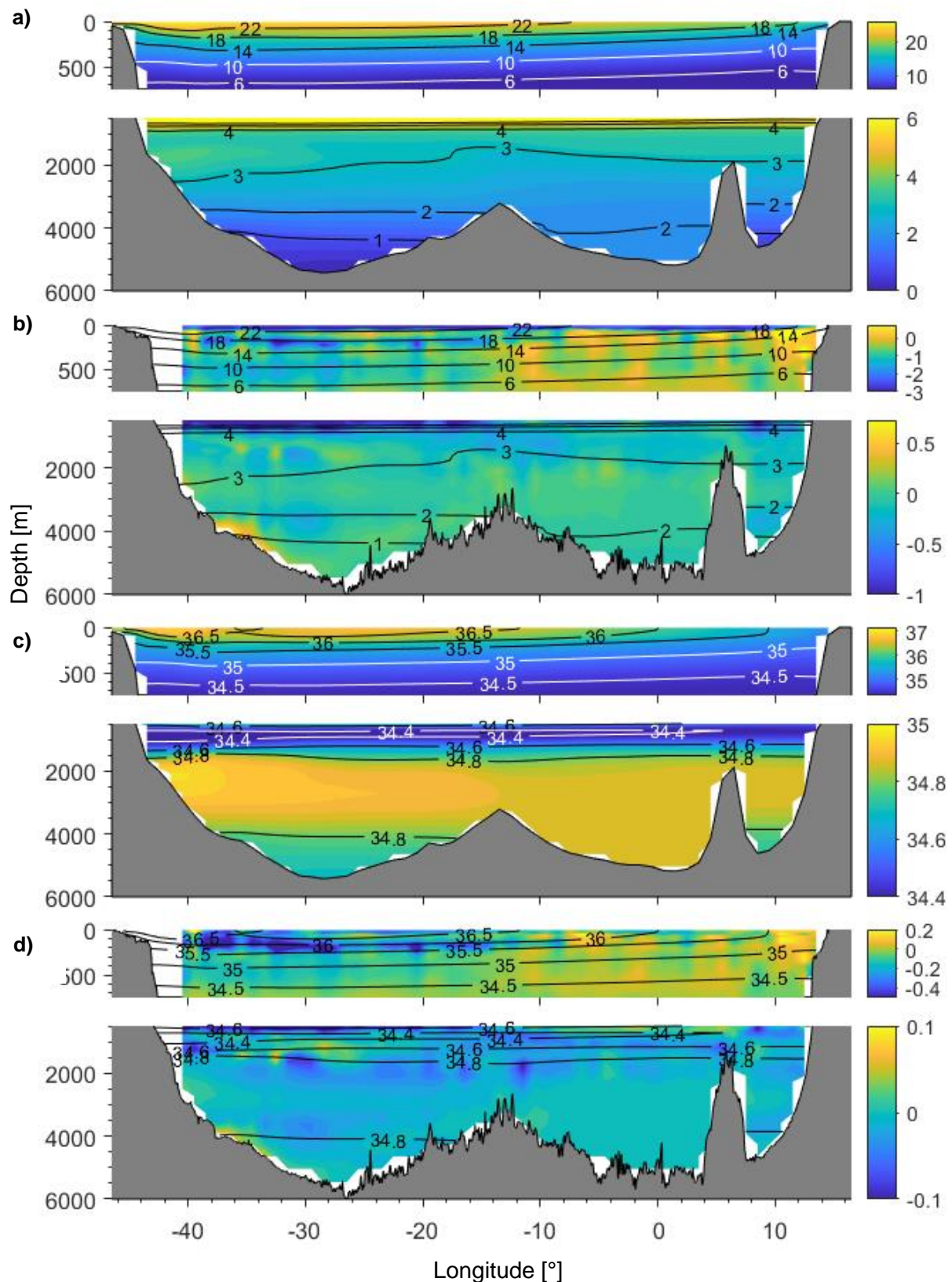


Figure 3.4 – Comparison of potential temperature ($^{\circ}\text{C}$) and salinity fields between an average of the initial 20 year period of the ECCO experiment (a & c) and the March/April 2018 observational data . Anomaly fields (ECCO – observations) are shown in panels b & d, for potential temperature and salinity respectively. Each panel is split into two depth sections (top 0 - 750 m, bottom 500 - 6000 m) to reveal the finer structure in the surface waters. Contours (black & white) show the potential temperature (a & b) and salinity (c & d) contours of the ECCO data. Note: On the anomaly plots, the colour axis differs between surface and deep waters. For observational fields see Figures 2.2 & 2.4.

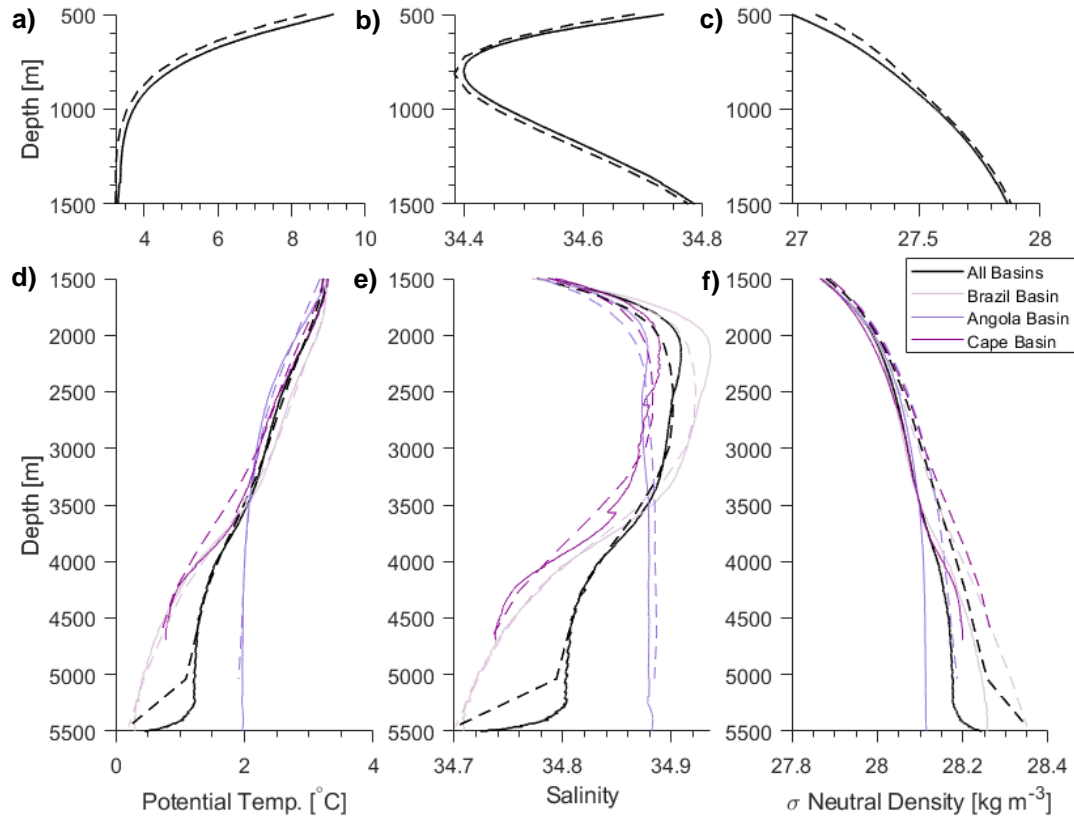


Figure 3.5 – Comparison of depth profiles of potential temperature (a & d), salinity (b & e) and neutral density (c & f) between an average of the initial 20 years in ECCO (dashed line) and observations in 2018 (solid line). Profiles have been averaged across the three basins at 24°S, and for each basin individually (see legend).

Depth profiles (Figure 3.5) show that in the depth range 500 - 1500 m, ECCO closely matches observations, with ECCO showing marginally lower temperatures and salinity. The salinity minimum, characteristic of AAIW, is well represented, both in thickness and in depth of the minimum (800 m). Deeper in the water column ECCO largely matches the observations, with the exception of salinity at around 2000 m where ECCO appears to underestimate salinity by 0.02 units. This underestimation is not only seen in the basin wide average, but also in all three of the individual basins. In the deep and bottom waters ECCO represents temperature and salinity well when compared on a basin scale. Though a cumulation of the small discrepancies in temperature and salinity appears to lead to an overestimation of the density of waters below 3500 m.

3.3.5 Model Stability

The ECCO set-up of MITgcm is a state estimate for a specific 20 year period. Here the forcing of those 20 years is repeated in order to create a longer 300 year model run in which the passive tracers can be propagated. One reason for using ECCO is because it has a good representation of modern global ocean circulation. It is important to evaluate the stability of the model to ensure that throughout the 300 years of the model run this circulation remains realistic.

Two metrics are used to gain an overall picture of the global circulation at the end of the 300 year run, and how this has changed from the initial circulation. Those metrics are the meridional overturning streamfunction (Figure 3.6) and the barotropic streamfunction (Figure 3.7). The meridional

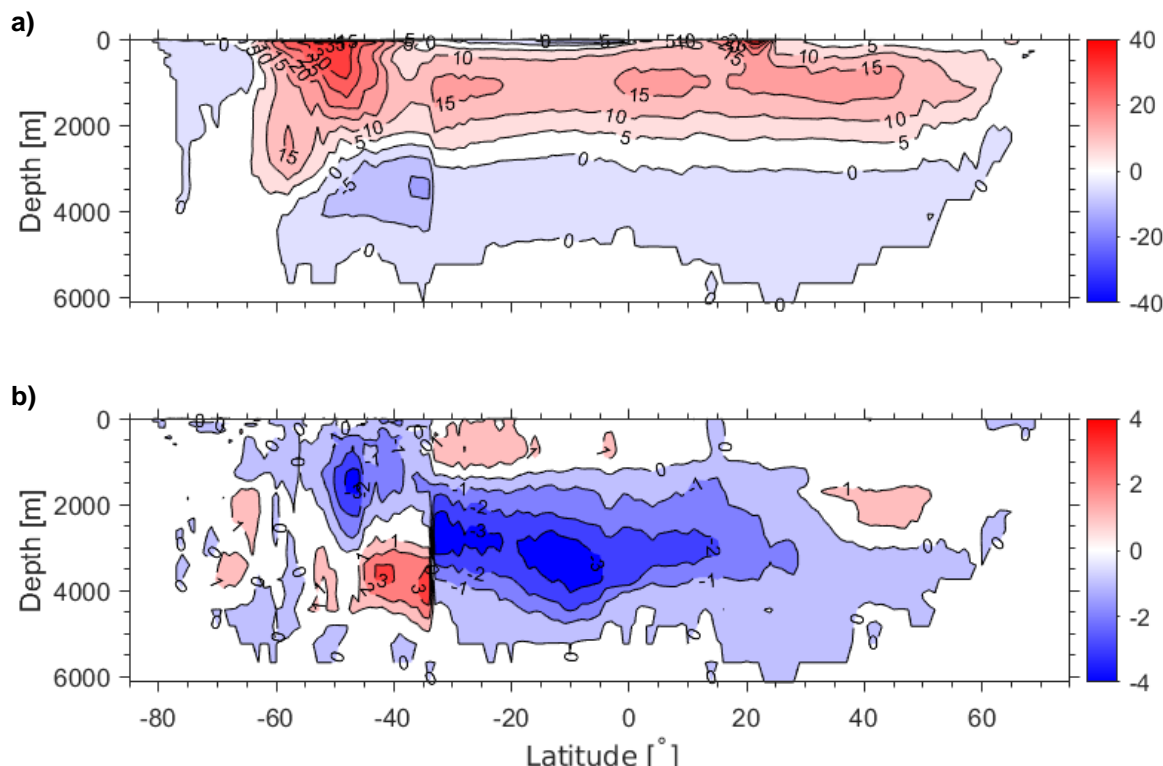


Figure 3.6 - Residual overturning circulation [Sv], zonally integrated over the Atlantic Sector north of 33°S, and over all longitudes south of 33°S. (a) Shows time mean circulation for 280 to 300 model years. (b) Shows the change in circulation from the first 20 years of the model run (280 to 300 years - 0 to 20 years).

overturning includes both the barotropic component and the eddy bolus component, and accounts for variable layer thickness.

The Atlantic meridional overturning at the end of the 300 year period (Figure 3.6a) has changed slightly but maintained its structure of a clockwise NADW cell above 2500 m and an anticlockwise AABW cell in deeper waters. The NADW cell has a northward transport of 17 Sv. A slight weakening is seen in the lower levels of the NADW cell, and a strong strengthening is seen in the AABW cell in the Atlantic (up to -3.5 Sv change on a background of -4 - 0 Sv). These changes result in a shallowing of the interface between the two cells by ~300 m, between the initial 20 year period and the final 20 year period. In the Southern Ocean (all basins) at the end of the 300 years the upper meridional overturning cell has weakened. However, this change is minimal with a weakening of up to 2 Sv on a background transport of 30 - 35 Sv. A more significant change in the Southern Ocean is a weakening of the lower meridional overturning cell by up to 3 Sv (on a background of 10 Sv).

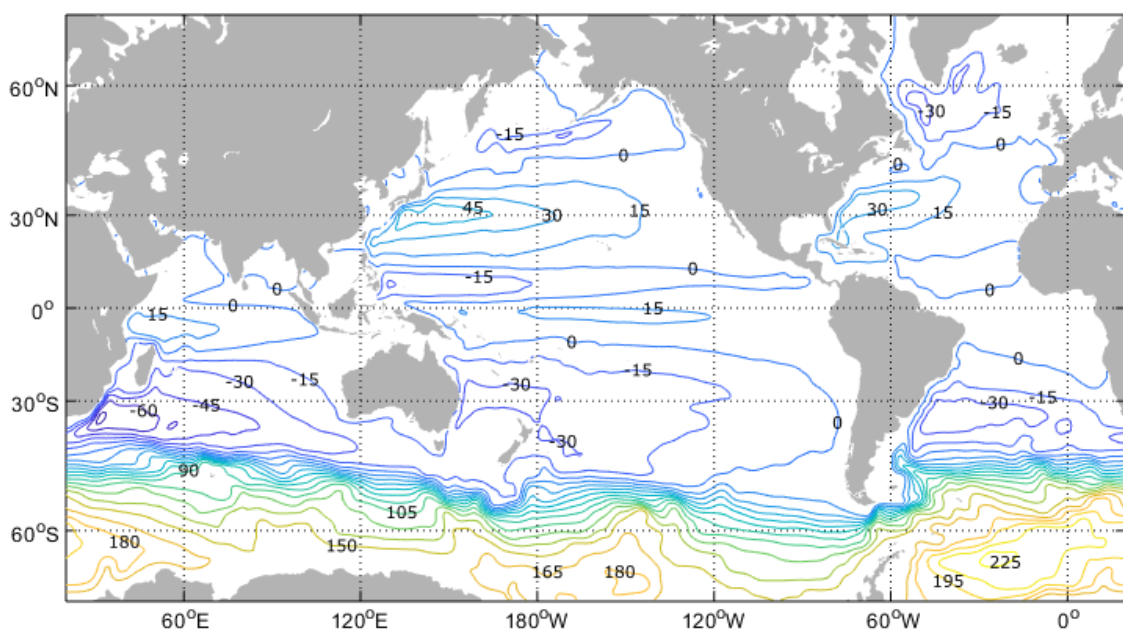


Figure 3.7 – Map of mean barotropic streamfunction for the final 20 years of the 300 year experiment.
Contours at 15 Sv intervals.

The barotropic streamfunction also indicates good stability of the model, with gyre circulations of each ocean basin and the ACC remaining realistic throughout the model run (Figure 3.7).

To further evaluate the stability of the model, the domain average temperature and Drake Passage transport are also considered. The domain average temperature is the average temperature of the entire ocean; large changes over time would indicate changes to temperature structure and stratification. As can be seen by the distinct repeating 20 year pattern in Figure 3.8a, the domain average temperature reflects the repeating cycle of the model forcing. A positive trend is seen in temperature over the 300 years but this change is small ($\sim 0.02^{\circ}\text{C}$), particularly when compared to inter-annual variability ($\sim 0.05^{\circ}\text{C}$). The forcing used is from the period 1992 - 2011 and so a warming trend is not unexpected as this 20 year forcing does include a period of climate change. It may also be that this apparent warming is simply the model equilibrating.

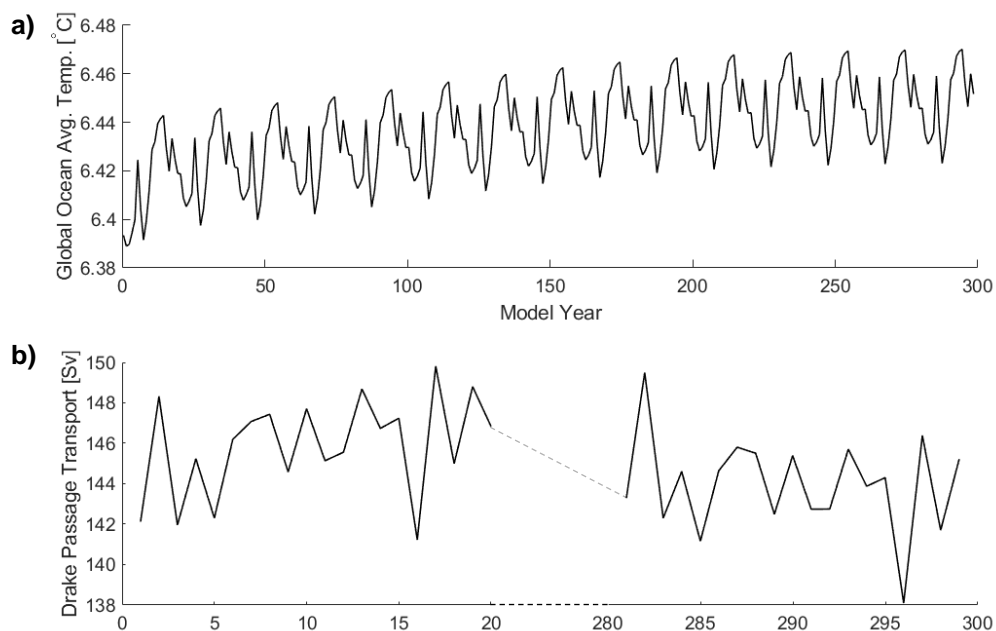


Figure 3.8 – (a) Domain average temperature ($^{\circ}\text{C}$) over the length of the model run. (b) Drake Passage Transport (Sv) for the first and last 20 years of the model run.

Drake Passage transport is calculated for the initial and last 20 years of the model run (Figure 3.8b). Transport was remarkably consistent between these two periods with an average transport of 146 Sv for the initial 20 years and 144 Sv for the final 20 years. Drake Passage transport is closely related to the isopycnal slope across the Southern Ocean. Hence, a stability in transport also indicates that global stratification remained largely the same. As well as being consistent with each other, these transports also fall within the range of Drake Passage transports derived from observations (134 Sv, Whitworth and Peterson, 1985; 137 ± 8 Sv, Cunningham *et al.*, 2003; 173.3 Sv, Donohue *et al.*, 2016).

3.3.6 Weddell Polynya Experiment

The Weddell Polynya Experiment (Chapter 5) uses the same ECCO set-up of MITgcm but is run for a shorter period of 80 years. The experiment is comprised of one control run and one perturbed run. The circulation in the control run is equivalent to the first 80 years of the 300 year Global Ocean Passive Tracer Experiment. The only difference between the two is in the input of passive tracers, which do not affect the physics of the model. For this reason the stability of the 300 year run (Section 3.3.5) is considered evidence for the stability of the 80 year control in the Weddell Polynya Experiment. Details of the set-up of the Weddell Polynya Experiment are given in Section 5.2.

3.3.7 Calculating ECCO Arrival Times

Both the Global Ocean Passive Tracer Experiment and the Weddell Polynya Experiment use continuous inputs of passive tracers to establish the geographic origin of water. Neither however use an age tracer, meaning that the time a tracer has taken to arrive at a particular location must be diagnosed. In

an attempt to put a timescale on tracer pathways two metrics are developed. The first is based on tracer reaching a threshold concentration at a particular location (referred to as ECCO arrival times), and the second is based on the rate of tracer arrival at a location (referred to as maximum rate of tracer arrival). Chapter 4 uses both metrics and Chapter 6 uses purely the second metric.

In order to calculate the ECCO tracer arrival times, first the equilibrium tracer concentration is found. This is defined as the concentration of a tracer at a particular location, where the concentration of tracer is no longer increasing over time. The assumption is made that after 300 model years all tracers will have reached equilibrium concentration at the salinity minimum (AAIW) at 24°S for the AAIW study.

Tracer concentration is found for all 18 tracers at each longitude in the model levels relevant to AAIW. The maximum value of each tracer at the salinity minimum across the whole section is found, and an average maximum value calculated by taking the mean of these values over a 10 year period (290 - 300 model years). This value is then deemed the equilibrium tracer concentration for each individual tracer at 24°S.

Using this equilibrium tracer concentration a series of thresholds are then calculated, corresponding to 1%, 5%, 10%, 20%, 50%, 75%, 95% and 99% of the equilibrium concentration (for each tracer separately). The model year in which each tracer threshold is first met at any point along the 24°S section (within the depth range of the salinity minimum) is then found. Following a similar methodology to that used by Zanowski and Hallberg (2017), the 1% threshold is interpreted as the time when the tracer first arrives at the section. The 95% threshold is interpreted as the tracer reaching equilibrium at 24°S. A

higher percentage is not used to reduce the sensitivity to the way in which the equilibrium concentration is calculated to represent the entire section, and to account for any long term trends/decadal variability that may cause the 290-300 year average to not be representative of the true equilibrium concentration.

The maximum rate of tracer arrival was calculated for both AAIW and AABW at 24°S. For AAIW an average tracer concentration at each time point is calculated across the three model levels surrounding the AAIW core (720 m, 815 m, 910 m), and across all longitudes in the section. For AABW a point core is established and the tracer concentration within a single grid cell, centred at 36.5°W, 4260 m, is evaluated through time. This creates a time series of tracer concentration for AAIW and AABW at 24°S for each tracer individually. For both the AAIW and AABW time series, the rate of tracer arrival is calculated. To remove inter-annual variability, a 20 year centred moving average is then applied to the time series of rate of tracer arrival. The maximum of the rate of tracer arrival is considered analogous to probability peaks presented in the MEM results (e.g. Figure 4.4). The basis of this analogy is that the time when the most tracer is arriving from a region, will be the dominant time signature that is detected by the MEM.

Chapter 4:

Temporal and Spatial Origins of AAIW at 24°S, from a Combined Maximum Entropy Method and ECCOv4 Approach

Abstract: An understanding of the origins of AAIW allows for estimations of the amount of heat and carbon being transported from the Southern Ocean to the interior Atlantic and how this is changing with climate change. In this chapter a Maximum Entropy Method is applied to transient tracer data from intermediate depths at 24°S in the South Atlantic. The results are used to estimate the most likely sources of AAIW in space and time, and evaluate the differences between observations taken on two cruises nine years apart. The results are compared to the results of a passive tracer experiment in ECCOv4r2, in order to identify the possible pathways of AAIW, and assess the feasibility of the Maximum Entropy Method results. The Maximum Entropy Method predicts 83% of water at the intermediate salinity minimum to originate from a Southern Ocean region, with half of the water predicted to originate from the region south of the Polar Front. Multiple potential temporal origins are identified in some of the AAIW layers, suggesting a contribution from young waters of 5 - 25 years from north of the Subantarctic Front and older waters of 35 - 55 years from south of the Polar Front. The ECCO passive tracer results generally agree with the Maximum Entropy Method results but predict a lower contribution of water from south of the PF to AAIW at 24°S. Differences in temporal origin are observed between the repeat cruises, with the less dense younger waters appearing to age by three years and more dense older waters appearing to age by nine years.

4.1 Introduction

In this chapter we explore the results of applying the MEM to water samples collected at 24°S in 2009 and 2018 between 300 and 2000 dbar. These results are described with a focus on the salinity minimum corresponding to the core of the AAIW and the three neutral density layers (AAIW 1, AAIW 2 and AAIW 3) associated with AAIW in the Atlantic (defined in Section 2.2.1). We will consider the regions from which water at the salinity minimum originates (Section 4.2.1), how these regional origins vary with depth (Section 4.2.2), the age of AAIW at 24°S (Section 4.3.1), how this age varies across the section (Section 4.3.2), and which season AAIW originates from (Section 4.4).

We will then consider the results of passive tracer experiments in ECCO (Section 4.5), focussing on how water travels from the Indian N of SAF (Section 4.5.2; see Figure 4.1 for regions), Pacific and Atlantic S of PF (Section 4.5.3) and Pacific PF to SAF (Section 4.5.4) regions to 24°S. The MEM and ECCO

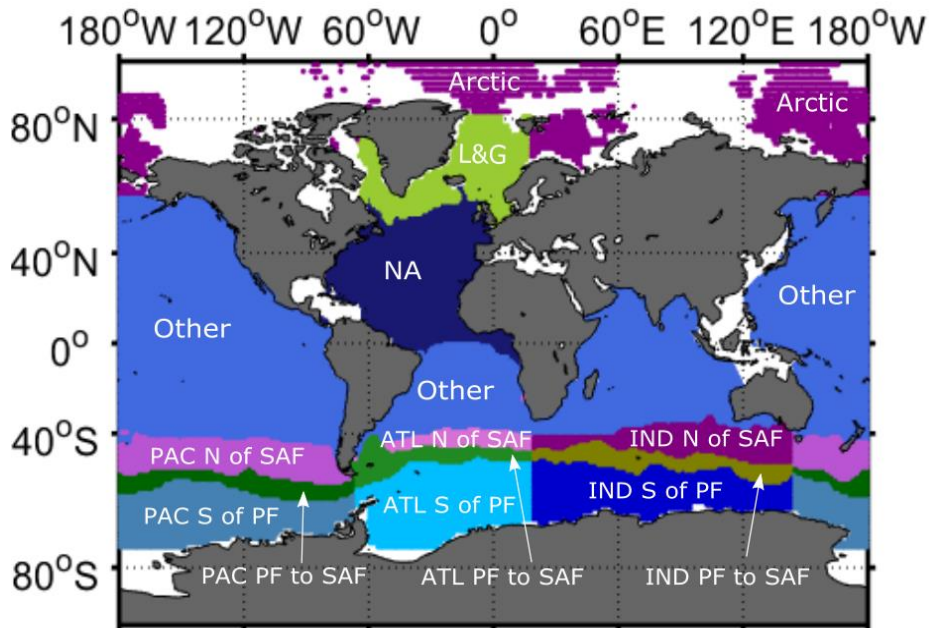


Figure 4.1 – Regions used to describe the MEM and ECCO results. See Section 3.2.2 and Figure 3.2 for more details. Regions in white are where source data was excluded from the application of the MEM, or not available. L&G = Labrador & GIN, NA = North Atlantic, PAC = Pacific, ATL = Atlantic, IND = Indian, N of SAF = North of Subantarctic Front, PF to SAF = Polar Front to Subantarctic Front, and S of PF = South of Polar Front.

results are then compared to the literature (Section 4.6). Finally we will discuss the temporal differences between the 2009 and 2018 data (Section 4.7) and consider the impact that the set-up of the MEM has on the results (Section 4.8).

4.1.1 Background of AAIW at 24°S

The 24°S oceanographic section cuts E-W across the South Atlantic, through the centre of the South Atlantic Gyre, crossing both the Mid-Atlantic Ridge (MAR) and the Walvis Ridge, which separate the Brazil, Angola and Cape Basins respectively (see Figure 2.1). The section cuts zonally across the Atlantic Meridional Overturning Circulation (AMOC), encompassing northward flowing SAMW, AAIW, UCDW and AABW, and southward flowing NADW, which lies below the UCDW but above the AABW. AAIW plays an important role in this overturning system, by transporting heat and carbon northward at intermediate depths. At 24°S the salinity minimum associated with this AAIW layer sits at a pressure of 700 - 900 dbar, and shoals towards the east of the section. Existing knowledge of AAIW in the South Atlantic (see Sections 1.2.3 and 1.2.4), suggests it is formed from two main components; water entering the South Atlantic from the west through Drake Passage (the cold pathway) and water entering from the Indian Ocean, passing eastward to the south of South Africa (the warm pathway).

The section has been occupied in 1958, 1983, 2009 and now 2018, and trends in salinity and temperature over this time have been studied (McCarthy *et al.*, 2010). Waters at the salinity minimum warmed between 1958, 1983 and 2009, and increased in salinity between 1958 and 1983, but showed no significant change in salinity between 1983 and 2009. Through a relationship with AOU (Apparent Oxygen Utilisation) McCarthy *et al.* ascribe these changes

to a weaker influence of Indian Ocean waters (via the warm water pathway) in 1958, than in 1983 and 2009. Waters above the salinity minimum (termed thermocline waters by McCarthy *et al.*) increased in salinity between 1958 and 1983, but freshened between 1983 and 2009. Waters below the salinity minimum (identified as UCDW) increased in salinity between 1958, 1983 and 2009.

4.1.2 Methods Specific to the AAIW Analysis

In this analysis, the MEM is applied to the data at 24°S using an inverse Gaussian and ECCO 300 prior (as described in Chapter 3). Due to issues with the MEM unrealistically gravitating towards extreme values in some of the marginal seas (similar to an issue with Mediterranean waters noted by Holzer *et al.*, 2010), some regions which were deemed of low relevance to AAIW are removed as potential sources. These include Hudson Bay, the Baltic Sea and the Mediterranean Sea.

To exclude outliers in the MEM output (samples that were clearly incongruous to those around them), a filter is applied. Any sample whose probability of originating from one of the three Southern Ocean regions (S of PF, PF to SAF or N of SAF) exceeds 2.5 standard deviations of the other samples within a 0.1 kg m⁻³ density bin is not included in the analysis.

The following sections present and discuss the results of the analysis.

4.2 Spatial Origin of Water

4.2.1 At the Salinity Minimum

First we consider the predicted origin of AAIW, regardless of the transit time taken for a parcel of water to arrive at 24°S. Although the method uses a 5°x 5° grid, here the results are grouped into seven main regions for the analysis, these regions can be seen in Figure 4.1 (see Section 3.2.2 for a discussion of the regions used). The water originating from each of these regions is described as percentage contributions, where if the contributions from all seven regions were added together, they would total 100%.

Region	JC032	Ensemble Uncert.	Averaging Uncert.	JC159	Ensemble Uncert.	Averaging Uncert.
S of PF	0.50	± 0.006	± 0.03	0.48	± 0.005	± 0.03
Pacific	0.17	± 0.001	± 0.01	0.17	± 0.002	± 0.01
	0.20	± 0.002	± 0.01	0.20	± 0.006	± 0.01
	0.12	± 0.003	± 0.02	0.11	± 0.002	± 0.01
PF to SAF	0.17	± 0.003	± 0.04	0.19	± 0.007	± 0.03
Pacific	0.10	± 0.001	± 0.02	0.10	± 0.003	± 0.01
	0.04	± 0.001	± 0.01	0.05	± 0.002	± 0.01
	0.03	± 0.001	± 0.01	0.03	± 0.002	± 0.01
N of SAF	0.17	± 0.006	± 0.03	0.16	± 0.009	± 0.02
Pacific	0.05	± 0.001	± 0.01	0.05	± 0.002	± 0.01
	0.02	± 0.001	± 0.01	0.02	± 0.001	± 0.01
	0.10	± 0.004	± 0.02	0.10	± 0.006	± 0.02
Lab & GIN	0.05	± 0.003	± 0.02	0.05	± 0.002	± 0.02
Arctic	0.01	± 0.002	± 0.01	0.01	± 0.007	± 0.01
NA	0.06	± 0.001	± 0.01	0.06	± < 0.001	± 0.01
Other	0.05	± 0.003	± 0.01	0.05	± 0.015	± 0.01

Table 4.1 – The fraction from each region, as predicted by the MEM, at the salinity minimum of an average profile at 24°S for JC032 (2009) and JC159 (2018). Ensemble uncertainty reflects 1 standard deviation within the 15 average profiles created using the ensemble. Averaging uncertainty reflects 1 standard deviation in the data used to create the average profile.

Regional contributions obtained from the MEM for each bottle sample are gridded onto the 27.37 kg m⁻³ σ_n surface, the average density of the salinity minimum for both cruises. The contribution from each region is shown in Table 4.1. These values show that according to the MEM, averaged between the two cruises, Southern Ocean waters contribute 83% to the identity of the AAIW core

at 24°S. Of the three Southern Ocean regions, the largest contributor, with half of the water predicted to originate from this region, is the S of PF region. The remaining Southern Ocean regions, the PF to SAF and the region N of SAF, contribute in fairly even measure, with contributions ranging from 16-19%.

These Southern Ocean contributions can be further dissected into the three major basin sectors, the Pacific, Atlantic and Indian. For waters originating from S of PF, the Pacific and Atlantic dominate, each contributing approximately twofold the Indian contribution. The PF to SAF region is dominated by the Pacific contribution, whilst the region N of SAF shows the strongest contribution from the Indian sector.

4.2.2 Variations with Depth

Although it is common to focus on the salinity minimum when studying AAIW in the South Atlantic, the MEM also allows us to look at how the contributions of different water masses vary with depth. Due to the varying depth of the AAIW core across the 24°S section, neutral density is used as a vertical coordinate to create average profiles at 24°S (Figures 4.2 & 4.3).

The PF to SAF region in the Pacific is considered to be one of the main regions for AAIW formation (Talley, 1996). In the MEM results, the peak in contribution from the PF to SAF region (Figures 4.2b & 4.3b) corresponds well to the salinity minimum ($27.36 \text{ kg m}^{-3} \sigma_n$) at $27.35 \text{ kg m}^{-3} \sigma_n$ in the 2009 data. In the 2018 data, the peak fraction in the average profile sits slightly above the salinity minimum ($27.37 \text{ kg m}^{-3} \sigma_n$) at $27.27 \text{ kg m}^{-3} \sigma_n$. However, the discrepancy is within one standard deviation of the MEM output and so is not significant.

Figure 4.2 – Neutral density profiles showing the MEM predicted fractions from different regions alongside profiles of other relevant variables for Cruise JC032. All profiles represent the average profiles across the 24°S section, grey shading represents one standard deviation of the ensemble output. Blue horizontal line corresponds to the density of the salinity minimum (27.36 kg m⁻³), maroon line corresponds to the density of the local CTD oxygen minima (27.60 kg m⁻³). Grey dashed horizontal lines represent the boundaries of the three density classes AAIW 1 (27.23–27.3 kg m⁻³), AAIW 2 (27.3–27.4 kg m⁻³), AAIW 3 (27.4–27.5 kg m⁻³). In a – c results are shown for the Pacific, Atlantic and Indian sectors of the Southern Ocean region combined (thick black line) and separately (purple, green and orange dotted lines, respectively).

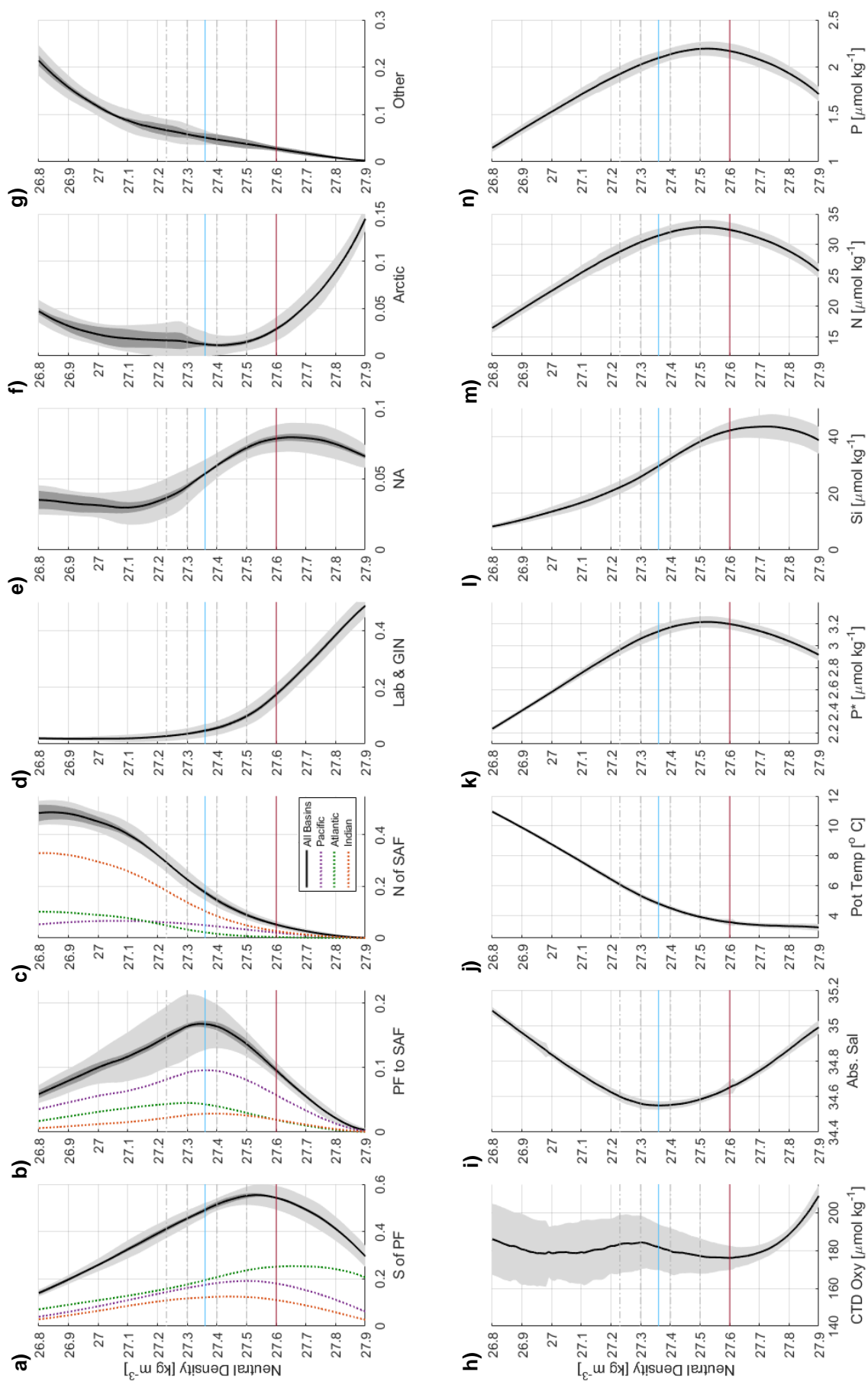
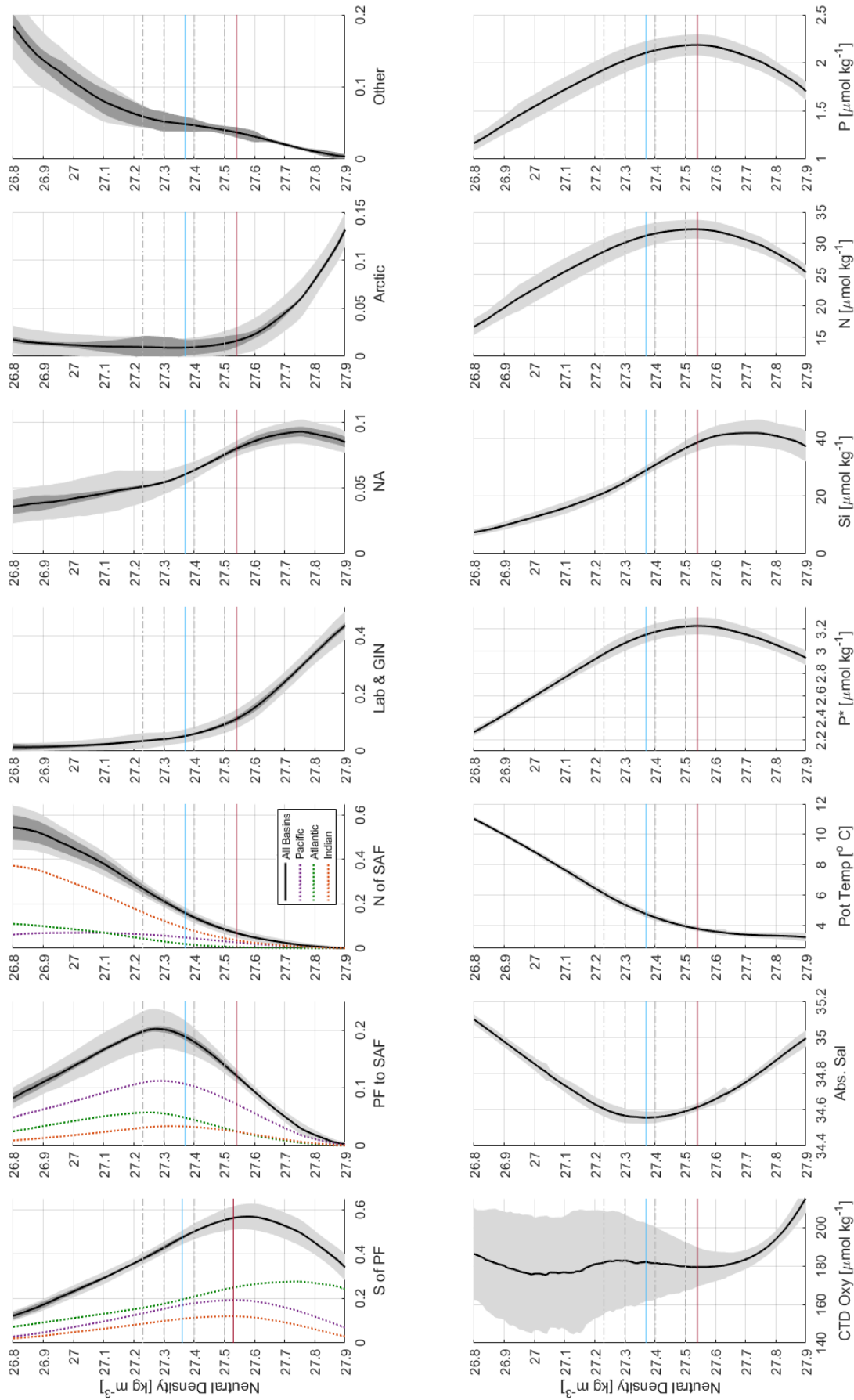


Figure 4.3 – Neutral density profiles showing the MEM predicted fractions from different regions alongside profiles of other relevant variables for Cruise JC159. All profiles represent the average profiles across the 24°S section, grey shading represents one standard deviation of the data used to create the average profile. Blue horizontal line corresponds to the density of the salinity minimum (27.37 kg m⁻³), maroon line corresponds to the density of the local oxygen minima (27.54 kg m⁻³). Grey dashed horizontal lines represent the boundaries of the three density classes AAIW 1 (27.23-27.3 kg m⁻³), AAIW 2 (27.3-27.4 kg m⁻³), AAIW 3 (27.4-27.5 kg m⁻³). In a – c results are shown for the Pacific, Atlantic and Indian sectors of the Southern Ocean region combined (thick black line) and separately (purple, green and orange dotted lines, respectively).



This suggests that although the water from between the PF and SAF is not the dominant source by percentage contribution, it may be responsible for the salinity minimum at 24°S.

Antarctic Surface Water (AASW), a surface water mass from south of the PF, is thought to contribute to AAIW in Drake Passage via subduction on the poleward side of the PF (Naveira Garabato *et al.*, 2009). In both the 2009 and 2018 data, the large contribution from S of PF increases with depth away from the salinity minimum (Figures 4.2a & 4.3a), peaking at $27.54 \text{ kg m}^{-3} \sigma_n$ (55% contribution) and $27.58 \text{ kg m}^{-3} \sigma_n$ (60% contribution) for each cruise respectively. This suggests that, although some contribution of S of PF waters to the salinity minimum may be due to surface water subducting directly into AAIW classes, some contribution is due to mixing of the AAIW core with deeper waters which have an even higher contribution of water from this southern region. At 24°S this deeper water is identified as UCDW, as the maximum of the S of PF contribution coincides with a local minima in oxygen and maxima in nitrates and phosphates, which are characteristic of UCDW (Larqué *et al.*, 1997).

The contribution from N of SAF (Figures 4.2c & 4.3c) shows the opposite pattern with a higher contribution in lighter waters, peaking at a 49% contribution at $26.84 \text{ kg m}^{-3} \sigma_n$ and a 54% contribution at $26.79 \text{ kg m}^{-3} \sigma_n$ in the 2009 and 2018 data respectively. This suggests that the contribution of water from N of SAF is due to mixing of the AAIW core with a lighter, overlying water mass. Subantarctic Mode Waters (SAMWs) are known to form in regions to the north of the SAF, with some suggesting these waters in the Pacific act as a precursor to AAIW (e.g. McCartney *et al.*, 1977). In the results shown here, although there is a small influence of a Pacific source, the deconvolution

suggests the Indian sector dominates the contribution of waters from N of SAF. Unless this water is able to transit eastward in the full path of the Antarctic Circumpolar Current (ACC) without changing composition, this suggests a westward pathway of water from the Indian sector into the South Atlantic.

4.3 Temporal Origin of Water

4.3.1 Origin of Each AAIW Class

The transient tracers and ^{14}C act as a temporal constraint in the MEM, allowing temporal origin to be estimated in the same way in which spatial origin is estimated. Although the method is given some temporal information in the form of the inverse Gaussian prior and some spatial information in the form of the ECCO300 prior (see Section 3.1.5), the MEM itself does not have any physical intuition or knowledge of the mechanisms of ocean circulation. Although the priors make it less likely, it is possible for the method to give unrealistic output. For example, in theory the MEM output could suggest water originating in the North Pacific has been transported to the South Atlantic in five years, even though considering average current speeds in the ocean this would be physically impossible. Here we first interpret the temporal results of the method and later, in Section 4.5, further consider the feasibility of these results using passive tracer experiments in ECCO.

When the probability is plotted against time (Figure 4.4), regardless of the region of origin, two distinct peaks are seen in AAIW 1 and AAIW 2 samples at 5-25 years and at 35-55 years. A third signal of much older waters is seen in the AAIW 2 and AAIW 3 samples, peaking after 70 years, corresponding to the time prior to when the CFCs and SF_6 were present in the atmosphere.

Variations in these signals between cruises are discussed in further detail in Section 4.7.

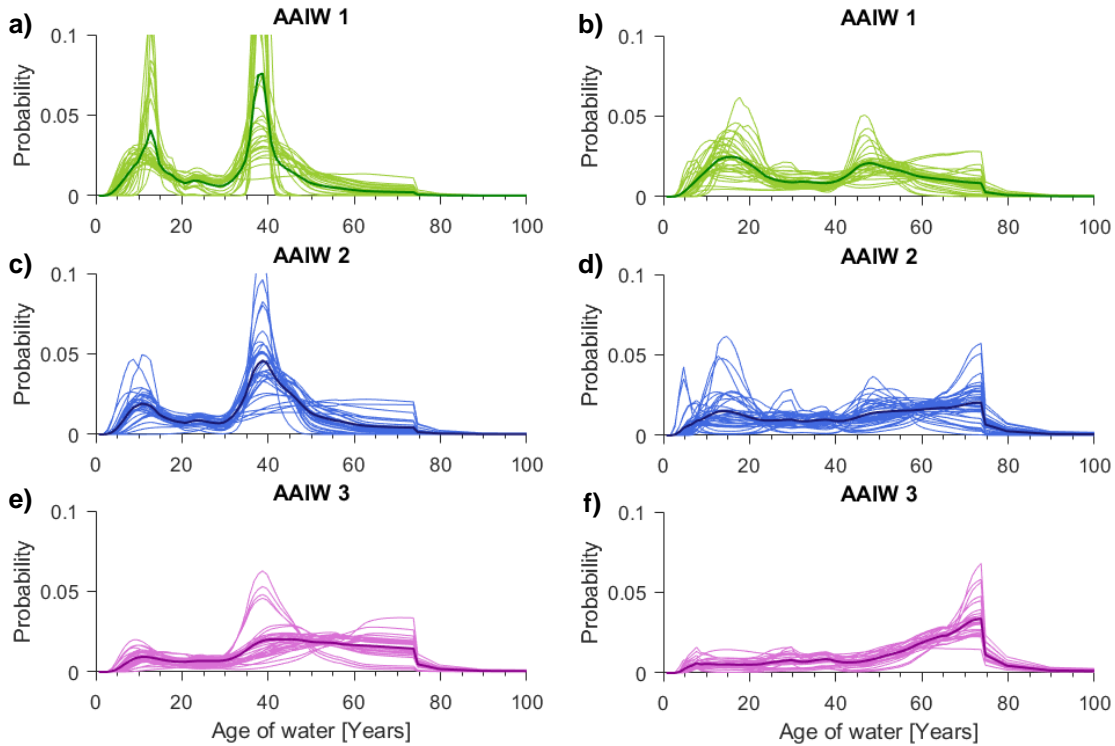


Figure 4.4 – The probability of a parcel of water having a certain age regardless of the region of origin. Samples are divided into the previously defined three classes of AAIW (Section 2.2.1). Thick dark line in each plot shows the average probability distribution for all samples in that AAIW class, thinner lighter lines show the probability distributions for each individual sample. (a,c,e) Show data from JC032 2009, (b,d,f) show data from JC159 2018.

When these same plots are made but also subdivided by region of origin (Figures 4.5 & 4.6), the older signal (35 - 55 years) is observed to be more dominant in waters originating from the S of PF region (Figures 4.5a-c & 4.6a-c), and the younger signal (5 - 25 years) to be more dominant in waters originating from the N of SAF region (Figures 4.5g-i & 4.6g-i). Both young and old signals are present in water originating from the PF to SAF region (Figures 4.5d-f & 4.6d-f), however the older signal is much weaker than the signal seen from the S of PF region.

When interpreting these results, it is important to consider how the MEM produces this output. As previously mentioned (Section 3.1.1), three of the

seven tracers used in the MEM act primarily as spatial constraints (temperature, salinity and P*) with the remaining four (CFC-11, CFC-12, SF₆ and ¹⁴C) acting primarily as temporal constraints. Due to the saturation dependence on temperature and salinity, the temporal tracers do also vary spatially and so provide some additional spatial constraints. The MEM identifies spatial regions whose characteristics combine in a satisfactory manner to produce the desired temperature, salinity and P* characteristics. The MEM also identifies points in time, which combine to give the desired ratio and magnitude of the temporal tracers.

If the temporal tracers (CFC-11, CFC-12, SF₆ and ¹⁴C) had no spatial variability (i.e. had globally uniform surface concentrations) you would expect the MEM to predict the same temporal pattern for all regions, scaled by the contribution from each region (as decided by the spatial tracers, temperature salinity and P*). In reality these temporal tracers do have spatial variability and so the signals are more complex. However, as the solver is not a perfect solution and the MEM is not governed by the physics of real ocean circulation, some relics of this simple case where temporal tracers have no spatial variability are still observed. This means that when the temporal results are dissected to a regional scale, the same temporal signal can be observed in multiple regions.

Figure 4.5 – The probability of a parcel of water having a certain age for three different regions of origin; S of PF, PF to SAF, N of SAF. Samples are divided into the previously defined three classes of AAW. Each line represents the probability distribution of a single sample, coloured by the neutral density at which this sample was collected. These graphs are created using data from JC032 only.

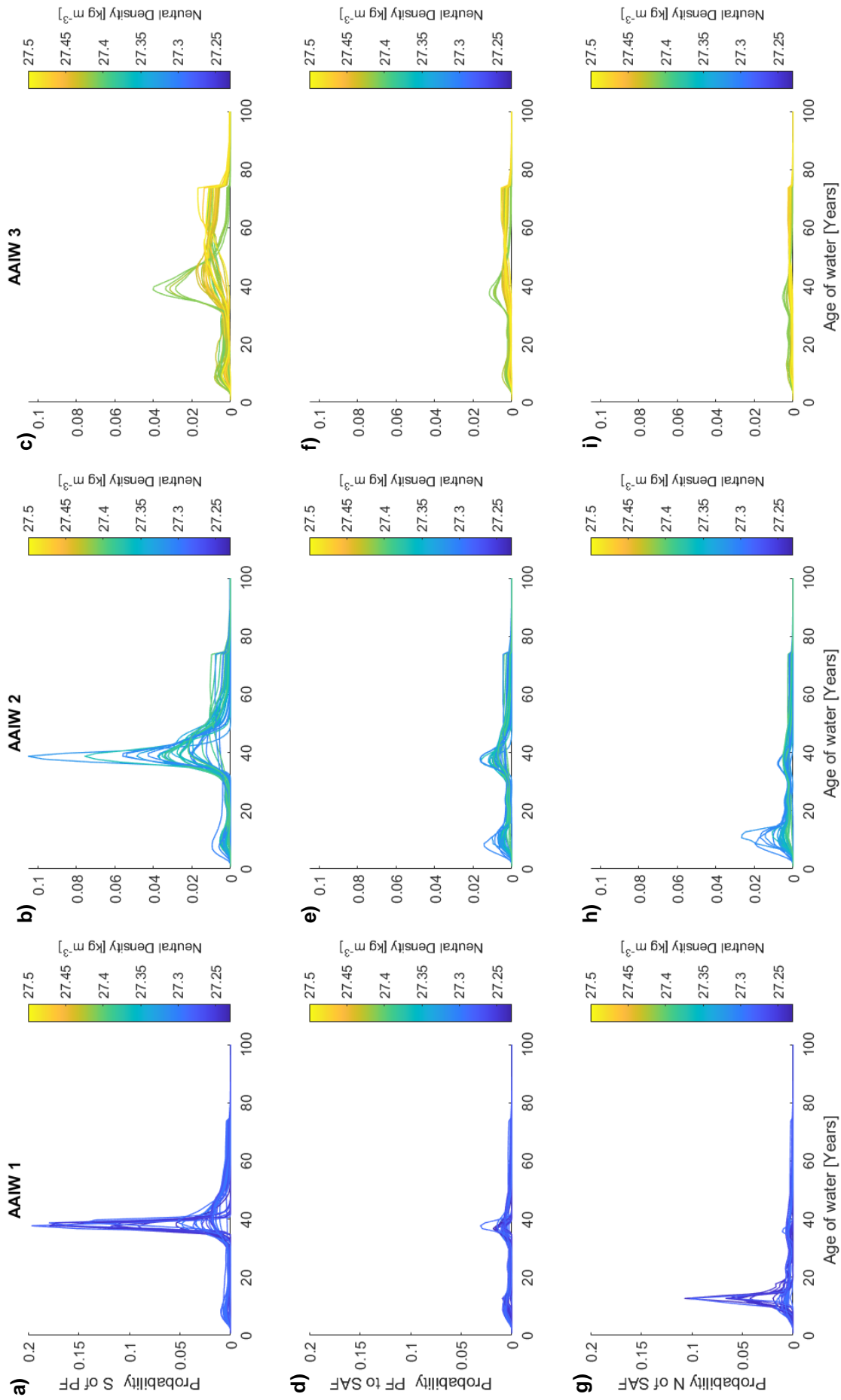
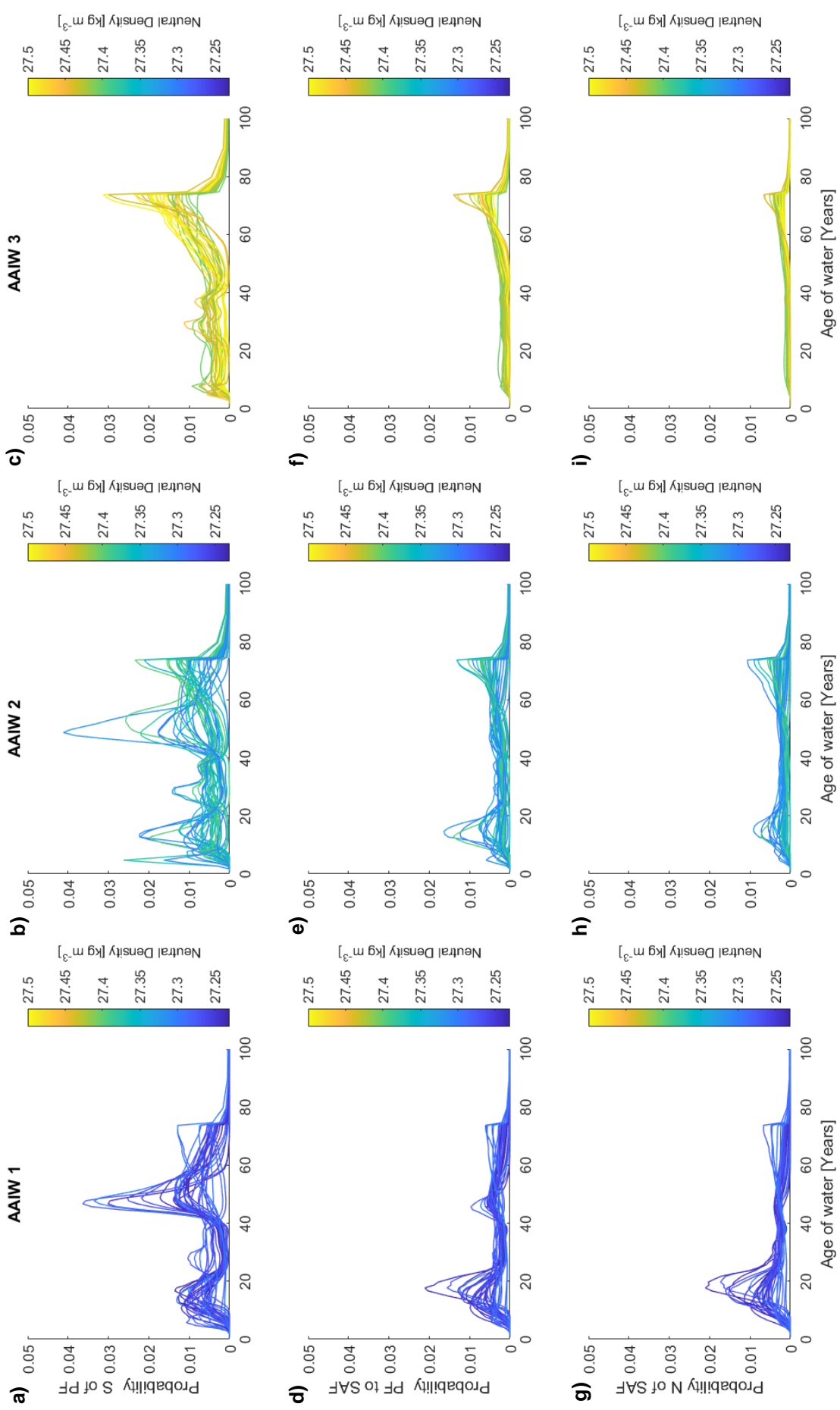


Figure 4.6 – The probability of a parcel of water having a certain age for three different regions of origin; S of PF, PF to SAF, N of SAF. Samples are divided into the previously defined three classes of AAIW. Each line represents the probability distribution of a single sample, coloured by the neutral density at which this sample was collected. These graphs are created using data from JC159 only.



With this context, it is suggested that AAIW at 24°S, particularly in the AAIW 1 and 2 classes, is a combination of water from the S of PF region with an age of 35 - 55 years, and water from the N of SAF region with an age of 5 - 25 years. The contribution from the PF to SAF region has a less well defined age, but is also thought to fall within the 5 - 25 year age range. The small older signal in waters from the N of SAF region and small younger signal in waters from the S of PF region are considered relics of the aforementioned way in which the information given by the tracers is used.

4.3.2 Variations across the Section

Figures 4.7 and 4.8 allow us to look further into the distribution of these different aged waters from the Southern Ocean regions, with depth and longitude. Three age brackets are considered in order to aid comparison; under 35 years (encompassing the young peak), 35 to 75 years (encompassing the older peak), and over 75 years. Although the method allows for ages up to 2000 years, here we primarily consider ages under 75 years, as prior to the 1930s when the first CFCs were used, ^{14}C is the only tracer acting as a temporal constraint. For this reason, the method is better constrained and more applicable for use with younger waters (under ~ 75 years), like AAIW. The observed patterns are broadly consistent between the two cruises and so the observations below apply to both cruises.

4.3.2.1 S of PF

As expected from the above analysis, waters originating from S of PF, show the strongest signal within the 35 - 75 year bracket, and specifically within the densest AAIW class. The < 35 year signal is much weaker and more

Figure 4.7 – Section plots at 24°S showing the probability of origin from the three Southern Ocean regions at different points in time. Within each time bracket probabilities have been summed. Note colour scale varies between regions. Plots made using data from JC032. Red dashed lines indicate the boundaries of the three previously defined AAIW classes.

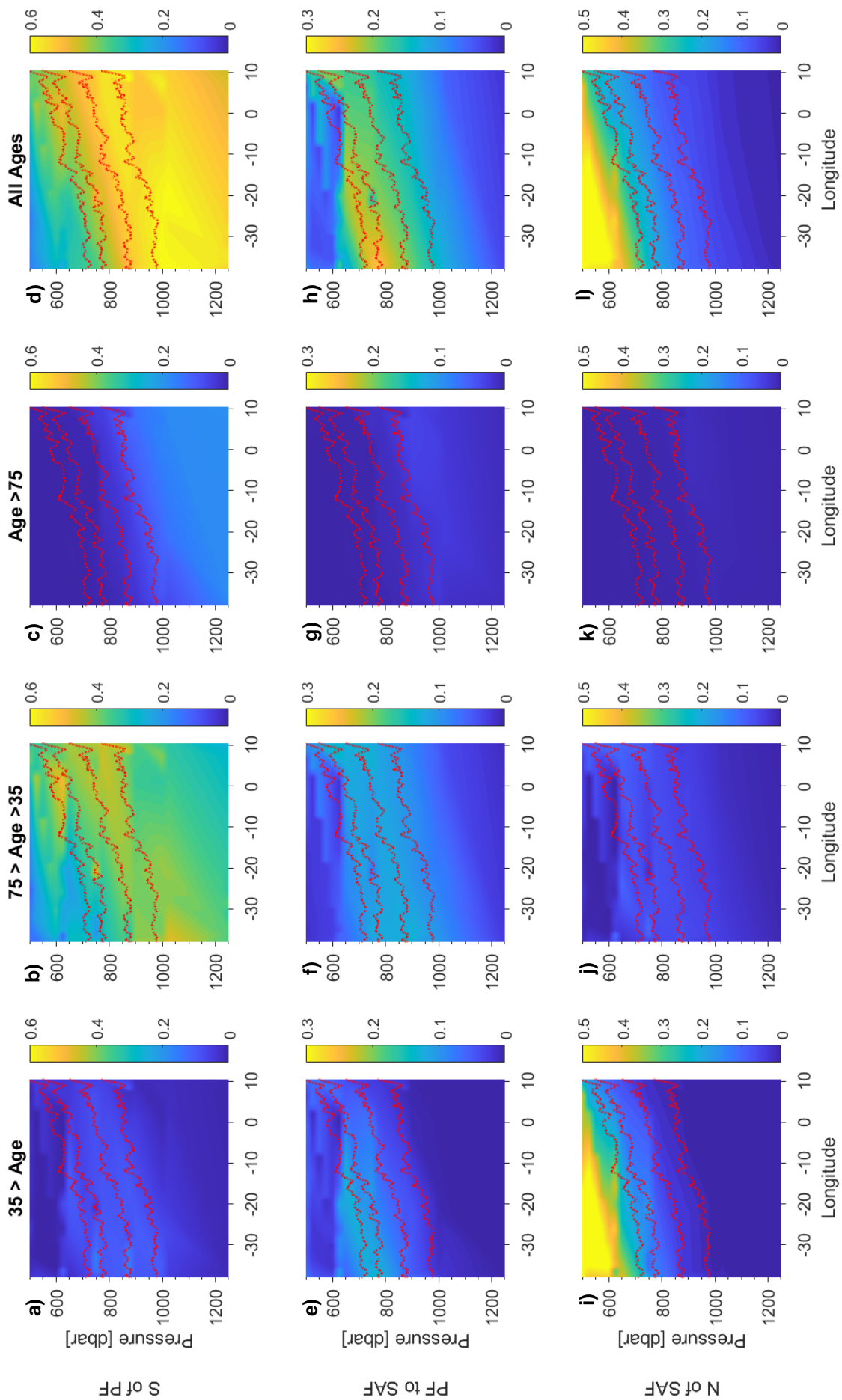
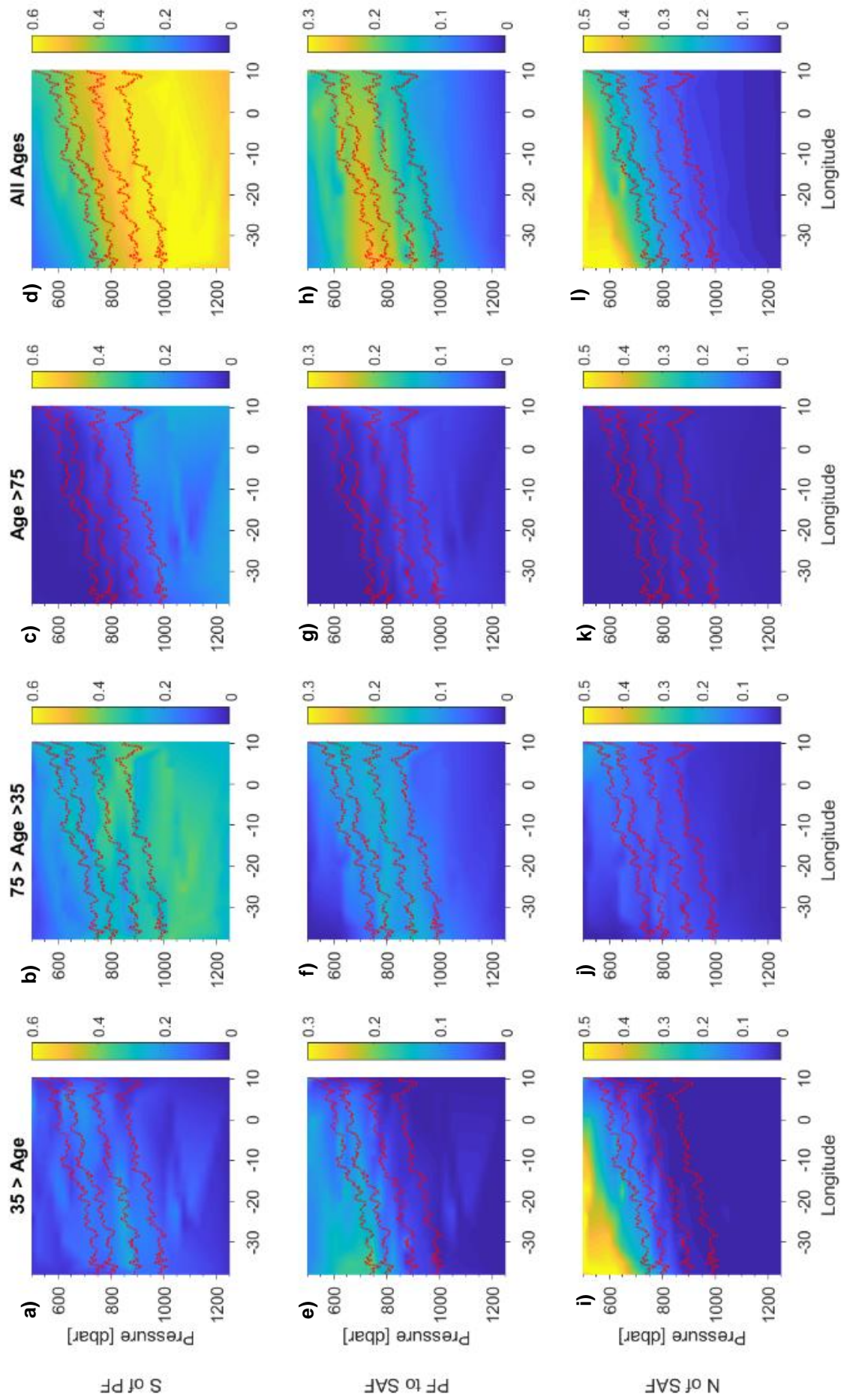


Figure 4.8 – Section plots at 24°S showing the probability of origin from the three Southern Ocean regions at different points in time. Within each time bracket probabilities have been summed. Note colour scale varies between regions. Plots made using data from JC159. Red dashed lines indicate the boundaries of the three previously defined AAIW classes.



diffuse, spanning all three AAIW classes. The influence of waters from this region older than 75 years is also low, but increases with depth away from the AAIW.

4.3.2.2 PF to SAF

Waters from the PF to SAF show an influence within the AAIW classes at both the < 35 year bracket and the 35 - 75 year bracket, but little influence from waters > 75 years. Though the magnitude of the influence is similar between < 35 years and 35-75 years, the spatial pattern differs. The < 35 year signal is strongest in AAIW 1 in the west, whereas the 35 - 75 year old signal is stronger in the remaining AAIW classes. In the previous section it was stated that the age signal for waters from this region was poorly defined, and the interpretation of these results should consider that. Further discussion on the age of PF to SAF water in conjunction with results from the ECCO tracer experiment can be found in Sections 4.5.4 and 4.6.2.

4.3.2.3 N of SAF

For waters originating from the N of SAF regions, the younger < 35 year contribution is more heavily focussed at depths above AAIW, with a small influence of this water seen in the lightest AAIW class (Figure 4.7i & 4.8i). A small diffuse signal is seen in all layers within the 35 - 75 year bracket, and no signal of waters > 75 years is observed.

In summary, these results show that the contributions from different regions and times vary little with longitude, but considerably with varying density. Younger waters from the N of SAF regions have the strongest signal within the lightest AAIW class, whereas waters from the S of PF regions have the strongest signal in the denser AAIW classes.

4.4 Seasonality

As the source region data for the MEM has monthly resolution, it is possible to look at the months in which water is predicted to have last been at the surface before being subducted. This can give further support to ideas of transport and also highlight results that may be unrealistic. The inverse Gaussian prior (see Section 3.1.5.1) only gives information on which years are more or less likely, and so any seasonality detected comes entirely from the information given by the tracers themselves.

Figure 4.9 shows that for all three Southern Ocean regions more water is ventilated in the austral winter (JJA) and spring (SON) than in summer (DJF) and autumn (MAM). This is in line with the two mechanisms by which AAIW is thought to be created and so provides confidence in the MEM results.

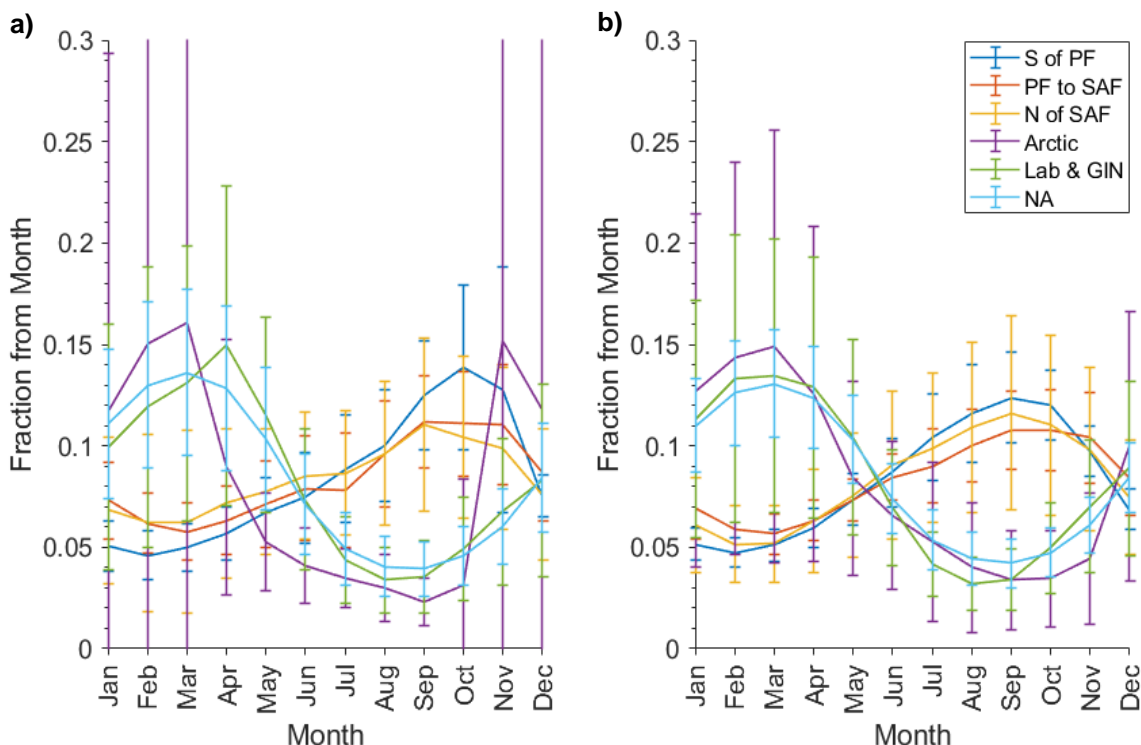


Figure 4.9 – The month in which water was predicted to last have been in contact with the atmosphere regardless of the year. Each line represents the mean of all samples within all three of the AAIW classes at 24°S for JC032 (a) and JC159 (b). Different regions are indicated by colour. Error bars show ± 1 standard deviation of the AAIW samples averaged. Each region has been separately normalised by the total probability of water originating from that region, so that summed over all 12 months the probability of each region equals 1.

AAIW is thought to either be created in association with the densest classes of SAMW (e.g. McCartney, 1977) or by subduction on the poleward side of the PF (e.g. Naveira Garabato *et al.*, 2009). Mode waters form when winter mixing creates deep well mixed surface layers which then subduct into the interior when waters begin to restratify in the spring, hence why mode waters carry the signal from the winter months.

Water subducting close to the PF is expected to carry this winter signal as it is only in winter that the density range of the AAIW salinity minimum outcrops at the surface in the Pacific sector allowing for direct subduction. In the remainder of the year these densities do not outcrop but are still fed by a subsurface reservoir of winter water which still carries the signals of the winter surface properties (Naveira Garabato *et al.*, 2001). In regions either dominantly or wholly within the Northern Hemisphere ('Arctic & GIN', 'NA', 'Lab', and 'Other'), the reverse monthly pattern is seen, reflecting the opposite pattern of seasons in the two hemispheres.

4.5 ECCO Passive Tracer Results

So far we have purely considered the output from the MEM. Now we consider the distribution of the ECCO passive tracers at 24°S and the pathways which the tracers take to arrive there. Although these tracers purely reflect the circulation in the model, they can act as a form of validation to the MEM results. First we look at average profiles of the tracers at 24°S, then we look further into the distribution of four relevant tracers in space and time.

4.5.1 ECCO Average Tracer Profiles at 24°S

Average profiles of potential temperature, salinity and the Southern Ocean tracers (Figure 4.10) were created for the 24°S section at 300 model years in the ECCO Global Ocean Passive Tracer Experiment (see Section 3.3.2). The salinity minimum falls at σ_n 27.40 kg m⁻³ at 300 years. The peak contribution of waters from the S of PF region was found below this density at σ_n 27.52, 27.51 and 27.54 kg m⁻³, for the Pacific, Atlantic and Indian, respectively. The peak contribution of waters from the PF to SAF region was found to be close to the salinity minimum in the Pacific and Indian at 27.37 kg m⁻³ and 27.44 kg m⁻³ respectively, whereas the Atlantic tracer peaked above the salinity minimum at the lower density of 27.24 kg m⁻³. Southern Ocean waters from N of SAF peaked at densities much lighter than the salinity minimum at, σ_n 27.29, 26.94 and 26.88 kg m⁻³, for the Pacific, Atlantic and Indian respectively.

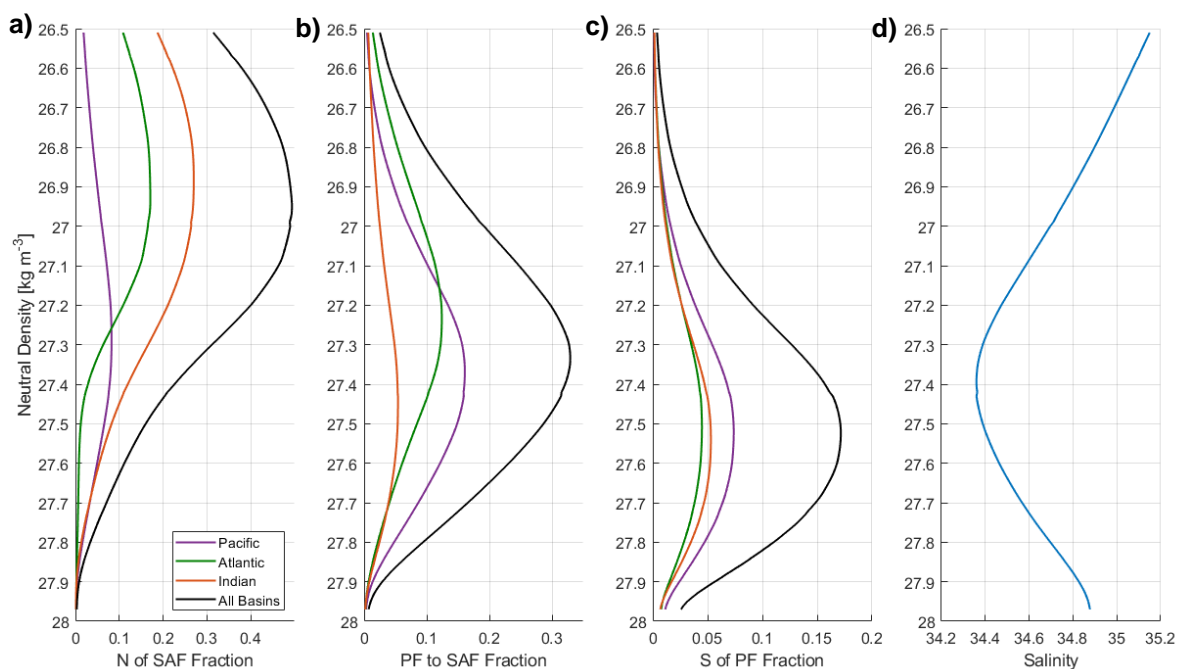


Figure 4.10 – Average profiles of passive tracer concentration (fraction) and salinity at 24°S, at 300 years in the ECCO tracer experiment.

Direct comparison of densities between the model data and observational data should not be made, as the model may form water masses at slightly different densities to the real world, however the patterns can be compared. The patterns shown in the MEM output are very similar to those shown in the ECCO output. In the MEM results and in ECCO the core of S of PF waters lies below the salinity minimum, PF to SAF waters are focused around the salinity minimum, and the waters from N of SAF lie considerably above the salinity minimum in density. Pacific N of SAF water also lies closer to the salinity minimum than Atlantic or Indian N of SAF water in both the MEM results and in ECCO. These large scale agreements between the methods give confidence to the MEM results.

The ECCO tracer output is used to generate the prior for the MEM (see Section 4.8 for evaluation of the prior's influence on results), and so some similarities are not surprising. However, differences in the results highlight where the observed tracers have given different information than the prior, and allowed the MEM results to deviate from the ECCO derived prior. The magnitude of the tracer/fraction peaks in the average density profiles for each of the three Southern Ocean regions (where all basins have been summed) are compared between the ECCO tracers (Figure 4.10) and the MEM output (Figures 4.2 & 4.3), highlighting some major differences.

For waters from N of SAF the two methods are in close agreement with the MEM suggesting a peak contribution of 49% (JC032) and 55% (JC159) and the ECCO tracer a contribution of 49%. Greater differences are seen in the remaining Southern Ocean regions. For waters originating from the PF to SAF region, MEM suggests a smaller contribution of 17% (JC032) and 20% (JC159) at the peak, compared to 33% in ECCO. The reverse is seen in waters from S

of PF with ECCO suggesting a peak contribution of 17%, and the MEM suggesting a much larger peak contribution of 56% (JC032) and 57% (JC159).

In the following paragraphs we look in further detail at the tracer pathways and timescales of circulation for four regions identified as important contributors to AAIW at 24°S by the MEM and ECCO results. These regions are the N of SAF region in the Indian Ocean, the S of PF regions in the Pacific and Atlantic, and the PF and SAF region in the Pacific. Section plots and σ_n surface maps are used to describe the tracer pathways, and the rate of tracer arrival (see Section 3.3.7) is used to explore the timescales of these pathways.

4.5.2 Water from N of SAF in the Indian Ocean: Pathways and Timescales in ECCO

The concentration of the Indian N of SAF tracer is mapped onto the 26.7 kg m⁻³ σ_n surface, the density at which the highest contributions of this tracer were observed at 24°S (Figure 4.11). At 24°S this density corresponds to a depth of ~400 m (with the salinity minimum at ~ 800 m) (Figure 4.12a). The tracer from this region appears to reach 24°S by propagating westward south of South Africa, then northwest parallel to the East African coastline, before starting to spread west after passing 30°S (Figure 4.11a). The core of this water is already seen at a depth of ~400 m to the south of Cape Agulhas (39°S, 20°E) (Figure 4.12b). When traced further east this intermediate maxima in tracer concentration extends across the width of the Indian Ocean sector (Figure 4.12c) past 140°E. A surface connection to this intermediate maxima is observed from 65°E to 140°E through outcropping isopycnals (or isopycnals reaching within the surface 50 m in which the tracer is added) (Figure 4.12d). East of 140°E is outside of the surface input area from the Indian N of SAF

tracer, but a surface connection is observed to extend in the Pacific Sector with the Pacific N of SAF tracer.

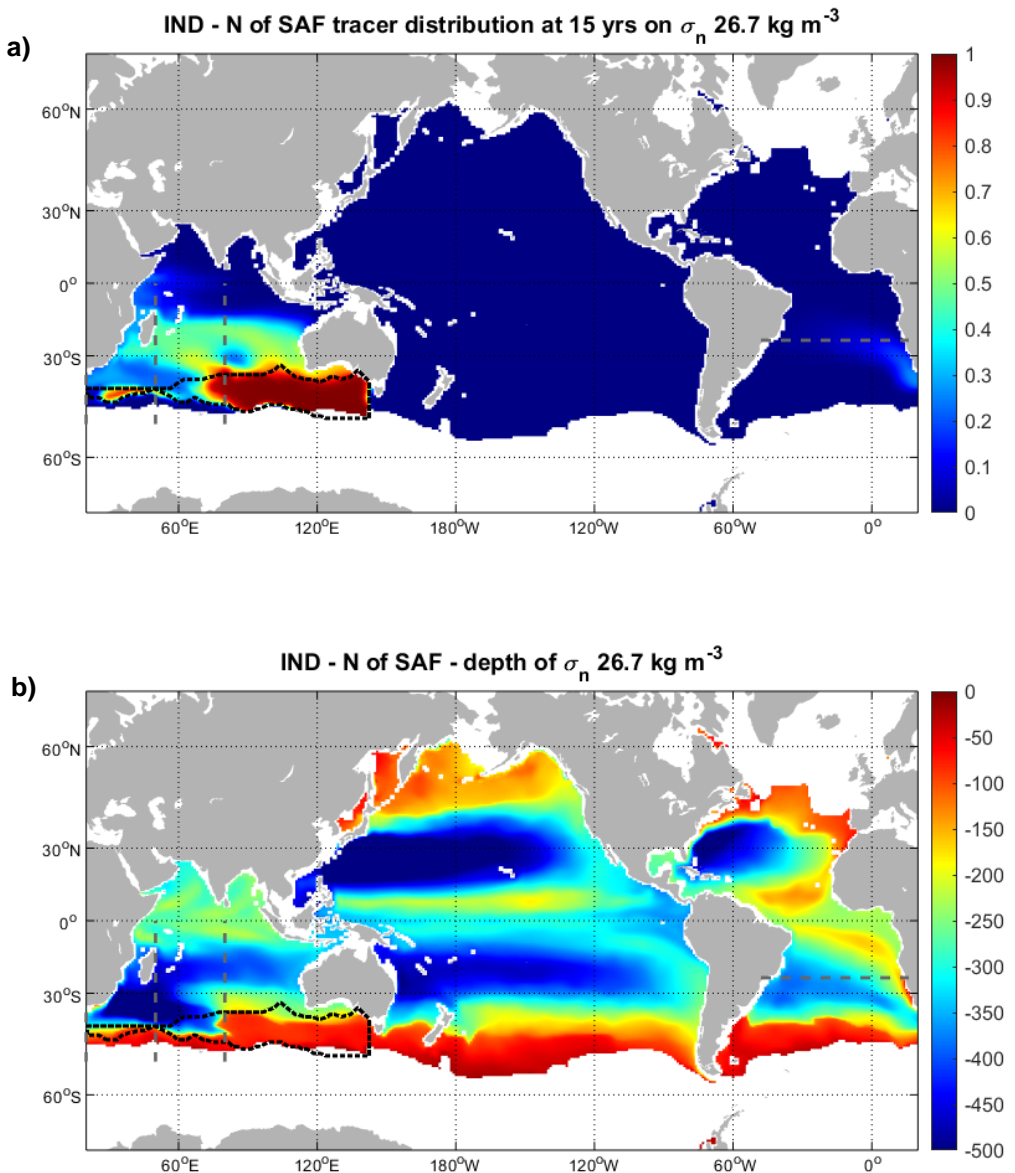


Figure 4.11 – (a) Global map of the concentration of passive tracer introduced in the Indian ‘N of SAF’ region on the $\sigma_n = 26.7 \text{ kg m}^{-3}$ neutral density surface at 15 model years in ECCO. (b) Global map of depth of $\sigma_n = 26.7 \text{ kg m}^{-3}$ neutral density surface at 15 model years. Grey dashed lines indicate locations of sections shown in Figure 4.12. Black dashed line indicates area where tracer was added at the surface.

The first arrival of the tracer at the salinity minimum at 24°S is at 18 years, with the maximum rate of arrival of tracer at 25-30 years (Figure 4.13d). In the years following, the rate of arrival continues to decrease, but even at 300 years the tracer concentration has not reached equilibrium, suggesting some water from this region travels to 24°S via a very long and/or slow pathway. Such pathways may include circulation within the Indian Ocean prior to eastward

transport in the Agulhas Current and/or circulation within the ACC prior to entering the Atlantic. In order to test these possible pathways sub-surface pulse inputs of passive tracer would be required in areas where the Indian N of SAF tracer is known to be present e.g. interior Indian Ocean or area south of Australia. This is because in the current configuration, after several decades,

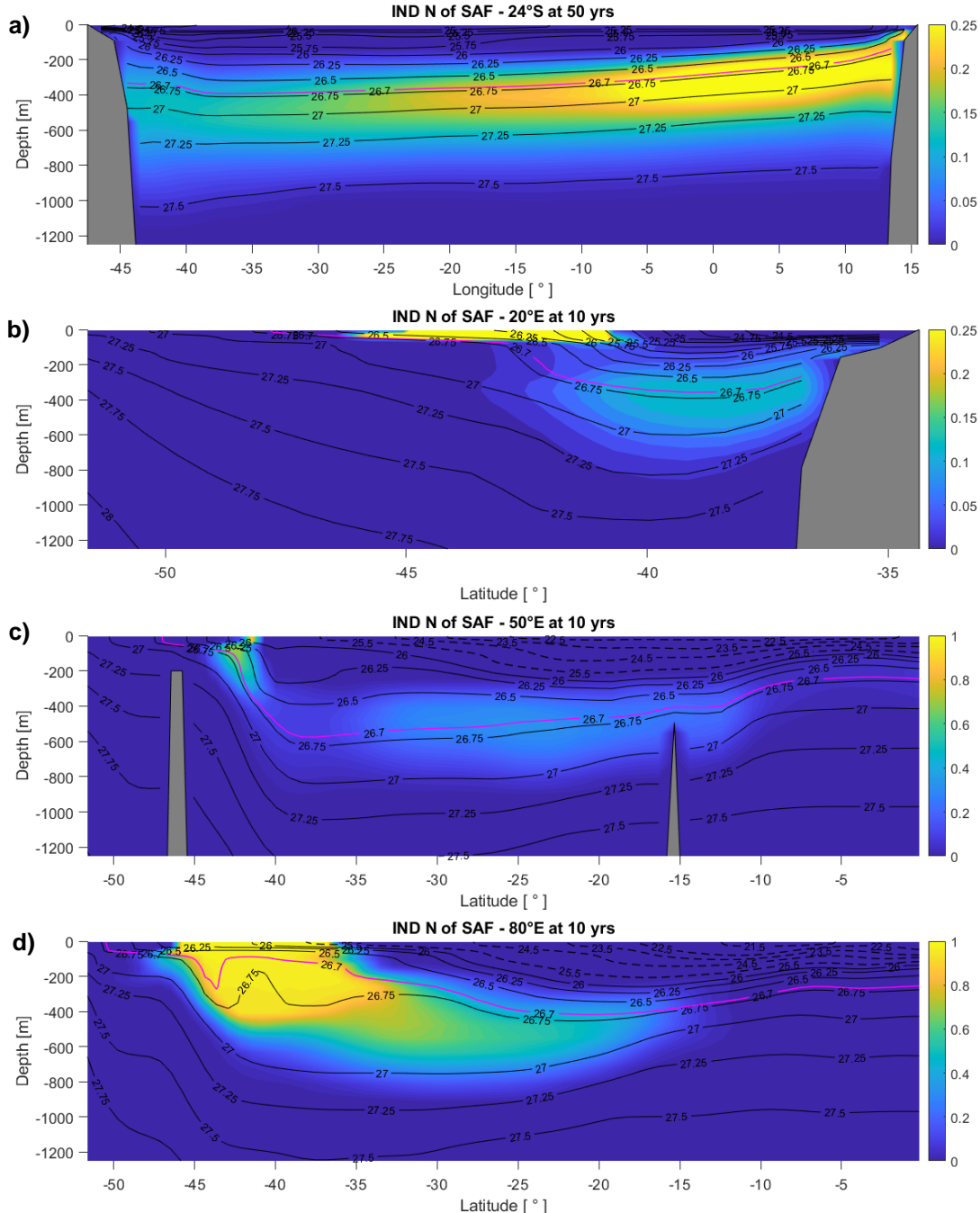


Figure 4.12 - Section plots showing concentration of Indian N of SAF in ECCO. Pink line indicates the σ_n 26.7 surface shown in Figure 4.11. (a) 24°S at 50 years, (b) 20°E at 10 years, (c) 50°E at 10 years, (d) 80°E at 10 years. Locations indicated of Figure 4.11.

the tracer which has taken separate pathways and then reconvened cannot be distinguished from itself.

It is evident from both the average profiles (Figure 4.10) and the section plot at 24°S (Figure 4.12a) that water from the N of SAF region in the Indian Ocean finds itself at the salinity minimum due to mixing with the underlying lower salinity waters. This means that the amount of vertical mixing in the model could also impact the arrival time. If the vertical mixing in the ocean was greater [less] than that in the model, you would expect an earlier [later] arrival time from the MEM results compared to the model.

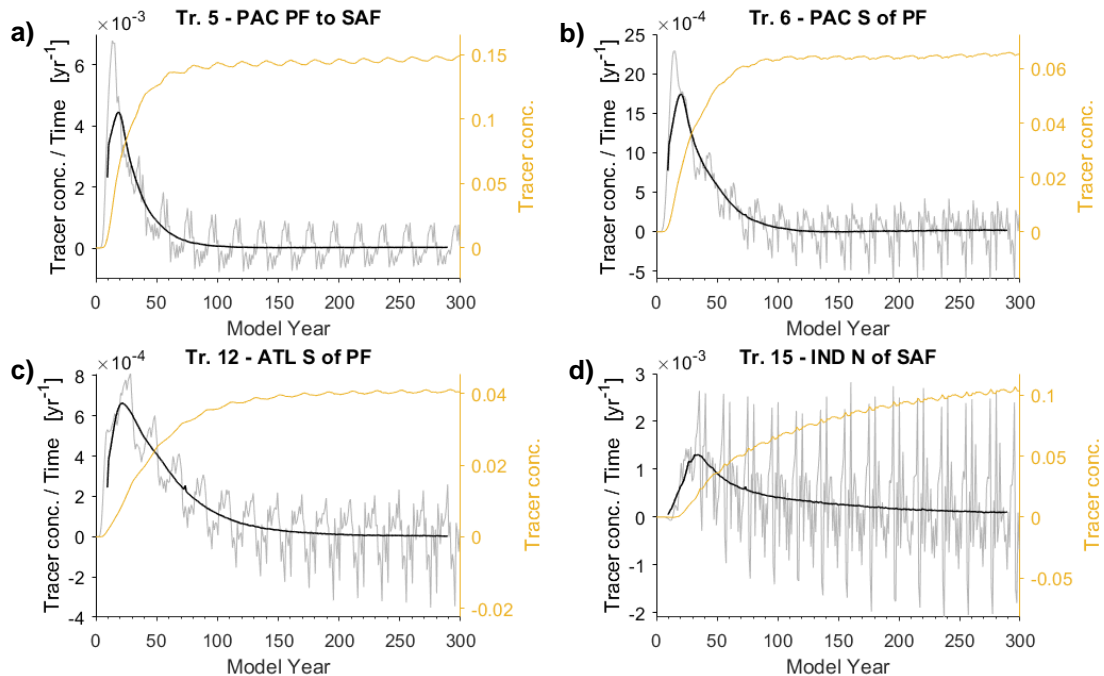


Figure 4.13 – Arrival of Southern Ocean tracers at 24°S in ECCO. Tracer concentration refers to the average concentration taken across all longitudes and 3 depth levels (720 m, 815 m, 910 m) which encompass the AAIW salinity minimum at 24°S. Annual rates of tracer arrival are shown in grey, a 20 year centred moving average is shown in black, both use the left axis. Tracer concentration is shown in yellow, and uses the right axis. Tracer region is indicated by individual plot title.

An additional consideration when exploring the connection between the Atlantic and Indian Ocean is that of Agulhas Rings. Though the model clearly shows a westward connection from the Indian Ocean to the Atlantic Ocean, the

resolution of the model is not high enough to resolve Agulhas Rings, which in the real ocean are thought to provide a significant input of Indian waters to the Atlantic (de Ruijter *et al.*, 1999). Although ECCO may accurately represent the volume of Indian Ocean water entering the South Atlantic, this connection in ECCO is represented as a mean flow and so likely creates a different distribution of tracer to what would be achieved by periodic input via Agulhas Rings.

4.5.3 Waters from S of PF in the Pacific and Atlantic Oceans: Pathways and Timescales in ECCO

The region south of the PF is known as a region of surface divergence with waters moving poleward as part of the lower limb of the meridional overturning circulation and waters moving northward as part of the upper limb of the meridional overturning circulation. At 24°S waters containing the highest concentrations of the S of PF tracers lie close to the $27.4 \text{ kg m}^{-3} \sigma_n$ surface (at Year 50), and so here tracer concentration on this surface is mapped, in order to study the pathways of this tracer (Figure 4.14 & 4.16). As can be seen in Figure 4.14b, this density surface lies very close to, or outcrops at, the surface in much of the Southern Ocean south of 60°S.

At 15 years the Pacific S of PF tracer is observed in all of the Southern Ocean sectors on the $27.4 \text{ kg m}^{-3} \sigma_n$ surface. Meridional sections at 185°W and 110°W demonstrate how the Pacific S of PF tracer is drawn into two pathways and how this process is not continuous throughout the area where the tracer is added (Figure 4.15e & f). At 110°W, although the tracer does mix down into deeper layers, the predominant pathway for tracer leaving the area of tracer addition is northward along the subducting density layers, with peak tracer concentration around the $27.5 \sigma_n \text{ kg m}^{-3}$ isopycnal. Whereas at 185°W tracer is

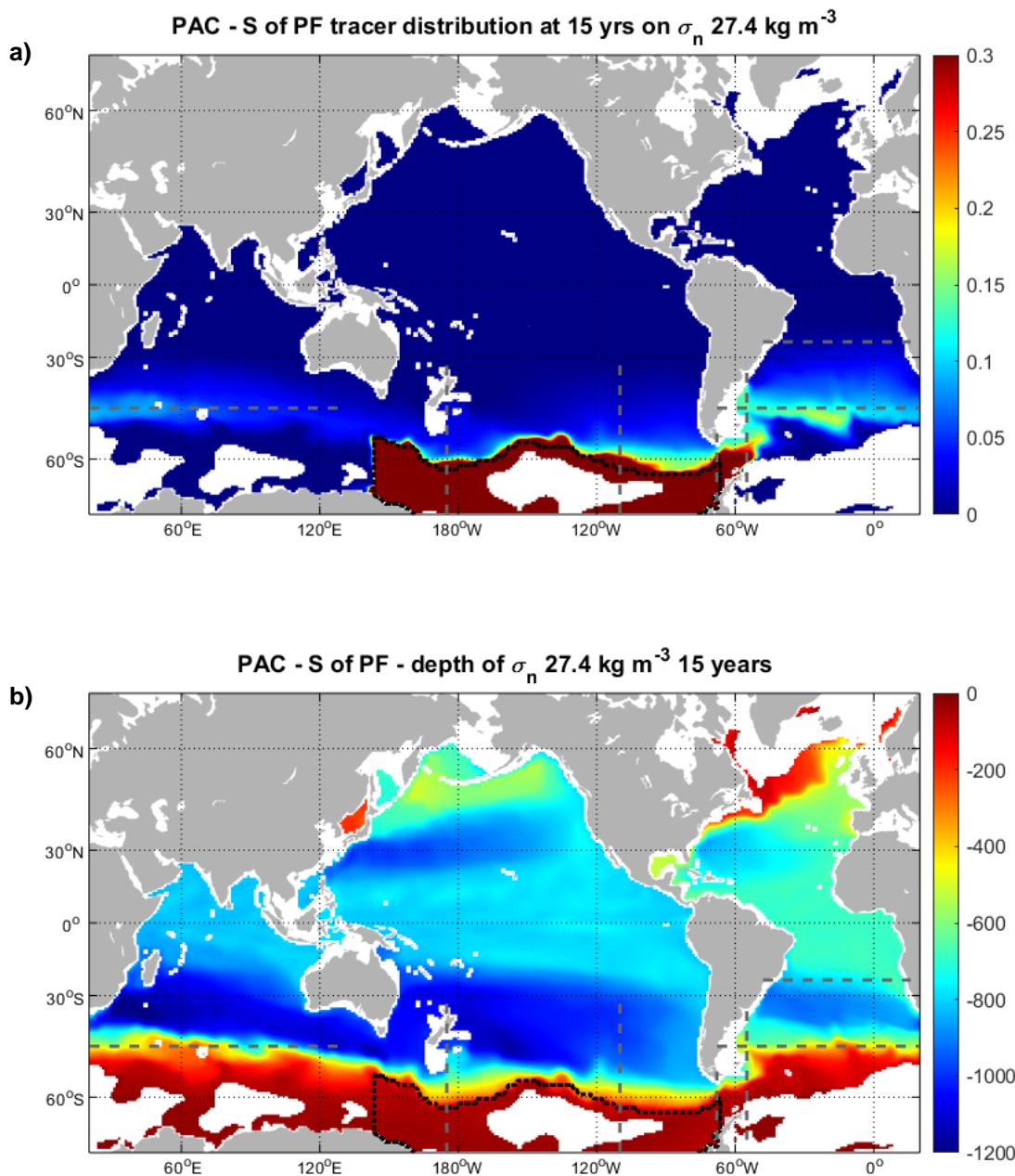


Figure 4.14 – (a) Global map of the concentration of passive tracer introduced in the Pacific S of PF region on the $27.4 \sigma_n$ surface at 15 model years in ECCO. (b) Global map of depth of the $27.4 \text{ kg m}^{-3} \sigma_n$ surface at 15 model years. Grey dashed lines indicate locations of sections shown in Figure 4.15. Black dashed line indicates area where Pacific S of PF tracer was added at the surface.

observed to enter deep waters, overflowing over the shelf break in addition to exiting via the subduction pathway observed at 110°W . The tracer flows eastward in the ACC, passing through Drake Passage (Figure 4.15c) and is then taken northward. A section at 55°W (Figure 4.15d) shows the tracer spreading from the concentrated area at 58°S as far north as 40°S (where it

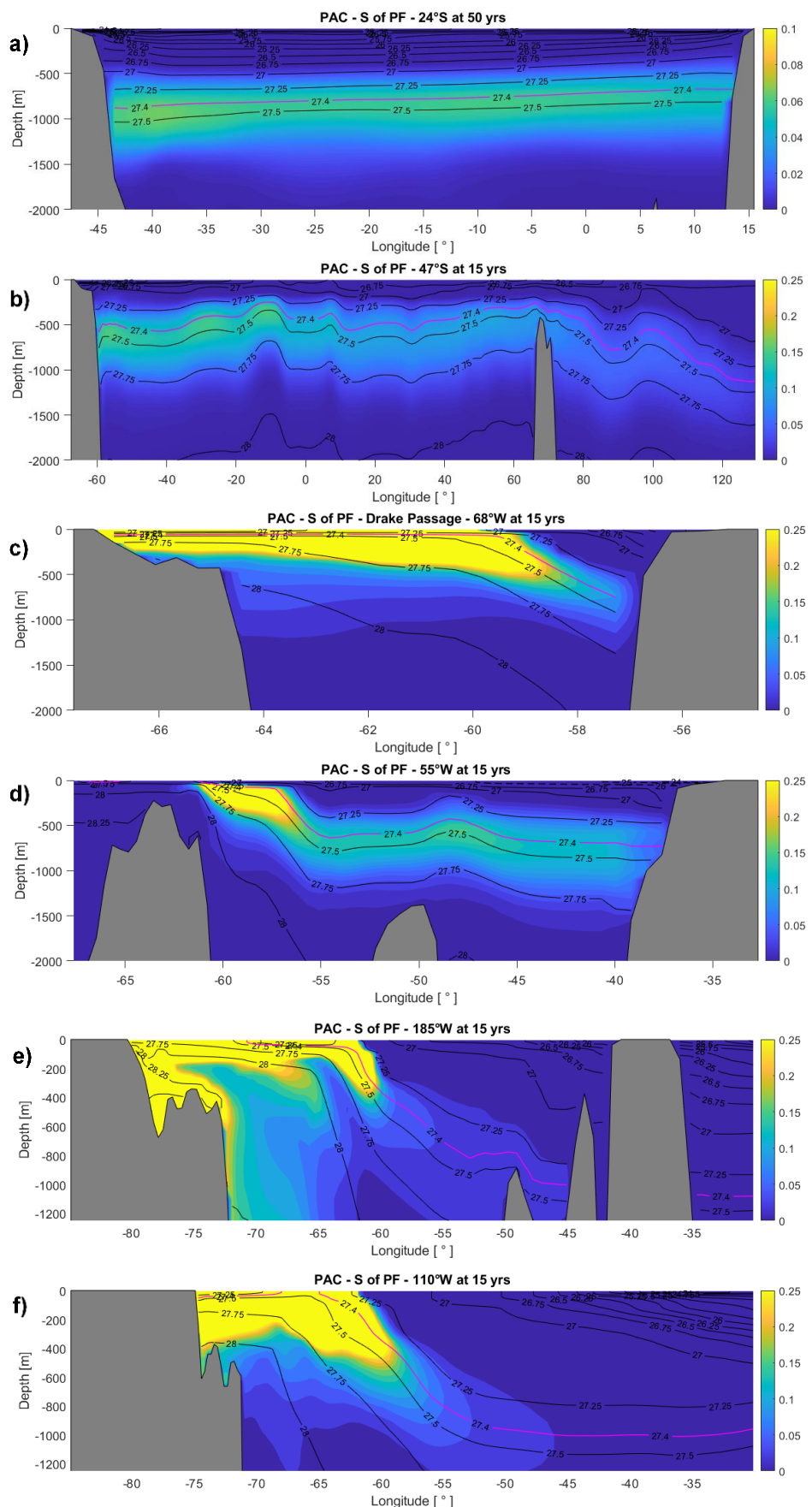


Figure 4.15 - Section plots showing concentration of Pacific S of PF tracer in ECCO. Pink line indicates the σ_n 27.4 kg m⁻³ surface shown in Figure 4.14. (a) 24°S at 50 years, (b) 47°S at 15 years, (c) 185°W at 15 years, (d) 110°W at 15 years, (e) Drake Passage 68°W at 15 years, (f) 55°W at 15 years . Locations indicated on Figure 4.14.

meets the coastline), again focussed at σ_n 27.5 kg m⁻³, but with concentrations of over 10% being seen between densities of 27.25 – 27.75 kg m⁻³ σ_n . A section at 47°S (Figure 4.15b) then follows a ribbon of tracer which travels though the Atlantic and Indian Southern Ocean sectors. Throughout this cross sector journey, the tracer appears to stay predominantly within the same density classes (27.25 – 27.75 kg m⁻³). It is from this ribbon of tracer that the tracer is observed to penetrate into the South Atlantic. The penetration of this tracer into the Atlantic is slow and very uniform across the width of the Atlantic Basin.

The Atlantic S of PF tracer shows a similar pattern of distribution as the Pacific S of PF tracer. On the 27.4 kg m⁻³ density surface at 15 years the tracer is observed in all three Southern Ocean sectors spreading northward into each of the basins (Figure 4.16). In the Atlantic sector the tracer can again be observed exiting the area of input via two distinct pathways, one in the intermediate water with peak concentration centred at σ_n 27.4 kg m⁻³ (marginally lighter than the core in the Pacific) and the second in the deep waters with densities of close to σ_n 28.25 kg m⁻³. The section at 30°W (Figure 4.17b) illustrates how the deep water is created along the coast and circulated within the Weddell gyre to create a high concentration of tracer in the northern part of the gyre (62°S) where it then enters the deep Atlantic basin along sloping isopycnals. Like the Pacific S of PF tracer, the Atlantic S of PF tracer spreads slowly northwards uniformly across the Atlantic basin. Some water appears to enter the Atlantic directly from the region of input and some appears to transit in the ACC prior to entering the intermediate depths of the South Atlantic. It is not possible to distinguish between the waters that took the ACC pathway and those that entered directly into the Atlantic in this experiment. The section at 50 years at 24°S (Figure 4.17a) shows the densities at which these waters are

present at 24°S with the peak contribution of 3% lying within the densities σ_n 27.25 – 27.50 kg m⁻³.

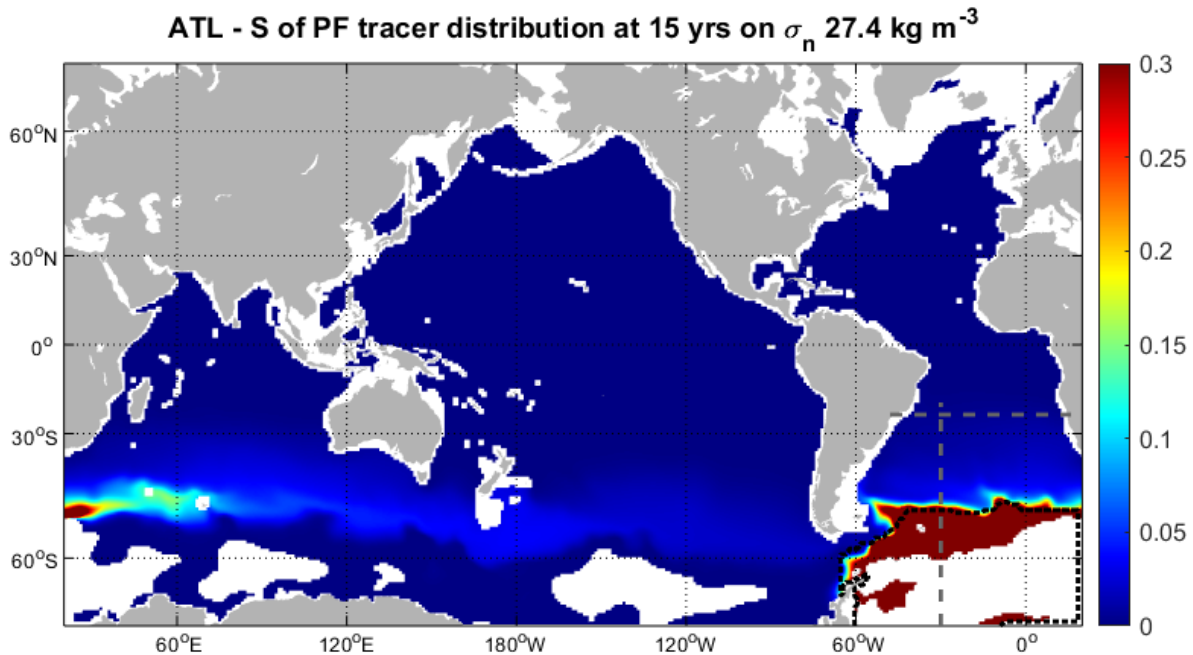


Figure 4.16 - (a) Global map of the Atlantic S of PF tracer on the 27.4 kg m⁻³ σ_n surface at 15 model years in ECCO. For map of depth of 27.4 kg m⁻³ σ_n surface see Figure 4.14b.

The noticeable difference between the Atlantic and Pacific S of PF tracers in ECCO is that the concentrations of the Pacific tracer at its peak at 24°S are close to double that of the Atlantic tracer (7% vs. 4%). The first arrival of the Atlantic S of PF tracer is at 6 years, with the maximum rate of tracer arrival at around 22 years (4.13c), 50% arrival at 40 years and 95% arrival at 112 years. The first arrival of the Pacific S of PF tracer is at 7 years, with the maximum rate of tracer arrival at around 15 years (Figure 4.13b), 50% arrival at 26 years and 95% arrival at 64 years. Though the first arrival times for both these tracers are very similar, the bulk of the Pacific tracer arrives much more quickly than the bulk of the Atlantic tracer. A possible explanation for this difference is hinted at by the higher concentration of Pacific S of PF waters in the west of the 24°S section. After passing through Drake Passage, Pacific waters seem more readily drawn northward into the Falklands Current

(Malvinas Current) where they can then be injected into the Atlantic interior. This would give higher overall concentrations as the Pacific waters have not been diluted by transit in the ACC, and it would also lead to a quicker arrival time of the majority of tracer.

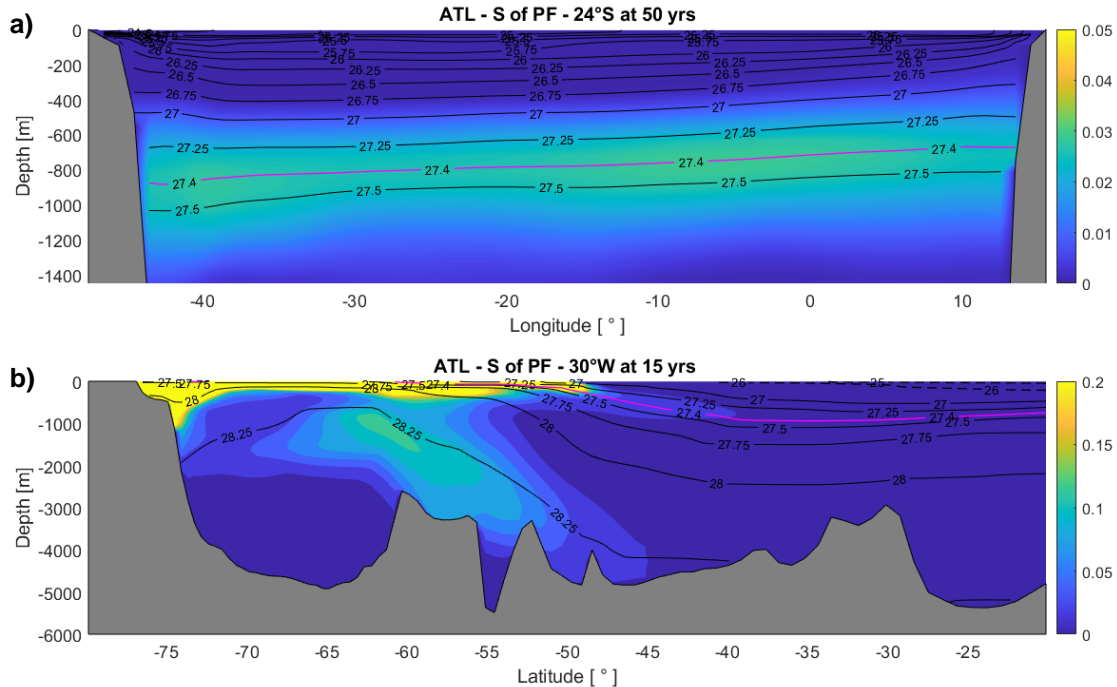


Figure 4.17 - Sections of Atlantic S of PF tracer in ECCO. Pink line indicates the σ_n 27.4 surface shown in Figure 4.16. (a) 24°S at 50 years, (b) 30°W at 15 years. Locations indicated of Figure 4.16.

4.5.4 Waters from PF to SAF in the Pacific Ocean: Pathways and Timescales in ECCO

Water from the PF to SAF region in the Pacific appears to follow a similar pathway to that of the water in the Pacific coming from S of the PF, however this tracer is found at lighter densities. A section at 90°W (Figure 4.19b) shows how tracer is subducted in the area of tracer input and spreads northward along the 27.25 kg m⁻³ σ_n density surface, a process observed along the length of the tracer patch. Much of this tracer is carried eastward in a sub-surface plume through Drake Passage (not shown) where it is observed at densities of

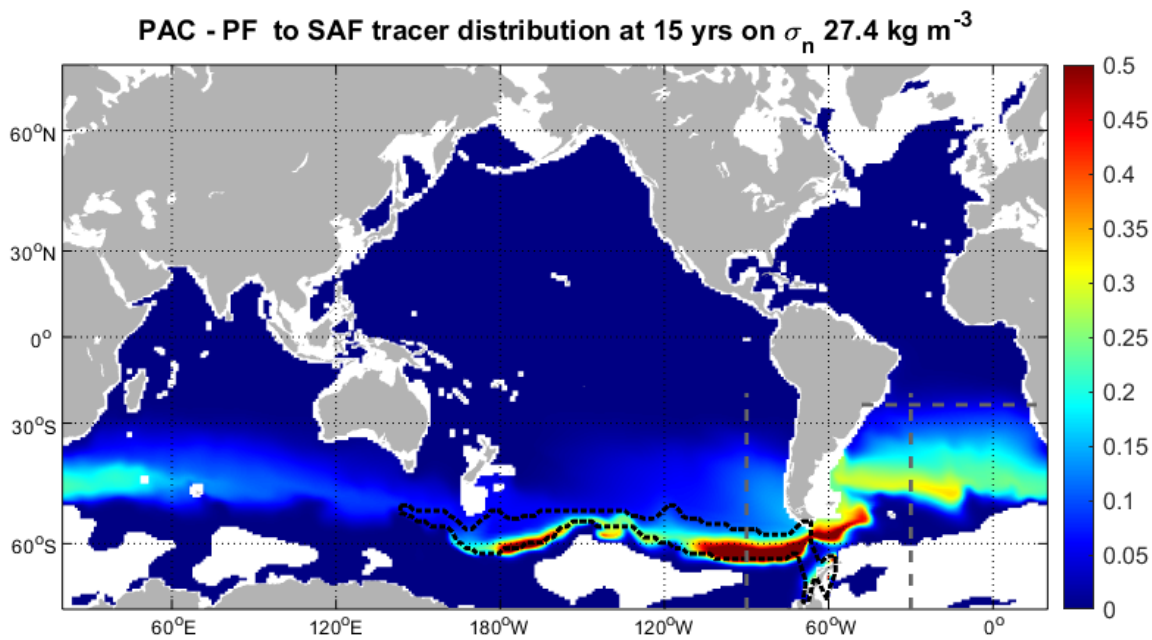


Figure 4.18 - (a) Global map of the concentration of passive tracer introduced in the Pacific PF to SAF region on the $27.4 \text{ kg m}^{-3} \sigma_n$ surface at 15 model years in ECCO. For map of depth of $27.4 \text{ kg m}^{-3} \sigma_n$ surface see Figure 4.14b.

σ_n 26.5 - 27.5 kg m⁻³ at concentrations of 20-70%. Such high concentrations indicate the importance of the Pacific PF to SAF region in the production of waters passing through Drake Passage. After passing through Drake Passage the tracer is swept northward and then eastward following the path of the ACC (Figure 4.18). The tracer reaches 24°S via the same slow but zonally uniform northward flow along isopycnals extending away from the high concentration of tracer within the ACC (Figure 4.18 & 4.19c). This layer sits above the waters originating from the PAC S of PF region. The tracer that does not spread northward in the Atlantic but continues eastward in the ACC appears to remain within the densities of 27.00 – 27.75 kg m⁻³ σ_n on its transit around Antarctica, suggesting tracer that has circulated around Antarctica could re-join newly subducted waters in the Pacific.

Much like the Pacific S of PF waters the PF to SAF waters arrive relatively quickly at 24°S, with the first arrival of the Pacific PF to SAF tracer at 7 years, the peak rate of arrival at around 14 years (Figure 4.13a), 50% arrival at

21 years and 95% arrival at 60 years. This suggests that most of the water from this region follows a fairly direct pathway to 24°S.

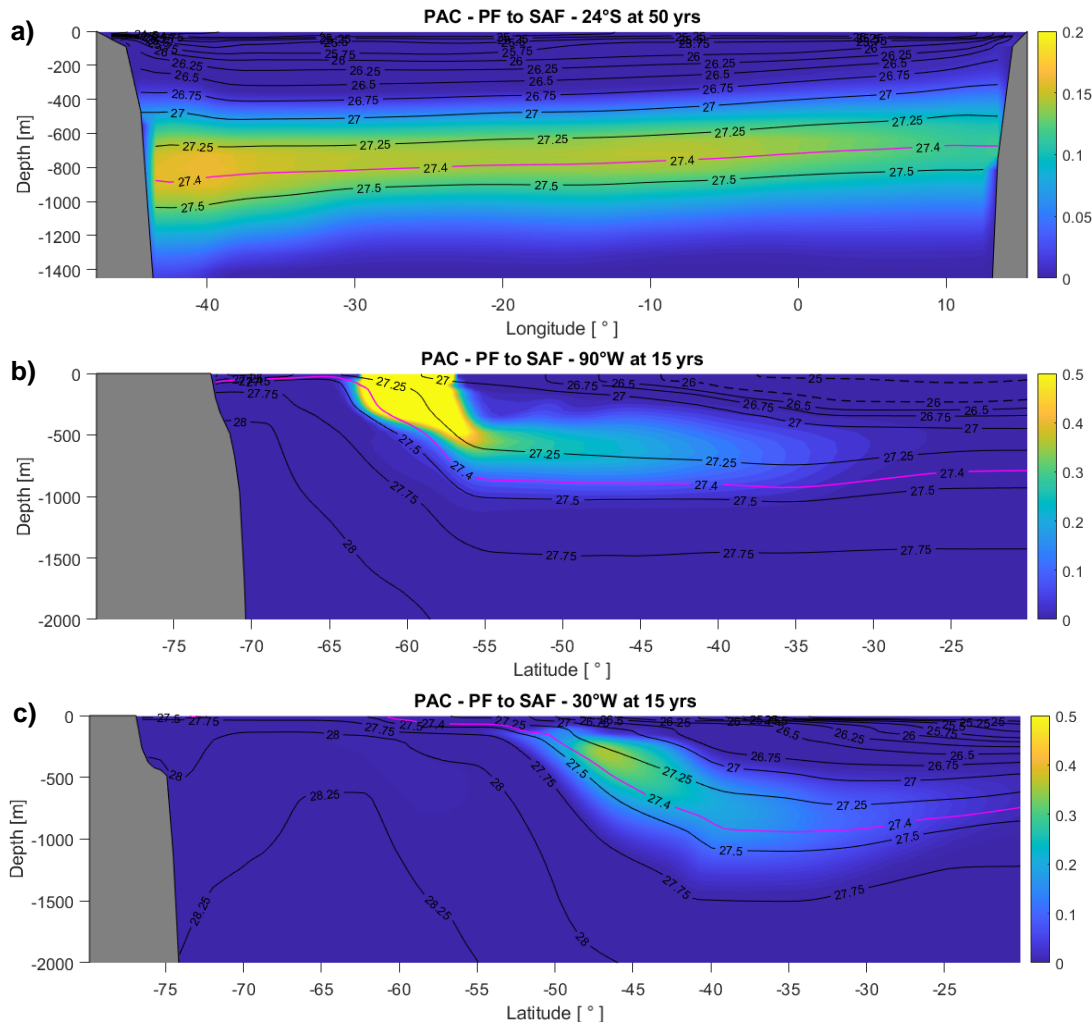


Figure 4.19 - Section plots showing concentration of Pacific PF to SAF tracer in ECCO. Pink line indicates the σ_n 27.4 surface shown in Figure 4.18. (a) 24°S at 50 years, (b) 90°W at 15 years, (c) 30°W at 15 years. Locations indicated of Figure 4.18.

4.6 Comparing MEM and ECCO Results to the Literature

We have so far largely looked at the results of the MEM and the ECCO passive tracer experiments separately, now we look to further explore the differences and similarities in the results and how the results fit with current understanding. This discussion is divided into three sections; AASW source, Southeast Pacific source and Indian Ocean source.

4.6.1 AASW Source

As described in Section 1.2.3, there is a strong link between the characteristics of AASW south of the PF to the west of the Antarctic Peninsula, and the characteristics of AAIW passing through Drake Passage (Naveira Garabato *et al.*, 2009). The MEM identifies the S of PF regions as major contributors to the salinity minimum at 24°S, with contributions of 17%, 20% and 12% for the Pacific, Atlantic and Indian respectively. Average profiles of tracer contribution at 24°S (Figures 4.2 & 4.3) indicate that this S of PF influence gets stronger in the denser classes of AAIW below the salinity minimum and in UCDW. The ECCO tracers indicate much smaller contributions of the S of PF water to the 24°S salinity minimum of 7%, 4% and 5%, for the Pacific, Atlantic and Indian sectors respectively. This suggests that the subduction of denser waters from S of PF into intermediate depths may be underrepresented in the ECCO simulation.

Evidence to support this theory of underrepresentation comes in two forms. The first is in the robustness of the MEM results; the MEM predicts a high contribution from S of PF waters at densities corresponding to UCDW even when no spatial priors are used (see Section 4.8). The second comes from comparing the structure of the tracer profile in density. In density, the S of PF peak contribution in ECCO is much closer to the salinity minimum than in observations (0.12 kg m^{-3} below the salinity minimum compared to 0.21 kg m^{-3} below the salinity minimum in observations). This suggests ECCO may not represent the water from S of PF in the UCDW well, as the higher contributions deeper in the water column are never reached.

It is unusual that the MEM associates a strong S of PF signal to the UCDW (identified by the oxygen minimum), as UCDW would be expected to show a strong North Atlantic source. This is because it is generally thought to be formed predominantly of old NADW, hence the low oxygen levels. This could be explained by a higher level of interaction between S of PF waters and the NADW, which supplies (in the form of CDW) the upper limb of the Southern Ocean Meridional overturning circulation, in the Southern Ocean.

The MEM suggests these S of PF waters have an age of 35 - 55 years. The ECCO tracers suggest that the majority of water from the S of PF region arrives in under 100 years with peak tracer arrival at around 15 years and 22 years, for the Pacific and Atlantic respectively. Although this peak arrival is younger than the MEM predicted age, Figure 4.13b & c still show a considerable amount of ECCO tracer arriving in the 35 - 55 year period and so the MEM age is not invalidated by the ECCO result.

The spread of the ECCO tracers (Figures 4.14, 4.15, 4.16 & 4.17) and literature (Naveira Garabato *et al.*, 2009; Sverdrup *et al.*, 1942) suggest that the waters from S of PF enter the Atlantic via subduction close to the PF. The ECCO ages suggest that S of PF water from the Pacific has the most direct pathway into the Atlantic, followed by Atlantic and Indian S of PF waters. Waters formed in the Atlantic and Indian sectors are likely drawn eastward in the ACC prior to penetrating northward into the Atlantic.

Overall the MEM prediction of older waters from S of PF seems realistic, as although not identical to the ECCO predictions, the ages are still similar and the proposed circulations fit with ideas in existing literature. However, the MEM does suggest a much more even contribution from the S of PF regions in each

Southern Ocean sector, whereas the literature weights the Pacific sector's contribution much higher than the contribution from the Atlantic and Indian sectors (e.g. Talley, 1996).

4.6.2 Southeast Pacific Source

The Southeast Pacific is commonly cited as one of the main sources of AAIW found in the Atlantic (e.g. McCartney, 1977; Sloyan and Rintoul, 2001; Sloyan *et al.*, 2010; You, 2002). However what constitutes the southeast Pacific region varies between studies. Some studies specifically reference the area of SAMW formation north of the SAF (e.g McCartney, 1977), whilst other studies reference the area close to the PF (e.g. Molinelli 1981, Santoso and England, 2004) and some the region close to the SAF (Deacon 1937). Here we focus on the PF to SAF region, but note that the N of SAF Pacific region contributed 5% (JC032 and JC159) and the Pacific S of PF contributed 17% (JC032 and JC159) to waters at the salinity minimum at 24°S, according to the MEM. The Southern Ocean regions used in the MEM analysis are based on climatological front positions (see Sections 3.2.2 & 3.3.3), which in reality are variable (Sallée *et al.*, 2008). For this reason, the region termed here as PF to SAF may at times have been more dominated by processes north of the SAF (e.g. mode water formation) and at others by those south of the PF (e.g. AASW subduction).

The MEM results showed the PF to SAF region of the Pacific to be responsible for the characteristic salinity minimum of AAIW in the Atlantic and a 10% contribution of water to the salinity minimum at 24°S. Confidence is given to this result by the results of the ECCO tracer experiment, which suggested a 16% contribution of waters from this region to the salinity minimum at 24°S. Literature also strongly supports the suggestion that this area is responsible for the salinity minimum in the Atlantic as it is an area where precipitation exceeds

evaporation and it is close to the region known for the densest, coldest and freshest form of SAMW (Talley *et al.*, 2011).

The age signal from the MEM for this region is not distinctive but is thought to most likely fall within the young peak, giving it an age of approximately 5 - 25 years. The ECCO passive tracers indicate that Pacific PF to SAF can arrive at 24°S in under 10 years, with the highest rate of arrival at around 14 years. This confirms that the timescale of 5 - 25 years (predicted by the MEM) is feasible. This short timescale suggests that AAIW formed in the Southeast Pacific enters the Atlantic directly, as opposed to undertaking a circumpolar navigation prior to heading north in the Atlantic basin.

In the analysis of McCarthy *et al.* (2011), they identify two ages of water at 24°S, a young fresh contribution which they suggest is from Drake Passage/the Southeast Pacific and an older salty contribution from the Indian Ocean. This differs from the results of the MEM which suggest the water from the southeast Pacific (excluding S of PF water) has a similar age to the Indian waters. The age difference noted by McCarthy *et al.* is based on the AOU of the respective waters, which only gives a general indication of age based on the principle that older waters tend to have lower oxygen levels (higher AOU) due to higher cumulative respiration. It is possible that both sources could have similar ages but that the Indian waters have higher AOU due to higher rates of respiration, but such investigations fall outside the scope of this thesis.

When looking at the temporal origins it is also interesting to compare the PF to SAF signals with those of the neighbouring regions. Despite being so close, the MEM predicted water from S of PF to have an older age of 35 - 55 years. ECCO predicted a more similar age between the regions, with the peak

arrival of Pacific S of PF tracer at around 15 years (14 years for Pacific PF to SAF). One theory to explain the differences in age between S of PF and PF to SAF waters (seen in the MEM results), is that denser waters may take longer to reach 24°S as they are either carried in the weaker lower levels of the surface currents, or in the slower abyssal currents. Although ECCO showed both Pacific PF to SAF and Pacific S of PF waters to reach 24°S relatively quickly, the pathway taken by the tracers (Figure 4.14 & 4.18) appears to follow a more abyssal circulation, with basin wide northward progression of the tracer.

The exact mechanism by which this water entered intermediate depths cannot be determined using the MEM method as this purely links sampled water to surface characteristics. The areas to the north of the PF to SAF region are thought to contribute to AAIW through the subduction of SAMW (McCartney, 1977) whereas the areas to the south are thought to contribute via the subduction of AASW close to the PF (Santoso and England, 2004). As the frontal positions in the analysis are constant (see discussion above) it is not implausible for the results of the MEM to be influenced by both mechanisms, a possible explanation for the ambiguity over age. The ECCO passive tracer fields do show water subducting along surfaced isopycnals, but the resolution of this output is annual and so it is not possible to observe the seasonal cycle of SAMW production.

Overall the suggestion by the MEM that the Pacific PF to SAF is responsible for the salinity minimum at 24°S fits well with current literature. The results of the ECCO tracers suggest that it would be feasible for these waters to contribute to the young (5 - 25 year) age signal.

4.6.3 Indian Ocean Source

Both the MEM and ECCO highlight the Indian sector as providing the largest contribution of N of SAF waters to 24°S. They also both show the vertical maximum concentration of waters from this region to lie above the salinity minimum in the water column. MEM does not however show any contribution of note from any Indian Ocean region north of the N of SAF region (i.e. main Indian Ocean). The MEM ages are largely compatible with the ECCO derived ages, although in ECCO the tracer arrival has a longer tail. The MEM predicts Indian N of SAF water to arrival at 24°S within the young peak at 5 - 25 years, and ECCO predicts the first arrival at 18 years and maximum rate of arrival at around 25-30 years (Figure 4.13d).

As mentioned in Section 4.5.2, it is thought that water enters the Atlantic from the Indian Ocean in Agulhas Rings and through Agulhas leakage (Talley *et al.*, 2011; P. Richardson, 2007). ECCO has a near 1° resolution, too coarse to resolve Agulhas Rings, and so the transport of water into the Atlantic from the Indian Ocean is not realistically represented in ECCO. This will contribute to (and possibly dominate) the difference in arrival times between the two methods.

During the 2018 cruise (JC159) a feature was observed in the ADCP (Acoustic Doppler Current Profiler) data, which was identified as either a meandering feature or an eddy. Eight CTD stations fell within this feature and it was speculated that it may be an Agulhas Ring or remnant thereof. It was hoped that this feature may have given more information about the Indian Ocean source of AAIW. The MEM does note some samples within these stations show a marginally older temporal signal, particularly those close to

what is deemed the core of the feature. However, when the spatial origins are explored there is no clear difference in origin. It is very possible this was an Agulhas Ring but due to mixing along its path (see McDonagh *et al.*, 1999) it has lost any strong signatures relating to its origin that would be detectable by the MEM. It may also be that no difference in spatial origin was observed as the background waters also carry water from the Indian Ocean which has entered the Atlantic through Agulhas leakage (Richardson, 2007), or that the eddy actually originated from the Atlantic (see Smythe-Wright *et al.*, 1996). However, there is not sufficient evidence to conclude either way.

The Indian Ocean AAIW that passes into the Atlantic is thought to be a mixture of newly formed AAIW, Red Sea Water (RSW) and recirculated AAIW from the Atlantic (Fine, 1993; Fine *et al.*, 1988). Here each of these three components and their detectability by the MEM is briefly addressed.

The high contribution of Indian N of SAF waters to AAIW (predicted by the MEM) strongly supports the idea of newly formed Indian AAIW contributing to AAIW found at 24°S. As this water is from north of the SAF, it would be expected that this AAIW formed via the SAMW (mode water subduction) mechanism. Deep mixed layers required for such subduction are found in the eastern Indian Ocean, although it is thought that it is the lighter form of SAMW which is formed here (Sallée *et al.*, 2010). Sallée *et al.* suggest that the denser form of SAMW predominantly subducts in the region south of Campbell Plateau (and in the central Pacific near the Eltanin Fracture Zone). You (1998) also identified AAIW source regions in the Indian Ocean, based on property distribution and known large-scale mixing and spreading. He identified source areas at 65°E, 42°S and 120°E, 37°S (Figure 1.6), which fall within, or very close to, the Indian N of SAF region, but he does not suggest which formation

mechanism occurs in these areas. As noted previously, the ECCO tracers do not have sufficient temporal resolution to observe mode water formation, but ECCO tracers did appear to show an area of subduction between 65°E to 140°E within this region. This suggests that both mode water subduction and direct subduction of surface waters along isopycnals may be at play in the Indian sector of the Southern Ocean.

Neither the MEM nor ECCO demonstrate a clear RSW influence, however, this does not contradict previous studies that have shown this to exist. RSW found in the Indian Ocean (also sometimes known as Red Sea Intermediate Water) originates from high salinity waters of the Red Sea which enter into the Arabian Sea (northwest area of Indian Ocean) at the sill depth of the Red Sea (Emery, 2001). In the MEM, the potential sources do include the Arabian Sea but do not include the Red Sea. As the characteristics of RSW are set by the surface characteristics of the Red Sea, the MEM would not be able to link observed high salinity waters back to this region. This is a key limitation of this particular configuration of the MEM for looking at AAIW with an Indian origin. The Red Sea was not included due to a lack of surface data in the region in the datasets used to create the source region characteristics. A development of this method for the future would be to source additional data for the Red Sea and incorporate this into the fields used to create the source boundary condition.

A passive tracer was added to the Red Sea and the Persian Gulf in the ECCO simulations. Despite a connection in the model between the Red Sea and the Gulf of Aden (which was a single grid cell in width and 19 vertical levels, 277 m, deep), no tracer from the Red Sea was observed to transit into the Atlantic in the 300 years of the model run. It is thus demonstrated that ECCO

does not resolve the overflow water from the Red Sea into the Arabian Sea (via the Gulf of Aden), explaining why no contribution of RSW is observed in AAIW near Cape Agulhas.

Overall the MEM prediction that waters from the N of SAF region in the Indian Ocean contribute more to the lighter classes of AAIW at 24°S fits well with both the ECCO tracer results and ideas of the warm pathway from the literature (e.g. Gordon *et al.*, 1992; You, 2002). The timescale of 5 - 25 years for these relatively light Indian Sector waters to reach 24°S is slightly short compared to the ECCO ages, but this may in part be explained by the lack of Agulhas Rings in the ECCO simulation.

4.7 Comparing Temporal Patterns in Decadal Repeat Observations

This analysis has used data from two cruises, the first in March 2009 (JC032) and the second nine years later in March 2018 (JC159). These are sufficiently separated in time that it may be possible to detect changes in circulation between the two cruises. Transient tracers have been widely used to study decadal change (e.g. Waugh *et al.*, 2013; Ting and Holzer, 2017) but recently a study by Lester *et al.* (2020) questioned the validity of doing so. They suggested that changes observed in decadal repeats are dominated by internal variability instead of external forcing (e.g. changes to the westerly winds). This work is acknowledged and taken into consideration, but it is nevertheless felt that long term changes in AAIW properties globally (see Section 1.3.1), motivate further investigation into the possible attribution of observed changes to forced changes in circulation.

Here the focus is given to AAIW 1, as this is the class where the clearest signal of older and younger water can be seen without the interference of much older (75+ years) water. Figure 4.20a shows probability plotted against the age of the water. If no change in circulation occurred between the two cruises, the two curves would be effectively identical. Here, the young peaks do not match, but instead overlap, with the 2009 data peaking at a slightly younger age of 13 years while the 2018 data peaks at 16 years. The older age peaks show a similar pattern, with the 2009 data again peaking at a younger age to the 2018 data, however, here the gap is much larger. The modal age in 2009 is 39 years, whereas the modal age suggested by the 2018 data is 48 years.

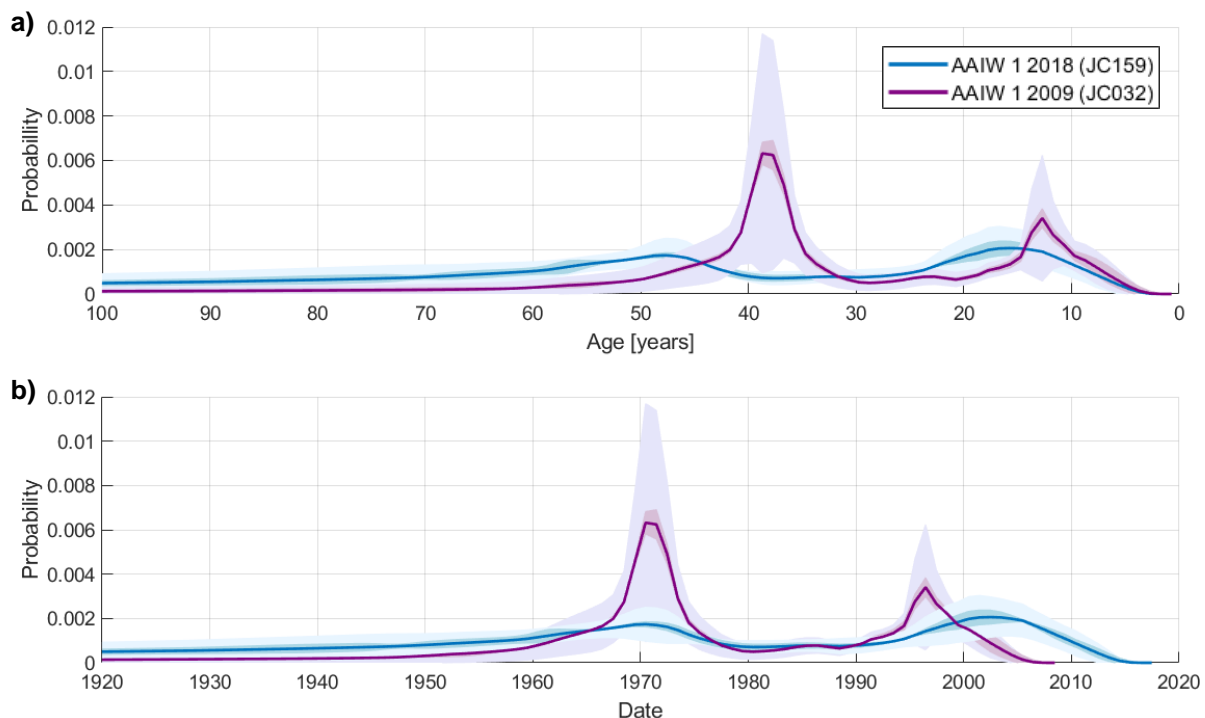


Figure 4.20 - The probability of a parcel of water having a certain age (a) or being from a certain period in time (b) regardless of the region of origin. Thick dark line in each plot shows the average probability distribution for all samples in the AAIW 1 class, dark shading indicates ensemble error, light shading indicates averaging error.

A feature that is noticeable in the 2009 data but not in the 2018 data is the prominence (spikiness) of the peaks in the temporal spread of probabilities (e.g. Figure 4.4). Investigations into the cause of this difference found no

evidence to attribute this spikiness to a specific property of a sample, such as tracer concentration, longitude, salinity or temperature. The most likely explanation is that due to more accurate measurements of tracer, the ratio of tracers in these samples allows for a better solution of the iterative solver, allowing the peaks of the signals to be stronger and less broad.

We now consider potential explanations for the observed differences in age. As the young and old peak have been shown to have different spatial origins, we will consider them separately, starting with the younger peak. Two theories are considered for the younger peak and three theories are considered for the older peak.

One of the most noticeable recent changes in the Southern Ocean is the poleward shift and intensification of the Southern Hemisphere Westerly Winds (Swart and Fyfe, 2012) linked to the positive trend in the SAM index in recent decades (Thompson and Solomon, 2002; Marshall, 2003). It is theorized and simulated in multiple model studies (Hall and Visbeck, 2002; Fyfe and Saenko, 2006; Bi *et al.*, 2002) that a strengthening of the winds will lead to an increase in northward Ekman transport which will in turn lead to increased subduction of intermediate waters. Assuming no other changes to the system, an increase in AAIW subduction would be expected to decrease the age of AAIW at 24°S. The results presented here do not show this, and instead show a small ageing of the lighter waters of AAIW. As discussed in Sections 4.2 and 4.5, the young signal in these results is thought to predominantly originate from Indian waters north of the SAF, with some potential contribution from Pacific waters north of the PF (PF to SAF and N of SAF regions). In a modelling study, Downes *et al.*, (2017) explored the effect of both the poleward shift of the winds and the intensification of the winds and the impact this has on SAMW and AAIW formation. They

found that although a strengthening of the winds without a poleward shift in position deepens the mixed layer and increases subduction, when strengthening of the winds is paired with a poleward shift in position, subduction of SAMW and AAIW decreases due to reduced heat loss and increases in freshwater input. If true, this response could explain the increase in age of AAIW seen here.

An alternate theory to explain an increase in age requires consideration as to whether other areas contribute to this young age signal. It was discussed previously how regions in the Southeast Pacific may also contribute to this young signal (Section 4.6.2) and how AAIW of Indian Ocean origin has multiple contributing sources (Section 4.6.3). If this Pacific water has a slightly older or younger signal than the Indian Ocean water or if the different components of Indian Ocean water have different ages, the relative contribution of these end members could impact overall age at 24°S. Although there is little to uphold this argument, it is not unreasonable for a change in relative contributions to be considered, as a poleward shift in the westerlies is thought to have increased Agulhas Leakage in recent years (Biastoch *et al.*, 2009). This said, the area under the probability curve for water < 30 years old is near identical, with a negligible increase of 0.02% between the 2009 curve and the 2018 curve. This would suggest that the contribution of water < 30 years old to AAIW at 24°S, does not change. It would therefore be unlikely for the relative contribution of end members (e.g. Southeast Pacific sources, Indian Ocean sources) of this younger water to shift whilst the contribution of < 30 year old water to AAIW at 24°S is maintained so consistently.

We now consider changes in the older signal. The older signal is thought to originate from south of the PF across all of the ocean sectors, but most

strongly from the Pacific. This water is more dense than the water responsible for the young peak, and is thought to contribute to AAIW via subduction of dense surface waters at the PF. The theory of increased Ekman transport and increased subduction also stands for these waters, but again is in disagreement with this study's findings of ageing AAIW.

An event that may not be able to account for all of the ageing, but that could cause some aging of this water, is a shutdown in formation. Naveira Garabato *et al.* (2009) observed a shutdown of Winter Water (the winter variety of AASW) subduction in 1998/1999. They attributed this shutdown to Ekman upwelling in and either side of the PF to SAF region, caused by an eastward wind stress anomaly associated with a positive SAM and negative ENSO. An arrest of AAIW formation in 1998/1999 would be expected to have the same influence on both the water sampled in 2009 and 2018, slowing them both a small amount, as in theory they were both subducted many years prior to this observed shutdown event. However, the 1998/1999 shutdown is evidence that such events exist. Between the period of 2009 and 2018 the SAM was often in a positive phase (Marshall and NCAR Staff, 2018) and the ENSO (NOAA ,2021) was predominantly in a negative phase (positive in years 2015-2017). In theory, if a shutdown in formation or a strong reduction had again been caused by this ENSO SAM interaction, this could have caused a slowdown of waters already in transport (i.e. subducted in previous years), due to no (or very little) new water entering this density class in the Atlantic.

A second possible explanation for the difference in the ages of the older signal is linked to larger ocean circulation. The Atlantic Meridional Overturning Circulation (AMOC) transports cool deep waters southward and warmer surface and intermediate waters northward. With climate change the AMOC is predicted

to slowdown (Hansen *et al.*, 2016) and in recent years, periods of slowdown have been observed at the RAPID array at 26.5°N (Smeed *et al.*, 2018). There is reluctance to draw long term trends from the RAPID data due to observations from the mooring array only extending back to 2004. That said, it has been stated that periods of strong AMOC weakening have been observed within this period, alongside high inter-annual variability. More specifically a period of weakening was observed from 2008 - 2017 (data stops in 2017) (Smeed *et al.*, 2018). The overturning is sustained by cool waters sinking in the north and warm waters being drawn northward. If this overturning weakens, water will be drawn northward more slowly, increasing the age of these waters. The measurements used in this study were taken in 2009 and 2018, closely matching the period of observed weakening. Hence this weakening could explain why water sampled in 2018 has an older age than that sampled in 2009.

The third possible explanation for the apparent aging of the older signal requires the probability to be considered against calendar year (Figure 4.20b). Here, if circulation remained the same the 2009 data would be expected to lag to the right of the 2018 data by approximately nine years, due to the gap between the cruises. In the young peak this lag is observed, although, as the ages differ between the cruises, the lag is less than nine years. In the old peak no lag is observed, with both peaks from the 2009 data and 2018 data aligning in the early 1970s. There are three ways this could be interpreted: 1) circulation has slowed so dramatically that the water has essentially stagnated and the water sampled in 2009 is the same water that was sampled in 2018, 2) a large episodic event in the 1970s caused a very large volume of water to subduct, all with the same age signature, some of which was sampled in 2009 and another

part of which was sampled in 2018, and 3) the MEM is artificially drawn to these years due to a particular feature in the transient tracer history.

The first hypothesis seems very dramatic and highly unlikely considering that no sign of a circulation shutdown has been observed at the RAPID array. The second hypothesis is more feasible as the years correlate closely to the presence of the Weddell Polynya in the 1970s, a feature known to form dense water. For this reason, time is taken to further explore this idea in a modelling study (Chapter 5). The third hypothesis is not unreasonable as the MEM has been known to be drawn to particular features in the source data (e.g. high salinity in the Mediterranean Sea). However, further investigation found no notable feature in the tracer histories that would draw the solver to the early 1970s.

In summary, an aging of three years was observed in the young less dense waters and an aging of nine years was observed in the older denser water. Two hypotheses to explain the changes to the young signal were explored; the first the role of the strengthening and poleward shifting westerly winds in the reduction of AAIW formation, and the second the potential for a change in the relative contributions of multiple end members. For the aging of the older signal three hypotheses were explored; The first related to periodic shutdown of AAIW formation in relation to atmospheric variability, the second linked to a slowdown in the AMOC, and the third related to a pulse input of water from the Weddell Polynya in the early 1970s.

4.8 Influence of the Prior

The MEM helps to solve a system of highly underdetermined equations. As discussed in Section 3.1.5, the prior acts as the first guess for the system, the solution is allowed to deviate from the given prior, but the prior does inevitably push the solver in the direction of what it deems to be the ‘correct’ answer. Here we briefly explore how the choice of prior has influenced the final results. The four sets of results compared are those using the ‘optimal prior’ which has inverse Gaussian distribution in time and uses the ECCO300 output to generate a spatial prior (IG-ECCO300), a prior using the ECCO300 spatial prior but uniform distribution of probability in time (UNI-ECCO300), a prior with uniform spatial probability and an inverse Gaussian distribution of probability in time (IG-UNI), and a prior with uniform distribution of probability in both space and time (UNI-UNI).

In order to establish the effect of the prior on the predictions of the origin of water we first compare neutral density profiles of the fractions for the three Southern Ocean regions. Here we discuss the results using the 2009 data (Figure 4.21a-c), however, the observed patterns were replicated in the 2018 data (Figure 4.21d-f).

The contributions of waters from S of PF are very consistent between the four priors, indicating a low sensitivity of this result to both the spatial (ECCO300) and temporal (IG) prior. Larger differences can be seen in the results of the contributions from the PF to SAF region and the N of SAF region. These profiles can clearly be split into two groups, those which use the

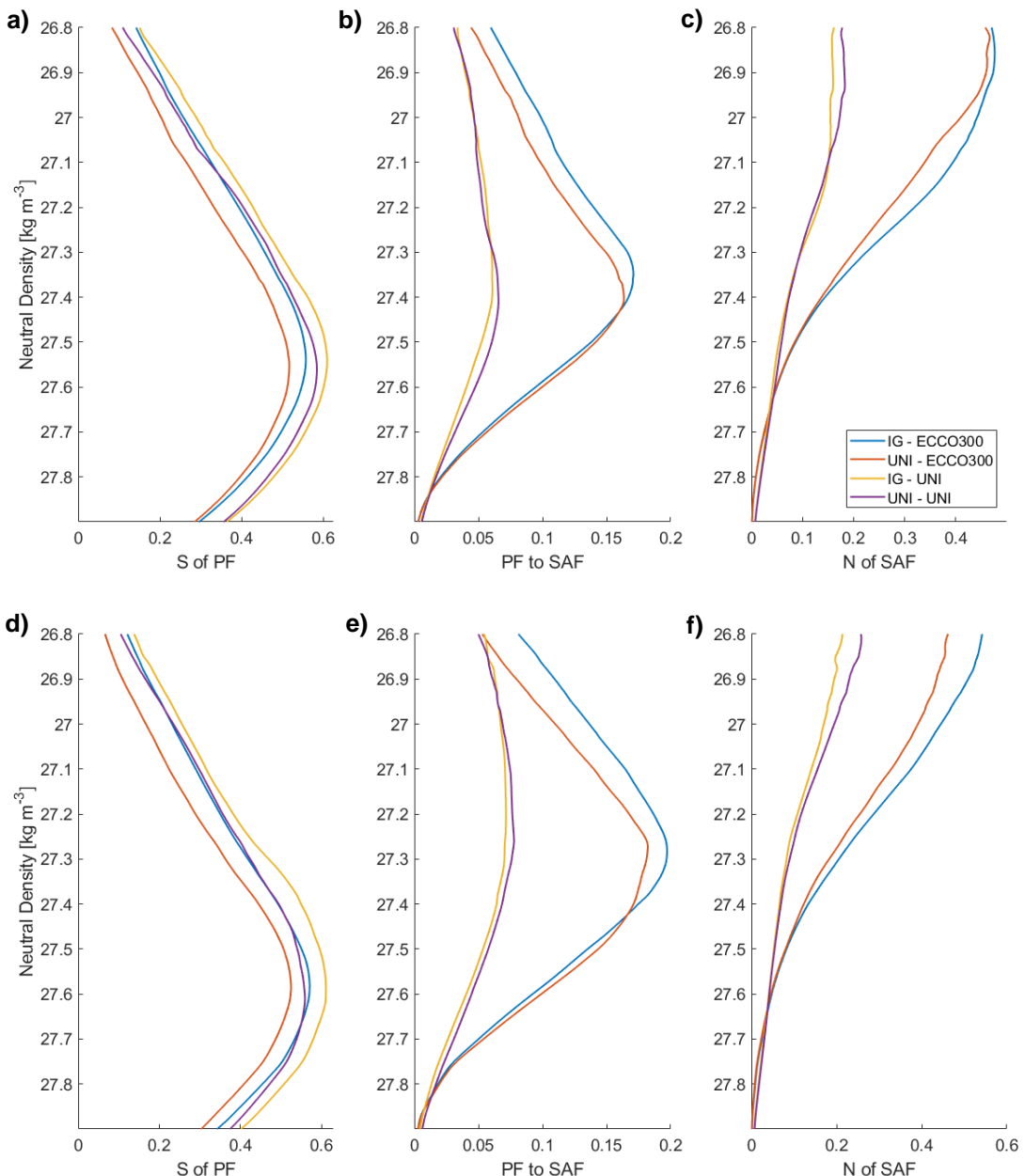


Figure 4.21 - Mean neutral density profiles at 24°S showing the MEM predicted fractions from three Southern Ocean regions using four different prior scenarios for 2009 JC032 (a,b,c) and 2018 JC159 (d,e,f).

ECCO300 spatial prior and those that do not. Those that use the ECCO300 prior indicate a much higher contribution from the respective regions at their peak contribution. For example, for all prior scenarios the PF to SAF contribution peaks between σ_n 27.35 – 27.41 kg m⁻³, however for the scenarios without the spatial prior the contribution at the peak is 6% and 7% and for scenarios with the spatial prior it is 16% and 17%. This shows the magnitude of the contribution from the region does have strong sensitivity to the prior, but that

the position of this peak within the water column is largely insensitive to the choice of prior, indicating it is a robust result. It appears the results have low sensitivity to the use of the IG temporal prior, which is expected as these profiles are integrals over time and so any sensitivity of the results would not be expected to be seen strongly in these profiles.

To establish the effect of the prior on the predicted age of the water we compare the predicted probabilities of the temporal origin of the water for the three AAIW classes. For simplicity we focus on the effect of different prior scenarios on the results of using the 2009 data (Figure 4.22a-c). Again the response can be clearly split into two groups, however here it is split into the scenarios which include the IG prior (IG-ECCO300 and IG-UNI) and those which do not (UNI-ECCO300 and UNI-UNI).

For the AAIW 1 and AAIW 2 samples the modal ages of the two peaks are consistent between all four scenarios, varying within one year of one another. A slight difference observed between those scenarios using the IG prior and those that do not, is that when the IG prior is used the probability of water originating in the most recent 3-5 years is reduced, steepening the younger peak. In the AAIW 2 samples this increases the size of the young peak. The use of the IG prior also appears to decrease the probability of AAIW 1 and AAIW 2 water being older (originating from prior to the 1930s). The results for AAIW 3 are broadly altered by the priors in the same way, although to a stronger degree. The young peak in the AAIW 3 results disappears when the IG prior is not used as opposed to just decreasing in magnitude. The older peak is shifted younger by approximately five years and the shape of the peak is altered to a less Gaussian form. The results from the 2018 data show a similar

response to those from the 2009 data, but with a more marked shift in the old peak of AAIW 2 waters.

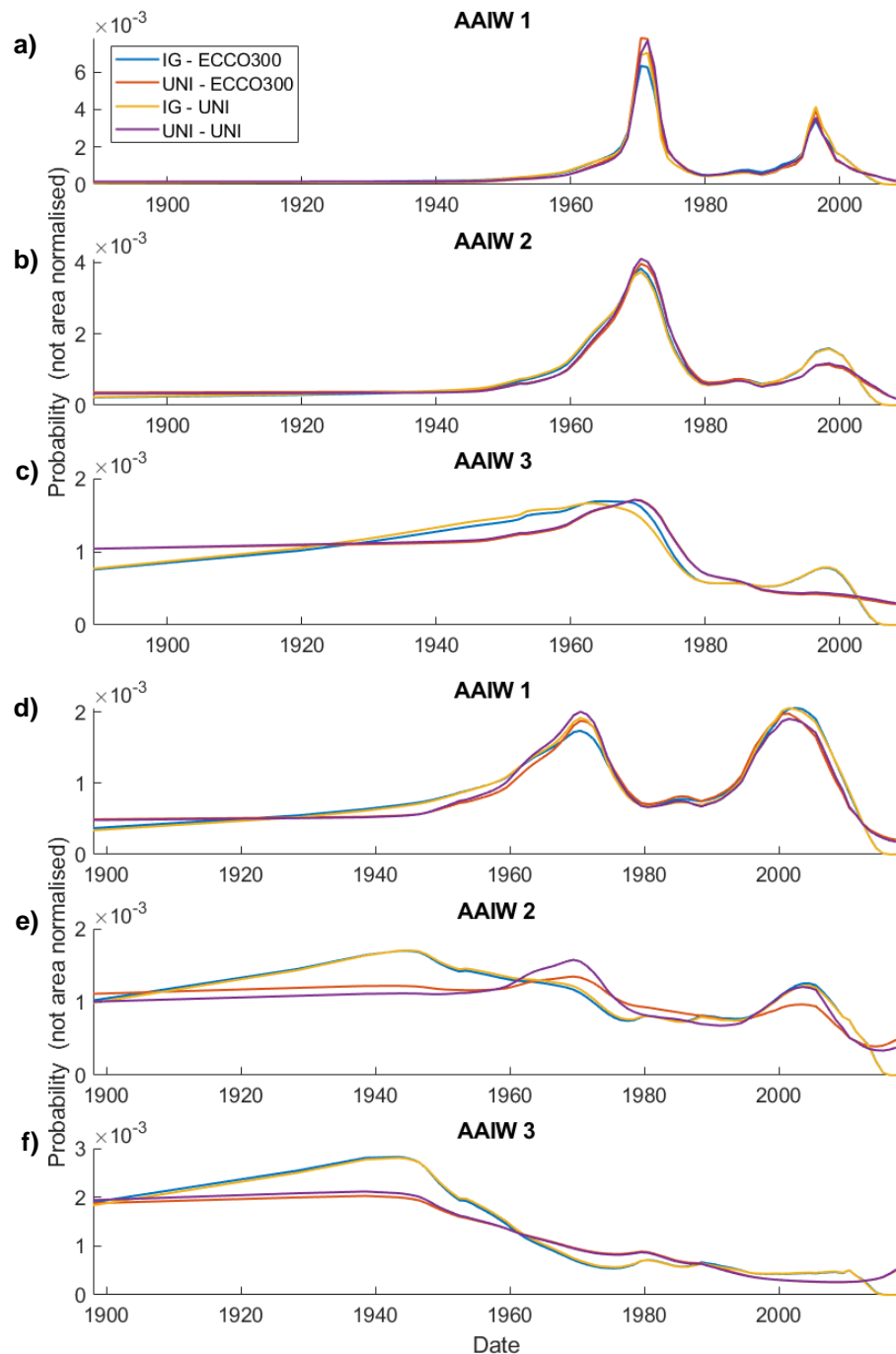


Figure 4.22 - The probability of a parcel of water originating from a certain period in time regardless of the region of origin, for four different prior scenarios. (a,b,c) Show results using 2009 JC032 data, (d,e,f) show results using 2018 JC159 data.

Overall these tests indicate that the use of the ECCO300 prior has very little effect on the predictions of age of the three classes of AAIW. They indicate that the use of the IG prior decreases probability in the most recent years and in years over a century ago, but that in the time-frame relevant to AAIW the results are largely insensitive to the choice of prior, indicating that they are strongly governed by the observational tracer values and associated spatial patterns and surface history of the source data. The exception to this conclusion is that of the older peak in the AAIW 2 2018 data results which shows a considerable shift of 25 years in modal age.

4.9 Summary & Conclusion

The initial aim of this work was to estimate the age of the AAIW at 24°S, and to do this independently for both cruises, to establish the differences between the decadal repeats, and identify any mechanism that would explain any observed changes. Upon analysis of AAIW at 24°S using the MEM, it became apparent that water within the AAIW density class has two clear temporal origins: a young age signal which dominates waters above the salinity minimum, and an older age signal which dominates waters below the salinity minimum.

The young signal was identified by the MEM as originating from waters north of the SAF. Using the MEM results, ECCO passive tracers and existing knowledge of ocean circulation, it was suggested that this water forms via subduction of SAMW in the eastern Indian Ocean N of SAF region and then travels westward entering the Atlantic via Agulhas Rings and Agulhas Leakage.

The MEM indicated that the older signal originates from waters south of the PF which have a strong association with UCDW. The ECCO tracers and existing literature suggested that these waters form from AASW which subducts close to the PF, predominantly but not exclusively, in the Pacific sector of the Southern Ocean. The MEM also showed PF to SAF waters from the Pacific to be responsible for the salinity minimum at 24°S, but an age for this water could not be unambiguously determined.

Once the locations of origin for the temporal signals were established, the differences in the age of these waters was compared between the 2009 and 2018 occupation of 24°S. The older temporal signature showed a slowdown of nine years, with a modal age of 39 years in 2009 and 48 years in 2018. The young temporal signature showed a slowdown of three years, with a modal age of 13 years in 2009 and 16 years in 2018. A single, unambiguous explanation for these changes was not determined; instead it is thought that a number of processes contributed to the change. The most likely contributors being a poleward shift and intensification of the westerly winds, a change in the contribution of end members, and a temporary shutdown in AAIW formation.

Chapter 5:

Evaluating the Reach of Waters Formed in the Weddell Polynya Using Passive Tracers in ECCO

Abstract: Previous results identify temporal signatures in AAIW at 24°S that closely match those of the Weddell Polynya in the 1970s. Here a Weddell Polynya is forced for three consecutive years in the ECCOv4r2 configuration of MITgcm. The water generated within the Polynya is tracked using passive tracers and its reach within the Weddell Basin, and the major ocean basins, is evaluated. It is found that water remains within the Weddell Basin for the first seven years and in doing so increases the meridional density gradient over the ACC. This leads to an increase in transport at Drake Passage of 1.6 Sv. Polynya Water is observed to enter into all three major ocean basins within the bottom waters, and low concentrations of Polynya Water are detected north of the equator in all basins by 80 years. No Polynya Water is observed at, or nearby, any densities associated with AAIW, casting doubt on any hypothesised link between Weddell Polynya Waters and the time signatures observed in AAIW at 24°S.

5.1 Motivation & Background

This chapter is motivated by the results of Chapter 4. In the analysis of the AAIW at 24°S in the South Atlantic, 55-60% of water at the salinity minimum is predicted to originate from the region south of the PF. Further analysis of the age of this water, using with the Maximum Entropy Method (MEM), predicts that the modal age of this water is 39 years, based on observational data collected in 2009, and 48 years, based on observational data collected in 2018. When these dates and ages are translated back in time to find the date of the origin of water, both water sampled in 2009 and 2018 is predicted to have last been at the surface in 1970. A number of possible explanations for this are discussed in

Chapter 4. However, here we explore the idea that this water is linked to the presence of an open ocean polynya observed in the Weddell Sea during the austral winters of 1974-1976 (Carsey, 1980).

A polynya is an area of open water surrounded by sea ice. They can be categorised into two groups: coastal polynyas and open ocean polynyas. The Weddell Polynya is an example of an open-ocean polynya. Open ocean polynyas form when warmer waters from depth are able to upwell and cause the sea ice to melt. These warm waters are then cooled at the surface and consequently increase in density and sink, being replaced with newly upwelled warm waters. Whereas open-ocean polynyas are sustained by overturning and the upwelling of warm waters, coastal polynyas are sustained by wind blowing sea ice away from the coastline. New sea ice continually forms at the sea surface, causing brine rejection and the densification of the surrounding water, which results in convective overturning (NSIDC, 2020).

The Weddell Polynya was first observed in satellite data in the 1970s (Carsey, 1980). A large polynya was present in the austral winters of 1974-1976 in the eastern Weddell Sea, smaller polynyas were observed in the same area (initially close to the Maud Rise seamount at 66°S, 3°E) in 1973 and 1977 and an area of weak ice was observed in 1980 (Martinson, 1991). The Weddell Polynya was observed during the infancy of polar satellite observations and so data prior to these years are lacking, although some evidence also suggests an occurrence in 1960 (Martinson, 1991). When first observed it was thought the Weddell Polynya was a common occurrence, but after 1980 no notable polynya was observed until 2017 when a small polynya was observed at Maud Rise (Swart *et al.*, 2018). This location is important as Maud Rise is a seamount which rises to within 1000 m of the ocean surface (Heezen *et al.*, 1972) and

which is thought to play an important role in the formation of Weddell Sea polynyas. This is due to the circulation around the seamount causing a local doming of isopycnals (e.g Holland, 2001; Cheon & Gordon, 2019).

The Maud Rise Polynya was observed from September to November 2017 and was considered comparable to the polynya observed at Maud Rise in 1973. It extended to a size of $\sim 50 \times 10^3 \text{ km}^2$ but did not evolve into what is considered a full scale Weddell Polynya like that observed from 1974-76. These much larger polynyas averaged $250 \times 10^3 \text{ km}^2$ across three consecutive winters (Cheon & Gordon, 2019).

The mechanism by which such polynyas form has been a focus of much of the research on Weddell Sea polynyas. The key principle is that a destabilisation must occur in order for the warm waters from depth to reach the surface in order to cool and set up convective overturning. There are many ways in which this destabilisation can occur, ranging from shallowing of the pycnocline (e.g. from doming isopycnals), decreasing the ratio of heat to salt within the pycnocline, to cooling of the atmosphere and weakening of the pycnocline (Martinson, 1991). These factors are largely controlled by regional scale processes such as the wind stress field, regional climate and thermohaline circulation (Martinson, 1991). Gordon *et al.* (2007) link the 1970s Weddell Polynya to a reduction in pycnocline stability caused by a prolonged negative phase of the Southern Annular Mode (SAM). The associated cold and dry atmospheric conditions acting to increase surface salinity and destabilise the stratification.

Cheon and Gordon (2019) explore the origin of the Maud Rise Polynya in 2017 and why it did not follow in the footsteps of the Weddell Polynya of the

1970s. They conclude that an increase in meso-scale Weddell Deep Water (WDW) eddies in the vicinity of Maud Rise led to the Maud Rise Polynya. This enhanced eddy activity was a result of the strengthened Weddell Gyre, linked to the positive SAM index and intensification and poleward shift of the Southern Hemisphere Westerly Winds. However, they also suggest that the positive SAM index (alongside a potential lack of heat at depth) may have prevented the development of the Maud Rise Polynya into a Weddell Sea Polynya in 2018 as the surface freshening (associated with a positive SAM) had strengthened the pycnocline.

Although polynyas are often described by their ice free area at the surface it is their sub surface signature and ability to alter the characteristics of large volumes of water that is of importance for larger scale ocean circulation. Using observational Salinity-Temperature-Depth (STD) and Conductivity-Temperature-Depth (CTD) profiles from cruises in the austral summers of 1973 (pre-polynya) and 1977 and 1978 (post-polynya) the impact of the polynya on the deep waters of the Weddell Sea can be evaluated. Gordon (1982) shows that the WDW in the region of the polynya cooled by 0.2°C (averaged from 200 m to 2700 m; 0.4°C of cooling at max) and freshened by 0.02 ‰ (0.03 ‰ at max). These data suggest that the amount of surface water transformed to deep water between 1974-76 was 1.6-3.2 Sv. Observations from 1977 show a cold, fresh homogeneous feature extending to 3000 m deep in the area close to the polynya two months after it had been present, suggesting that the convective overturning of the polynya was mixing water down to at least 3000 m (Gordon, 1982).

The fate of this large mass of water is difficult to trace in observations due to their sparsity and because the identity of the mass of water changes over

time as it mixes with its surroundings. This mixing obfuscates the original identity of the water. Using a GFDL coupled climate model, Zanowski & Hallberg (2017) looked at how signals from the Weddell Polynya propagate into other ocean basins via large-scale waves and advection. They found that waters modified within the polynya are transported (in deep abyssal waters) into the three major ocean basins (Atlantic, Pacific and Indian). Waters are advected northward most rapidly within deep western boundary currents. The advective tracer reaches the equatorial Indian and Pacific in ~ 50 years and the equatorial Atlantic in ~ 100 years.

It is these advective tracer signals that are closely comparable to measured transient tracer signals in the observations. This study aims to evaluate whether it is feasible for water modified within a Weddell Polynya to be responsible for certain levels of CFCs/SF₆ within UCDW and AAIW at 24°S in the South Atlantic at a timescale of 40-50 years.

5.2 Polynya Specific Methods

The polynya experiment described below uses the ECCOv4r2 set-up of MITgcm (see Section 3.3 for model details). The polynya is forced by modifying the vertical diffusivity fields for temperature and salinity within the polynya for the full water column depth (as in Naughten *et al.*, 2019). At the centre of the prescribed polynya the vertical diffusivity is set to 15 m²s⁻¹. In order to avoid instabilities caused by a single large step change, the vertical diffusivities of an inner ring surrounding the polynya are set to 7 m² s⁻¹ and those of an outer ring set to 2 m² s⁻¹. The average background level of vertical diffusivity within this column of water is 0.08 m² s⁻¹ (calculated over the first 5 months of Year 1; average monthly maximum of 4.11 m² s⁻¹). This high level of vertical diffusivity

mixes the water column completely when the forcing is applied. This mimics the overturning circulation which occurs in a polynya, due to brine rejection and surface cooling.

The polynya is forced in the same location from the start of June to the end of November each year for the first three years of the model run (see Figure 5.1). The polynya forcing is centred at 10°E 67°S in order to replicate the location of the Weddell Polynya observed in satellite data in the 1970s (Carsey, 1980). In this experiment the polynya is forced in the same location in every year of the forcing. In reality the polynya observed in the 1970s was a transient feature, which was observed to drift westward year on year. The most eastward signature observed are areas of weak ice in 1973, observed around 15°E, the most westward signal is the polynya in 1976 and weak ice in 1977, at around 20 - 25°W. In this experiment the polynya forcing is centred at 10°E as this lies between the most eastward signal of the polynya and Maud Rise (65°S, 5°E).

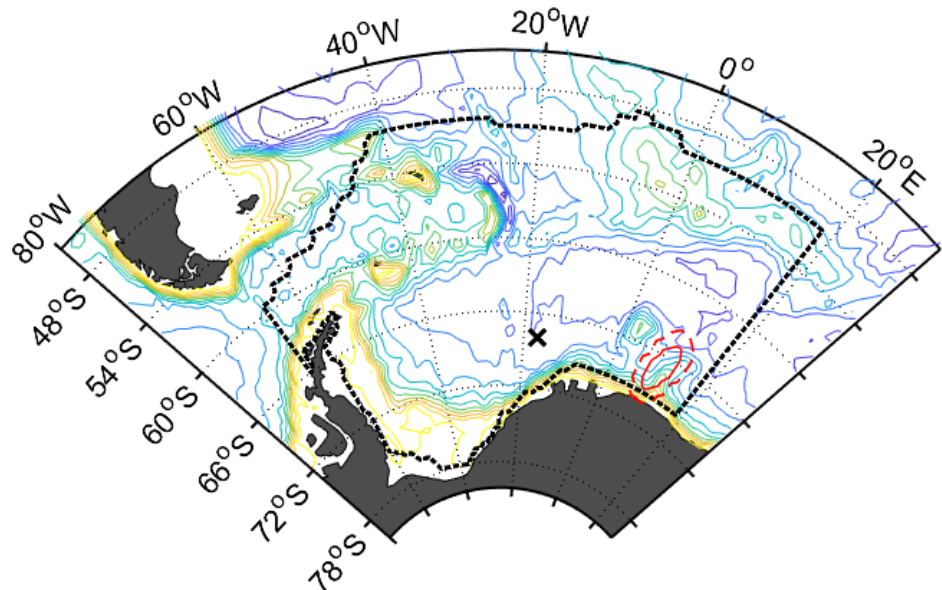


Figure 5.1 – A map of the Atlantic sector of the Southern Ocean showing the location of the polynya forcing and tracer addition. Solid red line indicates the centre of the polynya where forcing was strongest and tracer was restored to 1. Dashed red line indicates the outer limits of the polynya forcing (the space between solid and dashed line encompasses the ‘inner’ and ‘outer’ ring referred to in the text). Black dashed line indicates the boundary of input of the WedSurTr. Black ‘x’ marks the location of the additional polynyas at 17°W, 68°S. Real world bathymetry at 500 m intervals is shown by coloured contours.

The centre of the polynya (where forcing is $15 \text{ m}^2 \text{ s}^{-1}$) covers an area of $9.8 \times 10^4 \text{ km}^2$. When the areas of the inner and outer ring surrounding the polynya are also included, the total area covered by the modified forcing extends to $2.6 \times 10^5 \text{ km}^2$. This compares well to observations of the Weddell Polynya in the 1970s, which show the Weddell Polynya to cover a maximum area of $2-3 \times 10^5 \text{ km}^2$ in the winters of 1974, 1975 and 1976 (Carsey, 1980).

In order to trace the waters originating from this intensely mixed water column, three passive tracers are added. One at the surface where the polynya is forced (Polynya Surface Tracer; PolSurTr), one throughout the water column contained within the area of forcing (Polynya Column Tracer; PolColTr) and the third over the entire surface of the region south of the PF in the Atlantic sector (Weddell Surface Tracer; WedSurTr).

PolSurTr is initially set to 1 at the surface in the centre of the polynya. Below the surface the initial tracer concentration decays according to a trigonometric function over the top six model levels (5, 15, 25, 35, 45, 55 m) e.g. conc. at 15 m = conc. at 5 m $\cdot \cos(\pi/10)$, conc. at 25 m = conc. at 5 m $\cdot \cos(2\pi/10)$, etc.. The tracer is restored towards 1 in the surface model layer at the centre of the polynya and towards 0 everywhere else in that surface layer, every six time steps (hours). There is no restoration within the interior.

PolColTr is initially set to 1 for the entire water column in the polynya centre area. To prevent abrupt changes at the edge of the polynya, all depths for the inner ring are initially set to a tracer concentration of 0.866 and all depths for the outer ring are set to 0.500. The central column of the polynya is restored towards 1 every six time steps.

The third tracer, WedSurTr, is added to the surface of the Weddell Sea (see Figure 5.1) in an identical manner to that of tracer ‘Atlantic - S of PF’ used

in the Global Ocean Passive Tracer Experiment referred to in Chapters 4 and 6.

The tracer is initially set to a concentration of 1 at the surface and decays with depth in the same manner as PolSurTr. Like PolSurTr, WedSurTr is restored to 1 at the surface where it is initially added, and restored to 0 at the surface in areas outside of this region, there is no restoration within the interior. All tracers are added continuously in the same locations for the entirety of the model run regardless of whether the polynya is being forced or not.

The experiment is run for a total of 80 years, in order to surpass the 40 - 50 year timescales indicated by the MEM results as possible signals of the Weddell Polynya water at 24°S. Two 80 year runs are carried out, one with the forced polynya (referred to as FP) and the other a control run (referred to as CTRL).

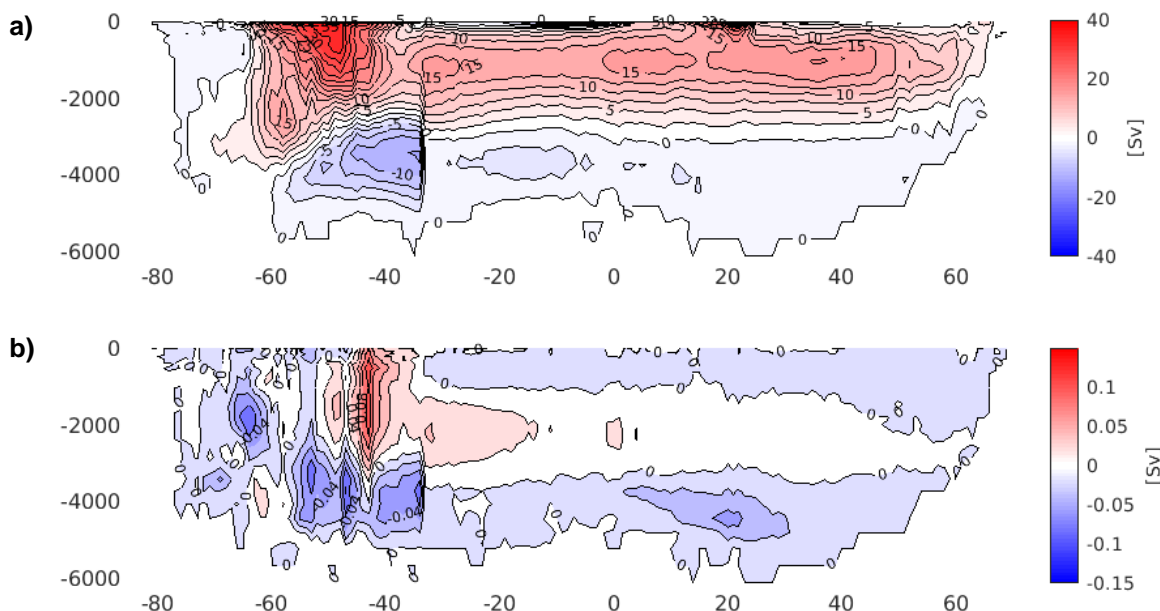


Figure 5.2 – Residual overturning circulation, zonally integrated over the Atlantic Sector north of 33°S, and over all longitudes south of 33°S. (a) Shows time mean circulation for years 70-80 (FP), contours at 2.5 Sv intervals. (b) Shows anomaly (FP - CTRL) for time mean for years 70-80, contours at 0.02 Sv intervals.

The impact of using repeat forcings on the stability of the ECCO model is evaluated fully in Section 3.3.5. Here, Figure 5.2a shows the mean meridional circulation for the Atlantic and Southern Ocean for the final 10 years of FP. The

recognisable structure of the clockwise NADW cell overlying an anticlockwise AABW cell is seen in the Atlantic representing the northward transport of surface waters and AABW (at depth) and the sinking and southward transport of NADW. In the Southern Ocean a strong upper meridional overturning cell is observed, with upwelling at around 60°S. This familiar circulation and minimal anomalies when compared to CTRL (Figure 5.2b) suggest the polynya forcing does not destabilise the model and only perturbs the circulation a minimal amount from the CTRL.

For the purpose of this analysis, tracer anomalies ($FP - CTRL$) are often used. For PolSurTr the anomaly is very similar to the standard PolSurTr field as the tracer spreads very little in CTRL. For PolColTr and WedSurTr, use of the anomaly allows for the PW to be traced but removes any tracer that would be spread under the CTRL circulation.

The following sections present and discuss the results of the analysis.

5.3 Polynya Development and Spread within the Weddell Sea

Water originating in the polynya can be studied both by looking at the passive tracers and perturbations of temperature and salinity. Here we look at these tracers along with the density structure of the water column and mixing parameters to explore how the polynya develops over the first years of the experiment, and how the various signals propagate through the Weddell Sea. We will look at the development of the polynya in Year 1 (Section 5.3.1), the presentation of the polynya in sea ice (Section 5.3.2), pathways of the polynya water within the Weddell Sea (Section 5.3.3), the volume of water generated by

the polynya (Section 5.3.4), and the cause of an observed additional polynya (Section 5.3.5).

The forced polynya is observed during winter every year for the first three years. The maximum spatial extent of the polynya grows each year, with maximum extent in October of Year 3. In Years 3 and 4, an additional polynya is observed to the west of the original polynya, despite no polynya being forced in the fourth year.

5.3.1 Polynya Development in Year 1

In the May prior to the start of the polynya forcing, the water column at 10°E 67°S is stably stratified. A cold and relatively fresh (-1.2°C, salinity 34.3) 100 m surface layer sits on top of a relatively warm, but more saline (0.5 -1°C, salinity 34.6) layer from 150 m to 1000 m. Below this, water gradually cools with depth whilst salinity remains near constant until reaching cool waters of < -0.5°C below around 2500 m (Figure 5.3a & b). Once forcing commences in June the water column becomes fully mixed (Figure 5.3c & d). The core column of the polynya obtains a density of 1027.84 kg m⁻³, which is maintained for the duration of the forcing in the first year.

An understanding of what happens to the structure of the water column after the polynya forcing stops at the end of November is key to understanding the development of the polynya's characteristics over several consecutive years. At the end of December (Figure 5.3e & f), after a month of relaxation, the surface 100 m starts to re-stratify. This surface layer is much warmer than its surroundings (1.5°C compared to 0°C of surrounding water). December is the start of summer in the Southern Hemisphere, meaning that the cold surface waters are being warmed by the atmosphere, creating a warmer top 50 m with a

cold subsurface temperature minima at around 100 m. In the area where the polynya is forced, the surface waters are already relatively warm. It is likely that the 1.5°C water has reached this heightened temperature due to atmospheric warming of this already relatively warm surface water. Although in this experiment the polynya the following year is forced, if this heightened surface warming is replicated in the real world scenario, it could lead to weaker sea ice and an increased likelihood of a polynya in the following winter.

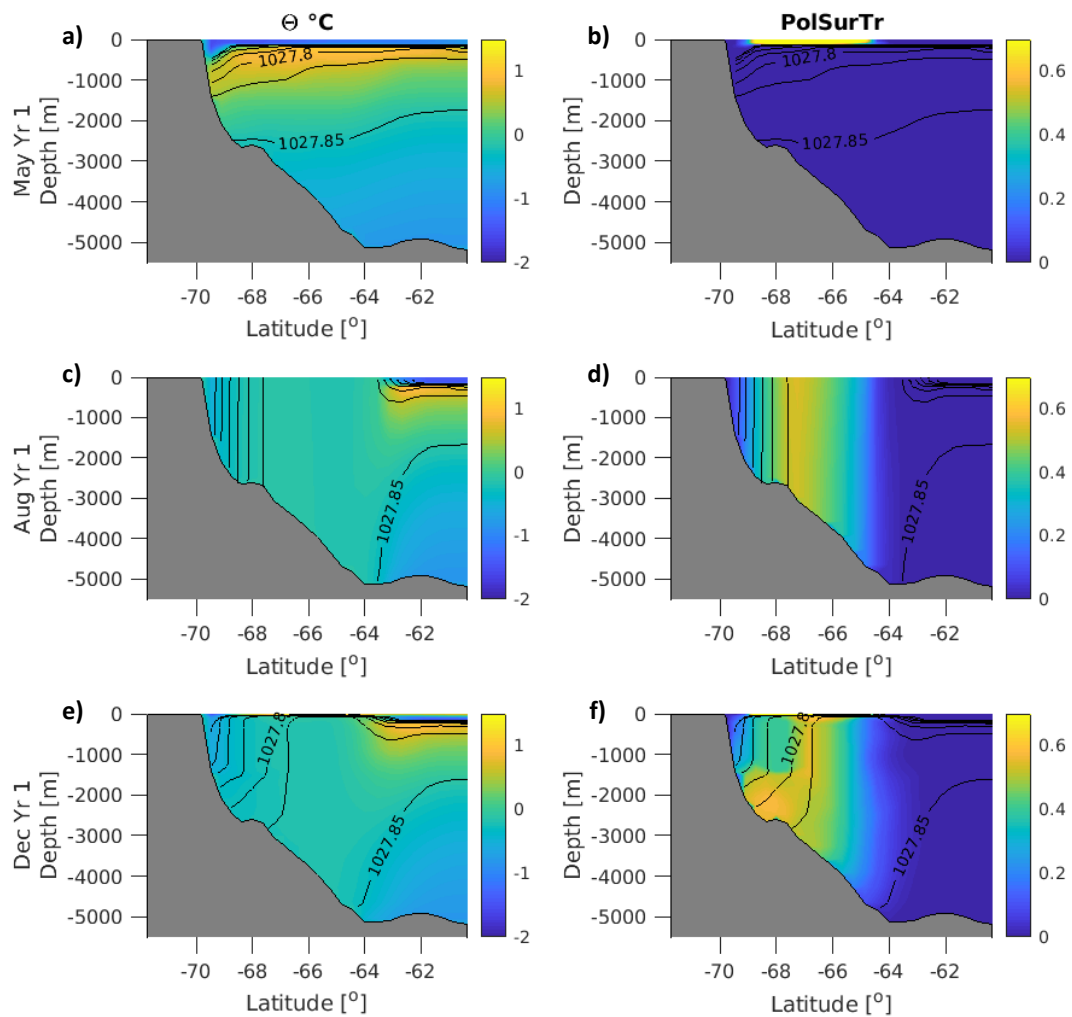


Figure 5.3 - Section plots of temperature (a,c,e; $^{\circ}\text{C}$) and PolSurTr (b,d,f; fractional concentration) through the location of polynya forcing at Yr 1 May (a,b), Yr 1 Aug (c,d), Yr 1 Dec (e,f). Potential density contours are shown from 1027.7 -1027.9 at intervals of 0.025 kg m^{-3} .

Below the newly stratified surface layer a well-mixed column of water remains. As the year progresses this column slowly starts to re-stratify. However, by the May preceding the start of the second period of forcing, the

water column is still colder than its surroundings from 150 - 2000 m and warmer than its surroundings for water below 2000 m.

5.3.2 Signatures of Polynyas in Sea Ice (Years 1-5)

In the real environment the characteristic feature of a polynya is the area of open water sustained by the constant supply of warmer water from depth. In the experiment, the polynya is artificially created by enforcing strong vertical mixing within the water column, as opposed to being sustained by the densification of recently surfaced water due to brine rejection and air-sea cooling. This mimics the convective circulation observed in polynyas and other forms of open ocean convection (Marshall & Schott, 1999). Despite the polynya not being maintained by ice-free areas, signatures of the artificial polynya are clearly identifiable in the model sea ice fractional coverage.

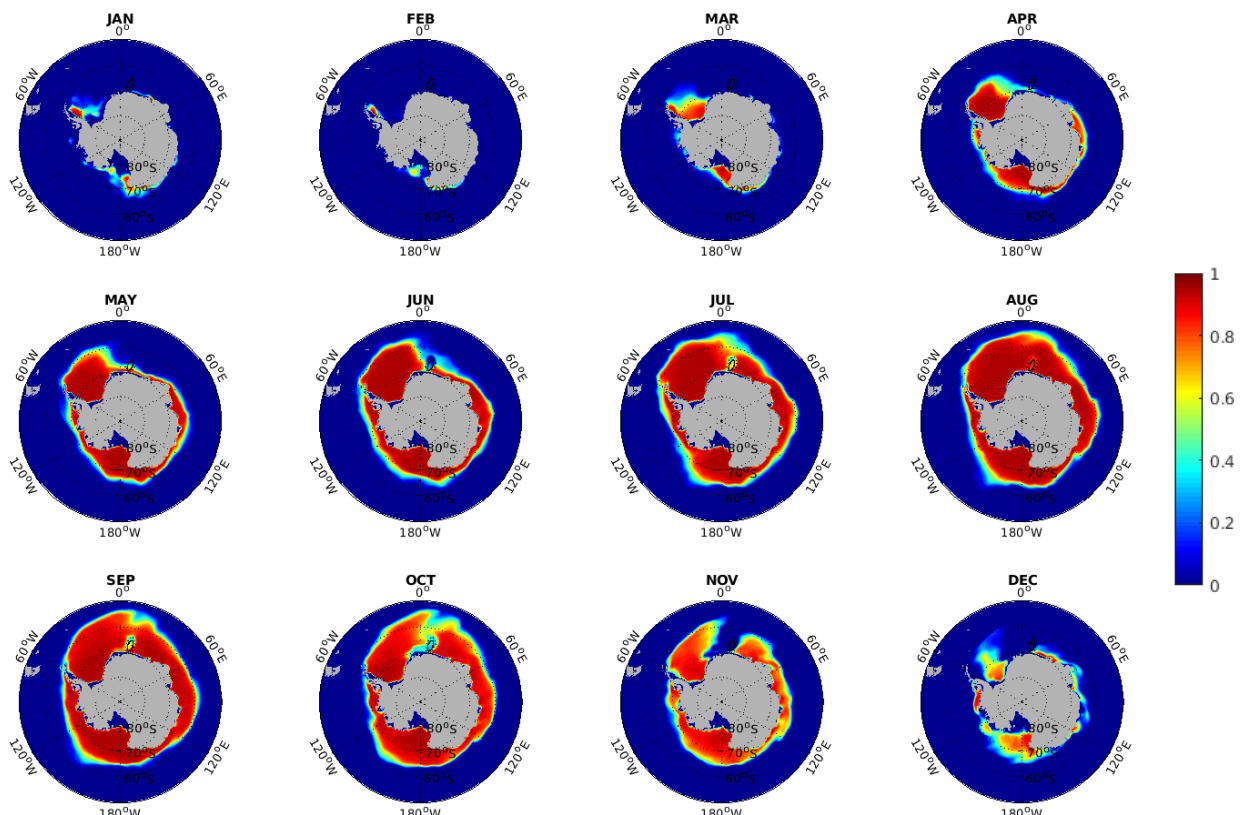


Figure 5.4 – Monthly sea-ice concentration for Year 1 of FP experiment. Black ring marks location of polynya forcing.

In June of the first year (when forcing begins) the area of forcing is within an area of marginal sea-ice (50% coverage) but a reduction in sea ice coverage is still seen, with sea-ice concentration dropping to < 20% in the area of forcing (Figure 5.4). Through July, August and September the surrounding area is covered by near 100% ice cover, but the polynya can still be identified as an area of reduced sea-ice with concentrations ranging between 50 - 75%. By October the area of lower sea-ice concentration (now 30 to 50%) has extended beyond the original area of forcing, and spread in a comma shape westward along the Antarctic coastline. This feature then transforms into a large embayment in November prior to the sea ice receding from the area in December.

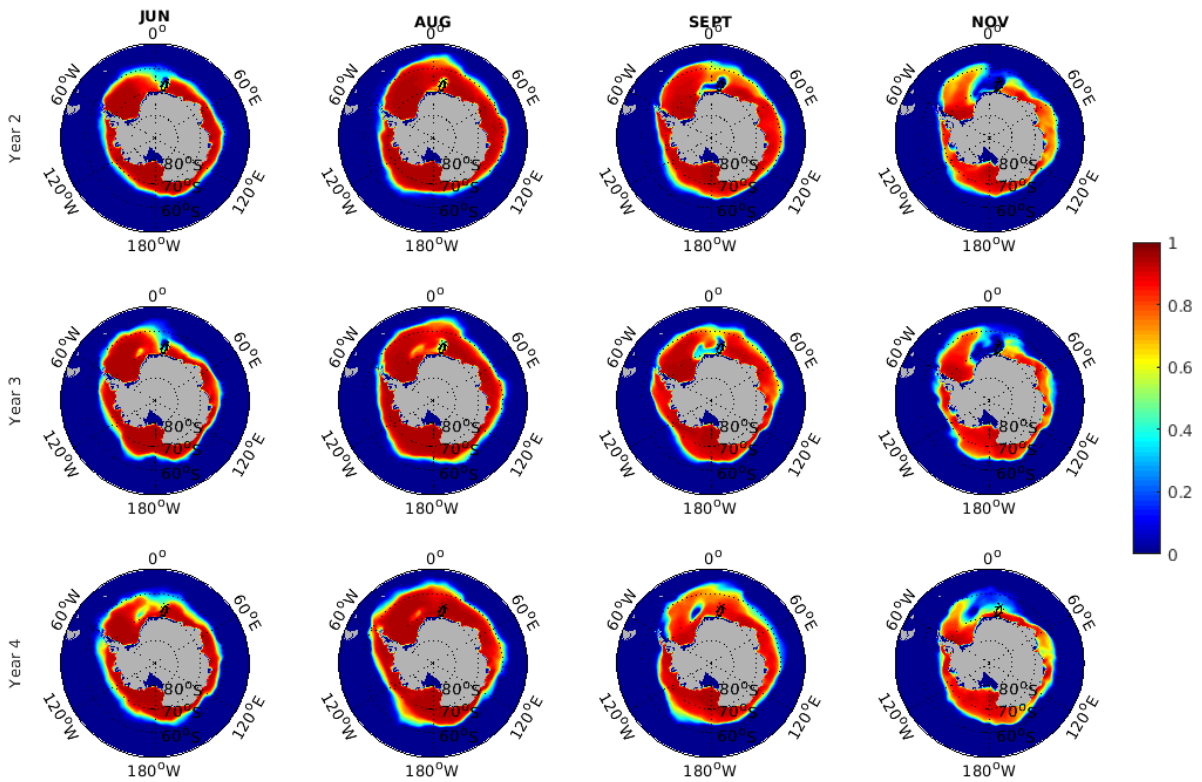


Figure 5.5 – Monthly sea-ice concentrations for June, August, September and November of years 2, 3 & 4. Black ring marks location of polynya forcing.

Sea-ice concentration can provide a good overview of the development of the polynya in each of the years following the initial forcing. In the second year

the patterns in sea ice are largely the same as those in the first year (Figure 5.5). The polynya maintains an area of open water when the marginal sea ice zone surrounds the area of forcing, but in July and August as the sea ice continues to grow in extent, the area is only observed as an area of reduced sea-ice concentration, with a coverage of around 50%. A difference between the two years is that as the area of reduced sea-ice coverage begins to form a comma shape in late winter, stretching west along the Antarctic coast, an area of open water forms. In Year 1 this comma shape was only observed as an area of reduced sea-ice concentration and did not display as an area of open water. The cause of this difference is apparent when the temperatures of surface waters are compared between EXP1 and CTRL for August of Year 2. Surface waters are 1 - 1.5°C warmer in EXP1 in the area in which the area of open water extends into in September of Year 2. This suggests that polynya induced warming of surface waters enables the polynya to grow bigger year on year.

In the third year an additional feature is seen. In June after sea ice has covered most of the Weddell Sea, an area of reduced levels of sea-ice (60% coverage, compared to surrounding > 80%) is seen centred at 17°W 68°S, this remains an area of lower sea-ice coverage through July and August before expanding to the north, opening up further, and merging with the open water at the site of the forced polynya in September and October of Year 3. This area of open water and reduced sea-ice concentration then forms part of the large embayment as sea ice extent starts to reduce in November.

In the fourth year of the experiment no forcing is applied, but the impact of the forcing in the previous years is still evidenced in the sea ice coverage. In the fourth year this same feature of reduced sea ice coverage at 17°W 68°S is observed from May through September. In October this feature grows and

becomes an area of open ocean (defined as < 15% sea ice concentration) covering an area of 8.6×10^4 km². The cause of this additional polynya is explored further in Section 5.3.5.

5.3.3 Pathways of Polynya Water

Passive tracer concentrations can be used to follow the route taken by waters that gained their characteristics through mixing within the polynya (known henceforth as Polynya Water, PW). Here we initially look at the distribution of PolSurTr. As PolSurTr only entered the deep waters when the polynya forcing was imposed, it is more useful for tracing PW than the PolColTr, which also marked water in the location of the forcing between polynya events.

Zonally, the surface tracer showed the PW to spread slowly at all depths at the latitude of the forcing (Figure 5.6b), but to spread more quickly westward as a mid-depth plume of water between 1500 m and 3500 m (densities 1027.84 - 1027.86 kg m⁻³). In the meridional plane at the longitude of the forcing (Figure 5.6a), PW is quickly drawn southward towards the coastline with the tracer indicating a high concentration of PW at densities of 1027.76 - 1027.83 kg m⁻³ (1000 m to 2500 m). This water is then transported westward close to the coast in the Antarctic Coastal Current (Figure 5.6 c & d). The coastal current is surface intensified with the strongest velocities of ~ 12 cm s⁻¹ in the upper 500 m. However, the current does extend down to 2500 m at velocities of ~ 4 cm s⁻¹. As the PW is transported westward in the current, it shallows to occupy depths of 500 m to 2000 m in high concentration (> 30%) at 5°W by May of Year 2. This plume of water continues to follow the coastline, with the percentage contribution of PW decreasing over time as the water mixes with surrounding water masses.

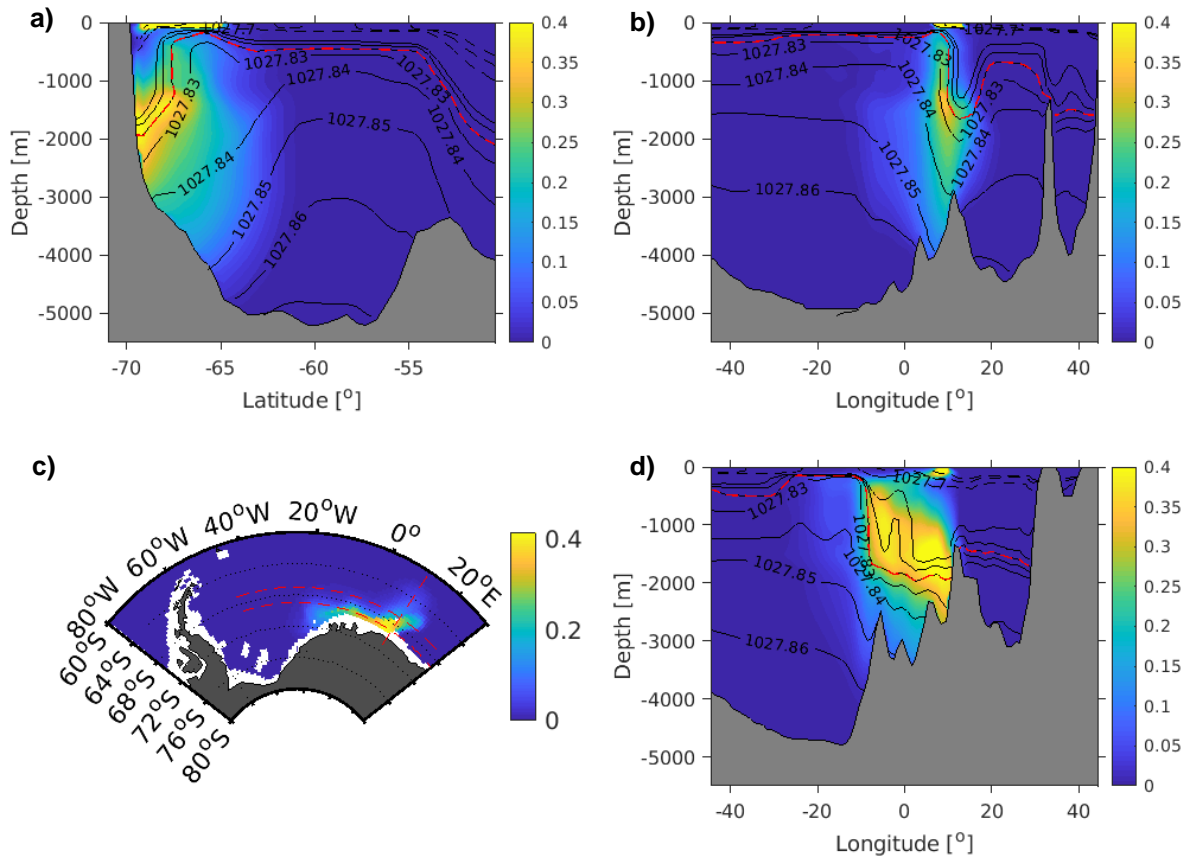


Figure 5.6 – Spread of Polynya Water within the Weddell Sea at 1.4 years. (a) Meridional section at 10.5°E of PolSurTr anomaly. (b) Zonal section of PolSurTr anomaly at 67°S (c) PolSurTr anomaly on the 1027.82 kg m^{-3} density surface. (d) Zonal section of PolSurTr anomaly at 69°S. Red dashed line in c indicates position of section plots a,b and d. Red dashed line in a,b and d highlights the 1027.82 kg m^{-3} density surface shown in c.

Three pulses of water are created by the three forced polynyas.

However, as these pulses of PW mix with the surrounding water within the Weddell Gyre the year from which the tracer water originated from becomes less clear. By 5.5 years contributions of 50-60% PW are observed over a large part of the western Weddell Sea (Figure 5.7). The highest concentrations appear to be centred at 1027.85 kg m^{-3} (2000 m) but waters containing a > 40% contribution are observed in the western part of the basin at depths ranging from 300 m to 3000 m. As the PW escapes the Weddell Basin through the South Scotia Ridge, it appears to enter into waters with densities > 1027.86 kg m^{-3} (Figure 5.7b).

In this experiment most of the PW leaves the area of forcing via the westward Antarctic Coastal Current. This leads to a dominant westward spread

of PW. Although overall the polynya induced in ECCO is a good representation of the polynyas observed in the 1970s, the chosen position means than the southern edge of the polynya is in the immediate vicinity of the coastal current. An extension of this experiment would be to move the position of the forced polynya further north to see if water is still drawn to the coastal current to leave the area.

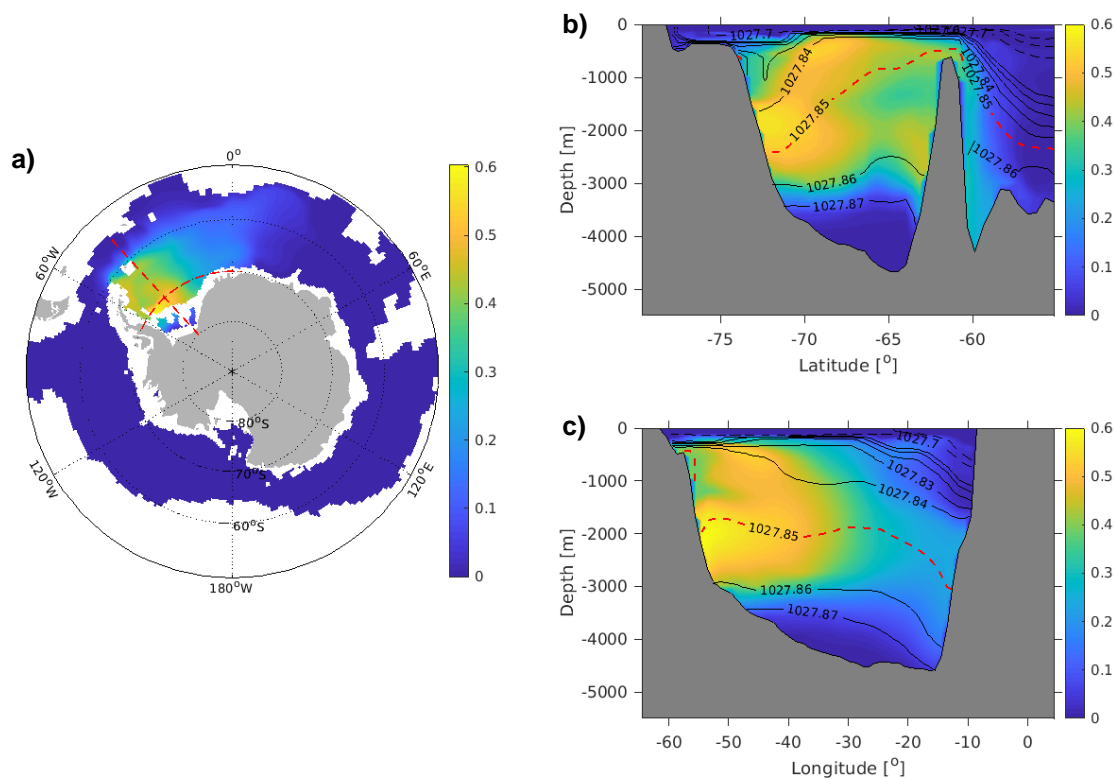


Figure 5.7 - Spread of Polynya Water within the Weddell Sea at 5.5 years. (a) WedSurTr anomaly on 1027.85 kg m⁻³ density surface. (b) Meridional section at 42.5°W of WedSurTr anomaly. (c) Zonal section of WedSurTr anomaly at 70°S. Red dashed lines in a indicate position of section plots b and c. Red dashed line in b and c highlights the 1027.85 Kg m⁻³ density surface shown in a.

5.3.4 Volume of Polynya Water

It is important to consider what information each tracer can provide, when considering the fractional contribution of PW. The two tracers that are useful to determine the contribution of PW to an area are PolSurTr, the tracer added at the surface of the polynya, and WedSurTr, the tracer added to the surface of the entire Weddell region. As noted in Section 5.2, the PolSurTr is added only in the centre of the polynya forcing. If the fully mixed water column is larger than this central ring, PolSurTr is assumed to underestimate the contribution/formation of PW. However, it is still useful to trace the pathways of the PW. An additional limitation of this tracer is that it is restored to 0 if it reaches the surface layer outside the region of forcing. This restoration is used to avoid labelling surface circulations. However, it does mean that where additional polynyas have formed in the Weddell Sea, this tracer has been removed from the water column as a consequence of being in contact with the atmosphere.

The second tracer that is useful is WedSurTr_{AN} (WedSurTr_{FP} - WedSurTr_{CTRL} = WedSurTr_{AN}). As WedSurTr covers the whole of the surface Weddell Sea it captures large amounts of deep water formation along the coastlines. Hence, the WedSurTr_{AN} is used under the assumption that the difference in tracer distribution between the CTRL and the FP run will be predominantly due to input by polynyas. For simplicity of interpretation, any change to the tracer field due to secondary processes (e.g. gyre strength change) are ignored. Unlike PolSurTr, this tracer will capture water modified in the forced polynya and water modified in the additional polynyas (at 17°W, 68°S).

Estimates of PW volume can be calculated using the concentrations of the passive tracers and the volume of the corresponding grid cells. For the above reasons, PW volume estimates based on PolSurTr concentrations are considered a lower bound and those based on the WedSurTr_{AN} are considered an upper bound. In December of Year 4, after the three forced polynyas and the two additional polynyas have occurred, total PW volume is estimated at $6.8 - 32.7 \times 10^{14} \text{ m}^3$. To put this into context, the Weddell Sea, designated here as the area between 60°S to 83°S and 61°W to 10°E has total volume of $1.6 \times 10^{16} \text{ m}^3$. The box is chosen to end at 10°E in order to only capture the polynya water that was transported west further into the Weddell Sea. The volume of PW inside this box is estimated at $6.1 - 30.9 \times 10^{14} \text{ m}^3$ which is equivalent to 3.8 – 19.0% of water within the Weddell box originating from one, or more, of the observed polynyas.

5.3.5 Additional Polynya

In years 3 and 4 a polynya forms in the Weddell Sea away from the area of forcing. These two instances of a polynya at 17°W 68°S (see Figures 5.1 & 5.5) are not present in the CTRL and therefore must be related to the imposed forcing and subsequent changes in the water column.

PW from the original polynya is observed to spread northward from the concentrated plume of PW along the coastline, into the area where the additional polynya formed. As the PW is a more homogenous cool temperature, in comparison to the CTRL, the surface 100 - 150 m of the water column is warmer, mid-depths of 200 - 1600 m are cooler and the deeper waters are largely the same temperature. This has the effect of reducing the stratification in the water column at 17°W 68°S (Figure 5.8a & b). This reduced stratification

results in a pre-conditioning of the water column, similar to that seen in open ocean convection (Marshall and Schott, 1999), increasing the likelihood of a polynya forming.

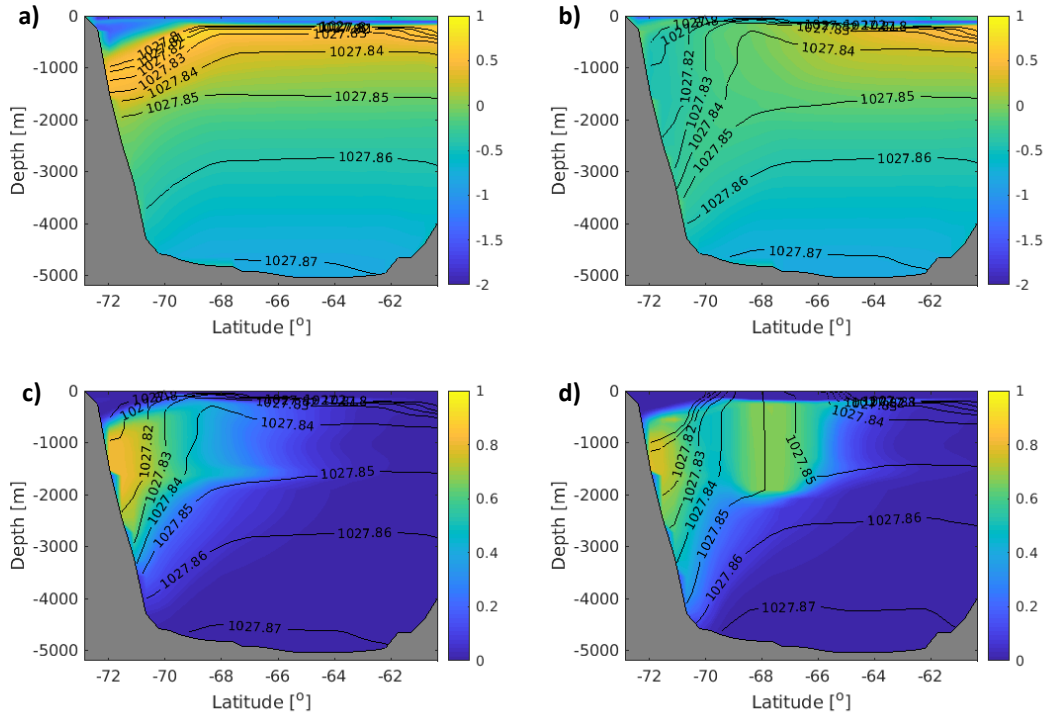


Figure 5.8 – Section plots at location of additional polynya (17°W). Temperature prior to the formation of the additional polynya in CTRL (a) and in FP (b) in April Year 3 (autumn). WedSurTr anomaly in April Year 3 (c) and after the polynya has formed in August Year 3 (d, winter). Line contours indicate densities (ρ_0) ranging from $1027.82 - 1027.88 \text{ kg m}^{-3}$.

The additional polynya enhances the amount of WedSurTr in the water column by drawing it down from the surface during winter heat loss (Figure 5.8c & d). The mixing reaches down to a maximum depth of 2000 m. By the following September, the waters created in this additional polynya have merged with the coastal plume of PW at depths spanning 500 m to 2500 m. After this first additional polynya the water column in that area remained largely homogeneous, at temperatures close to 0°C , and at a density of $1027.85 \text{ kg m}^{-3}$. Although the concentrations of WedSurTr_{AN} initially decline after the first additional polynya ceases, they remain at 50 - 60% throughout the summer, indicating the maintenance of a strong influence of PW in the area.

In Year 4 the additional polynya again enhances the amount of WedSurTr in the water column, with the tracer being mixed down to over 2000 m. In the autumn of the following year (Year 5) PW is still present at this location but concentrations drop to around 30%. This reduction is most likely attributable to the lower concentration of PW in the coastal current, as the coastal current is no longer being fed by the forced polynya upstream to the east. This reduced influence is likely why a third additional polynya did not form the following year, as the waters in the coastal current return to their previously more stratified state.

The presence of these additional polynyas in the experiment is interesting as it demonstrates how a polynya in one location in a previous year can incite another polynya somewhere else. The Weddell Polynya in the 1970s, although referred to as a single feature did reappear further westward each year (Carsey, 1980) in a similar manner to the additional polynya observed in the model results . As mentioned previously in the PW volume estimations, these additional polynyas may have led to a larger volume of PW being created than initially planned.

5.5 Long-term Impact of the Polynya

The previous section focussed on the production of PW and movement of PW within the Weddell Gyre. Here we look at the longer term, larger scale impacts that the polynyas have on the global ocean and evaluate whether signals of the PW can be detected in AAIW at 24°S in the South Atlantic.

5.5.1 Changes to Southern Ocean Circulation

Transport through Drake Passage is a common metric for evaluating the strength of the ACC, with higher transport through Drake Passage indicating a strengthened ACC. In the FP experiment, Drake Passage transport is always elevated with respect to CTRL (Figure 5.9a). As an anomaly time series (Figure 5.9b), we see that after three years Drake Passage transport increases steadily, reaching a peak anomaly of 1.6 Sv after seven years. This anomaly then decreases steadily, albeit slowly, decreasing to an anomaly of 0.5 Sv by Year 36. In the final year of the experiment (Year 80) an anomaly of 0.1 Sv is still consistently present in comparison to the CTRL.

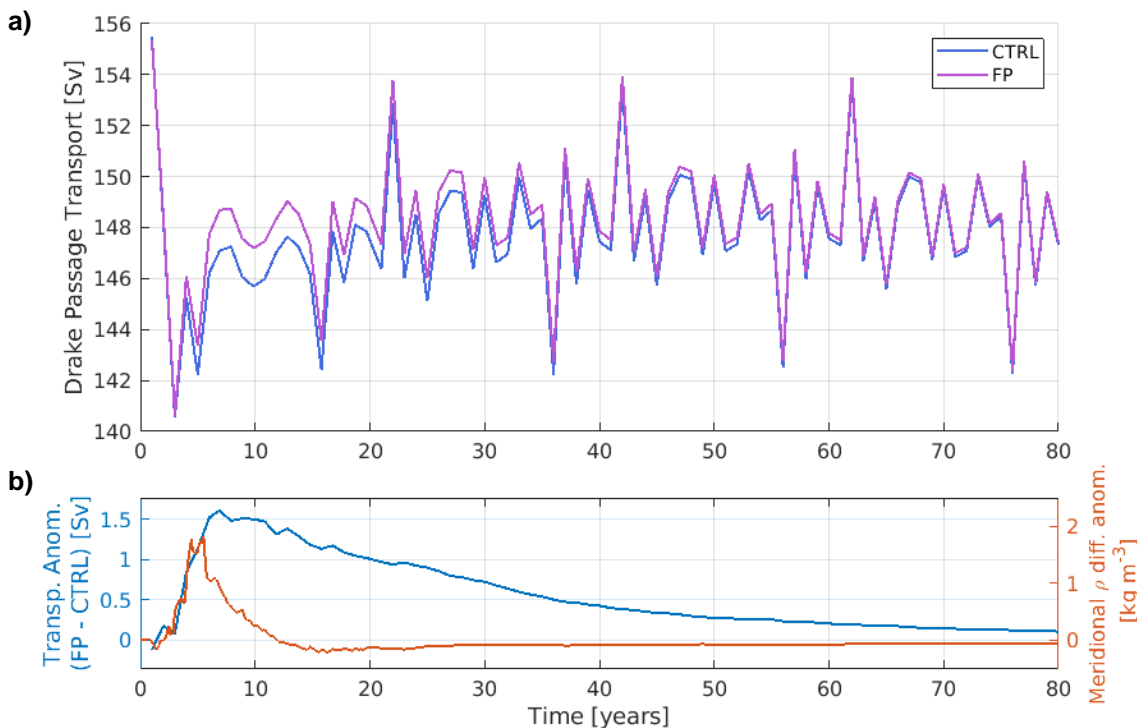


Figure 5.9 – Annual Drake Passage transport in CTRL and FP (top). Anomaly of Drake Passage transport ($\text{FP} - \text{CTRL}$) (b,blue). Anomaly ($\text{FP} - \text{CTRL}$) of the vertically integrated meridional density difference (b,orange) calculated between 61°S and 40°S for a zonal average density of the western Weddell region longitudes (57°W to 20°W).

In order to identify the cause of this change, the zonal average meridional density difference over the western Weddell Gyre is considered (see

Figure 5.10b). The vertical integral of this is related to zonal transport via thermal wind. The average value of this between 61°S and 40°S is shown in Figure 5.9b. This shows the density difference in the FP experiment to deviate considerably from the CTRL within the first eight years. The peak of this deviation is during June of Year 5, 1.4 years prior to the peak in Drake Passage transport.

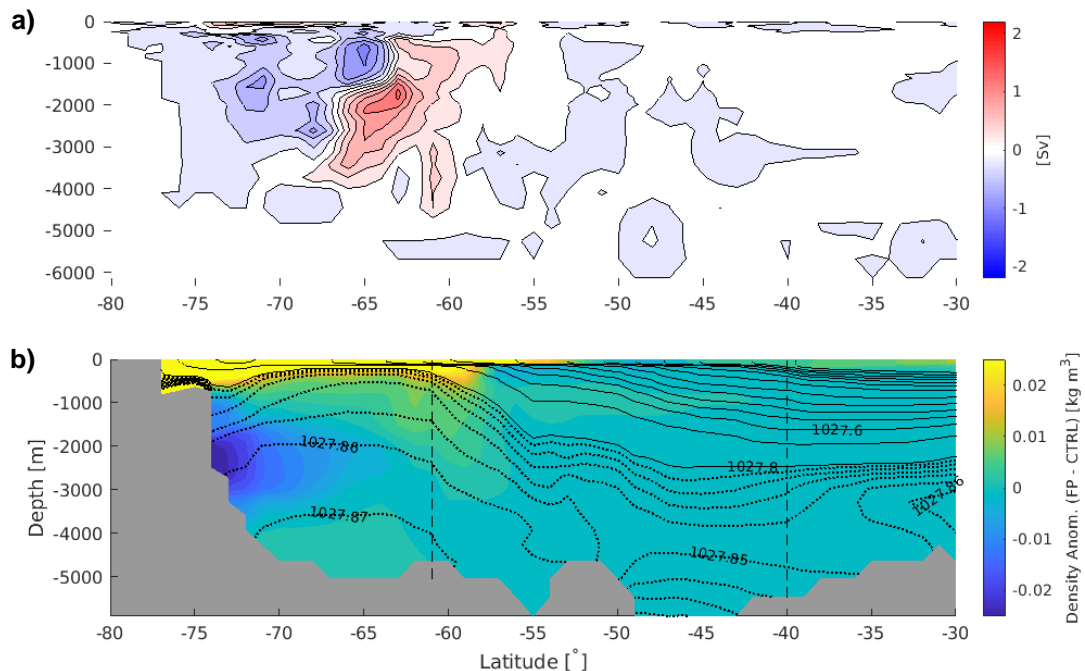


Figure 5.10 – (a) Anomaly (FP – CTRL) of zonal mean (all basins) bolus meridional overturning for Years 5 & 6. (b) Zonal mean of density anomaly (FP – CTRL) for western Weddell region longitudes (57°W to 20°W) at peak meridional p_0 difference (Yr 5 June). Vertical dotted lines indicate locations between which the meridional density difference (from Figure 5.9) was calculated. Line contours indicate densities (p_0) ranging from $1026.5 - 1027.8 \text{ kg m}^{-3}$ (solid) and $1027.8 - 1027.9 \text{ kg m}^{-3}$ (dotted).

The ACC is driven by barotropic and baroclinic processes. The main barotropic driver is the westerly winds interacting with the surface waters and driving eastward flow. In ECCO, atmospheric forcing is prescribed and so the presence of the Weddell Sea Polynya in the experiment can have no effect on surface wind forcing. We can therefore assume that the change in ACC transport is driven by the baroclinic process of the increased meridional density difference observed across the ACC. Although the model is not eddy resolving,

it does use the GM-Redi eddy parameterisation (Redi, 1982; Gent and McWilliams, 1990; Gent *et al.*, 1995), and so where isopycnals steepen across the ACC, eddy bolus transport would be expected to increase. This increase is not detected in the bolus overturning for the Southern Ocean (Figure 5.10a). However, the Southern Ocean meridional overturning is representative of a zonally averaged transport, and so changes elsewhere in the Southern Ocean could mask the strengthening in (negative) eddy bolus transport in the Atlantic sector.

Although some lag is expected as the system responds to change, a lag of 1.5 years between the peak meridional density difference and the peak transport is still longer than expected but has no clear explanation. Transport is also calculated for a meridional section between Antarctica and South Africa but the same 1.5 year lag is also observed here, suggesting the lag is not to do with the positioning of the density difference change downstream of Drake Passage. A similar lag (1.8 years) is also present when Drake Passage transport is compared to a circumpolar zonal integral of meridional density difference.

An anomaly of 1.6 Sv in Drake Passage transport would not be detectable in the observational record as this anomaly falls within the uncertainty of measurement of the transport at Drake Passage (Cunningham *et al.*, 2003). This result does however show that the Weddell Polynya in the 1970s has a large enough impact on the system that it can impact ACC transport and, though undetectable, we could still now be seeing a small effect on ACC transport from an event in the 1970s. This idea of a multidecadal timescale of adjustment is not unrealistic, as Allison *et al.* (2011) show multidecadal-centennial timescale of adjustment of the global pycnocline and baroclinic ACC to an abrupt change in Southern Ocean wind forcing.

5.5.2 Where does Polynya Water End Up?

In order to establish how PW circulates through the global ocean on longer timescales we first look at the presence of PW in different density classes and then look at the distribution of tracer at key densities. After the first six months of polynya forcing the $1027.83 - 1027.84 \text{ kg m}^{-3}$ density (ρ_0) class holds the highest volume of PW (Figure 5.11). This corresponds closely to the density of the fully mixed water column when the polynya is forced and so is henceforth regarded as the input density. At the start of Year 5, after the three forced polynyas and two additional polynyas have occurred, this peak volume has increased from $3.3 \times 10^{14} \text{ m}^3$ in Jan Year 2 to $11.4 \times 10^{14} \text{ m}^3$ and has shifted into the $1027.84 - 1027.85 \text{ kg m}^{-3}$ density class. This shift to heavier density classes is the start of a long term trend.

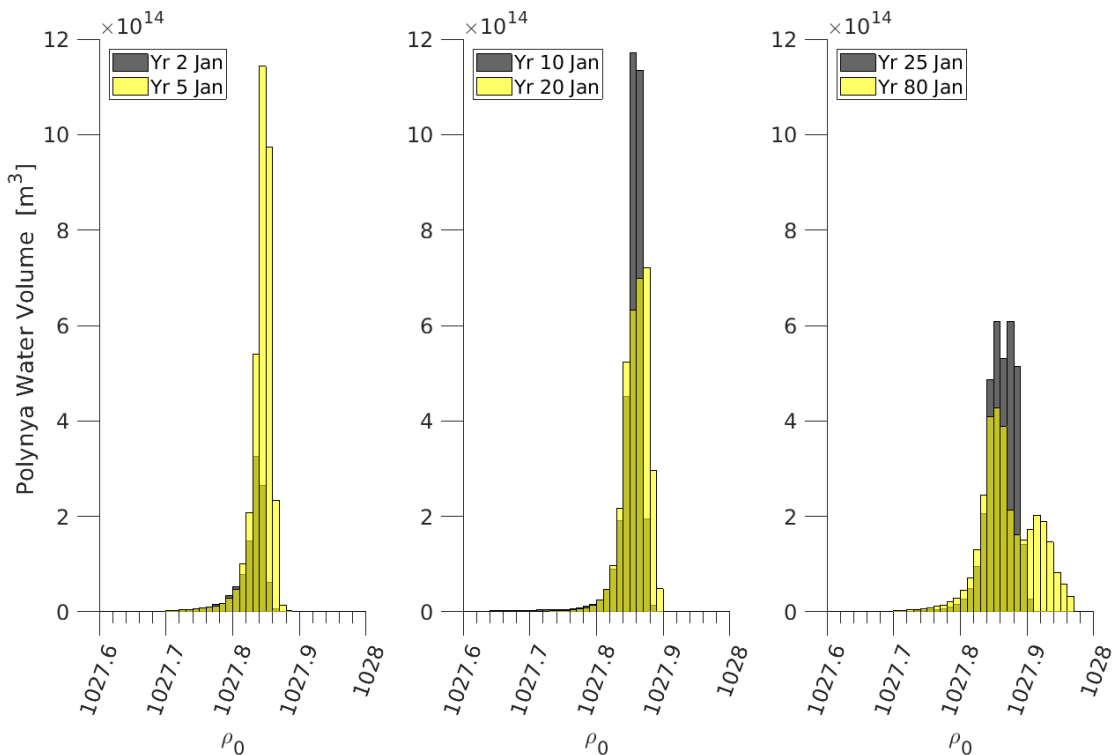


Figure 5.11 - Histogram showing volume of Polynya Water (defined by positive WedSurTr anomaly) present within different density classes (kg m^{-3}). Volume calculation based purely on positive anomalies of WedSurTr and does not account for any negative anomaly.

Generally as a water mass gets older it spreads across a larger density range as it has a greater amount of time to mix with surrounding water masses (Waugh *et al.*, 2004). Here, the PW appears to preferentially mix into more dense waters and decreases in volume in the lighter density classes (Figure 5.11). At 25 years the largest proportion of PW by volume sits within the density range of $1027.84 - 1027.89 \text{ kg m}^{-3}$. By 80 years a second peak in the volume distribution has formed at $1027.91-1027.92 \text{ kg m}^{-3}$.

Considering tracer concentrations on a density surface is a useful tool to follow the pathways of a particular tracer. Here, as the PW shifts to higher densities with time, tracer concentrations are considered at close to the density which the tracer initially entered the water column ($1027.85 \text{ kg m}^{-3}$) and at the higher density at which the volume peak is observed at 80 Years ($1027.92 \text{ kg m}^{-3}$).

Following the tracer at the injection density ($1027.85 \text{ kg m}^{-3}$), at 10 years (Figure 5.12a & b) the PW has largely left the Weddell Sea and extends in a plume from the Antarctic Peninsula along to 30°E in concentrations of up to 17%. By 45 years (Figure 5.12c & d) the PW has spread into the Indian sector of the Southern Ocean but not yet penetrated (except in very low concentrations) into the Pacific. In the South Atlantic some PW has moved northwards up the Atlantic Basin but has not yet reached 30°S . Concentrations of PW on this density level have dropped to a maximum of 3% as the water spreads and mixes with surrounding water of different densities. By 80 years (Figure 5.12 e & f) the geographical distribution of PW has altered very little from that observed at 45 years, but maximum concentrations have dropped slightly to 2%. As can be seen in Figure 5.12, the Atlantic is the only major ocean basin that contains water with a density of $1027.85 \text{ kg m}^{-3}$. This means in

order for PW to spread into the Indian and Pacific oceans it must mix or be transformed into lighter density classes.

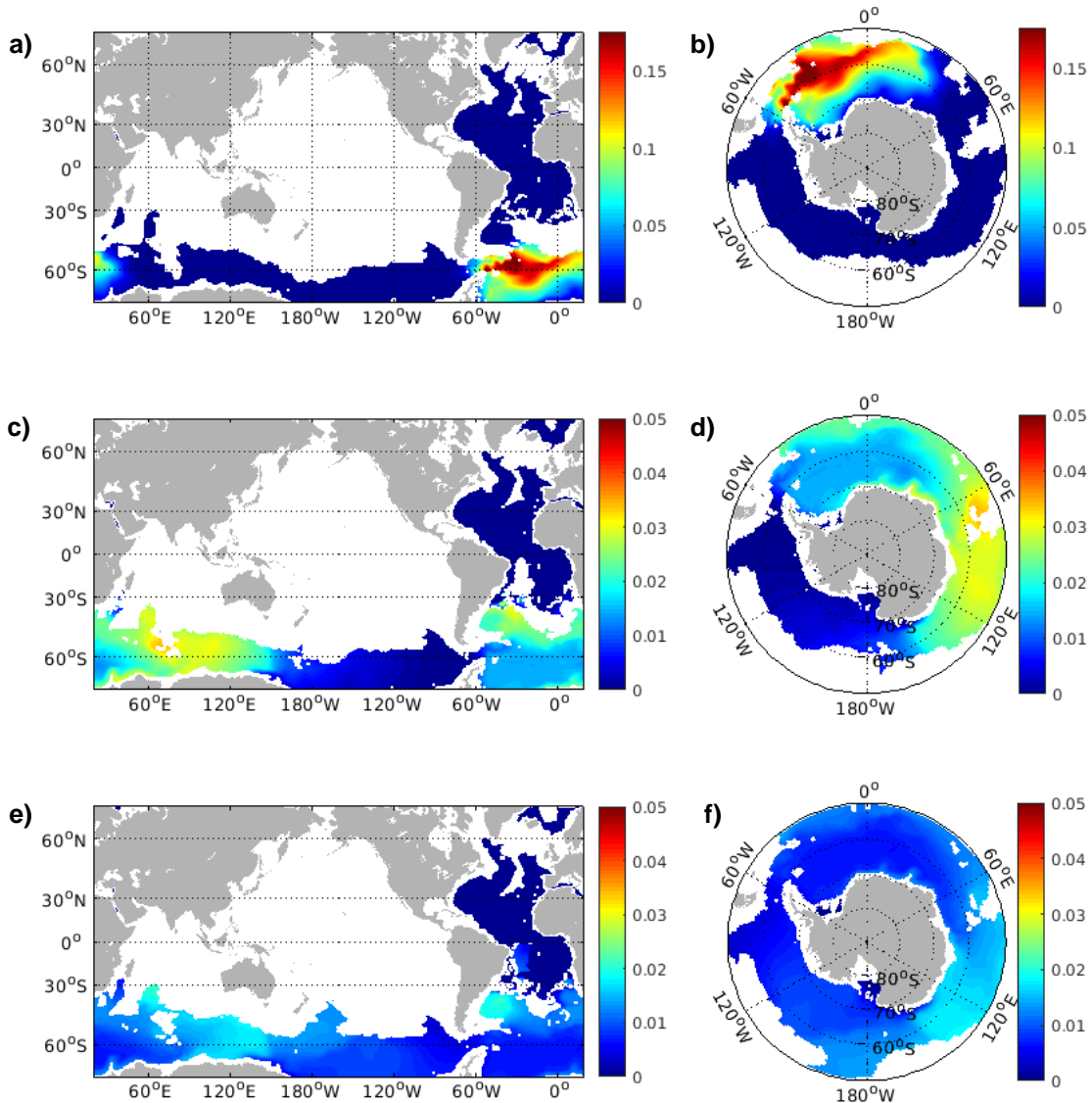


Figure 5.12 – Surface plots of WedSurTr anomaly on the density surface $1027.85 \text{ kg m}^{-3}$ at 10 (a & b), 45 (c & d) and 80 (e & f) years.

After a number of decades PW starts to be present at densities of $1027.92 \text{ kg m}^{-3}$. Comparing the distribution of the PW at 40 and 80 years on the density surface provides some interesting observations (Figure 5.13). With the exception of some waters in the Arctic and a small area of water in the western coastal Ross Sea and western coastal Weddell Sea, the only water with a density of $1027.92 \text{ kg m}^{-3}$ is that containing some contribution of PW. With time

the geographical extent of this dense water grows, spreading predominantly eastward but also expanding within the Weddell Sea and to the north in the Atlantic Sector of the Southern Ocean. This formation of dense water takes place in both the FP and CTRL suggesting the PW is not responsible for the formation of this dense water. This implies that the PW is entering pre-existing density classes via mixing processes and, potentially, surface buoyancy forcing.

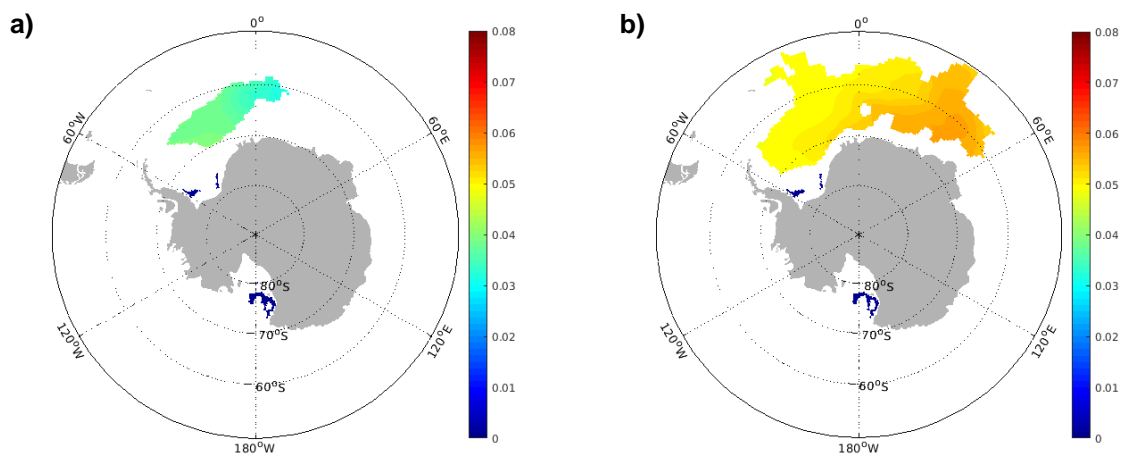


Figure 5.13 - WedSurTr anomaly on the density surface $1027.92 \text{ kg m}^{-3}$ at 40 (a) and 80 (b) years.

ECCO is constrained to observations within the first 20 years of the run. However, in these experiments forcing is repeated beyond the initial 20 years (see Section 3.3.5) and the model is no longer constrained. As this dense water starts to form after the initial 20 year period, it is likely that the formation of this denser water is an unwanted consequence of using repeat forcings and does not likely represent a real world shift to the production of denser waters in the Weddell Sea.

Not only does this water grow in spatial extent with time, but the contribution of PW increases with time with concentrations of 3-4% at 40 years increasing to concentrations of 5-6% at 80 years. It seems that this is achieved by water containing PW becoming more dense as opposed to the PW mixing

into denser layers. In the real ocean the two mechanisms by which this can occur is by surface buoyancy forcing or by cabbeling.

Surface buoyancy forcing would require a loss of buoyancy either by cooling or salinification (most likely due to brine rejection). However, it would require PW to be at or very near to the surface, which would cause the tracer concentration to be reduced towards 0, removing the signal of PW. Cabbeling is a result of the non-linearity of the equation of state, and occurs when the temperature and salinities of two water parcels combine to create a water parcel denser than either of the two original parcels (Foster, 1972).

As the dense water observed in the experiment carries a strong PW tracer signal, cabbeling is the more likely mechanism of the two. It is also a process known to occur in the Weddell Sea (particularly near Maud Rise) (Harcourt, 2005) and a process thought to contribute to AABW formation (Urakawa & Hasumi, 2012). This said, further investigation is required before any definitive conclusion can be made.

5.5.3 Zonal Basin Averages at Year 80

Zonal basin averages of WedSurTr_{AN} at Year 80 (Figure 5.14) provide a summary of how far the PW has progressed northward within each basin and at which densities the PW is present. In the Atlantic PW is most concentrated at densities $> 1027.91 \text{ kg m}^{-3}$ with maximum average concentrations of 6%. The PW appears to largely be within the deep Weddell Basin. Some PW has travelled northward and is present at 25°N at 80 years in very low concentrations (< 1%) in water of density 1027.87 kg m⁻³. The Indian Basin average shows a similar pattern with concentrations of 6% seen in the deepest waters south of 50°S. It is likely that this zonal average is dominated by deep

waters held within the Enderby Basin, a basin with a strong connection to the Weddell Basin. In the Indian Ocean, PW at concentrations of < 1% are observed as far north as 10°N at an average density of 1027.83 kg m⁻³. In the Pacific water is also seen as far north as 10°N (conc. < 1%) but at the slightly lighter density of 1027.81 kg m⁻³. A major difference with the Pacific zonal average is that the highest observed concentrations are not in the deepest waters of the Southern Ocean. This is most likely because the connection between the deep basins in the Indian Southern Ocean and Pacific Southern Ocean are more restricted due to bathymetric features such as the Kerguelan Plateau and Macquarie Ridge.

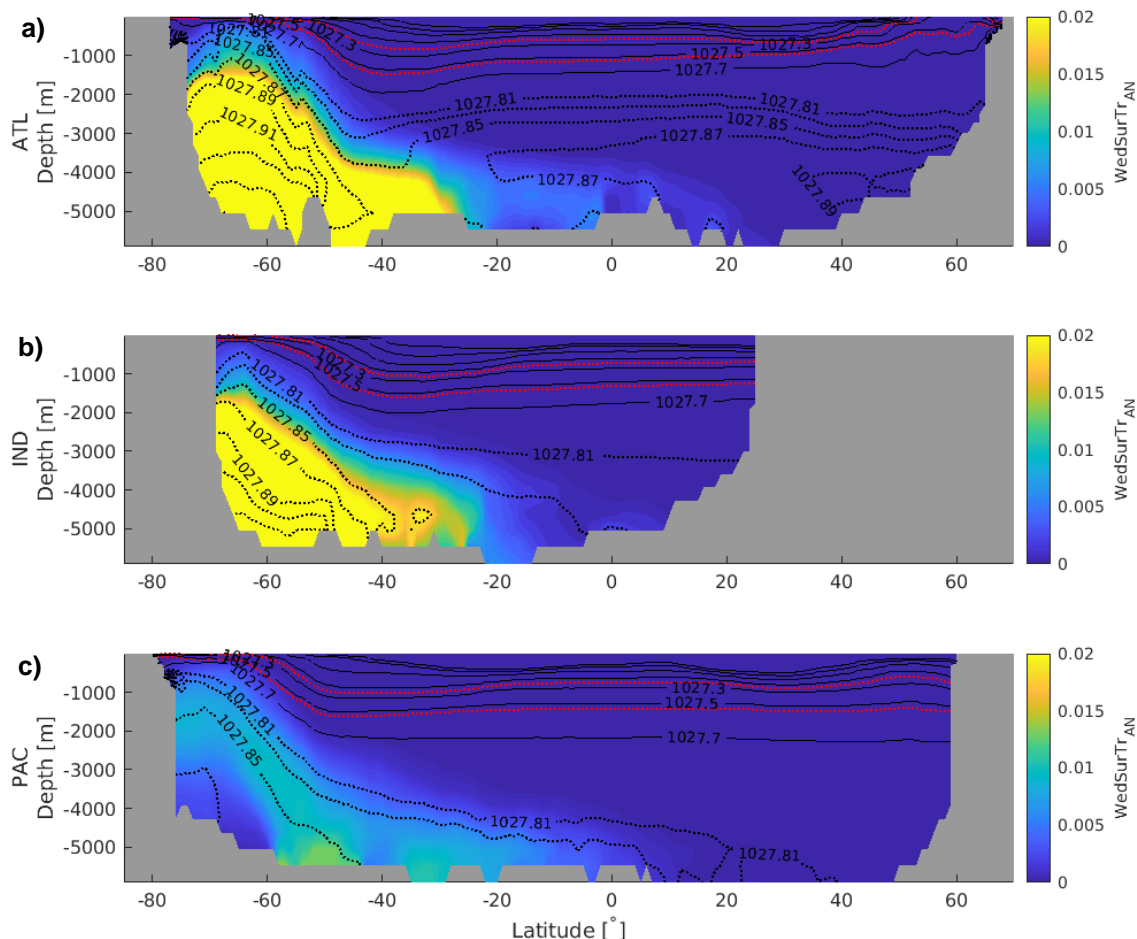


Figure 5.14 – Zonal basin averages of WedSurTr anomaly at 80 years for the Atlantic Ocean (a), Indian Ocean (b), and Pacific Ocean (c). Line contours indicate densities (ρ_0) ranging from 1026.50 – 1027.70 kg m⁻³ (solid) and 1027.81 – 1027.97 kg m⁻³ (dotted). Red dotted line indicates boundary of Atlantic AAIW & UCDW, 1027.20 – 1027.55 kg m⁻³.

5.5.4 Signals at 24°S

There is no presence of PW at AAIW densities at 24°S (Figure 5.15). The PW that is present at 24°S is seen in concentrations of 1-2% in the AABW in the Brazil Basin and in the Cape Basin to the east of the Walvis Ridge. It is clear that any mixing or buoyancy forcing that occurs is insufficient to allow PW into the densities of AAIW. It should however be noted that, although not in the correct density class, PW did reach 24°S within the decadal timescales which were predicted by the MEM.

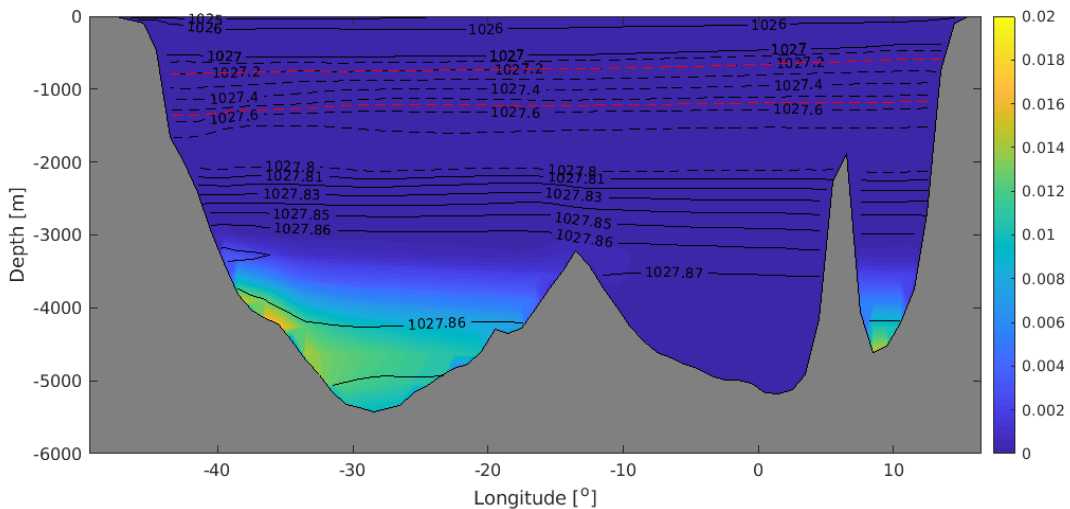


Figure 5.15 – Zonal section of WedSurTrAN at 24°S at Year 80. Line contours indicate densities (ρ_0) ranging from 1025.00 – 1027.00 kg m^{-3} (solid), 1027.10 – 1027.70 kg m^{-3} (dotted) and 1027.81 – 1027.87 kg m^{-3} (solid). Red dotted line indicates boundary of AAIW & UCDW, 1027.20 – 1027.55 kg m^{-3} .

5.6 Further Discussion & Conclusion

Overall the model does well at representing the polynya, maintaining a realistic size of polynya and a stable global overturning circulation. The PW progresses westward and appears as an anomalously cold mass as in observations (Foldvik, 1985), and the additional polynya that formed mimics the location of the Weddell Polynya in its latter years (1975 & 1976) (Carsey, 1980). Global distributions of PW in the deep waters of the Pacific, Atlantic and Indian

Oceans closely matched those described in a similar experiment by Zanowski & Hallberg (2017).

The results show that PW does not contribute in any amount to AAIW found at 24°S but that, as has been noted previously (Gordon, 1982), a Weddell Polynya does have the potential to modify very large volumes of water. These volumes are small compared to the global ocean, but can still have an impact for many decades on larger scale circulations like that of the Antarctic Circumpolar Current (ACC), as observed through Drake Passage transport.

The signal detected within the AAIW at 24°S that points to a Weddell Sea source in the 1970s showed the strongest signals in the UCDW below the AAIW. This experiment clearly shows no link between PW and either AAIW or UCDW but it is important to briefly consider why not. AAIW/UCDW and PW have different densities, σ_0 1027.20 -1027.55 kg m⁻³ and 1027.85 kg m⁻³ respectively (in ECCO). In order for PW to be present in AAIW it would have to reach these lighter densities or start at a lighter density.

Two ways in which this could happen is if there was enhanced diapycnal mixing to mix PW into lighter density classes, or if PW had a lighter original density, or a combination thereof. Although the polynya was well represented in the model, it mixed to the full water column depth, whereas in observations there has only been evidence of the PW mixing in a column down to depths of around 3000 m (Gordon 1982). It is difficult to induce a polynya to a limited depth as even if the modified mixing is restricted to shallower depths the full water column will often overturn. As Zanowski & Hallberg (2017) noted, this is not a major problem when evaluating the impact of PW in the global ocean as most of the deep waters are trapped within the deep Weddell – Enderby Basin

complex and so will not influence global circulations. This said, deeper mixing would lead to a higher average density of PW, putting it further away from the lighter densities of AAIW/UCDW. Another variable that could alter the initial density of PW is the location of the polynya, as a lighter overall water column would lead to lighter PW. However, Figure 5.16 shows that even if the water column were only mixed to a depth of 2000 m, there is nowhere in the Weddell Sea where a polynya could form and obtain a density matching that of AAIW/UCDW.

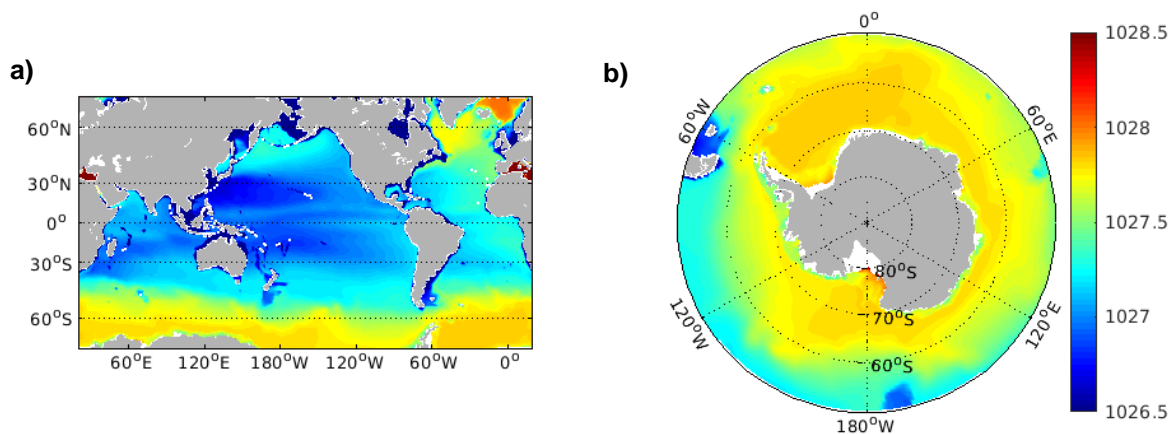


Figure 5.16 –Mean ρ_o of the surface 0 - 2000 m for September (Year 1 CTRL). AAIW/UCDW densities are $1027.20-1027.55 \text{ kg m}^{-3}$. Colour indicates density.

The second route to a presence of PW in lighter densities, enhanced diapycnal mixing, is the more likely explanation if (though unlikely) ECCO had misrepresented the pathway of PW. Mixing in the Southern Ocean is not well understood due to its high spatial heterogeneity and sparsity of observations. It is acknowledged that rough bathymetry in the Southern Ocean can lead to high diapycnal diffusivities close to bathymetry (Ledwell *et al.*, 2000; Mashayek *et al.*, 2017), and this is represented in ECCO. However, Naveira Garabato *et al.* (2004) suggest that there is also likely enhanced mixing higher in the water column caused by internal waves generated from rough bathymetry, something likely not represented in the model mixing scheme. The flows that cause these

internal waves can have a geostrophic or tidal origin and tides are not included in the ECCO set-up. Naveira Garabato *et al.* suggest that this mixing could lead to a higher interaction between the upper and lower limb of the Southern Ocean meridional overturning than previously thought, which would allow the PW to more readily mix into the lighter density classes of UCDW and eventually AAIW.

As an extension of this experiment it would be interesting to increase the diapycnal mixing in areas of the Southern Ocean to test whether PW could mix to lighter density classes with an increased level of diapycnal mixing. That said, considering the low concentrations of < 2% PW in AABW in the Atlantic basin, even if PW was present in AAIW through mixing, it would most likely be in incredibly low concentrations, too low to be responsible for the signals observed in the MEM results.

Chapter 6:

Temporal and Spatial Origins of AABW at 24°S, from a Combined Maximum Entropy Method and ECCOv4 Approach

Abstract: Antarctic Bottom Water (AABW) transports heat and carbon northward as part of the Atlantic Meridional Overturning Circulation. An understanding of the timescales of such transport and how it might be changing is important, as these transports influence the climate's response to increasing levels of anthropogenic carbon dioxide. In this chapter a Maximum Entropy Method is applied to transient tracer measurements from the bottom waters of the Brazil and Cape Basins at 24°S in the South Atlantic. The results are used to estimate the most likely sources of AABW in space and time, and evaluate the differences between observations taken on two cruises nine years apart. The results are compared to the results of a passive tracer experiment in ECCOv4r2, in order to assess the feasibility of the Maximum Entropy Method results. The Maximum Entropy Method predicts the Weddell Sea to be the dominant source of AABW in the South Atlantic and suggest that this water reaches 24°S in ~ 30 years. A strong influence of water of North Atlantic origin with a much older timescale of 75+ years is also observed, mixing with AABW from above. Ages derived from ECCOv4 support the ~30 year timescale suggested by the MEM, however ECCOv4 shows a much smaller contribution of older waters with a North Atlantic source.

6.1 Introduction

In this chapter we explore the results of applying the MEM to AABW samples collected at 24°S in 2009 and 2018, in the Brazil and Cape Basins of the South Atlantic. The analysis considers both core AABW (cAABW) and peripheral AABW (pAABW). pAABW is defined as waters within the density class of $\sigma_n = 28.20\text{--}28.27 \text{ kg m}^{-3}$ and cAABW is defined as waters within the density class $\sigma_n > 28.27 \text{ kg m}^{-3}$ (see Section 2.2.2).

Firstly, we will consider the spatial origin of AABW samples (Section 6.2), and then the temporal origin of AABW samples (Section 6.3). We will then compare the results from the 2009 and 2018 data and assess the validity of the observed differences (Section 6.4). Following this we will explore the seasonality of the results (Section 6.5), evaluate the sensitivity of the results to the choice of prior (Section 6.6), discuss the exclusion of ^{14}C as a constraint (Section 6.7), compare the MEM results to ECCO output (Section 6.8), and finally, summarise the findings of the chapter (Section 6.9 & 6.10).

6.1.1 Background of AABW at 24°S

The 24°S oceanographic section cuts E-W across the South Atlantic, through the centre of the South Atlantic Gyre, crossing both the MAR and the Walvis Ridge, which separate the Brazil, Angola and Cape Basins respectively (see Figure 2.1). The section cuts zonally across the AMOC, encompassing northward flowing SAMW, AAIW, UCDW and AABW, and southward flowing NADW, which lies below the UCDW but above the AABW. AABW plays an important role in this overturning system, by transporting heat and carbon northward in the bottom waters. At 24°S the cool, high nutrient AABW is found in the Cape Basin at the far east of the section and in the Brazil Basin in the

west of the section. Much less AABW is observed in the Angola Basin as the Walvis Ridge acts to isolate this basin from deep waters further south (Shannon and Chapman, 1991). The densest AABW at the section is found in the Brazil Basin. Existing knowledge of AABW in the South Atlantic (see Sections 1.2.6 and 1.2.7), suggests it forms predominantly from deep water formed in the western Weddell Sea (Meredith *et al.*, 2000), with a smaller contribution of waters from near Cape Darnley (Ohshima *et al.*, 2013).

6.1.2 Methods Specific to the AABW Analysis

In this analysis, the MEM is applied to the data at 24°S using an inverse Gaussian and ECCO300 prior (as described in Section 3.1.5). To avoid issues faced in the analysis of AAIW, the same regions are removed as source regions, as were removed in the AAIW analysis (Chapter 4). These are Hudson Bay, the Baltic Sea and the Mediterranean Sea. Unlike in the analysis of AAIW, no outliers have been removed, as no samples appeared incongruous to those around them.

The following sections present and discuss the results of the analysis.

6.2 Spatial Origin of Water

Firstly, we consider the predicted spatial origin from the MEM, regardless of the transit time taken for a parcel of water to arrive at 24°S. Figure 6.1 shows the predicted area of origin for both cruises, for both the cAABW samples and the pAABW samples. The same pattern is observed in the data from both cruises, and in both the cAABW and pAABW samples. Three areas are highlighted as likely source areas. The most prominent is the surface waters of the Weddell Sea, followed by the surface waters of the area between Iceland and Svalbard in the Greenland/Norwegian Sea. The third area is in the south-eastern North Atlantic Ocean.

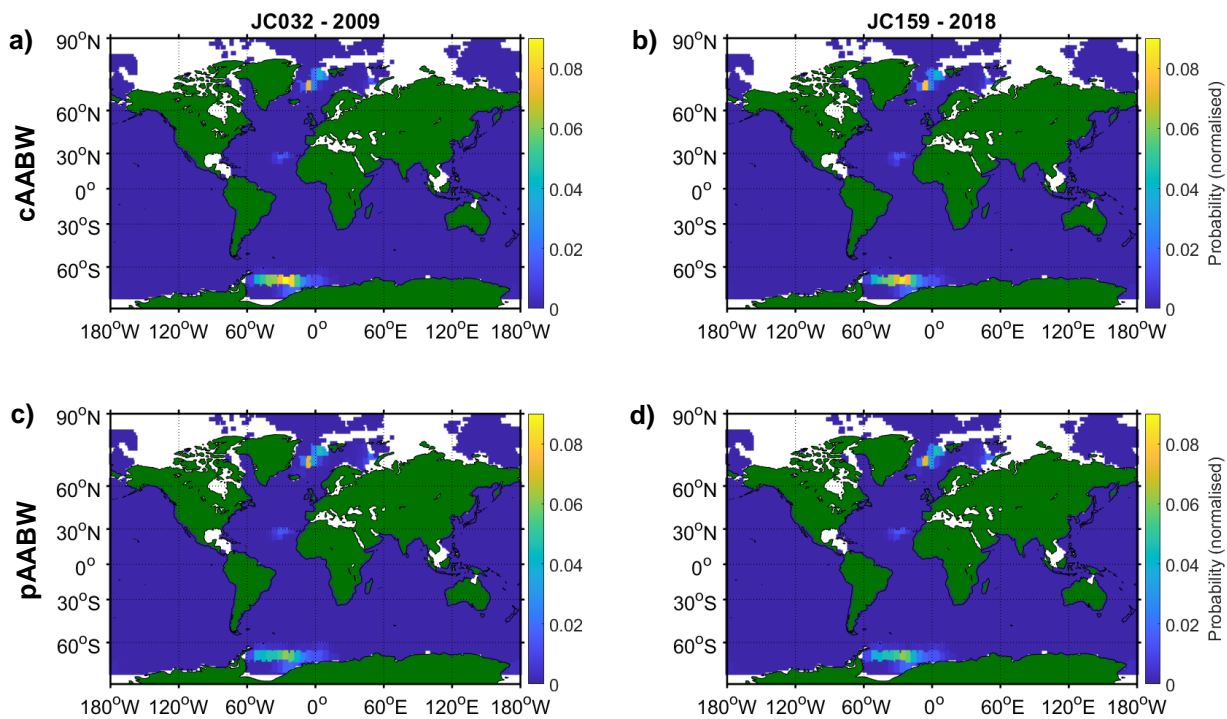


Figure 6.1 – Maps showing the spatial origin predicted by the MEM of cAABW (a & b) and pAABW (c & d) samples for cruise JC032 (a & c) and JC159 (b & d).

The identification of the Weddell Sea as a source region is as expected and lends confidence to the solution of the MEM, as this fits with the current understanding of AABW. The areas in the Greenland and Norwegian Seas can

be explained by an influence of NADW on these samples via two mechanisms. The first is that AABW forms as a mixture of HSSW and CDW, a water mass which originates from NADW and so likely carries signatures from this region. The second is that NADW overlies AABW in the South Atlantic and the analysed samples contain a contribution of NADW from entrainment. Evidence for the latter of these two explanations can be seen in the vertical distribution of Lab & GIN Seas water in Figure 6.2.

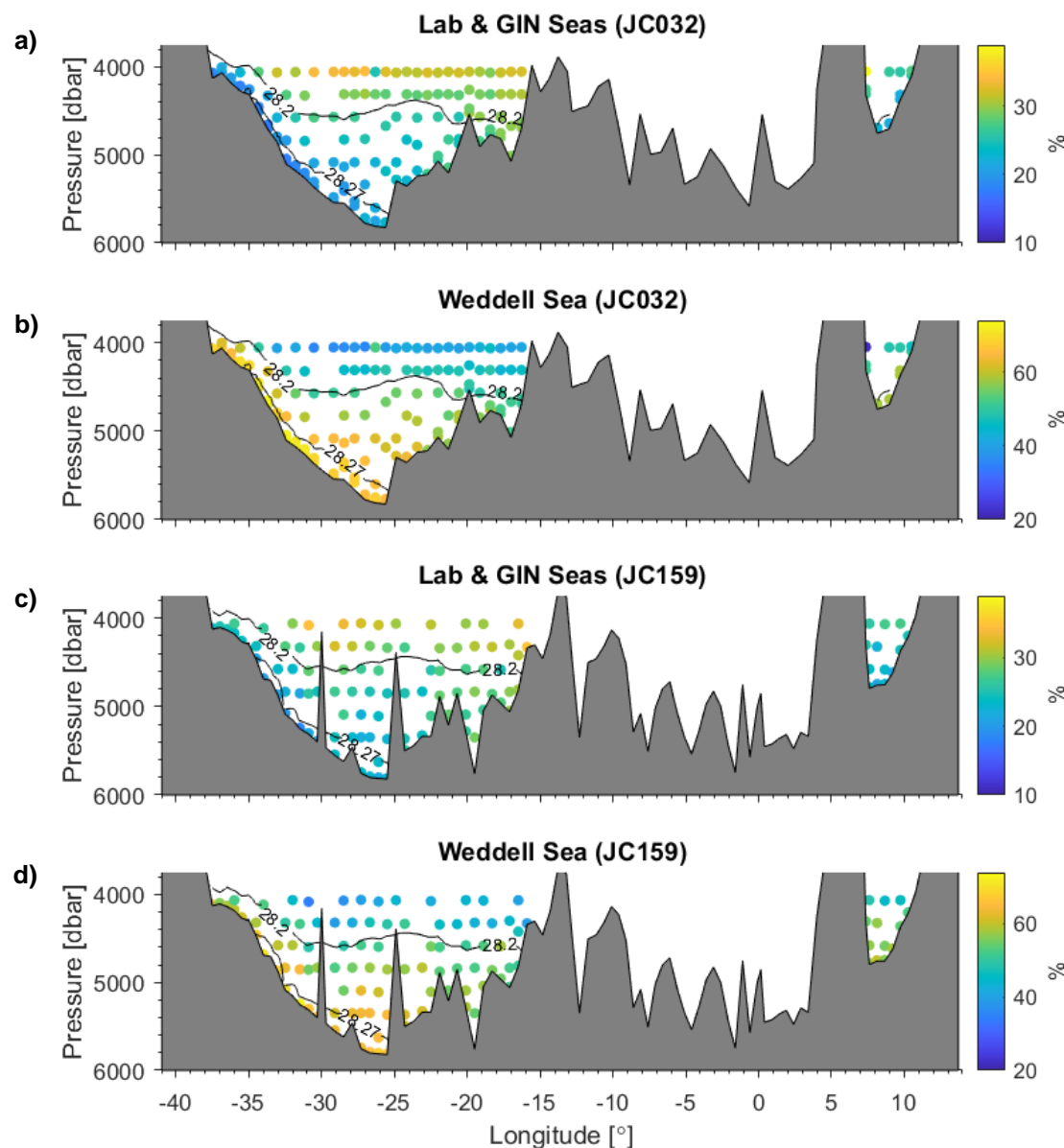


Figure 6.2 – Regional percentage contribution to individual water samples at 24°S, as predicted by the MEM. Contours indicate the 28.20 and 28.27 kg m⁻³ neutral density isopycnals associated with the defined boundary of pAABW and cAABW. *a* and *c*, show percentage contribution from the Labrador and GIN Seas region for cruise JC032 and JC159, respectively; *b* and *d* show percentage contribution from the Weddell Sea (Atlantic S of PF) region for the same cruises. Percentage includes predicted origin from all points in time.

The third identified region, the southeast North Atlantic, is an unexpected predicted source region for AABW. It is likely that identification of this region shows a weakness in the MEM as opposed to a true signal as this region is not known as a region of dense water formation and so it would be unlikely that waters from this surface region would be found in AABW.

6.3 Temporal Origin of Water

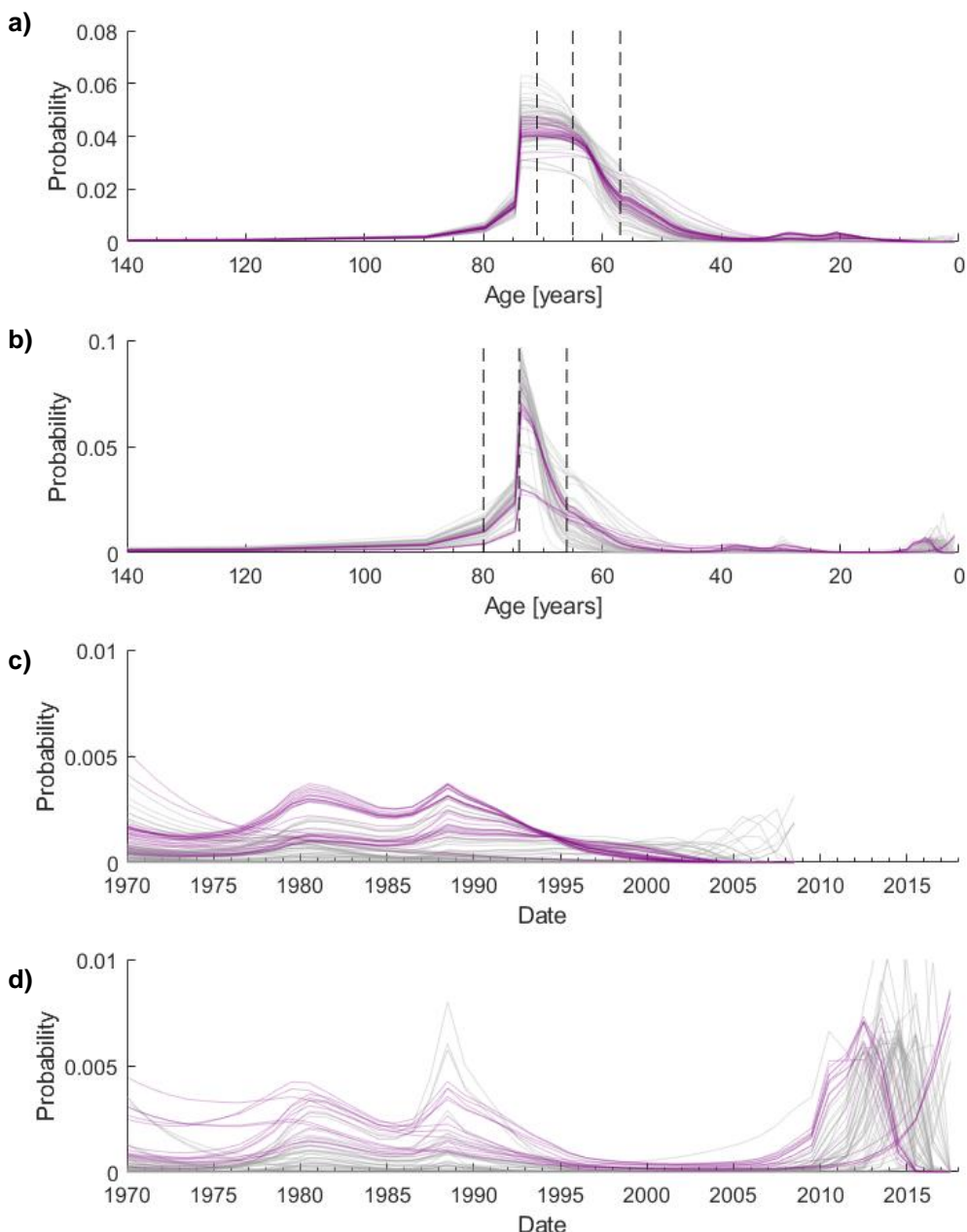


Figure 6.3 – Probability of cAABW (purple) and pAABW (grey) samples originating from different points in time as predicted by the MEM. (a & c) Show data from cruise JC032 (2009), (c) is restricted to ages 39 - 0 years (equivalent date: 1970-2009). (b & d) Show data from JC159 (2018), (d) is restricted to ages 48 - 0 years (equivalent date: 1970-2009). Vertical dashed lines (a & b), from left to right, indicate the years 1938, 1944 and 1952 which are the years from which CFC-12, CFC-11 and SF₆ are present in the surface water history respectively.

We now consider the temporal origins of AABW as predicted by the MEM. Unlike in the AAIW analysis of Chapter 4, ^{14}C is not used as a temporal constraint for AABW (see Section 6.7 for an explanation). This means that the only temporal constraints are CFC-12, CFC-11 and SF₆, whose presence in the surface waters only extends back to 1938, 1944 and 1952 respectively. Prior to 1938 it is purely the IG prior that has any influence on the predicted temporal probability. The transient tracers do still act as constraints but their concentration is constantly 0. As a result they cannot distinguish between water that is for example 300 years old and 2000 years old; this would have been the role of ^{14}C had it been included as a constraint.

The MEM predicts AABW to contain three temporal signatures. For the 2009 (JC032) samples (Figure 6.3a & c) the most dominant signature is between 45-75 years and for the 2018 (JC159) samples (Figure 6.3b & d) this signature is between 55-75 years. The second signal is much smaller and lies at 14-24 years for the 2009 data and 23-43 years for the 2018 data. The third signal is in the most recent 5 years (i.e. 0-5 years) for the 2009 data and the most recent 10 years for the 2018 data.

We now address each of these signals individually. The oldest of the three signals (ages 45-75; Figure 6.4a & d) corresponds to the time period where transient tracer concentrations were very low or close to 0 in surface waters. This suggests a contribution of older low transient tracer water in the AABW samples at 24°S. This is most likely explained by a contribution from NADW, either through entrainment with overlying water, or from older NADW present in the CDW that mixes with HSSW to form AABW in the Southern Ocean. A contribution of NADW from the Southern Ocean would be expected to be older than overlying NADW and contain no transient tracers. It is unlikely to

be identified by the MEM as, without ^{14}C , it is only the unimodal IG temporal prior (see Section 3.1.5.1) that governs the probability of older waters. It is likely that the majority of this signal comes from entrained water as the cAABW samples tend to have a lower probability of these 45-75 year old waters than

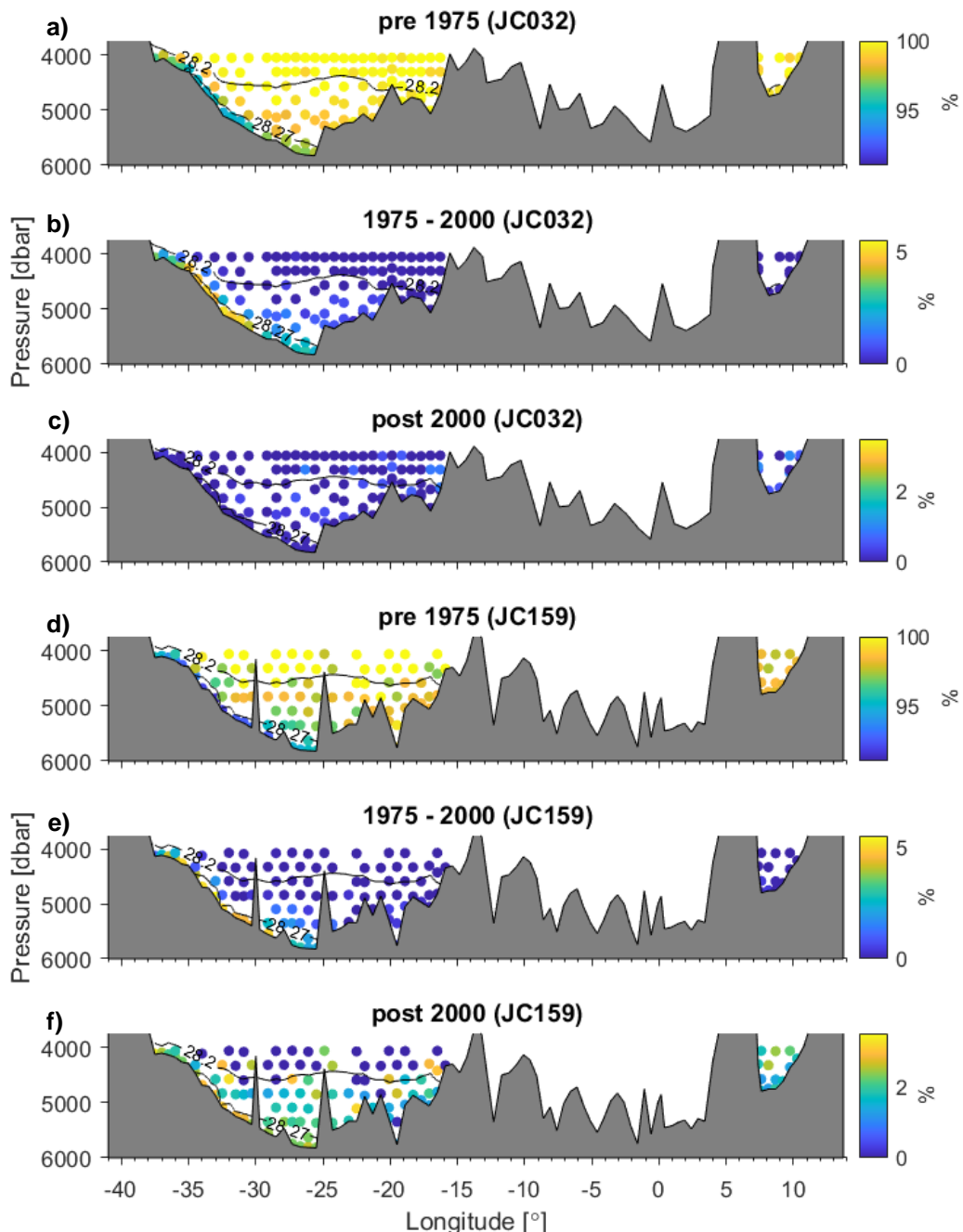


Figure 6.4 - Percentage contribution of different time periods to individual water samples at 24°S, as predicted by the MEM. Contours indicate the 28.20 and 28.27 kg m^{-3} neutral density isopycnals associated with the defined boundary of pAABW and cAABW. a-c Show results from the 2009 data, d-f show results from the 2018 data. a & d Show the percentage of water originating from before 1975, b & e from 1975 - 2000, and c & f from after the year 2000.

the pAABW samples (Figure 6.4a & d), which have undergone more mixing with surrounding waters.

The second temporal signal is the one of most interest. This temporal signal is considerably stronger in the cAABW than the pAABW samples (Figure 6.3c & d, Figure 6.4b & e), suggesting it is the age associated with the AABW/HSSW of the Southern Ocean. When considered on an axis of date as opposed to age, it is apparent that the signal is associated with the same years for both cruises. This is further discussed in Section 6.4.

The third temporal signal is that of the most recent 10 years. In the 2009 data this signal is not seen in the cAABW samples and is only a small signal in some of the pAABW samples (Figure 6.3; Figure 6.4e & f). The signal is much stronger in the 2018 data and is present in both the cAABW and pAABW samples. This signal is deemed to be unrealistic and is discounted as a weakness of the MEM. The dense cAABW and pAABW water at 24°S is far from any downwelling region and so a recent interaction with the atmosphere is highly unlikely. The MEM has been found in previous analysis to gravitate towards extremes, it may be that high levels of SF₆ in recent surface water have caused the MEM to gravitate towards these recent years.

Although it is easy to discount signals that are clearly unrealistic, what it is not easy to do is to evaluate the influence that an unrealistic signal has on the remainder of the solution. If, for example, the MEM solution identifies an (unrealistic) contribution of surface waters from the last 5 years this will provide a high contribution of SF₆ to the desired sample concentration that the MEM is trying to achieve. This will cause other temporal signals to be biased older in order to achieve a lower (than true) SF₆ concentration in order to compensate

for the over contribution from recent years.

6.4 Comparing Patterns in Decadal Repeat Observations

In Section 6.3 the 45-75 age signal is identified as the most likely age of the AABW when the NADW influence is ignored. As was seen in Chapter 4 (Section 4.7) much information can be gained by comparing the MEM output for both cruises on an axis of age (years since the cruise) and on date. If the MEM accurately predicts the age of AABW and the circulation/formation of AABW has remained constant between the two cruises, a lag of nine years between the 2009 data and the 2018 data would be expected when viewed against a horizontal axis of date. However, it is evident from Figure 6.5a that this is not the case.

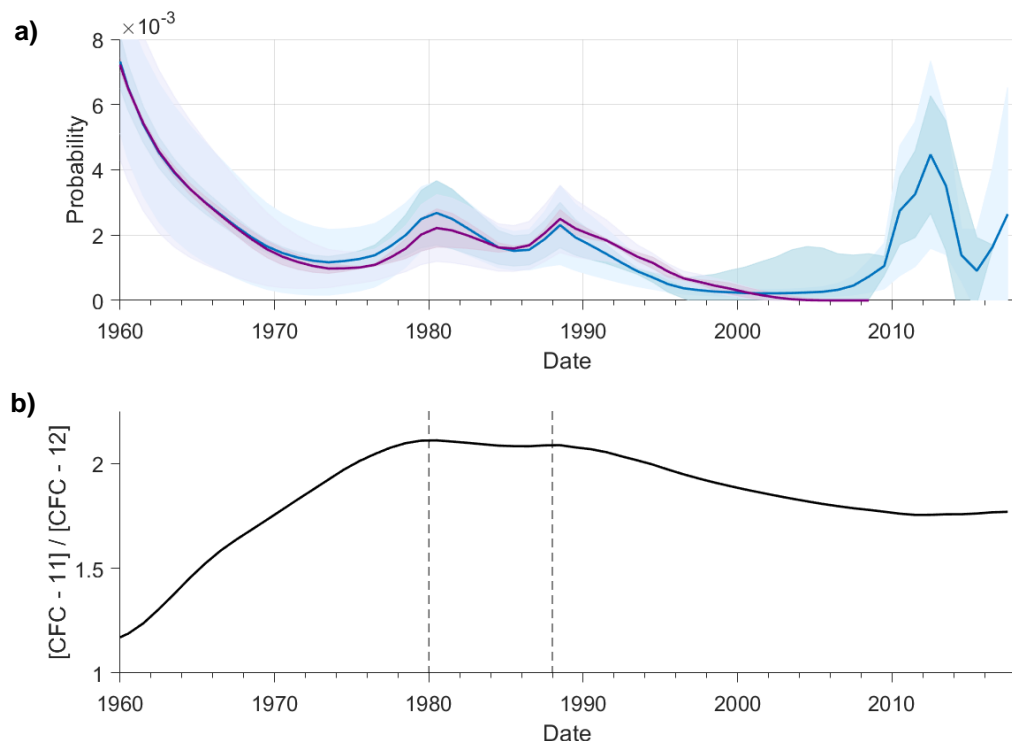


Figure 6.5 – (a) Mean Probability of cAABW samples originating from different points in time as predicted by the MEM. Average of 2009 (JC032) samples are shown in purple, average of 2018 (JC159) samples are shown in blue. Darker shading in each respective colour represents ± 1 standard deviation of the ensemble of mean probabilities, lighter shading represents ± 1 standard deviation of all cAABW samples averaged to create mean probability. (b) Global history of surface ocean CFC-11/ CFC-12 ratio. Vertical dashed lines indicate years 1980 and 1988.

The probabilities from the 2009 and 2018 samples overlay each other almost exactly. This could be interpreted in two ways: 1) AABW circulation northward in the South Atlantic has slowed so considerably that the water sampled in 2018 is the same as the water sampled in 2009, 2) the MEM can predict an approximate age but is drawn more so to particular points in time due to the interaction of the time histories of the different constraining tracers. A large episodic event, unlike in Chapter 3, is not considered a possibility due to the bi-modal characteristic of the signal with peaks in 1980 and 1988.

It has been suggested that the formation of AABW has slowed in recent decades but not that it has stopped altogether (Huhn *et al.*, 2013) and so the first interpretation is unlikely. In order to assess the second interpretation, the tracer histories must be studied with particular attention paid to 1980 and 1988. Although the individual histories themselves show no notable features at these time points, when the ratio between different transient tracers is studied, the relationship becomes more clear. Figure 6.5b shows the ratio of CFC-11 to CFC-12, and clearly shows the same bimodal peak structure as seen in the temporal origin results for cAABW. This is conclusive evidence that for AABW at 24°S the MEM cannot resolve the differences between repeat [near] decadal observations.

This said, it is important to remember that there is a difference between the validity of using the MEM to prescribe an age (with some error) to AABW and using the MEM to look at decadal change. The higher probability around 1980 and 1988 has a clear link to the core of the AABW and so it is still believed that this is a true signal of the age of AABW at 24°S.

It should also be considered that, although it may now be stabilising (Abrahamsen *et al.*, 2019), AABW formation is thought to have reduced in recent decades (Huhn *et al.*, 2013). If the MEM is drawn to particular years, then if the true age differs little between the two cruises this is likely to increase the likelihood of them being drawn towards the same years. For example, say the true age signal from the 2009 data was 1989 but it was drawn to the peak in 1988, if the true age signal from 2018 was 1998 ($1989 + 9$) it would be less likely to be drawn towards the 1988 peak than if circulation/formation had slowed/reduced and the true age signal from 2018 was (for example) 1995 ($1989 + 6$). The error margins shown in Figure 6.5a also indicate that there can be variability in age between individual samples (and in some places within the ensemble) of a few years and so the relative error of looking at changes in water age between cruises nine years apart is high.

6.5 Seasonality

As the source region data for the MEM has monthly resolution, it is possible to look at the months in which water is predicted to have last been at the surface before being subducted. This can give further support to ideas of transport and also highlight results that may be unrealistic. The IG prior (see Section 3.1.5.1) only gives information on which years are more or less likely, and so any seasonality detected comes entirely from the information given by the tracers themselves.

The data presented in Figure 6.6 are normalised (by the total fraction of water from that region) to highlight the seasonality of origin, regardless of the amount of water predicted to originate from a region. From the analysis of the

spatial origin of cAABW (Section 6.2) it is known that the S of PF (Weddell Sea) and Lab & GIN regions both contribute considerably to cAABW waters. In the 2009 and 2018 results, the S of PF region shows a higher contribution of water from the Southern Hemisphere winter and spring months of August, September and October. These months lie within the freezing season (Feb/Mar – Oct/Nov) of the Weddell Sea (Renfrew and King, 2002). This is the period in which the ocean is losing energy to the atmosphere, and high rates of sea-ice production are observed in the coastal polynyas of the western and southwestern Weddell Sea. It is this sea-ice production that produces the HSSW (through the process of brine-rejection) that later forms AABW. As the HSSW is the water that carries the surface transient tracer signature into AABW, the MEM predicted winter origin of AABW is in agreement with our understanding of AABW formation.

This gives confidence that the MEM is correctly predicting the origin of AABW.

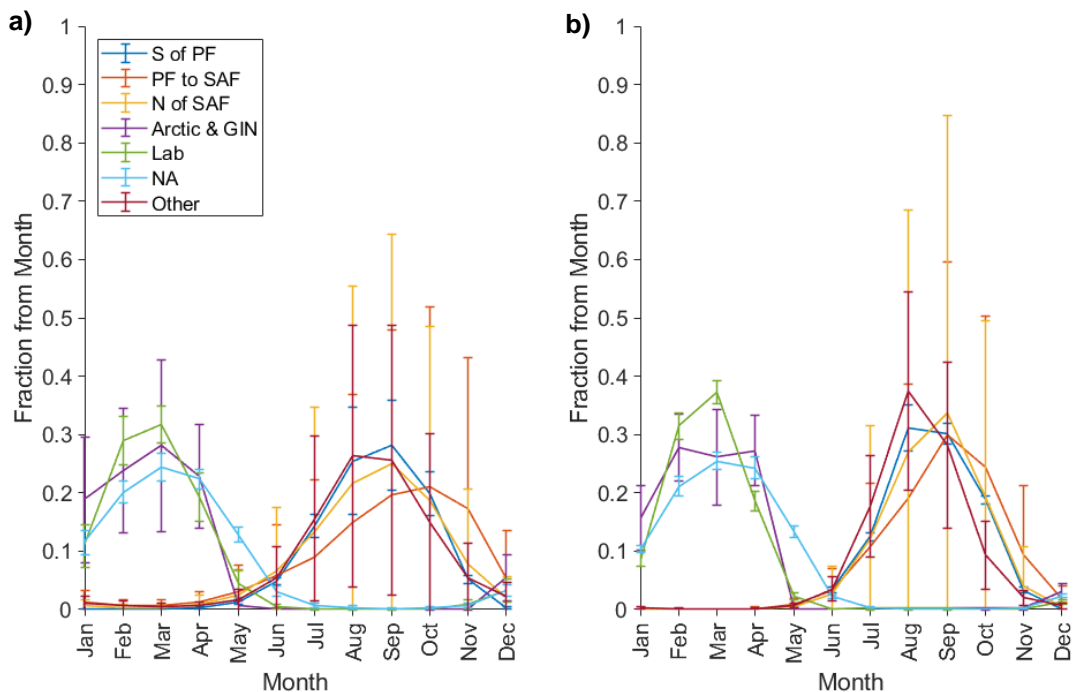


Figure 6.6 - The month in which water was predicted to last have been in contact with the atmosphere regardless of the year. Each line represents the mean of all cAABW samples at 24°S for JC032 (a) and JC159 (b). Different regions are indicated by colour. Error bars show ± 1 standard deviation within the samples that were averaged.

The Lab & GIN region shows a higher contribution of water from the Northern Hemisphere winter and spring months of February, March and April. This is also in agreement with current understanding, as NADW is known to form in the winter in the Greenland and Norwegian Seas due to surface cooling (Gordon, 2009).

6.6 Influence of the Prior

The MEM helps to solve a system of highly underdetermined equations. As discussed in Section 3.1.5 the prior acts as the first guess for the system of equations, the solution is allowed to deviate from the given prior, but the prior does inevitably push the solver in the direction of what it deems to be the ‘correct’ answer. Here we briefly explore how the choice of prior has influenced the final results. The four sets of results compared are: 1) those using the ‘optimal prior’ which has inverse Gaussian distribution in time and uses the ECCO300 output to generate a spatial prior (IG-ECCO300), 2) a prior using the ECCO300 spatial prior but uniform distribution of probability in time (UNI-ECCO300), 3) a prior with uniform spatial prior with inverse Gaussian distribution in time (IG-UNI), and 4) a prior with uniform distribution of probability both in space and time (UNI-UNI).

We first consider the impact of the prior on the predicted spatial origin of AABW at 24°S. All four priors result in a very similar prediction of the spatial origin of the cAABW samples (Figure 6.7). All priors pick out the same three regions discussed in Section 6.2. The only noticeable difference between the scenarios is that the solutions that used the ECCO300 prior show marginally lower probabilities in the Greenland/Iceland Seas. These same patterns were

observed in the 2018 (JC159) data (not shown). This lack of difference between the prior scenarios shows the spatial origin result to be insensitive to the choice of prior.

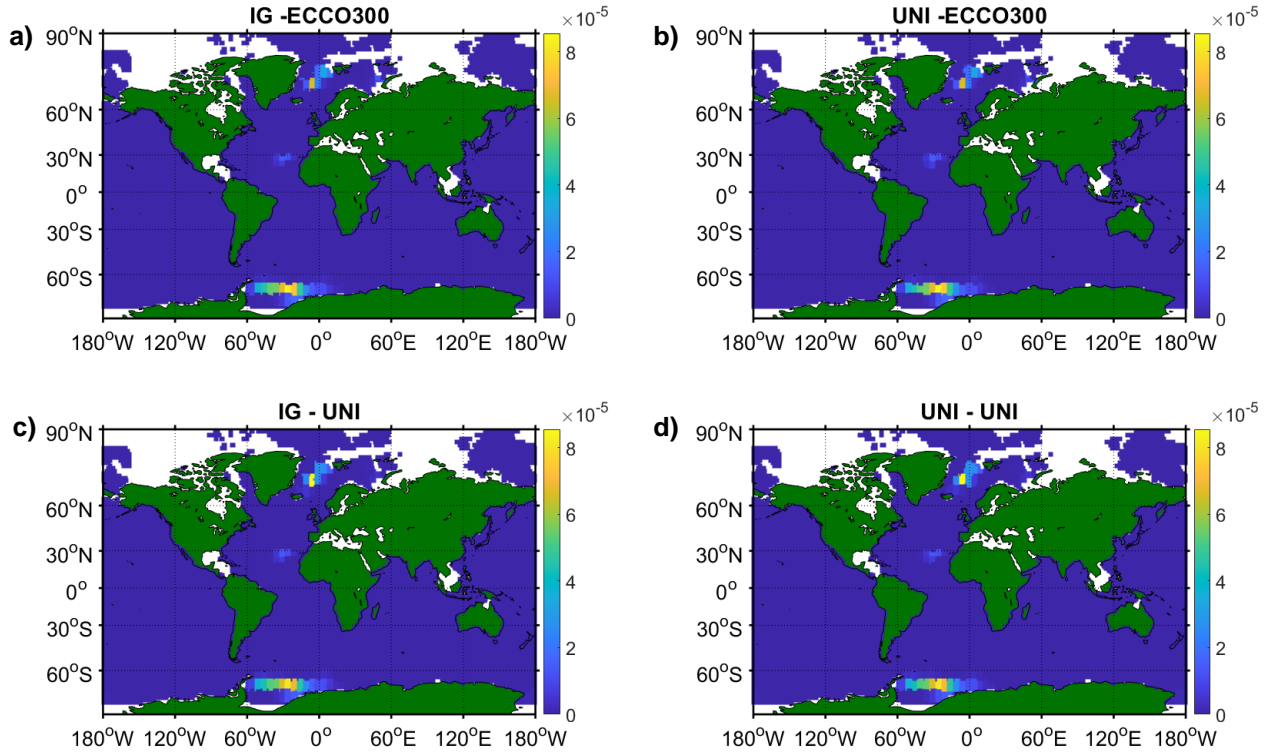


Figure 6.7 - Maps showing the spatial origin predicted by the MEM of cAABW for the 2009 (JC032) data for four different prior scenarios (indicated by title).

We now consider the impact of the prior on the predicted temporal origin of AABW at 24°S. The response of the results can be clearly split into two groups, those which use the IG prior and those which do not (Figure 6.8). For both the 2009 and 2018 data, where the IG prior is used the temporal signature at 45-75 years (~1930 – 1960) is considerably stronger compared to when the IG prior is not used. However, the signature still predicts the water to originate from the same points in time. An explanation for this difference can be understood if much older years are considered. Before 1880 (earliest date shown in Figure 6.8) in both the scenarios with and without the IG prior a very low probability extends all the way back to 2000 years before the cruise date (the limit of the

source time history). In the scenarios that use the IG prior, this probability tapers towards 0. However, the scenarios which do not use the IG prior maintain a very low, near constant, but still above 0 probability. As the total probability (area under the graph) is normalised to 1, the absence of this very long tail allows for a larger probabilities to be seen at 45-75 years.

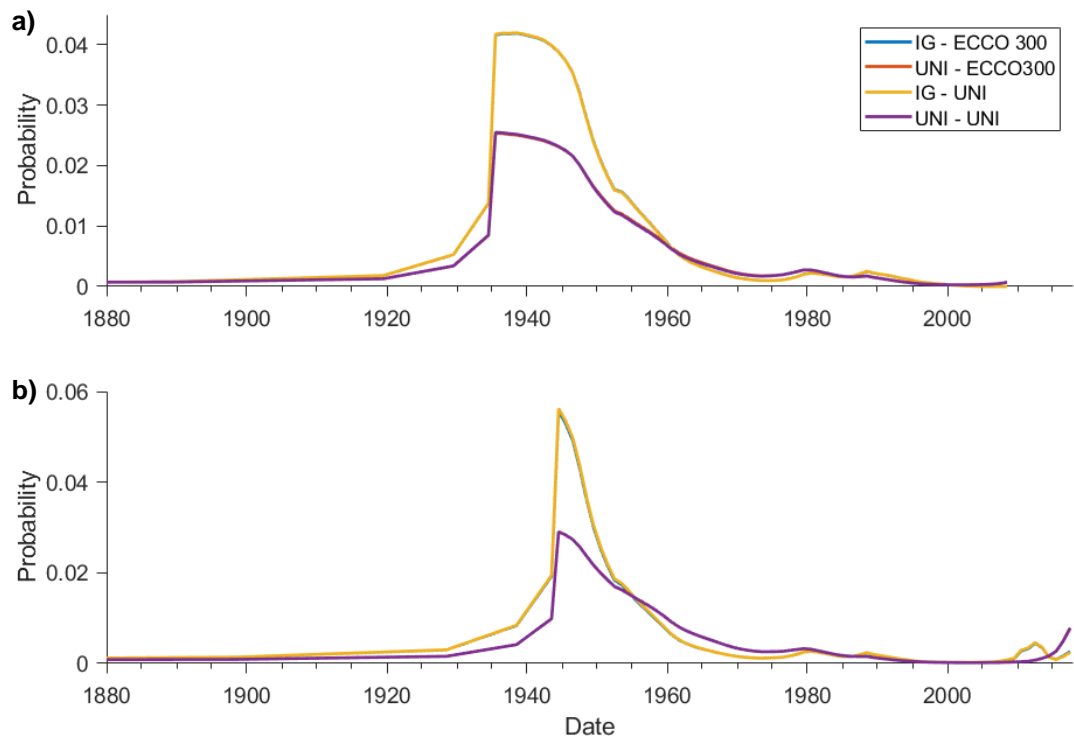


Figure 6.8 - Mean probability of cAABW samples originating from different points in time as predicted by the MEM using four different prior scenarios. (a) Shows results of 2009 (JC032) data. (b) Shows results of 2018 (JC159) data. Note: blue is obscured by yellow, orange is obscured by purple.

A small difference is seen at the peak thought to relate to the Weddell Sea waters (1975-1995), with the inclusion of the IG prior appearing to suppress the 1980 peak and inflate the 1988 peak. The final observed difference is in the peak from the most recent years. In the 2009 data, the IG prior appears to suppress a very small probability which increases towards the most recent year. In the 2018 data a similar phenomenon is observed, however

the IG prior does not suppress the signal but instead forces it into the preceding years.

In summary, the results show little sensitivity to the choice of spatial prior but some sensitivity towards the choice of temporal prior. However, although the temporal prior impacts the magnitude of the peaks, it changes their position very little, if at all.

6.7 Excluding ^{14}C as a Constraining Tracer

Each tracer provides distinct information to the MEM. The more tracers that are used the better constrained the system and (in theory) the more accurate the solution. For each tracer the MEM requires a good interior measurement of that tracer and a global surface boundary concentration of that tracer (see Section 3.1.3). ^{14}C is an important tracer as it provides a temporal constraint for years prior to when CFCs and SF₆ existed in the ocean (pre1930s). However, for the analysis of AABW, ^{14}C is not used as a constraining tracer for the reason given below.

When ^{14}C is used as one of the constraining tracers, the MEM output suggests a high contribution from very old (~2000 year old) waters (Figure 6.9b). This signal is deemed to be unrealistic as AABW is known to be a relatively young water mass (Orsi *et al.*, 1999). When the output of samples run with and without ^{14}C is compared (Figure 6.9a) the magnitude of the peaks are altered but their position remains largely the same, and so the removal of ^{14}C as a tracer for AABW is not considered to alter the results.

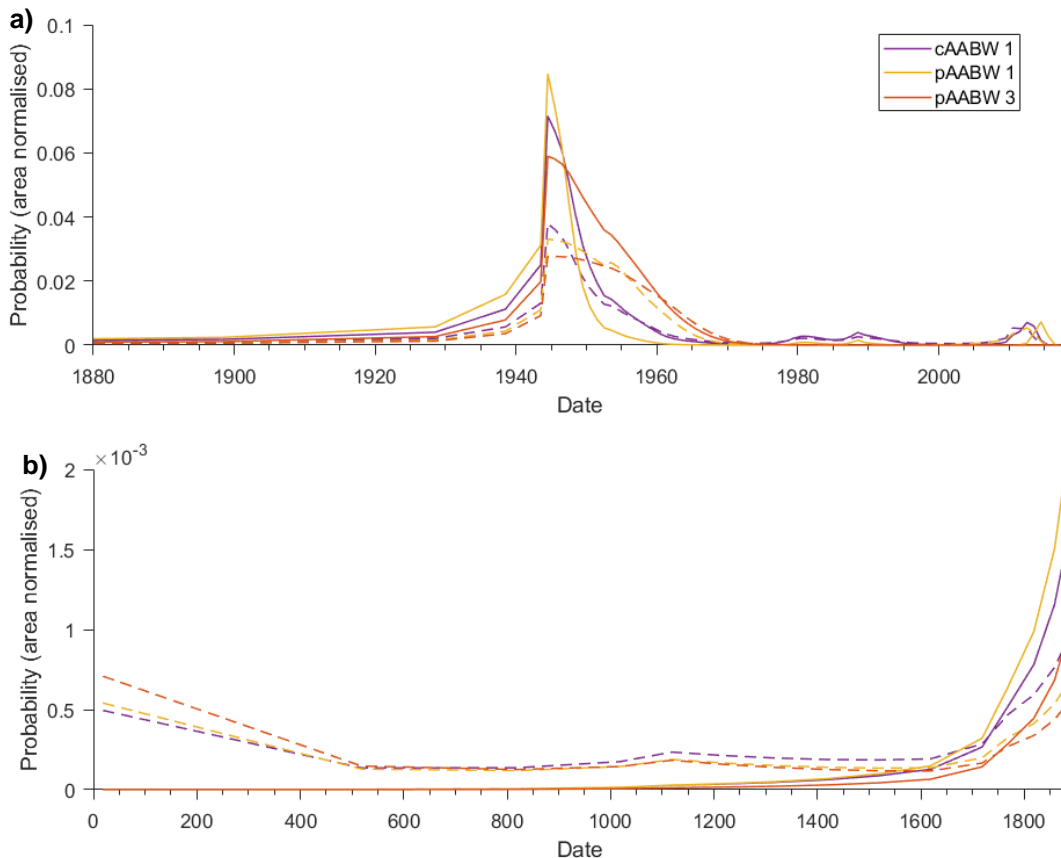


Figure 6.9 - Mean probability of a subset of cAABW & pAABW samples originating from different points in time as predicted by the MEM, with (dotted line) and without (solid line) using ^{14}C as a constraint. Samples relate to those in Table 6.1.

The reason for the unrealistic age signal is thought to be due to the boundary conditions used. When we refer to a ^{14}C value, what we are actually referring to is the ratio of $^{14}\text{C} / ^{12}\text{C}$ compared to a standard. Negative values (as are found in most of the ocean) indicate seawater is depleted in ^{14}C compared to the standard. Due to kinetic fractionation (Urey, 1947), this depletion is higher in the cooler high latitude waters.

Table 6.1 shows the measured ^{14}C values for cAABW and pAABW samples from the 2018 (JC159) occupation of 24°S (no measurements were taken on the 2009 occupation). The most negative value in the boundary condition (see Section 3.1.3) for the Weddell Sea is -150 ‰ (Figure 6.10). 180 years' worth of radioactive decay would be required for the value measured in the core AABW (-172.2 ‰) to be reached, assuming the AABW originated from

surface waters with the most negative ^{14}C value. This 180 year timescale seems unrealistic considering the levels of CFCs in this water, and that CFCs have only been present in the atmosphere since the 1930s.

Sample	Longitude [°]	Pressure [dbar]	^{14}C (‰)
cAABW 1	-34.5	4460	-172.2
pAABW 1	-34.5	4319	-165.5
pAABW 2	-34.0	4116	-154.7
pAABW 3	-30.9	4598	-170.3
pAABW 4	-30.3	4832	-170.8
pAABW 5	-26.7	4832	-169.7
pAABW 6	-24.3	4850	-168.4

Table 6.1 – ^{14}C values of one cAABW sample and six pAABW samples measured at 24°S in 2018 (JC159). Data provided by H. Graven (personal communication, September 2021).

It may be that, in reality, surface ^{14}C values in the Weddell Sea are more negative than the boundary condition suggests. Figure 6.10 shows the data points used to create the GLODAP gridded ^{14}C field, which is used as the boundary condition. These points are very sparse and so provide few constraining points for the gridded product (see Section 3.1.3 for discussion of temporal sparsity). Additionally, WSDW, a major precursor to AABW, is known to form in the south-western and western Weddell Sea (Meredith *et al.*, 2000),

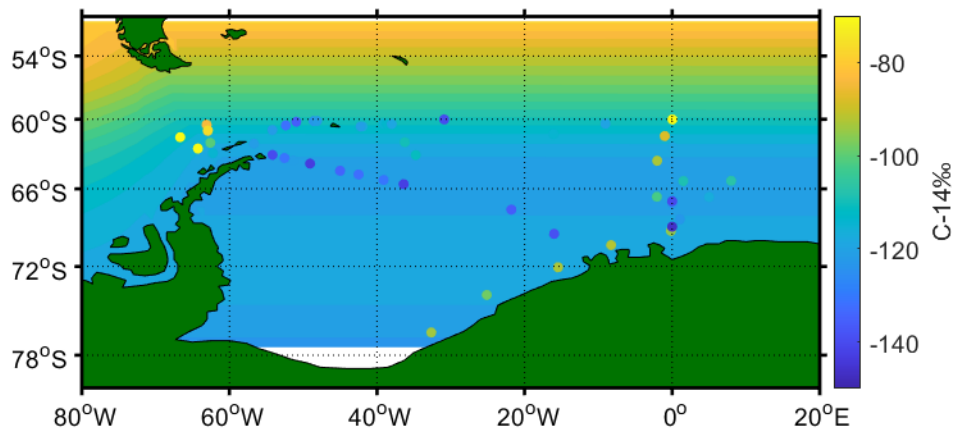


Figure 6.10 – ^{14}C (‰) at 20 m in the Weddell Sea region from GLODAPv2.2020 gridded product. Scattered points show ^{14}C from measured bottle samples within the surface 50 m, used to create the GLODAP gridded product.

an area which has no measured ^{14}C values. It is thought that with this poor boundary condition, use of ^{14}C as a tracer for AABW reduces the accuracy of the MEM result, hence it is not used.

6.8 Comparison of MEM Results to ECCO

So far we have purely considered the output from the MEM. We now consider the distribution and temporal evolution of the ECCO passive tracers at 24°S and use these findings to evaluate the feasibility of the MEM results. Firstly, we look at the distribution of the Weddell and Lab & GIN Seas' passive tracer at 24°S. Secondly, we look at the contribution of each region to cAABW and pAABW at 24°S. Finally, we consider the evolution of passive tracer concentration at 24°S over the entirety of the model run and assess how this aligns with the MEM predicted water mass ages. To aid comparison, cAABW and pAABW are defined according to the same definition used for the observational results (cAABW: $\sigma_n > 1028.27 \text{ kg m}^{-3}$ and pAABW: $1028.20 \text{ kg m}^{-3} < \sigma_n < 1028.27 \text{ kg m}^{-3}$). Although model water mass densities can differ from observational water mass densities (as noted previously, Section 4.5), cAABW and pAABW are still well represented by these bounds in the model.

The pattern of distribution (Figure 6.11) of both the Weddell and the Lab & GIN Seas passive tracers (at 24°S) closely matches the MEM predicted spatial origins (Figure 6.2). The concentration of the Weddell tracer increases towards the AABW core, up to a maximum contribution of 11%. Whereas the contribution from the Lab & GIN region increases away from the AABW core, with contributions of 4% in the cAABW and 6% in the pAABW. The magnitude of the contributions does, however, differ from those predicted by the MEM (see

Table 6.2). The MEM predicts a much higher contribution of 68% Weddell Sea (Atlantic S of PF) waters in cAABW and a 21% contribution of Lab & GIN waters.

	MEM				ECCO at 300 years	
	JC032		JC159		cAABW	pAABW
	cAABW	pAABW	cAABW	pAABW		
Lab & GIN Seas (ECCO Region 7)	20%	24%	22%	26%	4%	6%
Weddell Sea (ECCO region 12)	70%	60%	66%	57%	10%	8%

Table 6.2 – Contributions of Weddell Sea and Lab & GIN Sea water to cAABW and pAABW as predicted by the MEM and ECCO.

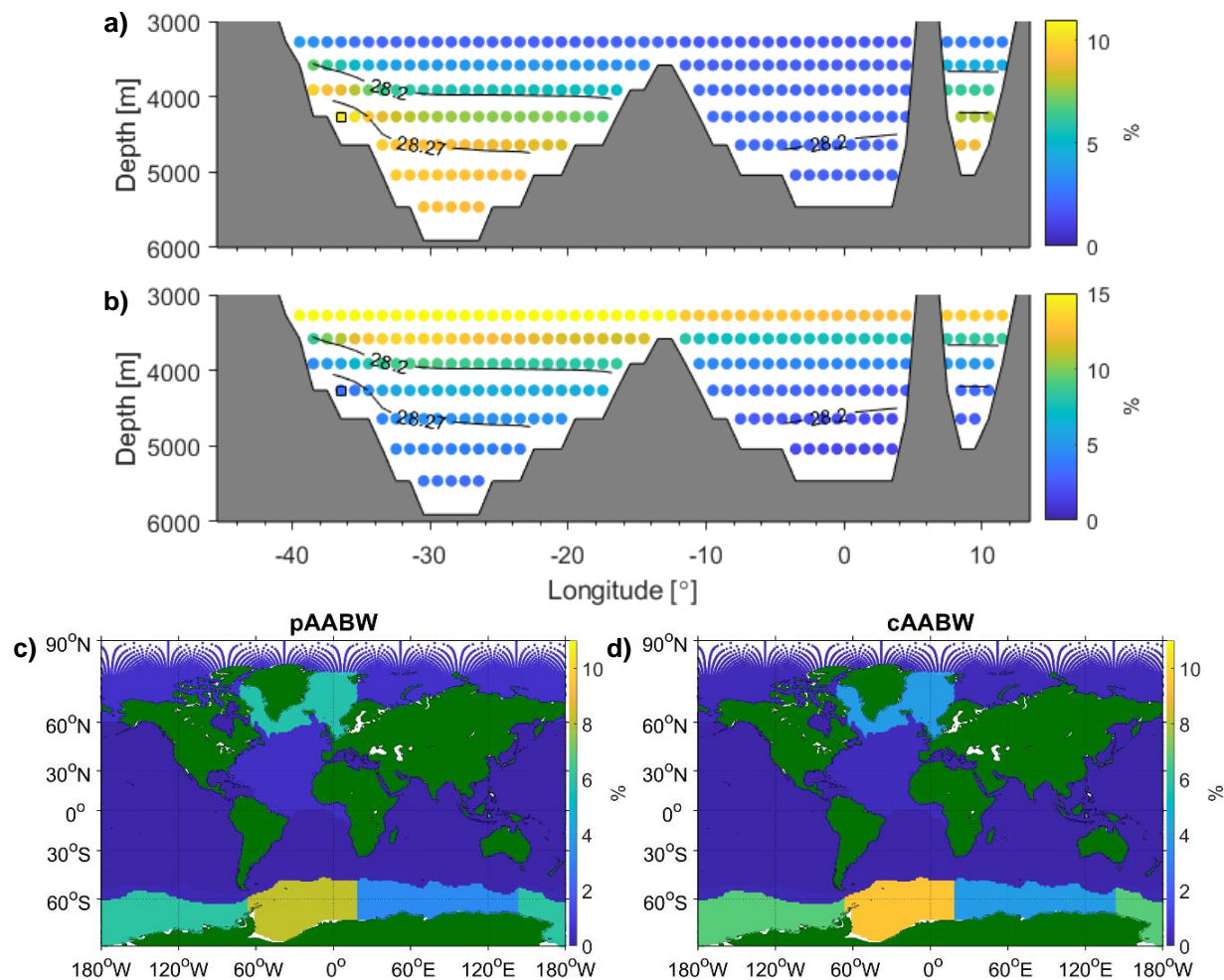


Figure 6.11 – (a & b) Distribution of ECCO passive tracer at 24°S, at 300 model years, for Region 12 (Weddell, a) and Region 7 (GIN seas, b). (c & d) Maps showing the % contribution of each ECCO passive tracer region to cAABW (c) and pAABW (d) waters in the Brazil Basin at 24°S. Black square on a and b indicates ‘point core’ referred to in text. Note: colour axis of (b) is restricted to 15%.

The Weddell Sea contribution in ECCO may be lower than in the MEM predictions due to higher contributions from the Indian and Pacific S of PF regions in ECCO (Figure 6.11c & d). The MEM did not predict any origin from the Pacific and Indian S of PF regions, whereas ECCO suggests a 6% and 3% contribution for pAABW and 7% and 4% contribution for cAABW, for the Indian and Pacific sectors respectively. An additional consideration when contemplating the relatively low contribution from the Weddell Sea in ECCO is that of timescale. Even at 300 model years the concentration of the Weddell ECCO tracer is still increasing (Figure 6.12), suggesting the result does not reflect the full Weddell Sea contribution at 24°S.

An explanation for the lower contribution from the Lab & GIN seas is less clear, but may also be due to the tracer not yet having reached equilibrium in cAABW and pAABW (Figure 6.12). It may also be due to lower entrainment of overlying waters into AABW in the model, compared to the real world.

Although ECCO does not include a time tracer, the evolution of tracer concentration at a location can reveal timescales of tracer transport (see Section 3.3.7). The evolution of the concentration of the Lab & GIN and Weddell tracers is explored at the point core of the AABW in ECCO. The point core is defined as the model grid-cell at 24°S in which the highest concentration of Weddell Sea tracer is found (36.5°W, 4260 m) (see Figure 6.11a & b).

The Weddell tracer is first seen at the AABW point core at 20 years and the concentration of the Weddell tracer continues to increase with time after this (Figure 6.12a & c). As mentioned, even at 300 years this tracer concentration has not stabilised and continues to increase. The maximum rate of increase has however peaked. The highest rate of tracer arrival is at 40 years. This age is in-

keeping with the conclusions drawn from the MEM results. The MEM suggests an age of \sim 30 years for the core AABW, a large proportion of which is predicted to originate from the Weddell Sea.

The MEM also predicts a strong contribution of NADW originating from the Iceland/Norwegian Sea. It predicts this water to be older (\sim 70 years), and with the limitations of the transient tracer history, this age signal is interpreted as a more general indication of 60+ year old waters with little or no transient tracers.

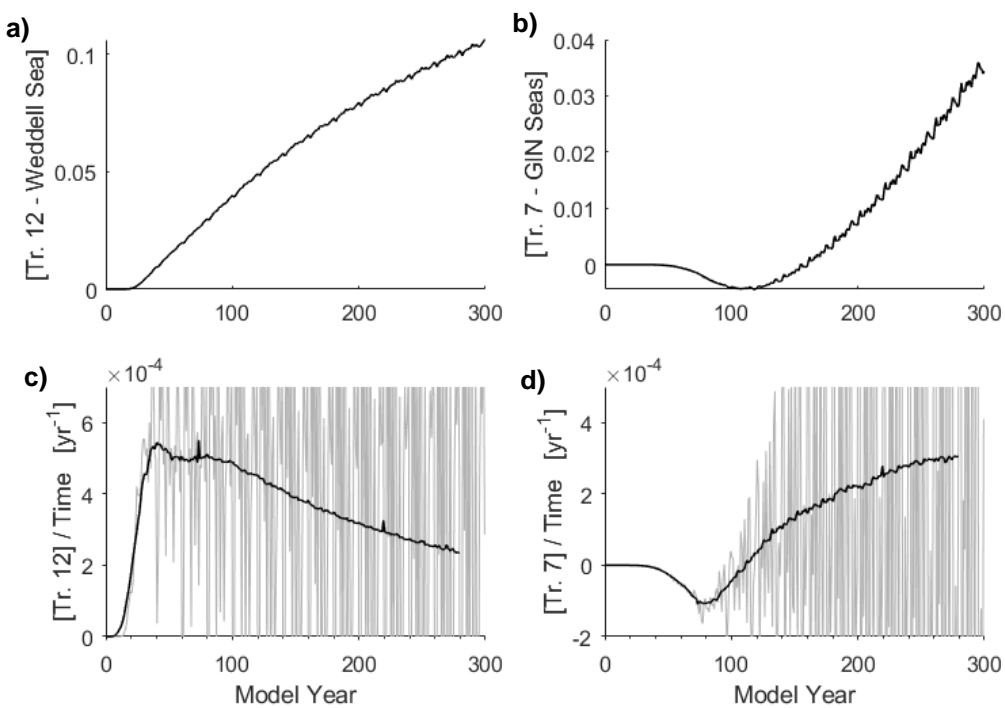


Figure 6.12 – Tracer concentration (a & b) and rate of tracer arrival (c & d) at the AABW point core (see text & Figure 6.11) at 24°S. In c & d, grey shows rate based on unsmoothed annual tracer concentration, black shows rate based on annual tracer concentration after a 20 year centred moving average has been applied.

The ECCO tracers suggest a first arrival of Lab & GIN waters in the point core of AABW at 110 years (Figure 6.12b & d). Like the Weddell tracer, the concentration of the Lab & GIN tracer is also still increasing at 300 years. However, unlike the Weddell tracer the Lab & GIN tracer has not yet reached a maximum rate of arrival (Figure 6.12b). There is also a period of negative tracer

concentration prior to the initial increase in tracer concentration, which is caused by an unwanted feature of the passive tracer configuration (see Section 3.3.2).

Although 110 years is several decades after/older than the MEM predicted age, the ECCO age is still considered to align with the MEM results. This is because they both indicate an influence of NADW older than 60+ years. As noted, compared to the MEM output, the contribution of the Lab & GIN seas to the AABW core in ECCO is very low. If there was lower levels of entrainment of overlying (high NADW) water, this could also explain the later arrival time of the Lab & GIN tracer.

6.9 Comparison of Main Findings to the Literature

The initial aims of this chapter were to assign an age to AABW at 24°S in the South Atlantic, and to assess how this age varied on a decadal timescale using repeat observational data. Unfortunately, the aim of assessing the difference between the repeats could not be met, due to an apparent biasing of the results to years with a particularly high CFC-11/CFC-12 concentration ratio. As a result of this, relationships were not drawn between observed global changes in AABW volume and temperature (see Section 1.3.2) and differences between repeat occupations at 24°S. However, an age for AABW at 24°S was successfully determined.

Previous studies suggested that AABW in the South Atlantic originates predominantly from the Weddell Sea region (e.g. Purkey *et al.*, 2018), with an additional influence of waters from the East of the Weddell Sea (Meredith *et al.*, 2000). These waters from the East are thought to originate from the Cape Darnley Polynya (Ohshima *et al.*, 2013). This work did not detect a Cape

Darnley influence, but did undoubtedly show that the Weddell Sea region is the dominant source of AABW in the Atlantic.

Few studies have focussed on the circulation timescales of AABW in the Atlantic, and so comparisons of age with the literature are limited. This work predicts that it takes ~ 30 years for water from this Weddell Sea source to reach 24°S as AABW. The closest age for comparison is the water leaving the Weddell Gyre at the Greenwich Meridian (58°-61°S, 4000-4500 m), which was predicted to have an age of 13.5 ± 2.5 years by Klatt *et al.* (2002).

If a back of the envelope calculation is undertaken, assuming a (fairly direct) pathway between this region and the western 24°S section of ~5000 km, and a transit time of 20 years (rough difference between age of water leaving Weddell Gyre and age of water at 24°S), water following this pathway would travel at an average speed of 0.008 m s^{-1} . This is only a very rough calculation, but 0.008 m s^{-1} is of the order of magnitude expected for an abyssal flow (e.g. Murty *et al.*, 2001). Overall, it is found that the results of this chapter affirm the existing knowledge of formation regions and further the knowledge of circulation timescales for AABW in the Atlantic.

6.10 Conclusion

In summary, the MEM predicted three spatial origins for AABW; the south-eastern North Atlantic, the Greenland and Norwegian Seas, and the Weddell Sea. The south-eastern North Atlantic signal was discounted as unrealistic. The Greenland and Norwegian Sea signal was linked to an influence of old (60+ years) NADW in the form of LCDW which appeared to mix into the AABW from above. The Weddell Sea signal was linked to a 30 year age signal,

suggesting a 30 year timescale for waters to form in the western and southwestern Weddell Sea and transit to 24°S in the South Atlantic.

The MEM predicted that water of Weddell Sea origin originally formed in the Southern Hemisphere winter and spring months of August, September and October. It predicted water of Greenland/Norwegian Sea origin, to form in the Northern Hemisphere winter and spring months of February, March and April.

The ECCO tracers supported the MEM results, with ECCO demonstrating the same spatial patterns of a strong contribution of Weddell Sea water to the bottom waters, and an increasing influence of Lab & GIN Seas' water with shallowing depth above this bottom water. The ECCO tracers suggested an initial arrival of Weddell Sea water at 20 years and a peak arrival at 40 years, fully supporting the MEM age of 30 years. The contributions of water from the Greenland/Norwegian Seas (Lab & GIN region) to AABW at 24°S was lower and older than predicted by the MEM, which was thought to be in part due to less entrainment in the model than in the real ocean.

In the future it would be beneficial to further explore the sensitivity of the results to the shape of the atmospheric history of each tracer. This would help to clarify the validity of inferring circulation change from decadal repeats of transient tracer measurements. It would also confirm whether a slowdown in AABW circulation has contributed to the MEM predicting the same year of origin for cAABW for both occupations of the 24°S section.

An extension of this work would also be to apply this same methodology to the AABW transient tracer measurements collected on the ANDREX (Antarctic Deep Water Rates of Export) section at 60°S in the Atlantic sector of the Southern Ocean. This would allow for changes between the decadal

repeats to be explored in more recently ventilated AABW. It would also allow for a more valid comparison of the ages predicted by this method with those of Klatt *et al.* (2002), due to the close proximity of the measurements used by Klatt *et al.* and those collected on ANDREX.

Chapter 7:

Overall Conclusion

AAIW and AABW are both globally important water masses, responsible for a large proportion of northward transport in the AMOC and responsible for sequestering carbon and heat within the interior ocean. Both water masses have demonstrated global property changes over the past decades, with AABW warming and decreasing in volume in many locations (Purkey and Johnson, 2010; Purkey and Johnson, 2012), and AAIW freshening globally (Wong, 1999; Curry *et al.*, 2003). There is concern that these property changes may hint at changes in formation rate and transport, potentially altering the uptake and transport of anthropogenic carbon and heat into the interior ocean. Despite this strong motivation, there is limited understanding of the timescales on which AAIW and AABW transport these properties into the interior ocean, and no baseline to assess changes to these timescales brought about by climate change.

The overarching aim of this thesis was to further develop knowledge of the transport of AAIW and AABW in the South Atlantic by assigning timescales to this northward transport, and assessing whether these timescales have changed between measurements taken in 2009 and 2018. This was achieved by applying a MEM to transient tracer observations and using the ECCOv4 ocean model to validate the results.

AAIW

As there is no clear consensus over the source of AAIW in the South Atlantic, nor the mechanism by which it is formed, part of understanding the timescales of AAIW transport was also to identify source regions and possible transport pathways. The current understanding of formation is that AAIW either forms from the densest layers of SAMW or via the subduction of AASW at the PF. It is also understood that AAIW in the Atlantic is comprised of a low AOU, fresher component from Drake Passage/the Southeast Pacific, the cold pathway contribution, and a saltier, higher AOU component from the Indian Ocean, the warm pathway contribution (e.g. Gordon *et al.*, 1992; You, 2002).

This thesis identified two distinct signals in the AAIW at 24°S; a younger signal of approximately 5-25 years which dominated the lighter AAIW layers and an older signal of approximately 35-55 years which dominated the denser AAIW layers. These lighter waters were thought to be formed via the SAMW subduction mechanism to the north of the SAF. Whilst the older waters were shown to originate from surface waters to the south of the PF, likely forming AAIW via the subduction of AASW at the PF.

These two temporal signals did not correspond directly to the warm and cold pathway. Instead, it was thought that the young signal was comprised of water from north of the SAF in the Indian Ocean (the warm pathway), and water which formed in the Southeast Pacific in the region to the north of the SAF and between the PF and SAF (part of the cold pathway). The older signal was purely linked to the cold pathway, and thought to be comprised of AASW from the Pacific, and AASW from the Atlantic and Indian Sectors, which has been transported eastward in the ACC prior to passing through Drake Passage.

As the volume of AAIW has been observed to be decreasing globally (Portela *et al.*, 2020), but it has also been demonstrated that a strengthening of the winds could lead to an increase in AAIW formation due to an a strengthening of the Southern Ocean meridional overturning (Waugh *et al.*, 2019); an important aspect of the thesis aims was to look for decadal changes. This thesis examined the differences in the MEM predicted temporal origin of AAIW between two occupations of the 24°S section, in 2009 and 2018. Both the younger and older temporal signal showed some degree of aging between the two occupations. The young signal had an average modal age (for AAIW 1) of 13 years using the 2009 measurements and an age of 16 years using the 2018 measurements. The older signal had an average modal age (for AAIW 1) of 39 years for the 2009 measurements, and 48 years for the 2018 measurements. No single unambiguous explanation for this aging of both the old and young components of AAIW was found, however it was thought the most likely explanation was a combination of several different processes. These included a poleward shift and intensification of the westerly winds, a change in the contribution of end members, a temporary shutdown in AAIW formation, and in the case of the older signal, whose year of origin was the same for both occupations, a large episodic event.

This possibility of a signal from a large episodic event led to the development of a hypothesis linking the Weddell Polynya to AAIW at 24°S. Southern Ocean polynyas are known as areas of formation of dense bottom water (e.g. Gordon, 2014), but are not known to contribute, either directly or indirectly, to the formation of intermediate waters. However, the temporal signals in the AAIW suggested a large contribution of waters from south of the

PF in the early 1970s in both the 2009 and 2018 data, which closely correlated to the years in which a large polynya was observed in the Weddell Sea.

This thesis explored the possibility of water formed within a Weddell Polynya influencing AAIW at 24°S. The Polynya Water was found to reach 24°S in the South Atlantic at low concentrations (< 2%) within 80 years, but no trace of the Polynya Water was observed at AAIW densities. It was however found that the volume of water modified by the polynya was large enough to result in a measurable impact on the meridional density gradient in the Weddell Sea region. This change in the density gradient temporarily increased the ACC transport by 1.5 Sv, an increase which was sustained to some degree for multiple decades after the density gradient returned to its original state. This suggested that, although below the current detectable limits, the Weddell Polynya in the 1970s may still have an impact on today's ACC transport.

AABW

Compared to AAIW, the existing understanding of the origin of AABW is much more accepted, and so the focus of the AABW aspect of this thesis was more on the temporal origin than the spatial origin. This thesis found the most pure form of AABW at 24°S to predominantly comprise of water from the Weddell Sea region, with an increasing contribution of waters of GIN Seas' origin with decreasing density. The Weddell Sea contribution did not however contain any temporal signal relating to the Weddell Sea Polynya in the 1970s, as might have been suggested by the Weddell Polynya Experiment, but instead a temporal signature of ~ 30 years. This timescale was thought to reflect the transit time of water which first forms as HSSW in the western and southwestern Weddell Sea before leaving the shelf and forming WSBW and

WSDW, which then becomes AABW after it leaves the Weddell Basin. The timescale associated with the water of GIN Seas' origin was 60+ years, and was not further constrained due to the limited time history of the transient tracers. It was thought that this water was NADW which had previously travelled southward, before transforming into LCDW in the Southern Ocean and returning north at depth.

Previously transient tracer derived ages in the Southern Ocean have suggested a strengthening of the upper overturning cell (reduction in water age) and a weakening of the lower overturning cell (increase in water age) (Waugh *et al.*, 2013; Ting and Holzer, 2017). This thesis focussed on AAIW and AABW further from its Southern Ocean source. Changes in the lower overturning cell (AABW) were not inferred due to limitations in the method. However, changes in the age of AAIW at 24°S indicated the opposite pattern to the above studies, instead suggesting waters in the upper limb of the overturning are aging, which would suggest a weakening of the upper cell.

Future Work

The following points cover improvements for future applications of the MEM to transient tracer measurements, and a suggestion of a way to enhance the value of the results found in this thesis.

1. In this thesis both prior sensitivity tests and ensemble standard deviations suggested that the results of the MEM are robust and strongly guided by the transient tracer measurements themselves. However, the link found between the tracer boundary condition and the probability of temporal origin for AABW (Figure 6.5) suggests that any boundary conditions may have a strong

influence on the results. This highlights the need for continued measurements of tracers in the surface ocean and atmosphere, and the importance of continual development of ocean gridded surface products in order to achieve the highest quality boundary conditions. It also indicates that in any future application of the MEM, a thorough assessment of the sensitivity of the results to the boundary condition should be made.

2. The true value of this work lies in its further application. Although transient tracer derived ages may be able to indicate decadal circulation change where decadal repeats are available, they can also be used to estimate the anthropogenic heat and carbon content of a measured water mass. As the output of the MEM is a form of discretized Green's function, it can be used as a boundary propagator to suggest the amount of anthropogenic heat and carbon held by a water mass, even if there are multiple temporal and spatial sources. A future aim would be to use the MEM output generated here to estimate the anthropogenic carbon and added heat content in AAIW and AABW at 24°S, and to compare this to both observations of temperature and carbon, and estimates of anthropogenic carbon and added heat produced using other methods.

References

- Abrahamsen, E. P., Meijers, A. J. S., Polzin, K. L., Naveira Garabato, A. C., King, B. A., Firing, Y. L., Sallée, J., Sheen, K. L., Gordon, A. L., Huber, B. A., and Meredith, M. P. (2019) Stabilization of dense Antarctic water supply to the Atlantic Ocean overturning circulation. *Nature Climate Change* 9(10): 742–746.
- Adcroft, A., Hill, C., Campin, J. M., Marshall, J., and Heimbach, P. (2004) Overview of the Formulation and Numerics of the MIT GCM. *Proceedings of the ECMWF Seminar Series on Numerical Methods, Recent Developments in Numerical Methods for Atmosphere and Ocean Modelling*. ECMWF Accessed: 20th September 2021 <<http://mitgcm.org/pdfs/ECMWF2004-Adcroft.pdf>>.
- Allison, L. C., Johnson, H. L., and Marshall, D. P. (2011) Spin-up and adjustment of the Antarctic Circumpolar Current and global pycnocline. *Journal of Marine Research* 69(2–3): 167–189.
- Alves, E. Q., Macario, K., Ascough, P., and Bronk Ramsey, C. (2018) The Worldwide Marine Radiocarbon Reservoir Effect: Definitions, Mechanisms, and Prospects. *Reviews of Geophysics* 56(1): 278–305.
- Azaneu, M., Kerr, R., Mata, M. M., and Garcia, C. A. E. (2013) Trends in the deep Southern Ocean (1958–2010): Implications for Antarctic Bottom Water properties and volume export. *Journal of Geophysical Research: Oceans* 118(9): 4213–4227.
- Banks, H. T., Wood, R. A., Gregory, J. M., Johns, T. C., and Jones, G. S. (2000) Are observed decadal changes in the intermediate water masses a signature of anthropogenic climate change? *Geophysical Research Letters* 27(18): 2961–2964.
- Belkin, I. M., and Gordon, A. L. (1996) Southern Ocean fronts from the Greenwich meridian to Tasmania. *Journal of Geophysical Research: Oceans* 101(C2): 3675–3696.
- Bi, D., Budd, W. F., Hirst, A. C., and Wu, X. (2002) Response of the antarctic circumpolar current transport to global warming in a coupled model. *Geophysical Research Letters* 29(24): 24-1-24–4.
- Biastoch, A., Böning, C. W., Schwarzkopf, F. U., and Lutjeharms, J. R. E. (2009) Increase in Agulhas leakage due to poleward shift of Southern Hemisphere westerlies. *Nature* 462(7272): 495–498.
- Biastoch, A., Durgadoo, J. V., Morrison, A. K., van Sebille, E., Weijer, W., and Griffies, S. M. (2015) Atlantic multi-decadal oscillation covaries with Agulhas leakage. *Nature Communications* 6(1): 10082.
- Bindoff, N. L., Willebrand, J., Artale, V., A, C., Gregory, J., Gulev, S., Hanawa, K., Quéré, C. Le, Levitus, S., Nojiri, Y., Shum, C. K., Talley, L. D., and Unnikrishnan, A. (2007) Observations: oceanic climate change and sea level. In Solomon, S., Qin, D., Manning, M., Chen, Z., Marquis, M., Averyt, K. B., Tignor, M., and Miller, H. L. (Eds.), *Climate Change 2007: The Physical Science Basis. Contribution of Working Group I to the Fourth Assessment Report of the*

Intergovernmental Panel on Climate Change. Cambridge and New York: Cambridge University Press.

Böning, C. W., Dispert, A., Visbeck, M., Rintoul, S. R., and Schwarzkopf, F. U. (2008) The response of the Antarctic Circumpolar Current to recent climate change. *Nature Geoscience* 1(12): 864–869.

Bullister, J. L. (2017) Atmospheric Histories (1765-2015) for CFC-11, CFC-12, CFC-113, CCl4, SF6 and N2O. *NOAA National Centers for Environmental Information*. doi:10.3334/CDIAC/otg.CFC_ATM_Hist_2015.

Bullister, J. L., Wisegarver, D. P., and Menzia, F. A. (2002) The solubility of sulfur hexafluoride in water and seawater. *Deep Sea Research Part I: Oceanographic Research Papers* 49(1): 175–187.

Buscaglia, J. L. (1971) On the circulation of the Intermediate Water in the southwestern Atlantic Ocean. *Journal of Marine Research* 29(203): 245–255.

Bracegirdle, T. J., Krinner, G., Tonelli, M., Haumann, F. A., Naughten, K. A., Rackow, T., Roach, L. A., and Wainer, I. (2020) Twenty first century changes in Antarctic and Southern Ocean surface climate in CMIP6. *Atmospheric Science Letters* 21(9): 1–14.

Broecker, W. S., Peacock, S. L., Walker, S., Weiss, R., Fahrbach, E., Schroeder, M., Mikolajewicz, U., Heinze, C., Key, R., Peng, T.-H., and Rubin, S. (1998) How much deep water is formed in the Southern Ocean? *Journal of Geophysical Research: Oceans* 103(C8): 15833–15843.

Bronsemaer, B., Winton, M., Griffies, S. M., Hurlin, W. J., Rodgers, K. B., Sergienko, O. V., Stouffer, R. J., and Russell, J. L. (2018) Change in future climate due to Antarctic meltwater. *Nature* 564(7734): 53–58.

Carsey, F. (1980) Microwave Observation of the Weddell Polynya. *Monthly Weather Review* 108(12): 2032–2044.

Cheon, W. G., and Gordon, A. L. (2019) Open-ocean polynyas and deep convection in the Southern Ocean. *Scientific Reports* 9(1): 1–9.

Coles, V. J., McCartney, M. S., Olson, D. B., and Smethie, W. M. (1996) Changes in Antarctic Bottom Water properties in the western South Atlantic in the late 1980s. *Journal of Geophysical Research: Oceans* 101(C4): 8957–8970.

Collins, M., Knutti, R., Arblaster, J., Dufresne, J.-L., Fichefet, T., Friedlingstein, P., Gao, X., Gutowski, W. J., Johns, T., Krinner, G., Shongwe, M., Tebaldi, C., Weaver, A. J., and Wehner, M. (2013) Long-term Climate Change: Projections, Commitments and Irreversibility. In Stocker, T. F., Qin, D., Plattner, G.-K., Tignor, M., Allen, S. K., Boschung, J., Nauels, A., Xia, Y., Bex, V., and Midgley, P. M. (Eds.), *Climate Change 2013: The Physical Science Basis. Contribution of Working Group I to the Fifth Assessment Report of the Intergovernmental Panel on Climate Change*. Cambridge and New York: Cambridge University Press doi:10.1017/CBO9781107415324.024.

- Cunningham, S. A., Alderson, S. G., King, B. A., and Brandon, M. A. (2003) Transport and variability of the Antarctic Circumpolar Current in Drake Passage. *Journal of Geophysical Research* 108(C5): 1–17.
- Curry, R., Dickson, B., and Yashayaev, I. (2003) A change in the freshwater balance of the Atlantic Ocean over the past four decades. *Nature* 426(6968): 826–829.
- Davies, B. (2020) Southern Westerly Winds. Accessed: 18th April 2022 <<https://www.antarcticglaciers.org/glaciers-and-climate/changing-antarctica/southern-annular-mode/sww/>>.
- de Ruijter, W. P. M., Biastoch, A., Drijfhout, S. S., Lutjeharms, J. R. E., Matano, R. P., Pichevin, T., van Leeuwen, P. J., and Weijer, W. (1999) Indian-Atlantic interocean exchange: Dynamics, estimation and impact. *Journal of Geophysical Research: Oceans* 104(C9): 20885–20910.
- Deacon, G. E. R. (1937) The Hydrology of the Southern Ocean. *Cambridge University Press* 15: 3–12.
- Dee, D. P., Uppala, S. M., Simmons, A. J., Berrisford, P., Poli, P., Kobayashi, S., et al. (2011) The ERA-Interim reanalysis: configuration and performance of the data assimilation system. *Quarterly Journal of the Royal Meteorological Society* 137(656): 553–597.
- Desbruyères, D. G., Purkey, S. G., McDonagh, E. L., Johnson, G. C., and King, B. A. (2016) Deep and abyssal ocean warming from 35 years of repeat hydrography. *Geophysical Research Letters* 43(19): 10,356–10,365.
- Donohue, K. A., Tracey, K. L., Watts, D. R., Chidichimo, M. P., and Chereskin, T. K. (2016) Mean Antarctic Circumpolar Current transport measured in Drake Passage. *Geophysical Research Letters* 43(22): 11,760–11,767.
- Downes, S. M., Bindoff, N. L., and Rintoul, S. R. (2010) Changes in the Subduction of Southern Ocean Water Masses at the End of the Twenty-First Century in Eight IPCC Models. *Journal of Climate* 23(24): 6526–6541.
- Downes, S. M., Budnick, A. S., Sarmiento, J. L., and Farneti, R. (2011) Impacts of wind stress on the Antarctic Circumpolar Current fronts and associated subduction. *Geophysical Research Letters* 38(11).
- Downes, S. M., Langlais, C., Brook, J. P., and Spence, P. (2017) Regional Impacts of the Westerly Winds on Southern Ocean Mode and Intermediate Water Subduction. *Journal of Physical Oceanography* 47(10): 2521–2530.
- Durgadoo, J. V., Loveday, B. R., Reason, C. J. C., Penven, P., and Biastoch, A. (2013) Agulhas Leakage Predominantly Responds to the Southern Hemisphere Westerlies. *Journal of Physical Oceanography* 43(10): 2113–2131.
- Evans, G. R., McDonagh, E. L., King, B. A., Bryden, H. L., Bakker, D. C. E., Brown, P. J., Schuster, U., Speer, K. G., and van Heuven, S. M. A. C. (2017) South Atlantic interbasin exchanges of mass, heat, salt and anthropogenic carbon. *Progress in Oceanography* 151: 62–82.

- Fahrbach, E., Hoppema, M., Rohardt, G., Boebel, O., Klatt, O., and Wisotzki, A. (2011) Warming of deep and abyssal water masses along the Greenwich meridian on decadal time scales: The Weddell gyre as a heat buffer. *Deep Sea Research Part II: Topical Studies in Oceanography* 58(25–26): 2509–2523.
- Fahrbach, E., Hoppema, M., Rohardt, G., Schröder, M., and Wisotzki, A. (2004) Decadal-scale variations of water mass properties in the deep Weddell Sea. *Ocean Dynamics* 54(1): 77–91.
- Farman, J. C., Gardiner, B. G., and Shanklin, J. D. (1985) Large losses of total ozone in Antarctica reveal seasonal ClO_x/NO_x interaction. *Nature* 315(6016): 207–210.
- Fine, R. A. (1993) Circulation of Antarctic intermediate water in the South Indian Ocean. *Deep-Sea Research Part I* 40(10): 2021–2042.
- Fine, R. A., Warner, M. J., and Weiss, R. F. (1988) Water mass modification at the Agulhas retroflection: chlorofluoromethane studies. *Deep Sea Research Part A, Oceanographic Research Papers* 35(3): 311–332.
- Forget, G., Campin, J., Heimbach, P., Hill, C. N., Ponte, R. M., and Wunsch, C. (2015) ECCO version 4 : an integrated framework for non-linear inverse modeling and global ocean state estimation. *Geoscientific Model Development* 8(10): 3071–3104.
- Foster, T. D. (1972) An Analysis of the Cabbeling Instability in Sea Water. *Journal of Physical Oceanography* 2(3): 294–301.
- Frölicher, T. L., Sarmiento, J. L., Paynter, D. J., Dunne, J. P., Krasting, J. P., and Winton, M. (2015) Dominance of the Southern Ocean in anthropogenic carbon and heat uptake in CMIP5 models. *Journal of Climate* 28(2): 862–886.
- Fyfe, J. C., and Saenko, O. A. (2006) Simulated changes in the extratropical Southern Hemisphere winds and currents. *Geophysical Research Letters* 33(L06701): 1–4.
- Gaspar, P., Grégoris, Y., and Lefevre, J.-M. (1990) A simple eddy kinetic energy model for simulations of the oceanic vertical mixing: Tests at station Papa and long-term upper ocean study site. *Journal of Geophysical Research* 95(C9): 16179.
- Gent, P. R. (2016) Effects of Southern Hemisphere Wind Changes on the Meridional Overturning Circulation in Ocean Models. *Annual Review of Marine Science* 8(1): 79–94.
- Gent, P. R., and McWilliams, J. C. (1990) Isopycnal Mixing in Ocean Circulation Models. *Journal of Physical Oceanography* 20(1): 150–155.
- Gent, P. R., Willebrand, J., McDougall, T. J., and McWilliams, J. C. (1995) Parameterizing Eddy-Induced Tracer Transports in Ocean Circulation Models. *Journal of Physical Oceanography* 25(4): 463–474.
- Gordon, A. L. (1982) Weddell deep water: Source and variability. *Journal of Marine Research* 40: 199–217.

- Gordon, A. L. (1985) Indian-Atlantic Transfer of Thermocline Water at the Agulhas Retroflection. *Science* 227(4690): 1030–1033.
- Gordon, A. L. (2009) Bottom Water Formation. In Steele, J. H., Thorpe, S. A., and Turekian, K. K. (Eds.), *Ocean Currents: A Derivative of Encyclopaedia of Ocean Sciences* (2nd edition). London: Elsevier.
- Gordon, A. L. (2014) Southern Ocean polynya. *Nature Climate Change* 4(4): 249–250.
- Gordon, A. L., Huber, B. A., and Busecke, J. (2015) Bottom water export from the western Ross Sea, 2007 through 2010. *Geophysical Research Letters* 42(13): 5387–5394.
- Gordon, A. L., Huber, B., McKee, D., and Visbeck, M. (2010) A seasonal cycle in the export of bottom water from the Weddell Sea. *Nature Geoscience* 3(8): 551–556.
- Gordon, A. L., Lutjeharms, J. R. E., and Gründlingh, M. L. (1987) Stratification and circulation at the Agulhas Retroflection. *Deep Sea Research Part A. Oceanographic Research Papers* 34(4): 565–599.
- Gordon, A. L., Visbeck, M., and Comiso, J. C. (2007) A Possible Link between the Weddell Polynya and the Southern Annular Mode*. *Journal of Climate* 20(11): 2558–2571.
- Gordon, A. L., Weiss, R. F., Smethie, W. M., and Warner, M. J. (1992) Thermocline and intermediate water communication between the South Atlantic and Indian oceans. *Journal of Geophysical Research* 97(C5): 7223–7240.
- Grey, D. C. (1969) Geophysical Mechanisms for C-14 Variations. *Journal Geophysical Research* 74(26): 6333–6340.
- Hall, A., and Visbeck, M. (2002) Synchronous Variability in the Southern Hemisphere Atmosphere, Sea Ice, and Ocean Resulting from the Annular Mode*. *Journal of Climate* 15(21): 3043–3057.
- Hansen, J., Sato, M., Hearty, P., Ruedy, R., Kelley, M., Masson-Delmotte, V., Russell, G., Tselioudis, G., Cao, J., Rignot, E., Velicogna, I., Tormey, B., Donovan, B., Kandiano, E., von Schuckmann, K., Kharecha, P., Legrande, A. N., Bauer, M., and Lo, K.-W. (2016) Ice melt, sea level rise and superstorms: evidence from paleoclimate data, climate modeling, and modern observations that 2 °C global warming could be dangerous. *Atmospheric Chemistry and Physics* 16(6): 3761–3812.
- Harcourt, R. R. (2005) Thermobaric cabling over Maud Rise: Theory and large eddy simulation. *Progress in Oceanography* 67(1–2): 186–244.
- Haumann, F. A., Gruber, N., Münnich, M., Frenger, I., and Kern, S. (2016) Sea-ice transport driving Southern Ocean salinity and its recent trends. *Nature* 537(7618): 89–92.

- Heezen, B. C., Tharp, M., and Bentley, C. R. (1972) Morphology of the Earth in the Antarctic and Subantarctic. Antarctic map folio series, no. 16, American Geographical Society
- Heuzé, C., Heywood, K. J., Stevens, D. P., and Ridley, J. K. (2015) Changes in Global Ocean Bottom Properties and Volume Transports in CMIP5 Models under Climate Change Scenarios*. *Journal of Climate* 28(8): 2917–2944.
- Heywood, K. J., Schmidtko, S., Heuzé, C., Kaiser, J., Jickells, T. D., Queste, B. Y., Stevens, D. P., Wadley, M., Thompson, A. F., Fielding, S., Guihen, D., Creed, E., Ridley, J. K., and Smith, W. (2014) Ocean processes at the Antarctic continental slope. *Philosophical Transactions of the Royal Society A: Mathematical, Physical and Engineering Sciences* 372(2019): 1–11.
- Holland, D. M. (2001) Explaining the Weddell Polynya--a Large Ocean Eddy Shed at Maud Rise. *Science* 292(5522): 1697–1700.
- Holzer, M., and Hall, T. M. (2000) Transit-Time and Tracer-Age Distributions in Geophysical Flows. *Journal of the Atmospheric Sciences* 57(21): 3539–3558.
- Holzer, M., and Primeau, F. W. (2010) Improved constraints on transit time distributions from argon 39: A maximum entropy approach. *Journal of Geophysical Research: Oceans* 115(12): 1–19.
- Holzer, M., Primeau, F. W., Smethie, W. M., and Khatiwala, S. (2010) Where and how long ago was water in the western North Atlantic ventilated? Maximum entropy inversions of bottle data from WOCE line A20. *Journal of Geophysical Research* 115(C7): 1–26.
- Holzer, M., Smethie, W. M. J., and Ting, Y.-H. (2018) Ventilation of the Subtropical North Atlantic: Locations and Times of Last Ventilation Estimated Using Tracer Constraints From GEOTRACES Section GA03. *Journal of Geophysical Research: Oceans* (123): 2332–2352. doi:10.1002/2017JC013698.
- Holzer, M., and Waugh, D. W. (2015) Interhemispheric transit time distributions and path-dependent lifetimes constrained by measurements of SF₆, CFCs, and CFC replacements. *Geophysical Research Letters* 42(11): 4581–4589.
- Hughes, C. W., and Ash, E. R. (2001) Eddy forcing of the mean flow in the Southern Ocean. *Journal of Geophysical Research: Oceans* 106(C2): 2713–2722.
- Huhn, O., Rhein, M., Hoppema, M., and van Heuven, S. (2013) Decline of deep and bottom water ventilation and slowing down of anthropogenic carbon storage in the Weddell Sea, 1984-2011. *Deep-Sea Research Part I: Oceanographic Research Papers* 76: 66–84.
- Hutchinson, K., Swart, S., Meijers, A., Ansorge, I., and Speich, S. (2016) Decadal-scale thermohaline variability in the Atlantic sector of the Southern Ocean. *Journal of Geophysical Research: Oceans* 121(5): 3171–3189.
- Jacobs, S. S., and Comiso, J. C. (1989) Sea ice and oceanic processes on the Ross Sea continental shelf. *Journal of Geophysical Research* 94(C12): 18195.

- Jacobs, S. S., Fairbanks, R. G., and Horibe, Y. G. (1985) Origin and evolution of water masses near the Antarctic continental margin: Evidence from H₂18O/H₂16O ratios in seawater. In Jacobs, S. S. (Ed.), *Oceanology of the Antarctic Continental Shelf* (Vol. 43).
- Jacobs, S. S., and Georgi, D. T. (1977) Observations on the southwest Indian/Antarctic Ocean. In Angel, M. V. (Ed.), *A Voyage of Discovery. Deep - Sea Research Supplement to Vol. 24.*
- Jacobs, S. S., and Giulivi, C. F. (2010) Large Multidecadal Salinity Trends near the Pacific–Antarctic Continental Margin. *Journal of Climate* 23(17): 4508–4524.
- Jacobs, S. S., Giulivi, C. F., and Mele, P. A. (2002) Freshening of the Ross Sea During the Late 20th Century. *Science* 297(5580): 386–389.
- Jackett, D. R., and McDougall, T. J. (1995) Minimal Adjustment of Hydrographic Profiles to Achieve Static Stability. *Journal of Atmospheric and Oceanic Technology* 12(2): 381–389.
- Jackett, D. R., and McDougall, T. J. (1997) A Neutral Density Variable for the World's Oceans. *Journal of Physical Oceanography* 27(2): 237–263.
- Johnson, G. C., and Doney, S. C. (2006) Recent western South Atlantic bottom water warming. *Geophysical Research Letters* 33(14): 1–5.
- Johnson, G. C., McTaggart, K. E., and Wanninkhof, R. (2014) Antarctic Bottom Water temperature changes in the western South Atlantic from 1989 to 2014. *Journal of Geophysical Research: Oceans* 119: 8567–8577.
- Jullion, L., Naveira Garabato, A. C., Meredith, M. P., Holland, P. R., Courtois, P., and King, B. A. (2013) Decadal Freshening of the Antarctic Bottom Water Exported from the Weddell Sea. *Journal of Climate* 26(20): 8111–8125.
- Kamenkovich, I., Garraffo, Z., Pennel, R., and Fine, R. A. (2017) Importance of mesoscale eddies and mean circulation in ventilation of the Southern Ocean. *Journal of Geophysical Research: Oceans* 122(4): 2724–2741.
- Katsumata, K., Nakano, H., and Kumamoto, Y. (2015) Dissolved oxygen change and freshening of Antarctic Bottom water along 62°S in the Australian-Antarctic Basin between 1995/1996 and 2012/2013. *Deep Sea Research Part II: Topical Studies in Oceanography* 114: 27–38.
- Key, R. M. (2001) Radiocarbon. In *Encyclopedia of Ocean Sciences*. Elsevier Ltd doi:10.1006/rwos.2001.0162.
- Key, R. M., Kozyr, A., Sabine, C. L., Lee, K., Wanninkhof, R., Bullister, J. L., Feely, R. A., Millero, F. J., Mordy, C., and Peng, T.-H. (2004) A global ocean carbon climatology: Results from Global Data Analysis Project (GLODAP). *Global Biogeochemical Cycles* 18(4).
- Khatiwala, S., Primeau, F., and Hall, T. (2009) Reconstruction of the history of anthropogenic CO₂ concentrations in the ocean. *Nature* 462(7271): 346–349.
- Kirtman, B., Power, S. B., Adedoyin, J. A., Boer, G. J., Bojariu, R., Camilloni, I., Doblas-Reyes, F. J., Fiore, A. M., Kimoto, M., Meehl, G. A., Prather, M., Sarr,

- A., Schär, C., Sutton, R., Oldenborgh, G. J. van, Vecchi, G., and Wang, H. J. (2013) Near-term Climate Change: Projections and Predictability. In Stocker, T. F., Qin, D., Plattner, G.-K., Tignor, M., Allen, S. K., Boschung, J., Nauels, A., Xia, Y., Bex, V., and Midgley, P. M. (Eds.), *Climate Change 2013: The Physical Science Basis. Contribution of Working Group I to the Fifth Assessment Report of the Intergovernmental Panel on Climate Change*. Cambridge and New York: Cambridge University Press. doi:10.1017/CBO9781107415324.023.
- Klatt, O., Roether, W., Hoppema, M., Bulsiewicz, K., Fleischmann, U., Rodehacke, C., Fahrbach, E., Weiss, R. F., and Bullister, J. L. (2002) Repeated CFC sections at the Greenwich Meridian in the Weddell Sea. *Journal of Geophysical Research* 107(C4): 1–5.
- Landschützer, P., Gruber, N., Haumann, F. A., Rödenbeck, C., Bakker, D. C. E., Heuven, S. Van, Hoppema, M., Metzl, N., Sweeney, C., and Takahashi, T. (2015) The reinvigoration of the Southern Ocean carbon sink. *Science* 349(6253): 1221–1224.
- Larqué, L., Maamaatuaiahutapu, K., and Garçon, V. (1997) On the intermediate and deep water flows in the South Atlantic Ocean. *Journal of Geophysical Research: Oceans* 102(C6): 12425–12440.
- Le Quéré, C., Rödenbeck, C., Buitenhuis, E. T., Conway, T. J., Langenfelds, R., Gomez, A., Labuschagne, C., Ramonet, M., Nakazawa, T., Metzl, N., Gillett, N., and Heimann, M. (2007) Saturation of the Southern Ocean CO₂ Sink Due to Recent Climate Change. *Science* 316(5832): 1735–1738.
- Ledwell, J. R., Montgomery, E. T., Polzin, K. L., Laurent, L. C. S., Schmitt, R. W., and Toole, J. M. (2000) Evidence for enhanced mixing over rough topography in the abyssal ocean. *Nature* 403(6766): 179–182.
- Lester, J. G., Lovenduski, N. S., Graven, H. D., Long, M. C., and Lindsay, K. (2020) Internal Variability Dominates Over Externally Forced Ocean Circulation Changes Seen Through CFCs. *Geophysical Research Letters* 47(9).
- Lingenfelter, R., E. (1963) Production of Carbon 14 by cosmic-ray neutrons. *Review of Geophysics* 1(1): 35–55.
- Loveday, B. R., Penven, P., and Reason, C. J. C. (2015) Southern Annular Mode and westerly-wind-driven changes in Indian-Atlantic exchange mechanisms. *Geophysical Research Letters* 42(12): 4912–4921.
- Lumpkin, R., and Speer, K. (2007) Global Ocean Meridional Overturning. *Journal of Physical Oceanography* 37(10): 2550–2562.
- Mantyla, A. W., and Reid, J. L. (1995) On the origins of deep and bottom waters of the Indian Ocean. *Journal of Geophysical Research* 100(C2): 2417–2439.
- Marsh, R., Nurser, A. J. G., Megann, A. P., and New, A. L. (2000) Water mass transformation in the Southern Ocean of a global isopycnal coordinate GCM. *Journal of Physical Oceanography* 30(5): 1013–1045.
- Marshall, G. J. (2003) Trends in the Southern Annular Mode from Observations and Reanalyses. *Journal of Climate* 16(24): 4134–4143.

- Marshall, J., Adcroft, A., Hill, C., Perelman, L., and Heisey, C. (1997) A finite-volume, incompressible Navier Stokes model for studies of the ocean on parallel computers. *Journal of Geophysical Research: Oceans* 102(C3): 5753–5766.
- Marshall, G., and National Center for Atmospheric Research Staff (Eds) (2018) The Climate Data Guide: Marshall Southern Annular Mode (SAM) Index (Station-based). Accessed: 5th September 2021
<https://climatedataguide.ucar.edu/climate-data/marshall-southern-annular-mode-sam-index-station-based>.
- Marshall, J., and Schott, F. (1999) Open-Ocean Convection: Observations, theory and Models. *Reviews of Geophysics* 37(1): 1–64.
- Marshall, J., and Speer, K. (2012) Closure of the meridional overturning circulation through Southern Ocean upwelling. *Nature Geoscience* 5(3): 171–180.
- Martinson, D. G. (1991) Open Ocean Convection in the Southern Ocean. In *Elsevier Oceanography Series* (Vol. 57).
- Mashayek, A., Ferrari, R., Merrifield, S., Ledwell, J. R., St Laurent, L., and Garabato, A. N. (2017) Topographic enhancement of vertical turbulent mixing in the Southern Ocean. *Nature Communications* 8: 1–12.
- Matsumoto, K. (2007) Radiocarbon-based circulation age of the world oceans. *Journal of Geophysical Research: Oceans* 112(9): 1–7.
- McCarthy, G., McDonagh, E., and King, B. (2011) Decadal Variability of Thermocline and Intermediate Waters at 24°S in the South Atlantic. *Journal of Physical Oceanography* 41: 157–165.
- McCartney, M. S. (1977) Subantarctic Mode Water. In Angel, M. V. (Ed.), *Voyage of Discovery: George Deacon 70th Anniversary Volume*. Oxford: Pergamon Press.
- McDonagh, E. L., Heywood, K. J., and Meredith, M. P. (1999) On the structure, paths, and fluxes associated with Agulhas rings. *Journal of Geophysical Research: Oceans* 104(C9): 21007–21020.
- Meredith, M. P. (2016) Understanding the structure of changes in the Southern Ocean eddy field. *Geophysical Research Letters* 43(11): 5829–5832.
- Meredith, M. P., Garabato, A. C. N., Gordon, A. L., and Johnson, G. C. (2008) Evolution of the Deep and Bottom Waters of the Scotia Sea, Southern Ocean, during 1995–2005*. *Journal of Climate* 21(13): 3327–3343.
- Meredith, M. P., Jullion, L., Brown, P. J., Garabato, A. C. N., and Couldrey, M. P. (2014) Dense waters of the Weddell and Scotia seas: Recent changes in properties and circulation. *Philosophical Transactions of the Royal Society A: Mathematical, Physical and Engineering Sciences* 372(2019): 1–11.

- Meredith, M. P., Locarnini, R. A., Van Scoy, K. A., Watson, A. J., Heywood, K. J., and King, B. A. (2000) On the sources of Weddell Gyre Antarctic Bottom Water. *Journal of Geophysical Research: Oceans* 105(C1): 1093–1104.
- Meredith, M., Sommerkorn, M., Cassotta, S., Derksen, C., Ekaykin, A., Hollowed, A., Kofinas, G., Mackintosh, A., Melbourne-Thomas, J., Muelbert, M. M. C., Ottersen, G., Pritchard, H., and Schuur, E. A. G. (2019) Polar regions. In Pörtner, H.-O., Roberts, D. C., Masson-Delmotte, V., Zhai, P., Tignor, M., Poloczanska, E., Mintenbeck, K., Alegria, A., Nicolai, M., Okem, A., Petzold, J., Rama, B., and Weyer, N. M. (Eds.), *IPCC Special Report on the Ocean and Cryosphere in a Changing Climate* (Vol. 3).
- Meredith, M. P., Watson, A. J., Van Scoy, K. A., and Haine, T. W. N. (2001) Chlorofluorocarbon-derived formation rates of the deep and bottom waters of the Weddell Sea. *Journal of Geophysical Research: Oceans* 106(C2): 2899–2919.
- Mikaloff-Fletcher, S. E. (2015) An increasing carbon sink? *Science* 349(6253): 1165.
- MITgcm Group (2002) MITgcm Release 1 Manual. *Massachusetts Institute of Technology*. Accessed: 20th September 2021
<<http://mitgcm.org/public/sealion/>>.
- Molinelli, E. J. (1981) The Antarctic influence of Antarctic Intermediate Water. *Journal of Marine Research* 29: 267–293.
- Montzka, S. A., Dutton, G. S., Yu, P., Ray, E., Portmann, R. W., Daniel, J. S., Kuijpers, L., Hall, B. D., Mondeel, D., Siso, C., Nance, J. D., Rigby, M., Manning, A. J., Hu, L., Moore, F., Miller, B. R., and Elkins, J. W. (2018) An unexpected and persistent increase in global emissions of ozone-depleting CFC-11. *Nature* 557(7705): 413–417.
- Morrison, A. K., Frölicher, T. L., and Sarmiento, J. L. (2015) Upwelling in the Southern Ocean. *Physics Today* 68(1): 27–32.
- Murty, V. S., Savin, M., Babu, V. R., and Suryanarayana, A. (2001) Seasonal variability in the vertical current structure and kinetic energy in the Central Indian Ocean Basin. *Deep Sea Research Part II: Topical Studies in Oceanography* 48(16): 3309–3326.
- Nakano, H., and Sugino, N. (2002) Importance of the eastern Indian Ocean for the abyssal Pacific. *Journal of Geophysical Research: Oceans* 107(C12): 1–14.
- Naughten, K. A., Jenkins, A., Holland, P. R., Mugford, R. I., Nicholls, K. W., and Munday, D. R. (2019) Modeling the influence of the Weddell polynya on the Filchner–Ronne ice shelf cavity. *Journal of Climate* 32(16): 5289–5303.
- Naveira Garabato, A. C., Heywood, K. J., and Stevens, D. P. (2002) Modification and pathways of Southern Ocean Deep Waters in the Scotia Sea. *Deep Sea Research Part I: Oceanographic Research Papers* 49(4): 681–705.

- Naveira Garabato, A. C., Jullion, L., Stevens, D. P., Heywood, K. J., and King, B. A. (2009) Variability of Subantarctic Mode Water and Antarctic Intermediate Water in the Drake Passage during the Late-Twentieth and Early-Twenty-First Centuries. *Journal of Climate* 22: 3661–3688.
- Naveira Garabato, A. C., Leach, H., Allen, J. T., Pollard, R. T., and Strass, V. (2001) Mesoscale Subduction at the Antarctic Polar Front Driven by Baroclinic Instability. *Journal of Physical Oceanography* 31(8): 2087–2107.
- Naveira Garabato, A. C., Polzin, K. L., King, B. A., Heywood, K. J., and Visbeck, M. (2004) Widespread Intense Turbulent Mixing in the Southern Ocean. *Science* 303(5655): 210–213.
- Naveira Garabato, A. C., Stevens, D. P., Watson, A. J., and Roether, W. (2007) Short-circuiting of the overturning circulation in the Antarctic Circumpolar Current. *Nature* 447(7141): 194–197.
- NOAA (2021) Multivariate ENSO Index Version 2. Accessed: 5th September 2021 <<https://psl.noaa.gov/enso/mei/>>.
- NOAA/ESRL (2021) Combined Chlorofluorocarbon-11 data from the NOAA/ESRL Global Monitoring Division. Accessed: 16th December 2021 <https://gml.noaa.gov/ftp/data/hats/cfcs/cfc11/combined/HATS_global_F11.txt>.
- NOAA/ESRL (2021) Combined Chlorofluorocarbon-12 data from the NOAA/ESRL Global Monitoring Division. Accessed: 16th December 2021 <https://gml.noaa.gov/ftp/data/hats/cfcs/cfc12/combined/HATS_global_F12.txt>.
- NOAA/ESRL (2021) Combined Sulfur hexafluoride data from the NOAA/ESRL Global Monitoring Division. Accessed: 16th December 2021 <https://gml.noaa.gov/ftp/data/hats/sf6/combined/GML_global_SF6.txt>.
- Núñez-Riboni, I., Boebel, O., Ollitrault, M., You, Y., Richardson, P. L., and Davis, R. (2005) Lagrangian circulation of Antarctic Intermediate Water in the subtropical South Atlantic. *Deep-Sea Research Part II: Topical Studies in Oceanography* 52(3–4): 545–564.
- NSIDC (2020) Sea Ice Features: Polynyas. *National Snow and Ice Data Centre: All About Sea Ice*. Accessed: 12th August 2021 <<http://nsidc.org/cryosphere/seaice/characteristics/polynyas.html>>.
- Ohshima, K. I., Fukamachi, Y., Williams, G. D., Nihashi, S., Roquet, F., Kitade, Y., Tamura, T., Hirano, D., Herreiz-Borreguero, L., Field, I., Hindell, M., Aoki, S., and Wakatsuchi, M. (2013) Antarctic Bottom Water production by intense sea-ice formation in the Cape Darnley polynya. *Nature Geoscience* 6(3): 235–240.
- Olbers, D., Borowski, D., Völker, C., and Wölfle, J. O. (2004) The dynamical balance, transport and circulation of the Antarctic Circumpolar Current. *Antarctic Science* 16(4): 439–470.
- Orsi, A. H., Johnson, G. C., and Bullister, J. L. (1999) Circulation, mixing and production of Antarctic Bottom Water. *Progress in Oceanography* 43: 55–109.

- Orsi, A. H., Smethie, W. M., and Bullister, J. L. (2002) On the total input of Antarctic waters to the deep ocean : A preliminary estimate from chlorofluorocarbon measurements. *Journal of Geophysical Research* 107(C8): 1–17.
- Orsi, A. H., Whitworth, T., and Nowlin, W. D. (1995) On the meridional extent and fronts of the Antarctic Circumpolar Current. *Deep-Sea Research Part I* 42(5): 641–673.
- Ozaki, H., Obata, H., Naganobu, M., and Gamo, T. (2009) Long-term bottom water warming in the north Ross Sea. *Journal of Oceanography* 65(2): 235–244.
- Pardo, P. C., Pérez, F. F., Khatiwala, S., and Ríos, A. F. (2014) Anthropogenic CO₂ estimates in the Southern Ocean: Storage partitioning in the different water masses. *Progress in Oceanography* 120: 230–242.
- Patara, L., and Böning, C. W. (2014) Abyssal ocean warming around Antarctica strengthens the Atlantic overturning circulation. *Geophysical Research Letters* 41(11): 3972–3978.
- PMEL (n.d.) Ocean Tracer: Atmospheric Inputs of Chlorofluorocarbons. Accessed: 22nd June 2018
[<https://www.pmel.noaa.gov/cfc/atmospheric-inputs-chlorofluorocarbons>](https://www.pmel.noaa.gov/cfc/atmospheric-inputs-chlorofluorocarbons).
- Portela, E., Kolodziejczyk, N., Maes, C., and Thierry, V. (2020) Interior Water-Mass Variability in the Southern Hemisphere Oceans during the Last Decade. *Journal of Physical Oceanography* 50(2): 361–381.
- Purkey, S. G., and Johnson, G. C. (2010) Warming of global abyssal and deep Southern Ocean waters between the 1990s and 2000s: Contributions to global heat and sea level rise budgets. *Journal of Climate* 23(23): 6336–6351.
- Purkey, S. G., and Johnson, G. C. (2012) Global contraction of Antarctic Bottom Water between the 1980s and 2000s. *Journal of Climate* 25(17): 5830–5844.
- Purkey, S. G., and Johnson, G. C. (2013) Antarctic Bottom Water Warming and Freshening: Contributions to Sea Level Rise, Ocean Freshwater Budgets, and Global Heat Gain*. *Journal of Climate* 26(16): 6105–6122.
- Purkey, S. G., Smethie, W. M., Gebbie, G., Gordon, A. L., Sonnerup, R. E., Warner, M. J., and Bullister, J. L. (2018) A Synoptic View of the Ventilation and Circulation of Antarctic Bottom Water from Chlorofluorocarbons and Natural Tracers. *Annual Review of Marine Science* 10(1): 503–527.
- Read, J. F., and Pollard, R. T. (1993) Structure and transport of the Antarctic Circumpolar Current and Agulhas Return Current at 40°E. *Journal of Geophysical Research* 98(C7): 281–295.
- Redi, M. H. (1982) Oceanic Isopycnal Mixing by Coordinate Rotation. *Journal of Physical Oceanography* 12(10): 1154–1158.

- Reid, J. L. (1989) On the total geostrophic circulation of the South Atlantic Ocean: Flow patterns, tracers and transports. *Progress in Oceanography* 23: 149–244.
- Reid, J. L., Nowlin, W. D., and Patzert, W. C. (1977) On the Characteristics and Circulation of the Southwestern Atlantic Ocean. *Journal of Physical Oceanography* 7(1): 62–91.
- Renfrew, I. A., and King, J. C. (2002) Coastal polynyas in the southern Weddell Sea: Variability of the surface energy budget. *Journal of Geophysical Research* 107(C6): 3063.
- Rhein, M., Rintoul, S., Aoki, S., Campos, E., Chambers, D., Feely, R. A., Gulev, S., Johnson, G. C., Josey, S. A., Kostianoy, A., Mauritzen, C., Roemmich, D., Talley, L. D., and Wang, F. (2013) Observations: Ocean. In Stocker, T. F., Qin, D., Plattner, G.-K., Tignor, M., Allen, S. K., Boschung, J., Nauels, A., Xia, Y., Bex, V., and Midgley, P. M. (Eds.), *Climate Change 2013 - The Physical Science Basis. Contribution of Working Group I to the Fifth Assessment Report of the Intergovernmental Panel on Climate Change*. Cambridge and New York: Cambridge University Press.
- Richardson, P. L. (2007) Agulhas leakage into the Atlantic estimated with subsurface floats and surface drifters. *Deep-Sea Research Part I: Oceanographic Research Papers* 54(8): 1361–1389.
- Rintoul, S. R. (1991) South Atlantic interbasin exchange. *Journal of Geophysical Research: Oceans* 96(C2): 2675–2692.
- Roquet, F., Madec, G., McDougall, T. J., and Barker, P. M. (2015) Accurate polynomial expressions for the density and specific volume of seawater using the TEOS-10 standard. *Ocean Modelling* 90: 29–43.
- Rubin, S. I., and Key, R. M. (2002) Separating natural and bomb-produced radiocarbon in the ocean: The potential alkalinity method. *Global Biogeochemical Cycles* 16(4): 52-1-52-19.
- Russell, J. L., Dixon, K. W., Gnanadesikan, A., Stouffer, R. J., and Toggweiler, J. R. (2006) The Southern Hemisphere Westerlies in a Warming World: Propping Open the Door to the Deep Ocean. *Journal of Climate* 19(24): 6382–6390.
- Sallée, J. B., Speer, K., and Morrow, R. (2008) Response of the Antarctic Circumpolar Current to Atmospheric Variability. *Journal of Climate* 21(12): 3020–3039.
- Sallée, J.-B., Speer, K., Rintoul, S., and Wijffels, S. (2010) Southern Ocean Thermocline Ventilation. *Journal of Physical Oceanography* 40(3): 509–529.
- Sallée, J.-B., Shuckburgh, E., Bruneau, N., Meijers, A. J. S., Bracegirdle, T. J., Wang, Z., and Roy, T. (2013) Assessment of Southern Ocean water mass circulation and characteristics in CMIP5 models: Historical bias and forcing response. *Journal of Geophysical Research: Oceans* 118(4): 1830–1844.

- Santos, G. C., Kerr, R., Azevedo, J. L. L., Mendes, C. R. B., and da Cunha, L. C. (2016) Influence of Antarctic Intermediate Water on the deoxygenation of the Atlantic Ocean. *Dynamics of Atmospheres and Oceans* 76: 72–82.
- Santoso, A., and England, M. H. (2004) Antarctic Intermediate Water Circulation and Variability in a Coupled Climate Model. *Journal of Physical Oceanography* 34: 2160–2179.
- Schmidt, C., Schwarzkopf, F. U., Rühs, S., and Biastoch, A. (2021) Characteristics and robustness of Agulhas leakage estimates: an inter-comparison study of Lagrangian methods. *Ocean Science* 17(4): 1067–1080.
- Schmidtko, S., and Johnson, G. C. (2012) Multidecadal Warming and Shoaling of Antarctic Intermediate Water. *Journal of Climate* 25(1): 207–221.
- Schmidtko, S., Johnson, G. C., and Lyman, J. M. (2013) MIMOC: A global monthly isopycnal upper-ocean climatology with mixed layers. *Journal of Geophysical Research: Oceans* 118(4): 1658–1672.
- Schouten, M. W., de Ruijter, W. P. M., van Leeuwen, P. J., and Lutjeharms, J. R. E. (2000) Translation, decay and splitting of Agulhas rings in the southeastern Atlantic Ocean. *Journal of Geophysical Research: Oceans* 105(C9): 21913–21925.
- Shannon, L. V., and Chapman, P. (1991) Evidence of Antarctic bottom water in the Angola Basin at 32°S. *Deep Sea Research Part A. Oceanographic Research Papers* 38(10): 1299–1304.
- Shao, A. E., Mecking, S., Thompson, L., and Sonnerup, R. E. (2013) Mixed layer saturations of CFC-11, CFC-12, and SF 6 in a global isopycnal model. *Journal of Geophysical Research: Oceans* 118(10): 4978–4988.
- Silvy, Y., Guilyardi, E., Sallée, J., and Durack, P. J. (2020) Human-induced changes to the global ocean water masses and their time of emergence. *Nature Climate Change* 10: 1030–1036.
- Sloyan, B. M., and Rintoul, S. R. (2001) Circulation, Renewal, and Modification of Antarctic Mode and Intermediate Water*. *Journal of Physical Oceanography* 31(4): 1005–1030.
- Sloyan, B. M., Talley, L. D., Chereskin, T. K., Fine, R., and Holte, J. (2010) Antarctic Intermediate Water and Subantarctic Mode Water Formation in the Southeast Pacific: The Role of Turbulent Mixing. *Journal of Physical Oceanography* 40(7): 1558–1574.
- Smeed, D. A., Josey, S. A., Beaulieu, C., Johns, W. E., Moat, B. I., Frajka-Williams, E., Rayner, D., Meinen, C. S., Baringer, M. O., Bryden, H. L., and McCarthy, G. D. (2018) The North Atlantic Ocean Is in a State of Reduced Overturning. *Geophysical Research Letters* 45(3): 1527–1533.
- Smythe-Wright, D., Gordon, A. L., Chapman, P., and Jones, M. S. (1996) CFC-113 shows Brazil eddy crossing the South Atlantic to the Agulhas retroreflection region. *Journal of Geophysical Research: Oceans* 101(C1): 885–895.

- Sokolov, S., and Rintoul, S. R. (2007) Multiple Jets of the Antarctic Circumpolar Current South of Australia. *Journal of Physical Oceanography* 37(5): 1394–1412.
- Son, S.-W., Polvani, L. M., Waugh, D. W., Akiyoshi, H., Garcia, R., Kinnison, D., Pawson, S., Rozanov, E., Shepherd, T. G., and Shibata, K. (2008) The Impact of Stratospheric Ozone Recovery on the Southern Hemisphere Westerly Jet. *Science* 320(5882): 1486–1489.
- Speer, K., Rintoul, S. R., and Sloyan, B. (2000) The Diabatic Deacon Cell*. *Journal of Physical Oceanography* 30(12): 3212–3222.
- Stöven, T., Tanhua, T., and Hoppema, M. (2014) Transient tracer applications in the Southern Ocean. *Ocean Science Discussions* 11(5): 2289–2335.
- Stöven, T., Tanhua, T., Hoppema, M., and Bullister, J. L. (2015) Perspectives of transient tracer applications and limiting cases. *Ocean Science* 11(5): 699–718.
- Stuiver, M., and Quay, P. D. (1980) Changes in Atmospheric Carbon-14 Attributed to a Variable Sun. *Science* 207(4426): 11–19.
- Sverdrup, H. U., Johnson, M. J., and Fleming, R. H. (1942) The Water Masses and Currents of the Oceans. In *The Oceans: Their Physics, Chemistry, and General Biology*. New York: Prentice Hall.
- Swart, N. C., and Fyfe, J. C. (2012) Observed and simulated changes in the Southern Hemisphere surface westerly wind-stress. *Geophysical Research Letters* 39(L16711): 1–6.
- Swart, S., Johnson, K., Mazloff, M. R., Meijers, A., Meredith, M. P., Newman, L., and Sallée, J.-B. (2018) Return of the Maud Rise Polynya: climate litmus or sea ice anomaly? In *State of the Climate in 2017. Bulletin of the American Meteorological Society* 99(8): S188-189.
- Talley, L. D. (1996) Antarctic Intermediate Water in the South Atlantic. In Wefer, G., Berger, W. H., Siedler, G., and Webb, D. (Eds.), *The South Atlantic: Present and Past Circulation* (1st ed.). Berlin: Springer Berlin Heidelberg.
- Talley, L. D., Pickard, G. L., Emery, W. J., and Swift, J. H. (2011) Atlantic Ocean. *Descriptive Physical Oceanography* : 245–301. doi:10.1016/b978-0-7506-4552-2.10009-5.
- Thompson, D. W. J., and Solomon, S. (2002) Interpretation of recent Southern Hemisphere climate change. *Science* 296(5569): 895–899.
- Ting, Y. H., and Holzer, M. (2017) Decadal changes in Southern Ocean ventilation inferred from deconvolutions of repeat hydroographies. *Geophysical Research Letters* 44(11): 5655–5664.
- Toggweiler, J. R. (2009) Shifting Westerlies. *Science* 323(5920): 1434–1435.
- Urakawa, L. S., and Hasumi, H. (2012) Eddy-resolving model estimate of the cabbeling effect on the water mass transformation in the Southern Ocean. *Journal of Physical Oceanography* 42(8): 1288–1302.

Urey, H. (1947) The Thermodynamic Properties of Isotopic Substances. *Journal of the Chemical Society* (0): 562–581.

Warner, M. J., and Weiss, R. F. (1985) Solubilities of chlorofluorocarbons 11 and 12 in water and seawater. *Deep Sea Research Part A. Oceanographic Research Papers* 32(12): 1485–1497.

Waugh, D. W. (2003) Relationships among tracer ages. *Journal of Geophysical Research* 108(C5): 3138.

Waugh, D. W. (2014) Changes in the ventilation of the southern oceans. *Philosophical Transactions of the Royal Society A: Mathematical, Physical and Engineering Sciences* 372(2019): 20130269–20130269.

Waugh, D. W., Haine, T. W. N., and Hall, T. M. (2004) Transport times and anthropogenic carbon in the subpolar North Atlantic Ocean. *Deep Sea Research Part I: Oceanographic Research Papers* 51(11): 1475–1491.

Waugh, D. W., Hall, T. M., Mcneil, B. I., Key, R., and Matear, R. J. (2006) Anthropogenic CO₂ in the oceans estimated using transit time distributions. *Tellus B: Chemical and Physical Meteorology* 58(5): 376–389.

Waugh, D. W., McC. Hogg, A., Spence, P., England, M. H., and Haine, T. W. N. (2019) Response of Southern Ocean Ventilation to Changes in Midlatitude Westerly Winds. *Journal of Climate* 32(17): 5345–5361.

Waugh, D. W., Primeau, F., DeVries, T., and Holzer, M. (2013) Recent Changes in the Ventilation of the Southern Oceans. *Science* 339(6119): 568–570.

Whitworth, T., and Peterson, R. G. (1985) Volume Transport of the Antarctic Circumpolar Current from Bottom Pressure Measurements. *Journal of Physical Oceanography* 15(6): 810–816.

Williams, G. D., Aoki, S., Jacobs, S. S., Rintoul, S. R., Tamura, T., and Bindoff, N. L. (2010) Antarctic Bottom Water from the Adélie and George V Land coast, East Antarctica (140–149°E). *Journal of Geophysical Research* 115(C4).

Wong, A. P. S., Bindoff, N. L., and Church, J. A. (1999) Large-scale freshening of intermediate waters in the Pacific and Indian oceans. *Nature* 400(6743): 440–443.

Wust, G. (1935) *Schichtung und Zirculation des Atlantischen Ozeans. Die Stratospäre. Wissenschaftliche Ergebnisse der Deutschen Atlantischen Expedition auf dem Forschungsund Vermessungsschiff "Meteor" 1925-1927*. Berlin.

Yabuki, T., Suga, T., Hanawa, K., Matsuoka, K., Kiwada, H., and Watanabe, T. (2006) Possible source of the antarctic bottom water in the Prydz Bay Region. *Journal of Oceanography* 62(5): 649–655.

Yao, W., Shi, J., and Zhao, X. (2017) Freshening of Antarctic Intermediate Water in the South Atlantic Ocean in 2005–2014. *Ocean Science* 13(4): 521–530.

- You, Y. (1998) Intermediate water circulation and ventilation of the Indian Ocean derived from water-mass contributions. *Journal of Marine Research* 56(5): 1029–1067.
- You, Y. (2002) Quantitative estimate of Antarctic Intermediate Water contributions from the Drake Passage and the southwest Indian Ocean to the South Atlantic. *Journal of Geophysical Research* 107(C4).
- Zanowski, H., Hallberg, R., and Sarmiento, J. L. (2015) Abyssal Ocean Warming and Salinification after Weddell Polynyas in the GFDL CM2G Coupled Climate Model. *Journal of Physical Oceanography* 45(11): 2755–2772.
- Zanowski, H., and Hallberg, R. (2017) Weddell Polynya Transport Mechanisms in the Abyssal Ocean. *Journal of Physical Oceanography* 47: 2907–2925.
- Zenk, W., and Morozov, E. (2007) Decadal warming of the coldest Antarctic Bottom Water flow through the Vema Channel. *Geophysical Research Letters* 34(14): L14607.
- Zenk, W., and Visbeck, M. (2013) Structure and evolution of the abyssal jet in the Vema Channel of the South Atlantic. *Deep Sea Research Part II: Topical Studies in Oceanography* 85: 244–260.